Recent Strain Rate and Deformation Field of Egypt by GPS and InSAR

Heft 47
Schriftenreihe der Fachrichtung Geodäsie
Bau- und Umweltingenieurwissenschaften
Technische Universität Darmstadt
ISBN 978-3-935631-36-5

Darmstadt, September 2015

TECHNISCHE
UNIVERSITÄT
DARMSTADT

Heft 47

Darmstadt, September 2015

Mohamed Saleh Ahmed Mohamed

Recent Strain Rate and Deformation Field of Egypt by GPS and InSAR

Schriftenreihe
Fachrichtung Geodäsie
Fachbereich Bau- und Umweltingenieurwissenschaften
Technische Universität Darmstadt

ISBN 978-3-935631-36-5

Schriftenreihe Fachrichtung Geodäsie der Technischen Universität Darmstadt
Zugl.: Darmstadt, Technische Universität, Dissertation, 2015
D17

Verantwortlich für die Herausgabe der Schriftenreihe:

Der Sprecher der Fachrichtung Geodäsie
im Fachbereich Bau- und Umweltingenieurwissenschaften
der Technischen Universität Darmstadt

Gedruckt bzw. veröffentlicht mit Unterstützung des
Deutschen Akademischen Austauschdienstes

Bezugsnachweis:

Technische Universität Darmstadt
Institut für Geodäsie
Franziska-Braun-Straße 7
64287 Darmstadt

ISBN: 978-3-935631-36-5

Recent Strain Rate and Deformation Field of Egypt by GPS and InSAR

Vom Fachbereich Bau- und Umweltingenieurwissenschaften
der Technischen Universität Darmstadt
zur Erlangung des akademischen Grades eines
Doktor-Ingenieurs (Dr.-Ing.) genehmigte Dissertation

vorgelegt von
M.Sc. Mohamed Saleh Ahmed Mohamed
aus Kairo, Ägypten

Referent:	**Prof. Dr.-Ing. Matthias Becker**
Korreferent:	**Prof. Dr.-Ing. Uwe Sörgel**
Tag der Einreichung:	**01. July 2015**
Tag der mündlichen Prüfung:	**01. September 2015**

Darmstadt, September 2015
D17

Acknowledgments

All praise is due to Almighty God for his guidance and helping me to bring forth the present study.

First and more foremost I would like to express my sincere appreciation and thanks to my supervisors Prof. Dr.-Ing. Matthias Becker and Prof. Dr.-Ing. Uwe Sörgel, Institute of Geodesy, Faculty of Civil and Environmental Engineering, Technische Universität Darmstadt, for their instant guidance and kind supervision at the highest standards during my study. I am also grateful to Dr. Stefan Leinen for his suggestions and valuable comments during this work. Thanks also go to all researchers and personnel at the chair of Physical and Satellite Geodesy, in particular to office mate Leonor Mendoza for her good humor. Other colleagues from the Geodetic Institute, Karlsruhe Institute of Technology especially, Prof. Bernhardt Heck and Thomas Fuhrmann for their kind help and support.

A lot of thanks go to all staff members of the Laboratory of Crustal Movement, Geodynamics Department, National Research Institute of Astronomy and Geophysics (NRIAG) for providing the GPS data used in this work. Special thanks are to my colleagues Prof. Abdel-Monem Sayed Mohamed and Dr. Nadia Abou-Aly for their help and encouragement to finish this study. Thanks also to Prof. Mustapha Meghraoui from Institut de Physique du Globe, Strasbourg, France for his valuable comments and discussion on the regional geodynamics.

I am grateful to the many individuals and institutions that support this work. ERS and Envisat Radar data used in this thesis were provided by the European Space Agency (ESA). SAR images were focused using the ROI_PAC software package developed by JPL/Caltech. Interferograms were created using the Delft University of Technology software package (DORIS). The PS processing was carried out using the Stanford Method for Persistent Scatterer (StaMPS) Software. Almost all maps in this thesis were generated using the public domain Generic Mapping Tools (GMT) software. Thanks to the German Academic Exchange Service (DAAD) for funding my stay at TU-Darmstadt through the grant (DAAD-57076387).

Finally, my heartfelt thanks go to my family especially my parents, my brother and my sisters for their encouragement and support. I am grateful to my wife and my daughter for giving me the time and comfort to complete this work. I can not find the words to express my deepest gratitude for the support they have given me.

Abstract

The Earth's crustal movements occur at local and regional scale with various intensities that depend on the tectonic settings. Egypt's surface deformation is controlled by its location. It is located in the northeastern corner of the African continent and affected from the North by the subduction between Nubian and Eurasian plates and from the East by activities along the Red Sea spreading, Gulf of Suez, and Gulf of Aqaba. Away from the tectonic activities, the ground deformation could be triggered by human activities such as artificial lakes, underground water pumping or oil extraction. Estimating the recent crustal movements of the Earth's crust and its relation to tectonic and/or human activities can assist in better understanding of such movements, identify its nature, and highlight the areas of high strain for the security of human, public facilities, and vital national constructions.

Due to the lack of geodetic data collected from Egypt, former estimates are rough at best. Using very few GPS stations in Egypt, previous studies indicate northward motion of northern Nubia with respect to Eurasia of about 5 mm/yr ((McClusky et al., 2000); (Reilinger et al., 2006); (Mahmoud et al., 2005)). In order to better constrain the movement rate of northern Nubia and the interaction between Nubian, Eurasian, and Arabian plates, 16 permanent GPS stations in combination with 47 non-permanent stations covering Egypt for the period 2006-2012 were used. The collected data for about seven years were processed using Bernese 5.2 GNSS Software (Dach et al., 2007). To establish a good configuration around the Egyptian stations, the processing is carried out including 86 permanent stations belonging to three different tectonic plates. This led to a considerably better coverage of the Sinai-Dead Sea region as it represents the border between the Nubian and Arabian plates. Also, 34 stations out of these 86 are included in the ITRF2008 and used for datum definition. The Bernese results are assessed using the time series analysis tool CATS (Williams, 2008).

The estimated absolute horizontal velocity field for Egypt is about $28-30$ mm/yr to the northeast direction. GPS sites show a relative motion between Nubia and Eurasia of about 6.5 ± 1 mm/yr, which increases towards the Hellenic trench, 8.2 ± 0.8 mm/yr in Sinai peninsula, 14.2 ± 1.4 mm/yr in the North of the Arabian plate and 22.3 ± 0.7 mm/yr in eastern and central Turkey. In the Nubia fixed frame the Gulf of Suez and southern Sinai do not show any significant horizontal velocities, which implies that Sinai may be still connected to Nubia. Applying the dislocation fault parallel analysis, the slip rate and the locking depth of the Dead Sea Transform (DST) fault are $5-7$ mm/yr and $12-18$ km, respectively. High strain rates are highly localized along the DST fault ($40-90 \times 10^{-9}$) and low to moderate strain rates are found in the Gulf of Suez and Southern Sinai ($20-40 \times 10^{-9}$). The rest of Egypt looks quite stable, and no intraplate deformation is found.

To overcome the problem of the coarse distribution of the GPS stations and low accuracy of the movement rate from GPS in the Up component, Interferometric Synthetic Aperture Radar (InSAR) is chosen as complementary technique to measure the ground deformation of the Nile Delta. The InSAR scenes from ERS1, ERS2, and Envisat descending tracks of 5.6 cm wavelength were used in this study. 36 and 37 scenes are acquired from Envisat tracks while 20 and 24 scenes are available from ERS tracks. The SAR scenes cover the time span 1992-2010. The magnitude and pattern of the Nile Delta subsidence are measured by the Permanent Scatterer Interferometry (PSI) technique. The PSI processing was carried out using Stanford Method for Persistent Scatterer (StaMPS) software (Hooper et al., 2012).

The InSAR velocity maps from ERS and Envisat show that the Nile Delta is almost stable, with good agreement with the GPS results, and the estimated ground deformation is strongly localized at the big cities. The time series plots for selected PS pixels from Cairo, Tanta, Mahala, Mansoura, Damietta, and Port Said showed that the estimated subsidence rates from Envisat scenes are $5.5-6.0 \pm 0.4$ mm/yr, 3.6 ± 0.6 mm/yr, $3.4-5.9 \pm 1.0$ mm/yr, $9.3-8.7 \pm 1.2$ mm/yr, 9.3 ± 1.6 mm/yr, and 4.4 ± 1.6 mm/yr, respectively. Whereas, the estimated subsidence rates from ERS scenes are $3.8-3.5 \pm 0.6$ mm/yr, $3.5 \pm$

1.0 mm/yr, 2.4−3.7±1.2 mm/yr, 4.4−9.3±1.6 mm/yr, 10.0±1.8 mm/yr, and 8.6±1.8 mm/yr for Cairo, Tanta, Mahala, Mansoura, Damietta, and Port Said, respectively. Generally, the subsidence rates of the highly populated cities like Cairo and Mahala determined from the ERS scenes are smaller than the rates estimated from the Envisat scenes by about 2 mm/yr. The localization of the subsidence rates at the big cities implies that the detected signals may be due to human activities, such as underground water pumping. The rapid increase of the underground water pumping rate in the last decade may be the cause of the difference in subsidence rates estimated from the ERS and Envisat of 2 mm/yr. The lack of in-situ data limited the verification of this interpretation.

This study presents the current state of the recent crustal movement in Egypt and its relation to tectonic and/or human activities. Also, the capabilities and limitations of the application of InSAR technique within a highly vegetated area like the Nile Delta are addressed in this thesis. Highlighted areas that suffered from high ground deformation present the need of regular and long-run monitoring for such deformation process.

Zusammenfassung

Die Krustenbewegungen der Erde treten auf lokaler und regionaler Ebene mit verschiedenen, von den tektonischen Gegebenheiten abhängigen Intensitäten auf. Die Oberflächenverformungen in Ägypten sind von der geografischen Lage des Landes bestimmt. Es befindet sich in der nordöstlichen Ecke des afrikanischen Kontinents und es wird im Norden durch die Subduktion zwischen der Nubischen und der Eurasischen Platte und im Osten durch die Tektonik des Golfs von Suez und Golf von Aqaba, sowie durch die Aufspreizung des Roten Meeres beeinflusst. Neben den tektonisch bedingten Aktivitäten können Deformationen und insbesondere Höhenänderungen durch menschliche Aktivitäten wie künstliche Seen, Entnahme von Grundwasser oder Ölförderung ausgelöst werden. Die Erfassung der Krustenbewegungen und die Identifikation der Ursachen in tektonischen und/oder menschlichen Aktivitäten ist zum besseren Verständnis der Folgen solcher Bewegungen nötig. Nur so können Risikoabschätzungen für die verschiedenen Regionen erstellt werden und die Gefährdung von öffentlichen Einrichtungen und lebenswichtigen nationalen Infrastrukturen abgeschätzt werden und deren Sicherheit gewährleistet werden.

In Ägypten sind die bisherigen Kenntnisse der Bewegungen wegen der fehlenden geodätischen Messungen bisher nur sehr pauschal bekannt. Auf der Basis von relativ wenigen GPS-Stationen in Ägypten, zeigen frühere Studien eine Bewegung des nördlichen Nubien in Bezug auf Eurasien von etwa 5 mm/yr ((McClusky et al., 2000); (Reilinger et al., 2006); (Mahmoud et al., 2005)) in nord-nordöstlicher Richtung. Zur besseren Beschreibung der Bewegungen des nördlichen Teils von Nubien, und der Interaktion zwischen der Nubischen, der Eurasischen und der Arabischen Platte, wurden im Zeitraum von 2006 bis 2012 16 permanente GPS-Stationen in Kombination mit 47 Epochenstationen in Ägypten eingerichtet und beobachtet. Die Daten aus etwa sieben Jahren wurden mit der Bernese GPS Auswertesoftware. Das ägyptische Netze wurde durch Einbeziehung von 86 umliegenden GPS Permanentstationen auf drei verschiedenen tektonischen Platten, erweitert. Dies führte zu einer deutlich besseren Abdeckung der Sinai-Totes Meer Region, die die Grenze zwischen der Nubische und arabischen Platte repräsentiert. Daneben sind 34 Stationen aus diesen 86 im ITRF2008 enthalten und konnten zur Datumsfestlegung des Netzes verwendet werden. Die Ergebnisse wurden unter Verwendung des Zeitreihenanalyse-Tool CATS statistisch analysiert und ihre Genauigkeit realistisch bewertet (Williams, 2008).

Das so bestimmte absolute horizontale Geschwindigkeitsfeld für Ägypten zeigt eine Bewegung von etwa $28-30\ mm/yr$ in nordöstlicher Richtung. Die Relativbewegung zwischen Nubien und Eurasien beträgt etwa $6.5 \pm 1\ mm/yr$, mit einer in Richtung des Hellenischen Grabens ansteigenden Rate von $8.2 \pm 0.8\ mm/yr$ für die Sinai-Halbinsel, $14.2 \pm 1.4\ mm/yr$ im Norden der arabischen Platte und $22.3 \pm 0.7\ mm/yr$ in der Ost- und Mittel Türkei. In Bezug auf die Nubische Platte hat der Golf von Suez und das südliche Sinai keine signifikante horizontale Geschwindigkeiten, was bedeutet, dass Sinai noch an die Nubische Platte gekoppelt ist. Die Bestimmung der Verschiebungsrate an der Dead-Sea-Transform-Verwerfung ergab eine Schlupfrate von $5-7\ mm/yr$ und die Blockade in einer Tiefe und $12-18\ km$. Die größten Spannungen von $40-90 \times 10^{-9}$ treten sehr lokal entlang der Verwerfung auf, nur geringe Strainwerte von $20-40 \times 10^{-9}$ sind im Golf von Suez und im südlichen Sinai zu beobachten. Der Rest von Ägypten ist recht stabil und zeigt keine signifikanten Intra-Plattendeformationen.

Um das Problem der spärlichen Punkteverteilung und der in GPS geringeren Höhengenauigkeit zu überwinden, wurde ergänzend die Interferometric Synthetic Aperture Radar (InSAR) Technik angewendet. Ziel war speziell die Höhenänderungen im Nildeltas zu messen. Die InSAR Szenen der absteigend Spuren von ERS1, ERS2, und des Envisat Satelliten mit 5.6 cm Wellenlänge wurden in dieser Untersuchung verwendet. Insgesamt wurden 36 plus 37 Szenen von Envisat und 20 plus 24 Szenen aus ERS Tracks verwendet. Die SAR-Szenen decken den Zeitraum 1992-2010 ab. Das Ausmaß und die Muster der Setzungen im Nildelta wurden mit dem Permanent Scatterer Interferometrie (PSI) Technik berechnet. Die

PSI Verarbeitung erfolgte mit der Stanford-Methode für Persistent Scatterer (StaMPS) Software (Hooper et al., 2012).

Die Karten der InSAR Geschwindigkeiten aus ERS und Envisat Daten zeigen, dass das Nil-Delta nahezu stabil ist, in guter Übereinstimmung mit den GPS-Ergebnissen. Soweit Bodenbewegungen bestimmt wurden, sind sie stark lokalisiert und konzentrieren sich in den großen Städten. Die Zeitreihen der Bewegungen aus Envisat-Daten für ausgewählte Reflektionen in Kairo, Tanta, Mahala, Mansoura, Damietta, und Port Said zeigen Subsidenzraten von $5.5{-}6.0 \pm 0.4\ mm/yr$, $3.6 \pm 0.6\ mm/yr$, $3.4{-}5.9 \pm 1.0\ mm/yr$, $9.3 - 8.7 \pm 1.2\ mm/yr$, $9.3 \pm 1.6\ mm/yr$, und $4.4 \pm 1.6\ mm/yr$. Die ERS-Daten sind mit Subsidenzraten von $3.8 - 3.5 \pm 0.6\ mm/yr$, $3.5 \pm 1.0\ mm/yr$, $2.4 - 3.7 \pm 1.2\ mm/yr$, $4.4 - 9.3 \pm 1.6\ mm/yr$, $10.0 \pm 1.8\ mm/yr$, und $8.6 \pm 1.8\ mm/yr$ für Kairo , Tanta, Mahala, Mansoura, Damietta, und Port Said ähnlich. Dabei sind die Raten für die dicht besiedelten Städte wie Kairo und Mahala bei ERS Szenen um etwa 2 mm/yr kleiner als die Envisat Raten. Die Lokalisierung der Subsidenzraten in den großen Städten lässt vermuten, dass sie auf menschliche Einflüsse zurückgehen. Sie zeigen Aktivitäten, wie Grundwasserentnahme, die in den letzten zehn Jahren deutlich zugenommen hat und damit auch die unterschiedlichen Raten von ERS und Envisat plausibel machen könnten. In-Situ Messungen, z.B. Nivellements wären nötig um diese Schlussfolgerungen zu verifizieren.

Diese Arbeit stellt den aktuellen Stand der Kenntnisse über die rezenten tektonischen Bewegungen in Ägypten und deren Beziehung zu tektonischen und/oder menschliche Aktivitäten dar. Darüber hinaus werden die Möglichkeiten und Grenzen der Anwendung der InSAR-Technik in Gegenden mit starkem Bewuchs, wie das Nil-Delta adressiert. Die in regionalen Bereichen identifizierten Gebiete mit großen Bodenbewegungen belegen die Notwendigkeit einer regelmäßiger und langfristiger Überwachung für solche Deformationszonen.

Contents

Abstract iii

Zusammenfassung iv

List of Tables ix

List of Figures x

List of Acronyms xiv

List of Symbols xv

1 Introduction 1
- 1.1 Contribution 1
- 1.2 Thesis Roadmap 2

2 Background 3
- 2.1 Tectonic Setting of Egypt 3
- 2.2 Global Navigation Satellite Systems (GNSS) 11
  - 2.2.1 GPS Components 11
    - 2.2.1.1 Space Segment 11
    - 2.2.1.2 Control Segment 11
    - 2.2.1.3 User Segment 11
  - 2.2.2 Satellite Signal 11
    - 2.2.2.1 Code Pseudoranges 12
    - 2.2.2.2 Phase Pseudoranges 12
    - 2.2.2.3 Navigation Message 12
  - 2.2.3 Source of Errors 12
  - 2.2.4 Forming Differences and Linear Combinations 13
  - 2.2.5 IGS Products 15
- 2.3 Interferometric Synthetic Aperture Radar (InSAR) 16
  - 2.3.1 History 16
  - 2.3.2 SAR Interferometry 16
    - 2.3.2.1 Differential InSAR 18
    - 2.3.2.2 Multi-temporal InSAR 19
    - 2.3.2.3 Multi-dimensional InSAR 20

3 Data Processing 23
- 3.1 GPS Data 23
  - 3.1.1 Processing setup 28
  - 3.1.2 GPS Combined Solution 31
  - 3.1.3 Error Assessment (Scaling) 31
  - 3.1.4 Time Series Analysis 34
  - 3.1.5 Euler Pole Parameters 36
  - 3.1.6 Strain Rate Tensor 43
- 3.2 Interferometric Synthetic Aperture Radar (InSAR) 44

3.2.1 InSAR Data 44
3.2.2 Persistent Scatterers InSAR Processing 45
3.2.2.1 Image Formation 45
3.2.2.2 Master-scene Selection 46
3.2.2.3 Oversampling 50
3.2.2.4 Coregistration 50
3.2.2.5 Interferogram Generation 50
3.2.2.6 Permanent Scatterers Selection 50
3.2.2.7 Phase Unwrapping 51

4 Results and Discussion 53
4.1 GPS Results 53
4.1.1 Absolute Horizontal Velocity Field 53
4.1.2 Relative velocity Field 55
4.1.2.1 Eurasia Fixed Frame 55
4.1.2.2 Nubia Fixed Frame 62
4.1.2.3 Sinai Fixed Frame 64
4.1.2.4 Slip Rate and Locking Depth Estimation 65
4.1.2.5 Strain Results 68
4.1.3 Absolute Vertical Velocity Field 71
4.2 InSAR Results 72
4.2.1 ERS Results 72
4.2.1.1 Time Series 75
4.2.2 Envisat Results 78
4.2.2.1 Time Series 78
4.3 Discussion 83
4.3.1 Nubia-Eurasia 83
4.3.2 Arabia-Sinai 83
4.3.3 Sinai-Nubia 84
4.3.4 DST Slip Rate and Locking Depth 86
4.3.5 Strain Accumulation 86
4.3.6 Sinai Sub-plate 88
4.3.7 Nile Delta Subsidence 89

5 Conclusions and Future Work 97
5.1 Conclusions 97
5.2 Future Work 102

References 105

Appendix 111
Tables 111
Figures 117
Curriculum Vitae 118

List of Tables

2.1 GPS satellite orbits in addition to satellite and station clocks (IGS, 2015). 15

3.1 Equipment of permanent and non-permanent Egyptian stations. 26
3.2 Estimation of the average scaled error for Aswan (AS), Greater Cairo (GC), Gulf of Suez (GS), Nile Valley (NV), Abu-Dabbab (AD), EPGN (Egyptian Permanent GPS Network) stations in North, East, and Up components. 33
3.3 Velocities and their standard deviations from different stochastic models for stations PHLW, SAFG, WIND, and SOFI in mm/yr. 36
3.4 Availability of the InSAR data from ERS and Envisat satellite missions with incidence angles. The values between parentheses represent the incidence angle of the middle of the swath. 45

4.1 CATS velocities and uncertainties, stochastic model used is white noise plus power law noise, for permanent stations in addition to Bernese velocities and scaled error for the non-permanent stations. IGS stations (P-IGS), ITRF08 stations used for datum definition (P-IGS*), Egyptian permanent stations (P-EGY), Egyptian Epoch stations (E-EGY), SOPAC stations (P-SOP) and UNAVCO stations (P-UNA). 53
4.2 Estimated Euler vectors from this study, absolute and relative. 56
4.3 Comparison between the achieved results from both satellite missions (ERS and Envisat) in both tracks (207 and 436). (*) stands for the estimated trend excluding the scene in 1992. 95

List of Figures

2.1 Focal mechanisms for earthquakes occurred in Nubian, Eurasian, Arabian and Somalian plates from `http://www.globalcmt.org/CMTsearch.html` ((Dziewonski et al., 1981) and (Ekström et al., 2012)), 1976 to December 2012, with plate boundaries ((Bird, 2003) and (Argus et al., 2010)), red lines represent the plate boundary. NU = Nubia; AR = Arabia; SOL = Somalia; LW = Lwandle; AN = Anatolia; EU = Eurasia. 4

2.2 Geologic map of Egypt, generalized by (Hammad, 1975), after (Said, 1962), Geological Survey of Egypt. 5

2.3 Egypt's geological provinces, (Said, 1962). 6

2.4 Plate motion model proposed by (Reilinger et al., 2006) for Nubia-Arabia-Eurasia interaction. 8

2.5 Seismic activity recorded by ENSN from 1997 to 2012. Red lines are the surface faults (Egyptian Geological Survey and Mining Authority (EGSMA), 1981). Blue lines represent the Dead Sea Transform fault. 9

2.6 Focal mechanisms for earthquakes occurred in Egypt for the period 1976 to 2012. Greens are the solution from Global CMT `http://www.globalcmt.org/CMTsearch.html` ((Dziewonski et al., 1981) and (Ekström et al., 2012)) and Reds are the solution from (Abou Elenean, 2007). 10

2.7 Past, current, and future satellite SAR missions. 17

2.8 SAR imaging geometry. 18

2.9 Interferometeric configuration of two SAR antennas separated by a baseline B, $B_\perp$ is the perpendicular baseline, θ_1 and θ_2 are the look angles of SAR1 and SAR2, ρ_1 and ρ_2 are the range (slant range) for SAR1 and SAR2, respectively, and h_t is the point's height. . . . 19

2.10 Simulated phase for (a) a distributed scatterer pixel and (b) a persistent scatterer pixel. The brighter scatterer in b is three times brighter than the sum of the smaller scatterers (Hooper, 2006). 20

2.11 Combination of the results of both Ascending and Descending information. (a) in case of vertical motion, the target is moving away from the satellite in both directions and (b) in case of horizontal motion, the target is moving away from one satellite and toward the second. 21

2.12 SAR geometry in case of imaging the same area by two adjacent tracks. 21

3.1 Geographic distribution of the Egyptian GPS stations, red triangle (Aswan), green triangle (Nile Valley), yellow triangle (Gulf of Suez), blue triangle (Greater Cairo), violet triangle (Abu-Dabbab) and violet circles (EPGN stations) in addition to SOPAC sites (black triangle). 24

3.2 Some photos for typical stations of the Egyptian Permanent GPS Network (EPGN) and non-permanent station (AD01 from Abu-Dabbab network). 25

3.3 Availability of the EPGN stations. 27

3.4 Availability of the campaign data for each local network, for the period 2006-2012. 28

3.5 Selected permanent stations (IGS, EPN, UNAVCO, and SOPAC) and the Egyptian stations with plate boundaries (as in Figure 2.1). 29

3.6 Flow diagram of the processing steps in Bernese GPS Software Version 5.2. The orange boxes represent programs. 30

3.7 Repeatability of EPGN (a) and the selected stations from IGS, EPN, SOPAC, and UNAVCO (b). 32

3.8 Flow diagram of the CATS processing scheme. 35

3.9 The estimated parameters $[k, a_k, a]$ of the white noise plus power law noise model over the data period. Each station represented by one dot in each component (East, North, and Up). . . . 37
3.10 Bernese raw time series (blue line) and the estimated CATS time series (red line) for station PHLW in the left hand side and the residuals in the right hand side in each component. Stochastic model used is white noise plus power law noise. . . . 38
3.11 Bernese raw time series (blue line) and the estimated CATS time series (red line) for station SAFG in the left hand side and the residuals in the right hand side in each component. Stochastic model used is white noise plus power law noise. . . . 39
3.12 Bernese raw time series (blue line) and the estimated CATS time series (red line) for station SOFI in the left hand side and the residuals in the right hand side in each component. Stochastic model used is white noise plus power law noise. . . . 40
3.13 Bernese raw time series (blue line) and the estimated CATS time series (red line) for station WIND in the left hand side and the residuals in the right hand side in each component. Stochastic model used is white noise plus power law noise. . . . 41
3.14 Selected sites for Euler poles estimation. Red: sites close to plate boundaries or in deformation zones. Blue: sites with observations less than two years. Black: sites with repeatability larger than 3 mm. Green: the final selection of 91 sites. . . . 42
3.15 Key map of the Nile Delta 44
3.16 Satellite tracks covering the Nile Delta. (a) descending and (b) ascending tracks. . . . 45
3.17 Simplified scheme of the PS processing steps. . . . 47
3.18 SAR images of track 207, Envisat satellite mission. Plotted circles are the SAR acquisitions. Circle's color represents the Doppler Centroid Frequency (F_{DC}). Square indicates master chosen for Persistent Scatterer InSAR analysis. . . . 48
3.19 SAR images of track 436, Envisat satellite mission. Plotted circles are the SAR acquisitions. Circle's color represents the Doppler Centroid Frequency (F_{DC}). Square indicates master chosen for Persistent Scatterer InSAR analysis. . . . 48
3.20 SAR images of track 207, ERS1&2 satellite mission. Plotted circles are the SAR acquisitions. Circle's color represents the Doppler Centroid Frequency (F_{DC}). Square indicates master chosen for Persistent Scatterer InSAR analysis. . . . 49
3.21 SAR images of track 436, ERS1&2 satellite mission. Plotted circles are the SAR acquisitions. Circle's color represents the Doppler Centroid Frequency (F_{DC}). Square indicates master chosen for Persistent Scatterer InSAR analysis. . . . 49

4.1 Estimated ITRF2008 horizontal velocities of the selected permanent stations in addition to Egyptian stations, permanent and epoch, with 95% confidence region. Red lines represent the plate boundaries (as in Figure 2.1). . . . 57
4.2 Estimated ITRF2008 horizontal velocities for Egypt-Sinai-DST fault region, with 95% confidence region. Red lines represent the plate boundaries (as in Figure 2.1). . . . 58
4.3 The estimated horizontal velocity in the Eurasia fixed reference frame with 95% confidence regions. Red lines represent the plate boundaries (as in Figure 2.1). . . . 59
4.4 The estimated horizontal velocity in the Eurasia fixed reference frame with 95% confidence regions for Egypt-Sinai-DST fault region. Red lines represent the plate boundaries (as in Figure 2.1). . . . 60
4.5 Estimated Nubia-Eurasia Euler poles with uncertainties in addition to Euler poles from different authors ((McClusky et al., 2003); (Reilinger et al., 2006); NUVEL1-A (DeMets et al., 1994); (Sella et al., 2002)) and GPS station residuals with 95% confidence level. Residuals in Arabia, Somalia and Sinai are from Arabia-Eurasia, Somalia-Eurasia, Sinai-Eurasia, respectively. Red lines represent the plate boundaries (as in Figure 2.1). . . . 61

4.6 GPS horizontal velocities of Arabian and Sinai sites with 95% confidence level in the Nubia fixed frame. Red lines represent the plate boundaries (as in Figure 2.1). 63
4.7 GPS horizontal velocities of Sinai with 95% confidence level in Nubia fixed frame. Red lines represent the plate boundaries (as in Figure 2.1). Black boxes contain the GPS sites used for the fault parallel inversion. 64
4.8 GPS horizontal velocities of the Arabian sites with 95% confidence level in Sinai fixed frame. Red lines represent the plate boundaries (as in Figure 2.1). 66
4.9 Fault parallel velocities for the DST fault: (a) for the whole DST fault , (b) the northern segment of DST fault, and (c) the southern segment of the DST fault. Green dashed curve represents the observed fault parallel velocities and the blue curve shows the best fit model. For each plot (a, b, and c), both observed and modeled estimates show very good agreement when choosing the best respective locking depth. 67
4.10 Maximum shear strain of northeastern corner of Africa. Brown lines represent surface faults (as in figure 2.4). Red lines represent the plate boundaries (as in Figure 2.1). 68
4.11 Dilatation strain of northeastern corner of Africa, where negative values represent compression and positive values represent extension. Brown lines represent surface faults (as in figure 2.4). Red lines represent the plate boundaries (as in Figure 2.1). 69
4.12 Principle strain rate of northeastern corner of Africa, where blue arrows represent extension and green arrows represent compression. Brown lines represent surface faults (as in Figure 2.4). Red lines represent the plate boundaries (as in Figure 2.1). 70
4.13 Estimated ITRF2008 vertical velocities for Egypt from EPGN. Red lines represent the plate boundaries (as in Figure 2.1). 71
4.14 LOS velocities of ERS tracks 207 and 436 over the Nile Delta. Green circle represents the reference location. Hollow circle represents the selected PS from each city for the time series plot. 73
4.15 Standard deviation of the LOS velocities of ERS tracks 207 and 436 over the Nile Delta. Green circle represents the reference location. 74
4.16 Displacement versus time for Cairo city from ERS descending scenes. Red dots represent the results from track 436 with the velocity trend (the red line). Whereas mauve triangles represent the track 207 results, the mauve line represents the velocity trend. 75
4.17 Displacement versus time for Tanta city from ERS descending scenes. Mauve triangles represent the results from track 207. The mauve line represents the trend. 76
4.18 Displacement versus time for Mahala city from ERS descending scenes. Red dots represent the results from track 436 with the velocity trend (the red line). Whereas mauve triangles represent the track 207 results, the mauve line represents the velocity trend. 76
4.19 Displacement versus time for Mansoura city from ERS descending scenes. Red dots represent the results from track 436 with the velocity trend (the red line). Whereas mauve triangles represent the track 207 results, the mauve line represents the velocity trend. . . . 76
4.20 Displacement versus time for Damietta city from ERS descending scenes. Red dots represent the results from track 436. The red line represents the trend. 77
4.21 Displacement versus time for Port Said city from ERS descending scenes. Red dots represent the results from track 436. The red line represents the trend. 77
4.22 LOS velocities of Envisat tracks 207 and 436 over the Nile Delta. Green circle represents the reference location. Hollow circle represents the selected PS from each city for the time series plot. 79
4.23 Standard deviation of the LOS velocities of Envisat tracks 207 and 436 over the Nile Delta. Green circle represents the reference location. 80
4.24 Displacement versus time for Cairo city from Envisat descending scenes. Red dots represent the results from track 436 with the velocity trend (the red line). Whereas mauve triangles represent the track 207 results, the mauve line represents the velocity trend. . . . 81

4.25 Displacement versus time for Tanta city from Envisat descending scenes. Mauve triangles represent the results from track 207. The mauve line represents the trend. 81
4.26 Displacement versus time for Mahala city from Envisat descending scenes.Red dots represent the results from track 436 with the velocity trend (the red line). Whereas mauve triangles represent the track 207 results, the mauve line represents the velocity trend. . . . 81
4.27 Displacement versus time for Mansoura city from Envisat descending scenes. Red dots represent the results from track 436 with the velocity trend (the red line). Whereas mauve triangles represent the track 207 results, the mauve line represents the velocity trend. . . . 82
4.28 Displacement versus time for Damietta city from Envisat descending scenes. Red dots represent the results from track 436. The red line represents the trend. 82
4.29 Displacement versus time for Port Said city from Envisat descending scenes. Red dots represent the results from track 436. The red line represents the trend. 82
4.30 Comparison between the Euler poles estimated from this study for Arabia-Sinai and Sinai-Nubia with the ones estimated from different authors ((Joffe and Garfunkel, 1987); (Wdowinski et al., 2004); (Reilinger et al., 2006) and (Le Beon et al., 2008)) with plate boundaries(as in Figure 2.1). 85
4.31 Fault parallel velocities for the DST fault: (a) for the whole DST fault , (b) the northern segment of DST fault, and (c) the southern segment of the DST fault. Green dashed curve represents the observed fault parallel velocities and the blue curve shows the best fit model. Blue triangles show the stations that did not fit the dislocation model. 87
4.32 GPS horizontal velocity field of Sinai in Nubia-fixed frame with seismic activity recorded from ENSN during 1997-2012. Red lines represent the surface faults (as in Figure 2.4) . . 88
4.33 GPS vertical velocity field for the Nile Delta. Red star represents the Cairo earthquake on October 12, 1992 of magnitude 5.9. 90
4.34 Sensitivity of SAR satellite for the ground motion (Bamler and Hartl, 1998). 91
4.35 The LOS velocity field for Cairo from ERS1&2 tracks. Blue line represents the River Nile. . 93
4.36 The LOS velocity field for Cairo from Envisat tracks. Blue line represents the River Nile. . 94
4.37 Displacement versus time for Cairo city from ERS descending scenes without the scenes acquired in 1992. Red dots represent the results from track 436 with the velocity trend, the red line. Whereas mauve dots represent the track 207 results, the mauve line represents the velocity trend. 94
4.38 Egypt's population according to the World Bank (World-Bank, 2015). 95

5.1 Schematic map of the Nubia-Arabia-Anatolia-Eurasia zone of plate interaction illustrating the principal results of this study. Paired arrows show the direction of the strike-slip motion. Rates in parentheses represent the slip rate along the DST fault. Dark arrows are the GPS-derived velocity rates (mm/yr) the in Eurasia fixed frame. Red lines represent the plate boundaries (as in Figure 2.1) 101
5.2 Updated figure of the Egyptian GPS station geographic distribution. Triangles for epoch stations and circles for the permanent stations. Violet for existing stations (permanent and epoch), Green for stations established during the time of this work that are currently operating, and yellow for the proposed stations. 103

List of Acronyms

ADDNEQ2	Adding Normal Equations-2 (Bernese GPS Software module)
AN	Anatolian plate
AR	Arabian plate
C/A	Coarse Acquisition
Caltech	California Institute of Tecnology
CATS	Create and Analyze Time Series
CODE	Center for Orbit Determination in Europe
DEM	Digital Elevation Model
D-InSAR	Differential InSAR
DLR	Deutsche Zentrum für Luft- und Raumfahrt
DORIS	Delft Object-oriented Radar Interferometric Software
DST	Dead Sea Transform
ENSN	Egyptian National Seismic Network
Envisat	Environmental Satellite
EPGN	Egyptian Permanent GPS Network
EPN	EUREF Permanent Network
ERS1	European Remote Sensing-1
ERS2	European Remote Sensing-2
ESA	European Space Agency
EU	Eurasian plate
GNSS	Global Navigation Satellite System
GPS	Global Positioning System
IGS	International GNSS Service
InSAR	Interferometric Synthetic Aperture Radar
ITRF2008	International Terrestrial Reference Frame 2008
JPL	Jet Propulsion Laboratory
LOS	Line Of Sight
LW	Lwandle plate
MLE	Maximum Likelihood Estimation
NNR	No Net Rotation
NRIAG	National Research Institute of Astronomy and Geophysics
NU	Nubian plate
P	Precise or Protected
PSI	Persistent Scatterer InSAR
ROI-PAC	Repeat Orbit Interferometry Package
SBAS	Small Baseline
SLC	Single Look Complex
SOL	Somalian plate
SOPAC	Scripps Orbit and Permanent Array Center
SRTM	Shuttle Radar Topography Mission
StaMPS	Stanford Method for Persistent Scatterer
UNAVCO	University NAVSTAR Consortium

List of Symbols

P_k^i	Code pseudorange
c	Speed of light
t	Signal reception time
δ_k	Receiver clock error at time t
τ	Signal traveling time (from satellite to receiver)
δ^i	Satellite clock error at the emission time $(t-\tau)$
$(t-\tau)$	Emission time
ϱ_k^i	Geometric distance between the receiver and satellite f frequency
$\psi_{fk}^i(t)$	Phase measurement (in cycles)
$\phi_{fk}^i(t)$	Phase of the receiver oscillator at the reception time t
$\phi_f^i(t-\tau)$	Phase of the satellite oscillator at emission time $(t-\tau)$
n_{fk}^i	Unknown integer number of cycles (initial phase ambiguity)
λ_F	Carrier wavelength
δ_k	Clock error
δ^i	Satellite clock error
L_{fk}^i	Phase measurement(in meters)
$\Delta\varrho_k^i$	Tropospheric refraction
I_k^i	Ionospheric refraction
$L_{fk\ell}^i$	Single difference in observations from satellite i recorded at receivers k and ℓ
$L_{fk\ell}^{ij}$	Double difference between two receivers k and ℓ and two satellites i and j
L_{IF}	Ionosphere Free Linear Combination
L_{GF}	Geometry Free Linear Combination
L_{WL}	Wide-Lane Linear Combination
L_{MW}	Melbourne-Wübbena Linear Combination
$\Delta\phi$	Interferometric phase
$\Delta\rho$	Change in the path length
λ	Radar wavelength
ϕ_{base}	Phase difference caused by the different positions of the satellites during the two images
ϕ_{topo}	Phase difference due to topography contribution
ϕ_{defo}	Phase difference due to ground deformation contribution
ϕ_{atm}	phase difference due to the atmospheric delay
ϕ_{noise}	Phase difference due to system noise
B	Baseline between two SAR satellites
θ	Look angle
ρ	Slant range
h_t	Point's height
σ_r	Repeatability
σ_f	Formal error
σ_s	Scaled error
$P_\chi(f)$	Power Spectral Density
f	Frequency
k	Spectral index
a	Scale factors of the amplitude of the white noise
a_k	Scale factor of the amplitude of the colored noise
I	Identity matrix
J_k	Co-variance matrix for the colored noise

ε_{en}	Strain rate tensor
λ_1	Positive strain eigenvalue
λ_2	Strain eigenvalue
ε_{max_shear}	Maximum shear strain
$\theta_{1,2}$	The possible two directions of the maximum shear strain
δ	Dilatation
T	Time interval
ρ_{total}	Correlation
$B_{\perp}$	Perpendicular baseline between two SAR satellites
(F_{DC})	Doppler Centroid Frequency
C	Amplitude and phase of the InSAR scene
A	Amplitude of the interferogram
ϕ	Phase of the interferogram
D_A	Amplitude dispersion
σ_A	Amplitude standard deviation
μ_A	Amplitude mean
ϕ_W	Wrapped phase
ϕ_{Def}	Phase contribution due to the pixel motion in the Line-Of-Sight (LOS) direction
ϕ_{Atm}	Phase contribution due to the atmospheric delay
$\Delta\phi_{Orb}$	Residual phase contribution due to orbit errors
$\Delta\phi_{\theta}$	Residual phase contribution due to look angle error
ϕ_N	Phase noise
$W\{.\}$	Wrapping operator
σ_e	Error in East
σ_n	Eror in North
σ_a	Eror in Angular velocity
V_e	Velocity in East
V_n	Velocity in North
$V(X)$	Modeled velocity perpendicular to the fault
V_1	Velocity along the fault plane relative to a fixed reference frame
D	Locking depth
x	Surface distance to the fault
V_0	Far-field velocity (slip rate)
$[d_{LOS}]$	Velocity in the line of sight
d_u	Displacement in Up component
d_e	Displacements in East component
d_n	Displacement in North component
θ	Incidence angle
ϕ	Azimuth of the heading vector

1 Introduction

Determining the recent crustal deformation along the active regions adds more knowledge in the understanding of tectonics, earthquakes, and landslides. Even with the limitations in the Global Positioning System (GPS), the spatial resolution, and Interferometric Synthetic Aperture Radar (InSAR), the temporal resolution, both techniques play a vital role in modeling these crustal processes. The spreading at the Red Sea and the activities at the Gulf of Suez and Gulf of Aqaba-Dead Sea Transform (DST) fault are the main effects on the surface deformation of Egypt. Several attempts were made to constrain the ground deformation in Egypt and the interaction of the northeastern corner of Nubian plate with the surrounding tectonic plates. In the light of the fact that the GPS data in the northeastern corner of the Nubian plate was not available, the majority of the published deformation rates are rough estimates at best. Using very few GPS observations in Egypt, about 7 non-permanent stations, (McClusky et al., 2000) and (Reilinger et al., 2006) provided a northward motion of northeastern Nubia of $5 \pm 2\ mm/yr$ with respect to Eurasia. Based on 5-7 GPS campaign data collected along the southern part of Sinai Peninsula and Gulf of Suez, (Mahmoud et al., 2005) introduced a separate Sinai sub-plate between Nubian and Arabian plates and a relative motion between Sinai and stable Nubia of $1.4 \pm 0.8\ mm/yr$ north and $0.4 \pm 0.8\ mm/yr$ east. Several attempts are made to constrain the slip rate along the DST fault. A rate of $3.5 - 5\ mm/yr$ is provided by ((Wdowinski et al., 2004); (Reilinger et al., 2006); (Gomez et al., 2007); (Le Beon et al., 2008); (Sadeh et al., 2012)). All these previous studies suffered from the lack of GPS sites in the Egyptian region. Therefore, more than 60 GPS sites (16 out of 60 are permanent stations and belonging to the Egyptian Permanent GPS Network (EPGN)) in Egypt were used for the first time covering the period 2006-2012 to better constrain the ground deformation in Egypt from one side and from the other side study the differential motion between Nubia and the surrounding plates, Eurasia, Arabia, and Sinai sub-plate.

On the other hand, the man-made changes in the free-flowing rivers for the aim of energy generation and/or irrigation projects can accelerate changes in the relation between the delta and the coast leading to delta subsidence and coastal erosion, the Nile Delta is not an exception. Therefore, it is considered as one of the most vulnerable zones in Egypt. After the establishment of the Aswan High Dam in 1970, which resulted in the absence of the sediment supply, Nile Delta is suffering from high rates of land subsidence and coastal erosion ((Stanley and Warne, 1994) and (Stanley, 1996)). Prior to this work, very few subsidence rates are published. Using radiocarbon-age-dating (Stanley, 1990) observed a subsidence rate of $2.5 - 5\ mm/yr$ for the northern part of the Delta. (Aly, 2006) captured from 34 ERS SAR data a subsidence rate of 7, 9, and 5 mm/yr for Mahala, Mansoura, and Cairo cities in Nile Delta, respectively. (Becker and Sultan, 2009), from 17 ascending ERS SAR scenes, provided a rate of $4 - 8\ mm/yr$ for the northern end of Damietta branch. All the previous results are limited spatially by covering a few areas in the Nile Delta (Mahala, Mansoura, the northern part of Damietta branch, and Cairo). For that fact, all the available SAR data from ERS1, ERS2, and Envisat satellite missions for the period 1992-2010 were used to better estimate the subsidence rate of the Nile Delta. An attempt to combine the InSAR results with the GPS ones is made as well.

1.1 Contribution

There are two main focuses of this thesis. The first, to introduce a new horizontal velocity field of the northeastern corner of Nubia by using the previously unpublished GPS data from Egypt. Also, try to answer some questions about the interaction between the tectonic plates in the Eastern-Mediterranean region, the slip rate along the DST fault, and the existence of the Sinai sub-plate. The second, to provide a picture of the present state of the subsidence rate of the whole Nile Delta using Persistent Scatterers InSAR (PSI) approach. The main contributions of this work can be summarized as:

1. Evaluate the Egyptian stations, permanent and non-permanent, by estimating the horizontal velocity field of these stations in ITRF2008.
2. Estimate the ITRF2008 and relative Euler vectors of plate motion for the Eurasia, Nubia, Arabia and Sinai plates.
3. Provide a new relative motion of northern Nubia with respect to Eurasia.
4. Test the existence of a Sinai plate sandwiched between Nubian and Arabian plates.
5. Apply the fault parallel analysis to calculate the slip rate along the DST fault.
6. Estimate the strain rates at the northeastern corner of Nubia.
7. Design a plate motion model for the Eastern-Mediterranean region.
8. Present the Line Of Sight (LOS) velocity for the Nile Delta from PSI analysis.
9. Provide a subsidence rate for the Nile Delta and highlighting the areas of high subsidence rates.

1.2 Thesis Roadmap

The work in this thesis is mainly aimed to determine the recent strain rate and highlight the deformation field in Egypt, in addition to better constrain the interaction of the northeastern corner of Nubia with the surrounding plates using GPS data. Moreover, presenting the actual subsidence rate of the Nile Delta using the available SAR data. The thesis is presented in five chapters; a brief outline of each chapter is given here:

- Chapter 2 contains in its first part a short review of the tectonic setting, geology, and seismicity of Egypt. The second part provides the GPS fundamentals, its components, the satellite signal, the source of errors, and the techniques to mitigate the effect of these errors. A short overview of InSAR , system description, strengths, and limitations are presented in the third part.
- Chapter 3 provides the softwares and techniques used for the GPS data processing and the SAR data processing as well.
- Chapter 4 deals with the achieved results from GPS, absolute velocity field in ITRF2008, relative velocity field, slip rate estimates, and strain rate calculations; in addition to InSAR results, LOS velocity, subsidence rates, and time series for selected regions. A discussion section is also presented in this chapter.
- Chapter 5 provides the conclusions of this thesis in addition to the suggested future work.

2 Background

The movement of the Earth's crust is considered as a natural phenomenon that occurs at the level of the globe and with different rates from one area to another, according to tectonic activity. Due to its location, in the northeastern corner of Africa, Egypt is subjected to several hazards. Recently, in Egypt, GPS has been applied to seismo-active areas by establishing geodetic networks to monitor the recent crustal movements in those areas. Epoch and continuous observation of GPS data give the availability to study recent crustal movements for the whole Egyptian territory and to understand the geodynamical behavior of the entire Egypt. As a complementary geodetic technique, InSAR (Interferometric Synthetic Aperture Radar) can image the earth's surface deformation in millimeter level accuracy over large areas reached hundreds of kilometers. The agreement between information on movements, determined by analyses of measured and adjusted data and other geophysical tools increases the weight of final geodynamical interpretations. In this chapter a review of the tectonic setting of Egypt including the active regions and the two techniques that used in this work, GPS (Global Positioning System) and InSAR (Interferometric Synthetic Aperture Radar), their principles, strengths, and weaknesses are presented.

2.1 Tectonic Setting of Egypt

Egypt is located in the northeastern corner of the African continent. It is influenced tectonically from the North by the subduction between Nubia and Eurasia and from the East by the Red Sea-Gulf of Suez and Gulf of Aqaba-Dead Sea Transform (DST) fault activities, (Said, 1990). The subduction between Nubian and Eurasian plates (Cyprus and Hellenic) and the opening at the Red Sea Ridge represent the boundaries between Nubian (NU), Arabian (AR) and Eurasian (EU) plates and may control the surface deformation in this area, Figure 2.1. The Arabian-Nubian massif is structurally bisected by the Red Sea Rift and its continuation (as continental rifts) of gulfs of Suez and Aqaba, and in the Levantine countries recent structures represent the most active regions of this Precambrian shield. In this area, the basement rocks outcrops of the Precambrian geosyncline are extended in Ethiopia, Sudan, the eastern part of Egypt, Sinai, and most of the Levantine countries. The geologic map of Egypt (Figure 2.2), shows that the basement occupies about 10% of the surface area, and the Phanerozoic sediments and volcanics cover about 90%. However, most of the older sedimentary rocks, especially those belonging to the Paleozoic, are hidden in relatively deep basins under younger rocks. Phanerozoic volcanics are well distributed, both in space and time, invading the sedimentary cover as well as the basement. The volcanics are associated with crustal disturbances, but Egypt has behaved as a craton throughout the Phanerozoic.

Egypt is divided primarily into four major geological provinces; the Arabian-Nubian shield, stable shelf, unstable shelf, and Gulf of Suez-Red Sea graben, (Said, 1962). The Arabian-Nubian shield is extending over large parts of the Eastern Desert, the southern Sinai Peninsula, and the extreme southern part of the Western Desert at Owienat area (southwest of Egypt). It consists mainly of Precambrian rocks. (El Shazly, 1977) distinguished several stages within these metamorphic sequences of geosynclinal Archean formations with frequent intrusions of plutonic and volcanic rocks. The stable shelf is located North and West of the Arabian-Nubian Shield and exhibits gentle tectonic deformation, its sedimentary cover is mainly represented by continental and epicontinental deposits such as the Mesozoic Nubian Sandstone. The sedimentary sequence on the stable shelf is relatively thin of about 400 m near the Arabian-Nubian shield and increasing to as much as 2500 m near the transition zone into the unstable shelf in the North. It is composed of sands and shales in its lower locations and of shallow water carbonates in its upper part. However, the unstable shelf is situated north of the stable shelf with a transition zone between the two structural depositional units following a line approximately set from the Siwa Oasis through Farafra Oasis and Suez into Central Sinai (Figure 2.3).

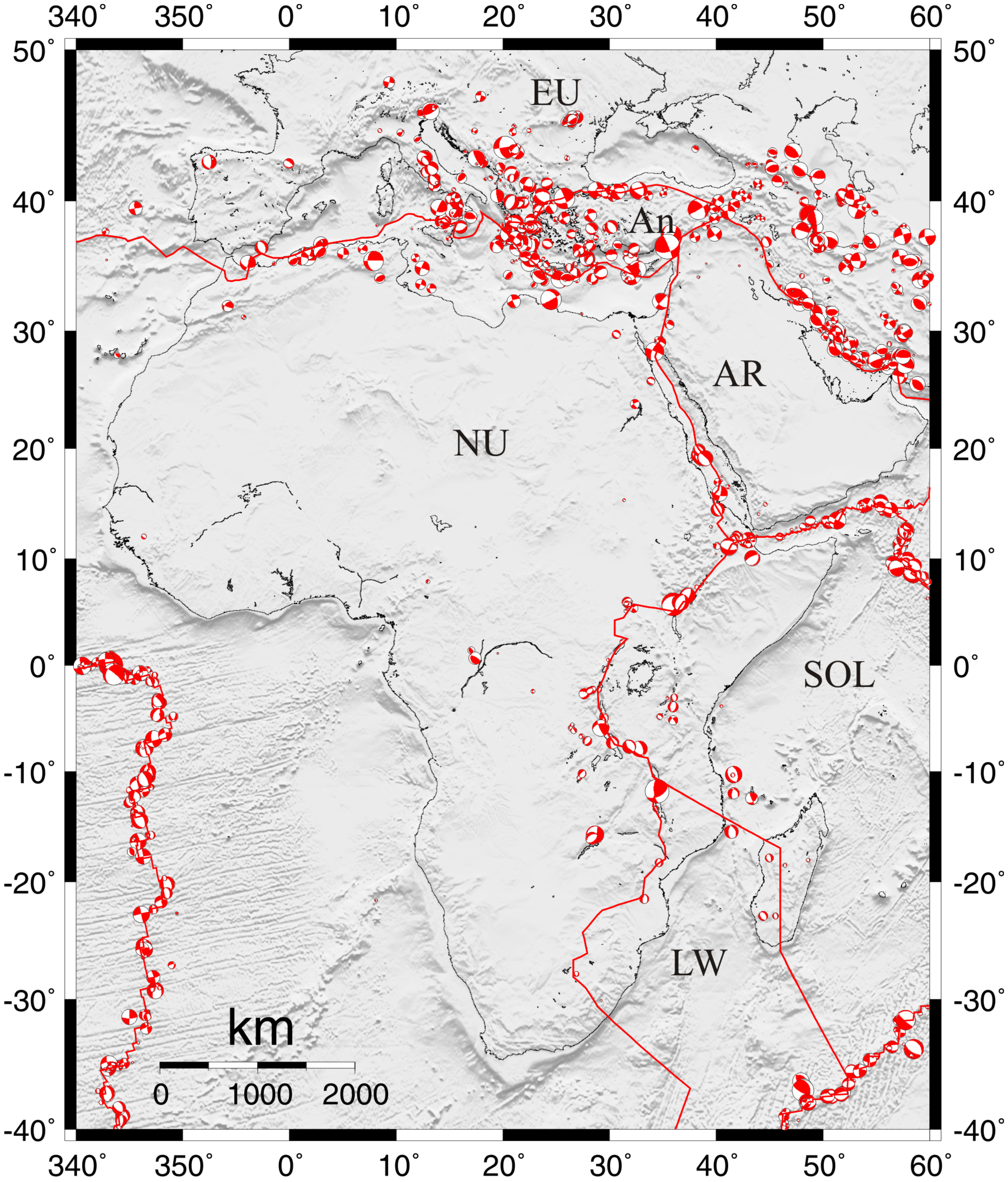

Figure 2.1: Focal mechanisms for earthquakes occurred in Nubian, Eurasian, Arabian and Somalian plates from `http://www.globalcmt.org/CMTsearch.html` ((Dziewonski et al., 1981) and (Ekström et al., 2012)), 1976 to December 2012, with plate boundaries ((Bird, 2003) and (Argus et al., 2010)), red lines represent the plate boundary. NU = Nubia; AR = Arabia; SOL = Somalia; LW = Lwandle; AN = Anatolia; EU = Eurasia.

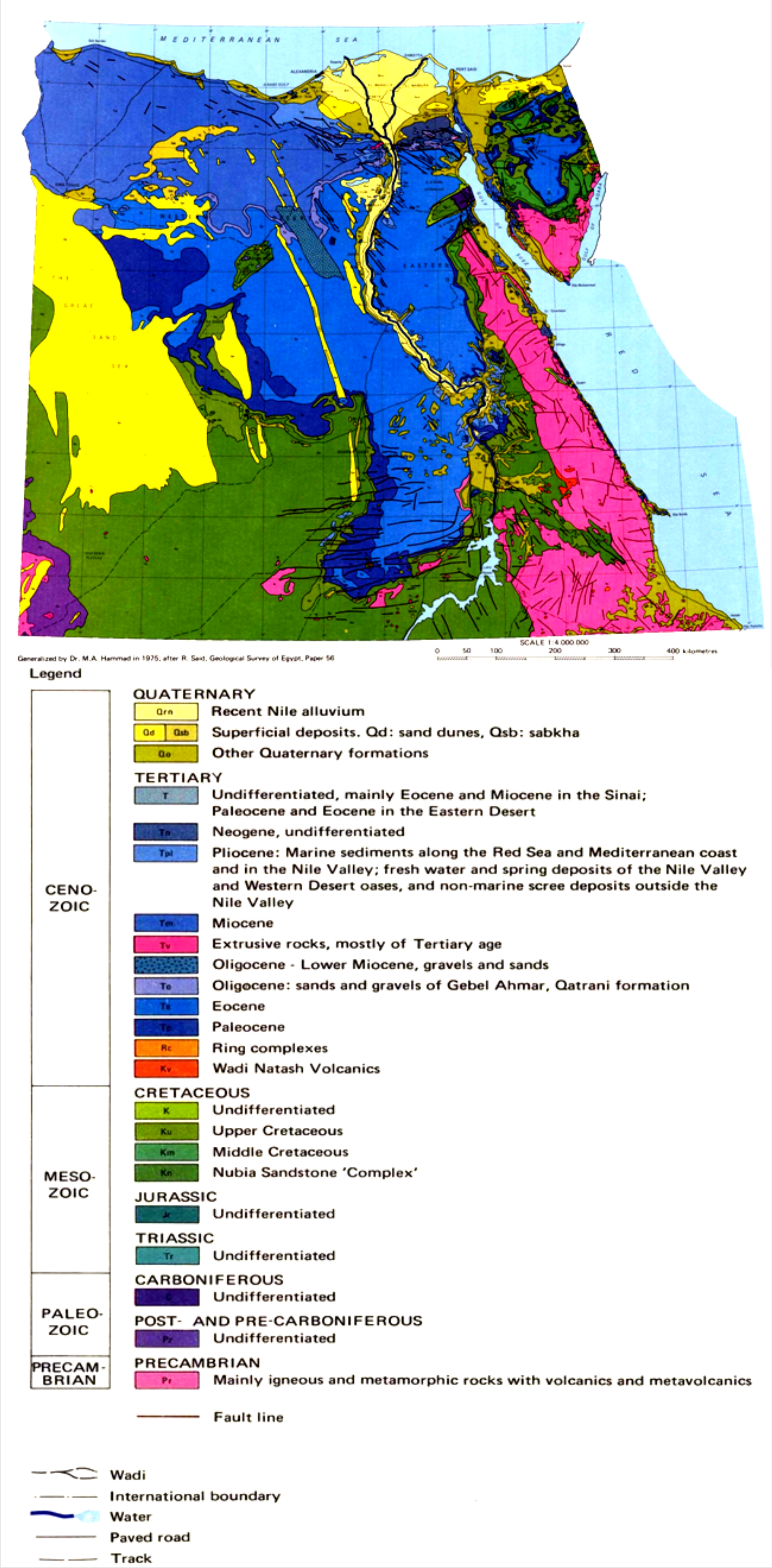

Figure 2.2: Geologic map of Egypt, generalized by (Hammad, 1975), after (Said, 1962), Geological Survey of Egypt.

Figure 2.3: Egypt's geological provinces, (Said, 1962).

The Gulf of Suez-Red Sea Graben is an area of subsidence within the stable shelf and the northern part of the Arabian-Nubian Shield. The Gulf of Suez was formed initially during the early Paleozoic time as a narrow embayment of the Tethys and intensively rejuvenated during the rifting phase of the great East African rift system in lower to middle Tertiary time. The Red Sea originated during Oligocene time after the arching and crustal thinning in the general area of the Arabian-Nubian Shield and subsequent collapse in the context of the East African rifting. Spreading of the Red Sea floor was and is still related to the relative motion of the various plates present in northeastern Africa and the near East. The spreading of the Red Sea is due to the northeastward drift of the Arabian plate along the DST fault. This left-lateral strike-slip fault, also known as Levant fault system, extends 1000 km and representing a tectonic boundary between the Arabian and Nubian plates. It connects the mid-oceanic ridge of the Red Sea in the South to the Caucasus mountains in the North. The DST fault was initiated 15-20 Ma ago ((Freund et al., 1970); (Garfunkel, 1981)). Based on geological observation, the total left lateral displacement along the DST fault is about 105 km ((Quennell, 1958); (Freund et al., 1968)).

Plate motion models NUVEL-1 (DeMets et al., 1990) and NUVEL-1A (DeMets et al., 1994), based on geophysical data (277 spreading rates, 121 transform fault azimuths, and 724 earthquake slip vectors), indicate that the Nubian and Arabian plates are moving to North and North to Northwest direction relative to Eurasia of about 10 mm/yr and $18-25$ mm/yr, respectively, which means a differential motion between Nubia and Arabia of about 10 mm/yr. Taking advantage of the wide coverage of GPS, (McClusky et al., 2000) used 9 years (1988-1997) of collected GPS data (from Caucasus mountains to the Adriatic Sea, and from the southern edge of the Eurasian plate to the northern edge of the Nubian plate). They presented a northward motion of northern Nubia and northern parts of Arabian plate with respect to Eurasia, of about 5 ± 2 mm/yr northward and 18 ± 2 mm/yr at $N25° \pm 5°E$, respectively, which is less than NUVEL-1A, and a counterclockwise rotation of central/western Turkey and southern Aegean/Peloponnesus. With a new GPS data set, 1988-2005, (Reilinger et al., 2006) showed a similar counterclockwise rotation that increases toward the Hellenic trench system, 5 mm/yr relative motion between northern Nubia and Eurasia, 17.8 ± 1.1 mm/yr in the North of the Arabian plate and south-eastern Turkey, 20.6 ± 0.8 mm/yr in eastern and central Turkey, 24.6 ± 1.0 mm/yr in western Turkey, and 31.1 ± 0.9 mm/yr in the central and southern Aegean as shown in Figure 2.4. (Mahmoud et al., 2005) suggested a separate Sinai sub-plate bounded by the Gulf of Aqaba-DST fault, Gulf of Suez, and Cyprus Arc of motion 1.4 ± 0.8 mm/yr North and 0.4 ± 0.8 mm/yr East relative to the stable Nubia plate. Along the DST fault, and based on geological and geodetic data, the left-lateral strike-slip motion are varied from 2 to 10 mm/yr. (Freund et al., 1968) and (Meghraoui et al., 2003) observed slip rates of 8.5 mm/yr and 6.9 mm/yr from geological and paleoseismicity data, respectively. A rate of $3.5-5$ mm/yr was estimated directly from GPS by ((Wdowinski et al., 2004); (Reilinger et al., 2006); (Gomez et al., 2007); (Le Beon et al., 2008); (Sadeh et al., 2012)).

Egypt is not a major seismic zone. Its activity is characterized by earthquakes of low to moderate magnitude which concentrated in active seismic zones. Many authors studied the seismicity of Egypt (e.g., (Ismail, 1960); (Gergawi and El-Khashab, 1968); (Maamoun et al., 1984); (Kebeasy, 1990); (Abou Elenean, 1997)). Due to the lack of seismic stations in the northeastern corner of the African continent before 1980, these studies were of lower accuracy, therefore the activity is scattered and clustered closer to the location of the seismic stations, (Abou Elenean, 2007). After the establishment of the Egyptian National Seismic Network (ENSN), in 1997, more seismic events with high accuracy were recorded. Figure 2.5 shows the recorded earthquakes by ENSN from 1997 to 2012.

The highest seismic activity is located at the Gulf of Aqaba, which represents the southern end of the DST fault, and the Gulf of Suez, the northern part of the Red Sea. The significant seismic activity along the Gulf of Suez is extended on the northern part of the Eastern Desert towards the Nile Delta through the E-W and WNW faults and ends close to the West of Cairo on the location of the October 12, 1992 earthquake. Further East at the Gulf of Aqaba-DST fault, a clustered seismicity takes place in different focal regions over the fault trace. The major faults bounding both Suez and Aqaba gulfs control the seismic activity recorded in this area. The seismic activity in the northern Red Sea is concentrated on the rift itself. Some of these clusters along the Red Sea rift have a remarkable effect on the western coast of the Red Sea, which is represented by the seismicity clusters at Abu-Dabbab and Shalaten areas. Two seismicity clusters are located in Aswan and Abo-Simple, South of Egypt. The activities at these two areas are controlled by E-W tectonically active faults (e.g. Kalabsha and sayal faults) and reservoir-induced seismicity around Aswan Lake (Abou Elenean, 2007). To the North and along the Nile valley, there are a few clusters at Idfu and Beni Suef. Some of the earthquakes happened in Egypt in the last century caused enormous losses in death and injuries and structural damages; such as the November 1, 1981 in Aswan, South of Egypt, the October 12, 1992 Dahshour, close to Cairo and the November 22, 1995 Aqaba earthquakes. From the distribution of the seismic activity, it is clear that the highest activities are concentrated along the plate boundaries, and a high deformation is expected. The intraplate deformation is very small and characterized by low size earthquakes. Figure 2.6 shows the focal mechanism solution for some earthquakes occurred in Egypt during the period 1976-2012. The focal mechanism parameters of these earthquakes are presented in Table 1A in the Appendix.

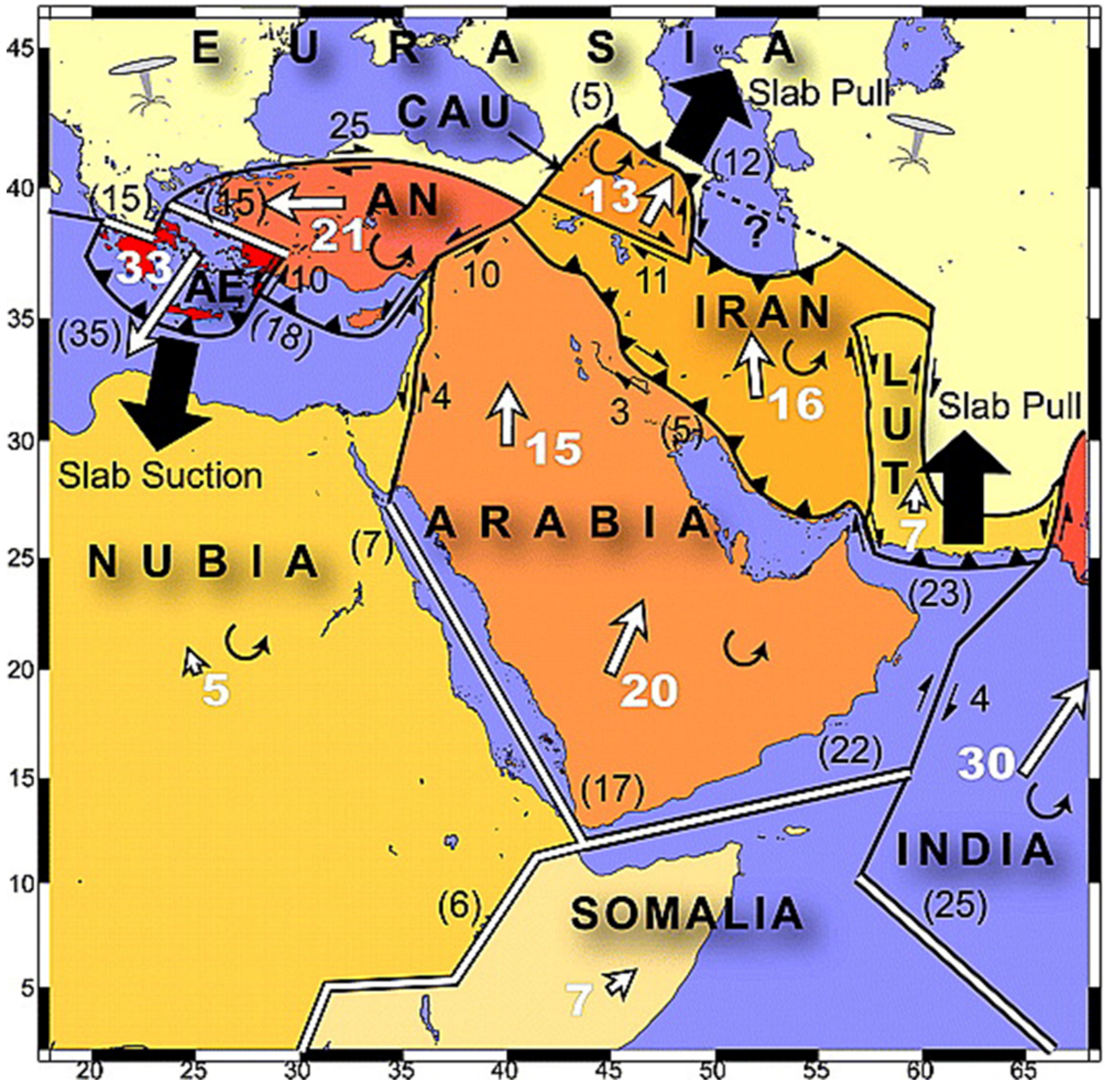

Figure 2.4: Plate motion model proposed by (Reilinger et al., 2006) for Nubia-Arabia-Eurasia interaction.

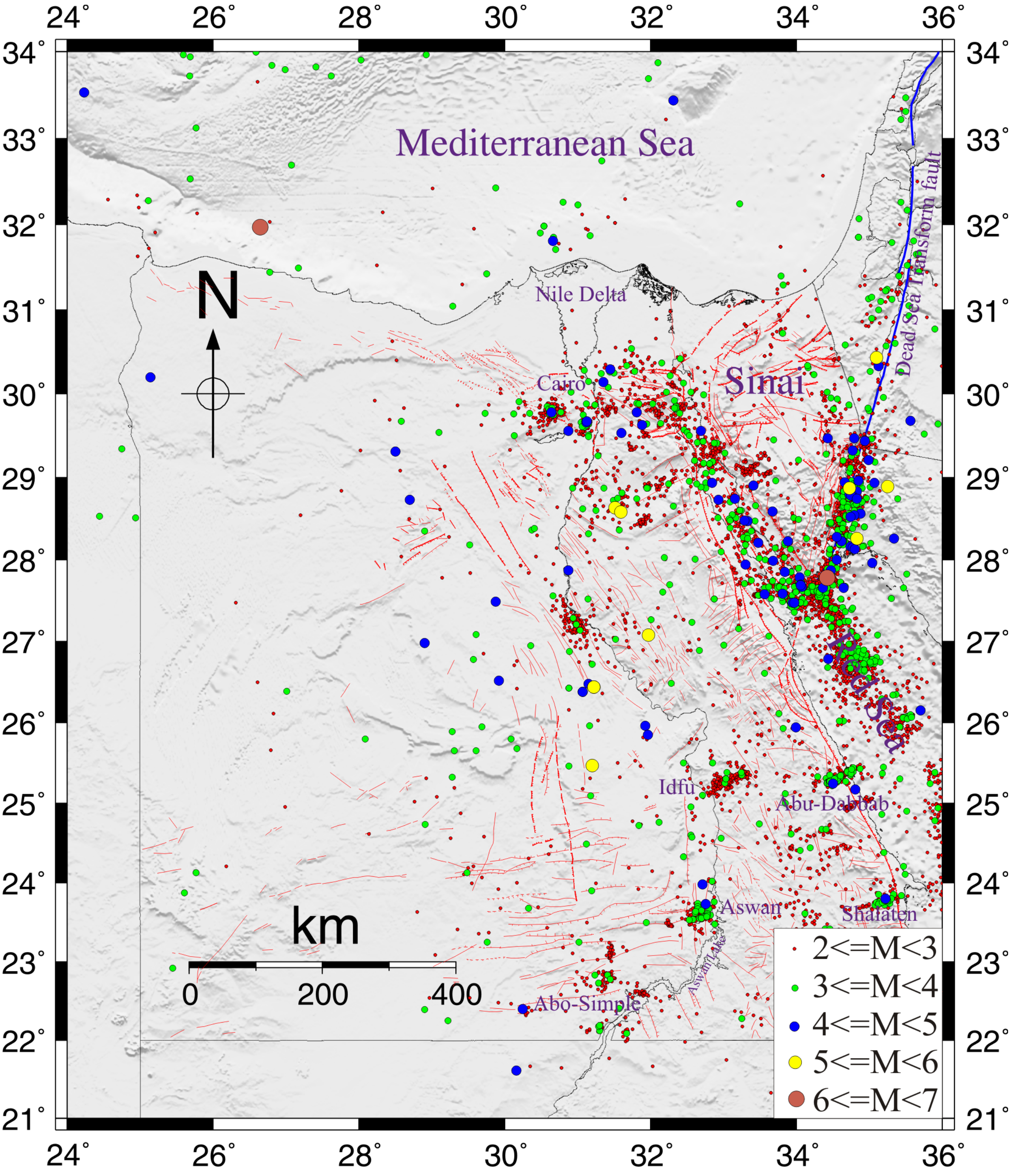

Figure 2.5: Seismic activity recorded by ENSN from 1997 to 2012. Red lines are the surface faults (Egyptian Geological Survey and Mining Authority (EGSMA), 1981). Blue lines represent the Dead Sea Transform fault.

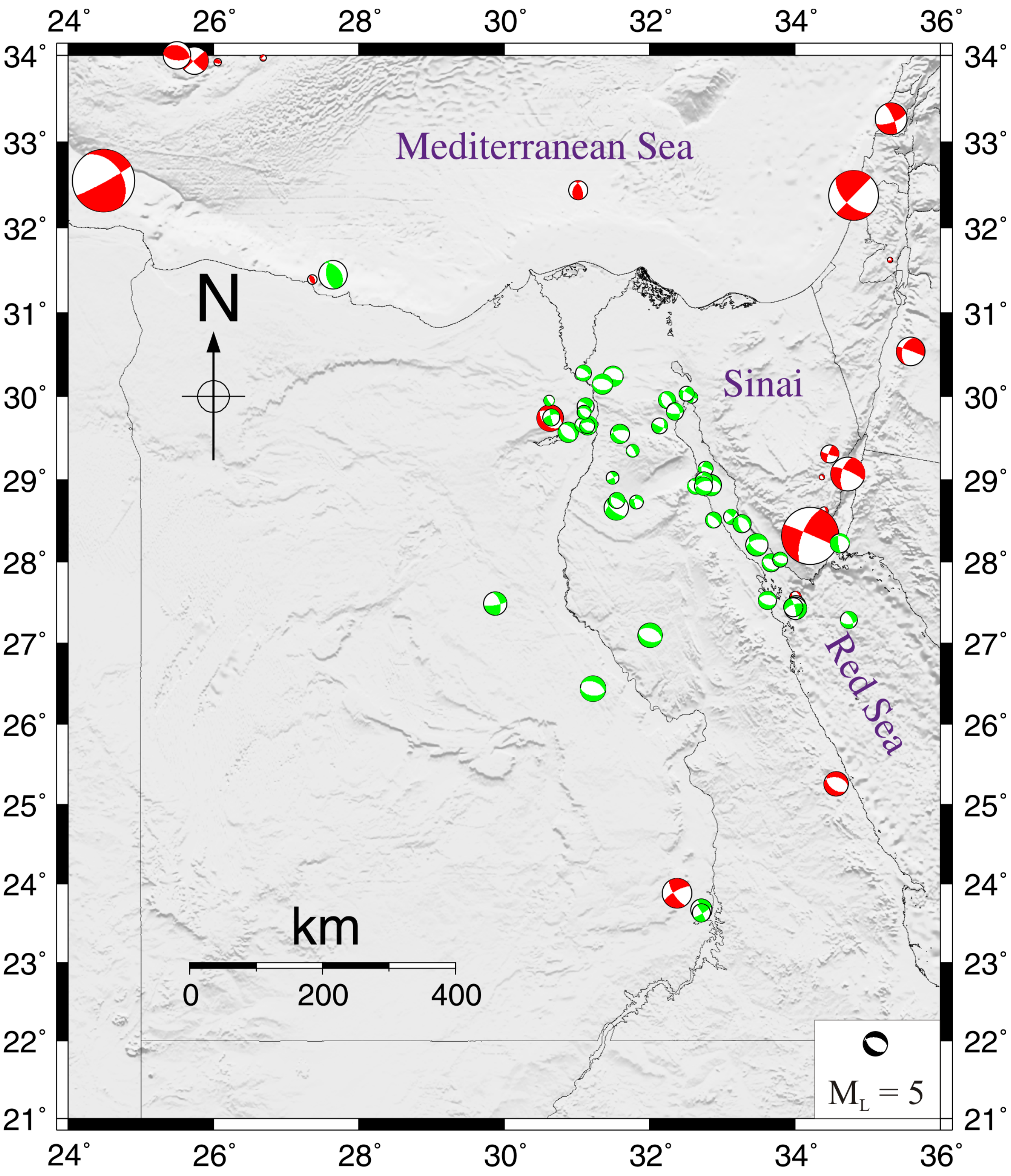

Figure 2.6: Focal mechanisms for earthquakes occurred in Egypt for the period 1976 to 2012. Greens are the solution from Global CMT `http://www.globalcmt.org/CMTsearch.html` ((Dziewonski et al., 1981) and (Ekström et al., 2012)) and Reds are the solution from (Abou Elenean, 2007).

2.2 Global Navigation Satellite Systems (GNSS)

Currently, beside the fully operational the United States GPS (Global Positioning System) and the Russian GLONASS (GLObal NAvigation Satellite System), there are other navigation systems that either under expanding or deployment phases. The Chinese Navigation system is in the process of expanding its coverage from regional (BeiDou) into the global (Compass) by 2020 and the European GALILEO GNSS is in development at the present time. For this work, only the GPS data will be used due to the lack of GLONASS observations from the Egyptian stations.

GPS is a relatively low cost and portable technique that provides accurate three-dimensional coordinates (latitude, longitude, and height), velocity, and time. It is usable in all weather conditions, anywhere, on or near the Earth (on the ground, at sea, in the air, and in the near space). The GPS delivers time, time interval, and frequency anywhere in the world with precision more than adequate for many applications. In this section a review of the GPS satellite constellation, observation equations, error sources, and techniques for reducing the error effects such as forming differences and linear combination are presented.

2.2.1 GPS Components

The GPS system, as any satellite navigation system, consists of three segments; space segment, control segment, and user segment.

2.2.1.1 Space Segment

The present full constellation of GPS, nominally 24 satellites, provides a global coverage of four to eight observable satellites simultaneously. The GPS satellites are distributed in six orbital planes with an altitude of 20200 km above the Earth's surface. The orbital planes are inclined with 55° with respect to the equator with orbital period $\simeq$ 12 hours, (Dach et al., 2007). The first GPS satellite, belonging to the first generation called Block I, was launched on February 22, 1978. The Block I satellites had a different configuration with respect to the current ones, inclined at 63° to the Earth's equator. Today, all Block I satellites are retired and replaced by satellite blocks II, IIA, IIR and IIF.

2.2.1.2 Control Segment

This segment comprises the Operational Control System, which consists of a control center and some worldwide ground control stations. Some of the main functions of the control station are satellite orbit and clock corrections determination. Ground control stations are capable of transmitting data up to satellites including new ephemerides, clock corrections, and other broadcast message data.

2.2.1.3 User Segment

The user segment consists of the GPS users and their receivers. This segment is not a part of the system itself, but it represents the part who interact with the system. Since GPS is continuously available and very precise positioning technique, almost unlimited possibilities are opened up for its use in geodesy, surveying, and navigation. In this thesis, the GPS as a very precise tool is mainly used for the monitoring of the ground deformation along the active areas in Egypt.

2.2.2 Satellite Signal

GPS signals consist of electromagnetic waves. The two fields, magnetic and electric, are propagating perpendicular to each other and to the propagation direction. The information contained in GPS signals includes carrier frequencies, Coarse Acquisition (C/A) and Precise (P) codes as well as satellite message.

2.2.2.1 Code Pseudoranges

The code is composed of a series of chips, which have values of 1 or 0. The C/A code (Coarse Acquisition or Clear Acquisition) has a frequency of 1.023 MHz while the P code (Precise or Protected) has a frequency of 10.23 MHz. The chip lengths are 293 m and 29.3 m for the C/A and P codes, respectively. Therefore, the P code is ten times more accurate than the C/A code. Code measurements are the difference in time between transmitted code from a satellite and code received at a GPS receiver, multiplied by the speed of light.

$$P_k^i = c((t+\delta_k)-(t-\tau+\delta^i)) \tag{2.1}$$

where the P_k^i is the code pseudorange between satellite i and receiver k, c is the speed of light, t is the signal reception time, δ_k is the receiver clock error at time t, τ is the signal traveling time (from satellite to receiver), and δ^i is the satellite clock error at the emission time $(t-\tau)$.

The P_k^i called pseudorange because it is biased by the receiver and satellite clock errors. When introducing the geometric distance ϱ_k^i, the code pseudorange for a carrier frequency f will be

$$P_{fk}^i = \varrho_k^i + c\delta_k - c\delta^i \tag{2.2}$$

2.2.2.2 Phase Pseudoranges

Currently, signals from GPS satellites are continuously transmitted on carrier frequencies 1575.42 MHz, 1227.60 MHz, and 1176.45 MHz denoted as L_1, L_2, and L_5 respectively. The signal wavelengths for L_1, L_2, and L_5 are 19.03 cm, 24.42 cm, and 25.48 cm, respectively. The receiver measures the difference between two phases, the phase of the satellite oscillator generated at the emission time $(t-\tau)$ and the phase of the receiver oscillator generated at the reception time t.

$$\psi_{fk}^i(t) = \phi_{fk}(t) - \phi_f^i(t-\tau) + n_{fk}^i \tag{2.3}$$

where $\psi_{fk}^i(t)$ is the phase measurement (in cycles) at time t and carrier frequency f, $\phi_{fk}(t)$ is the phase of the receiver oscillator at the reception time t, $\phi_f^i(t-\tau)$ is the phase of the satellite oscillator at emission time $(t-\tau)$ and n_{fk}^i is the unknown integer number of cycles (initial phase ambiguity).

After introducing the carrier wavelength λ_f and taken into account the receiver clock error δ_k and satellite clock error δ^i, the phase measurement L_{fk}^i in meters will be

$$L_{fk}^i = \varrho_k^i + c\delta_k - c\delta^i + \lambda_f n_{fk}^i \tag{2.4}$$

2.2.2.3 Navigation Message

The satellite message contains among other information that are mainly about satellite clock, satellite orbit, and health status. The ephemerides include the parameters necessary to compute a satellite's position in space for a given time (Dach et al., 2007).

2.2.3 Source of Errors

The GPS signal is affected by both, systematic and random errors. To meet the up-to-date accuracy, the majority of the error sources should be modeled. To name the dominant effects; errors in satellite orbits and clocks, receiver clocks, propagation medium, and in addition effects like antenna phase center variations, relativistic effects, and multipath. In addition to the contribution of satellite and receiver clock errors (in phase and code) and the ambiguity term (in the phase only), equations (2.2) and (2.4), Tropospheric and Ionospheric refraction are two more error sources that affect the GPS signal.

The tropospheric refraction $\Delta\varrho_k^i$ is the effect of the non-ionized part of the Earth's atmosphere on the GPS signal. The effect of the troposphere is identical on all signal frequencies and on phase and code measurements. There are a possibility to model the tropospheric delay for the (GNSS) by using the a priori models such as NIELL (Niell, 1996), SAASTAMOINEN (Saastamoinen, 1972), HOPFIELD (Hopfield, 1963), and GMF (Böhm et al., 2007) or through the estimation of the wet and the dry components for the troposphere. The ionospheric refraction I_k^i is the effect of the ionized part of the Earth's atmosphere on the GPS signal and frequency-dependent. The Ionosphere works as a dispersive medium for the GPS signal and causes delays in code measurements and advances in carrier phases. The effect of the ionosphere is treated by combining the observations of two different frequencies, more details are in the next section.

Taking these two effects into considerations, Equations (2.2) and (2.4) may be written as

$$P_{fk}^i = \varrho_k^i + c\delta_k - c\delta^i + I_k^i + \Delta\varrho_k^i \tag{2.5}$$

$$L_{fk}^i = \varrho_k^i + c\delta_k - c\delta^i - I_k^i + \Delta\varrho_k^i + \lambda_f n_{fk}^i \tag{2.6}$$

2.2.4 Forming Differences and Linear Combinations

Due to the difficulty of modeling all error sources sufficiently, different techniques are used to eliminate or reduce the effect of some of these errors, such as observation differences or linear combinations, by using the raw observation to create a new observation free from some effects.

Single difference is the difference in the observations from satellite i recorded at receivers k and ℓ.

$$L_{fk\ell}^i = L_{fk}^i - L_{f\ell}^i \tag{2.7}$$

The double difference is between two receivers k and ℓ and two satellites i and j.

$$L_{fk\ell}^{ij} = L_{fk\ell}^i - L_{fk\ell}^j \tag{2.8}$$

The double difference offers the elimination of the receiver and satellite clock errors, therefore the observation equations will be

$$P_{fk\ell}^{ij} = \varrho_{k\ell}^{ij} + I_{k\ell}^{ij} + \Delta\varrho_{k\ell}^{ij} \tag{2.9}$$

$$L_{fk\ell}^{ij} = \varrho_{k\ell}^{ij} - I_{k\ell}^{ij} + \Delta\varrho_{k\ell}^{ij} + \lambda_f n_{fk\ell}^{ij} \tag{2.10}$$

The triple difference is a double difference from two different times t_1 and t_2. The main advantages of the triple difference are the elimination of the phase ambiguity, for data pre-processing, and reducing the tropospheric refraction.

$$L_{fk\ell}^{ij}(t_2) - L_{fk\ell}^{ij}(t_1) = \varrho_{fk\ell}^{ij}(t_2) - \varrho_{fk\ell}^{ij}(t_1) - \left(I_{fk\ell}^{ij}(t_2) - I_{fk\ell}^{ij}(t_1)\right) \tag{2.11}$$

Linear combinations are built for simultaneous observations to the same satellite on different carrier frequencies. Reducing the errors (such as ionospheric refraction) and generating observations of different wavelengths are the two main goals of forming linear combinations. The most common linear combinations of GPS observations on L_1 and L_2 are:

Ionosphere Free Linear Combination L_{IF}: Often the modeling of the ionosphere effect is not sufficient, therefore most of the processing schemes are based on the L_{IF} combination. The effect of the Ionosphere is considerably reduced by combining the observation of two frequencies. For phase observations the ionosphere free linear combination L_{IF} can be written as

$$L_{IF} = \frac{1}{f_1^2 - f_2^2}\left(f_1^2 L_1 - f_2^2 L_2\right) \tag{2.12}$$

and for code observations, the ionosphere free linear combination L_{IF} is expressed as:

$$P_{IF} = \frac{1}{f_1^2 - f_2^2}\left(f_1^2 P_1 - f_2^2 P_2\right) \tag{2.13}$$

Geometry Free Linear Combination L_{GF}: This combination retains only the ionospheric delay and the phase ambiguity. This linear combination is suited for modeling the ionosphere. The Geometry Free Linear Combination L_{GF} is given by

$$L_{GF} = L_1 - L_2 \tag{2.14}$$

Wide-Lane Linear Combination L_{WL}: The main goal of this combination is to increase the observation wavelength. The wide-lane linear combination has the form

$$L_{WL} = \frac{1}{f_1 - f_2}\left(f_1 L_1 - f_2 L_2\right) \tag{2.15}$$

Melbourne-Wübbena Linear Combination L_{MW}: In this combination, both carrier phase and code are combined ((Wübbena, 1985) and (Melbourne, 1985)). The Melbourne-Wübbena Linear Combination L_{MW} is given by

$$L_{MW} = \frac{1}{f_1 - f_2}\left(f_1 L_1 - f_2 L_2\right) - \frac{1}{f_1 + f_2}\left(f_1 P_1 + f_2 P_2\right) \tag{2.16}$$

The International GNSS Service (IGS) is an umbrella that contains more than 200 worldwide research institutes, agencies, and universities that provide the high quality open-access GNSS data and contributes to the precise products determination in addition to the International Terrestrial Reference Frame (ITRF) definition (Dow et al., 2005). IGS offers different satellite orbits, each type has its accuracy. The broadcast orbits are available in real time with an accuracy of approximately one meter, while the precise orbits are available two weeks after the observation with a centimeter accuracy. The rapid and ultra-rapid orbits are available after one day and three hours, respectively, with a decimeter accuracy (IGS, 2015).

In addition to the satellite orbits, IGS offers also the estimation of the Earth rotation parameters, satellite clock information, Zenith tropospheric path delay estimates, and global ionosphere maps. Similar to the satellite orbits products, these products are also available as final, rapid, and ultra-rapid products. For applications in geodynamics and other high applications with post processing, the final precise products are used. Table 2.1 shows the GPS satellite orbits, satellite clock, and stations clocks (IGS, 2015).

Table 2.1: GPS satellite orbits in addition to satellite and station clocks (IGS, 2015).

Type		**Accuracy**	**Latency**
Broadcast	orbits	$\sim$ 100 cm	real time
	Sat. clocks	$\sim$ 5 ns RMS	
Ultra-Rapid (predicted half)	orbits	$\sim$ 5 cm	real time
	Sat. clocks	$\sim$ 3 ns RMS	
Ultra-Rapid (observed half)	orbits	$\sim$ 3 cm	3 - 9 hours
	Sat. clocks	$\sim$ 150 ps RMS	
Rapid	orbits	$\sim$ 2.5 cm	17 - 41 hours
	Sat. & Stn. clocks	$\sim$ 75 ps RMS	
Final	orbits	$\sim$ 1.0 cm	12 - 18 days
	Sat. & Stn. clocks	$\sim$ 75 ps RMS	

2.3 Interferometric Synthetic Aperture Radar (InSAR)

InSAR, Interferometric Synthetic Aperture Radar, is an active side looking remote sensing technique with the ability to map the terrain surface with a few meters accuracy and the surface deformation within millimeter level. InSAR has the capability of large-scale imaging in all weather conditions over days to years which has been successfully used worldwide for, but not limited to, mapping the earth's surface, measuring the crustal deformation, monitoring the active volcanoes, glacier dynamics, and land subsidence. This section contains the InSAR principles, the traditional InSAR technique and its limitations, the multi-temporal, and multi-dimensional InSAR methods to overcome the shortcomings of the traditional InSAR.

2.3.1 History

Radar stands for radio detection and ranging that has been initially developed in the first half of the twentieth century. Radar system sends an electromagnetic pulse in the radio and microwave range and receives the echo signal from an object in the line of sight (LOS). The two-way travel time is used to estimate the range, the distance to the object, and the echo intensity infer some of the object's physical characters like surface roughness and size. From a terrestrial based radar, the first echo from moon was received in 1946 (Buderi, 1996). In 1970s, the radar were brought to space to investigate the planetary surface with Earth-orbiting satellite (Hanssen, 2001).

The imaging radar class was started by air-borne side-looking radar (SLR), using a physically long antenna, and later by Synthetic Aperture Radar (SAR). The Seasat satellite, which launched in 1978, was the first equipped with L-band SAR system. Due to the success of the Seasat mission, several space satellite missions were equipped with SAR, starting from 1981 with SIR-A (L-band) which operated for 2.5 days. SIR-A was replaced by SIR-B in 1984 which had the ability for digital recording. The Russian (S-band) SAR satellite, Cosmos-1870, launched in 1987 and operated for two years. Followed by ALMAZ-1 in 1991 and 1.5 years lifetime. A remarkable increase in using the SAR data for different applications was happened since the launch of the European Remote Sensing satellite (ERS-1) in 1991 by the European Space Agency (ESA) due to the systematic data acquisition (C-band), the orbit control, and the data policy (Hanssen, 2001). ERS-2 launched in 1995 by ESA, which enabled the tandem mode operation of ERS-1 and ERS-2. The tandem mode (ERS-2 followed ERS-1 in the same orbit) acquired SAR data with a one-day interval for nine months. Nowadays, the SAR data are available from ESA's satellite missions ERS-1, ERS-2, Envisat, and Sentinel-1A. RADARSAT-1 and RADARSAT-2 from the Canadian Space Agency, JERS and ALOS from the Japanese Space Agency, the Italian Cosmo-Sky-Med, and TerraSAR-X and Tandem-X from the German aerospace center (DLR). Figure 2.7 shows the current and future satellite SAR missions.

2.3.2 SAR Interferometry

SAR systems, either spaceborne or airborne, have a side looking antenna that illuminates the Earth, with radar in the microwave range, in swath or track parallel to the sensor's flight direction (Figure 2.8). The satellite's flight direction is called Azimuth direction while the direction perpendicular to the flight direction is called Range direction. The antenna receives the echos of the transmitted pulses when it is inactive between transmission of pulses. To form an image from the raw SAR data, a focusing process is needed by combining echos of multiple locations, that spatially overlapped, to synthesize a large antenna aperture. Three bands of the electromagnetic spectrum are commonly used in InSAR applications, L-band with 23.6 cm wavelength, C-band with 5.6 cm wavelength, and X-band with 3.1 cm wavelength. The imaging geometry presented in Figure 2.8 is named the strip mapping mode. Even with new modern modes of collecting the SAR data like ScanSAR or spotlight SAR, the strip mapping mode still the most common mode in the current satellites.

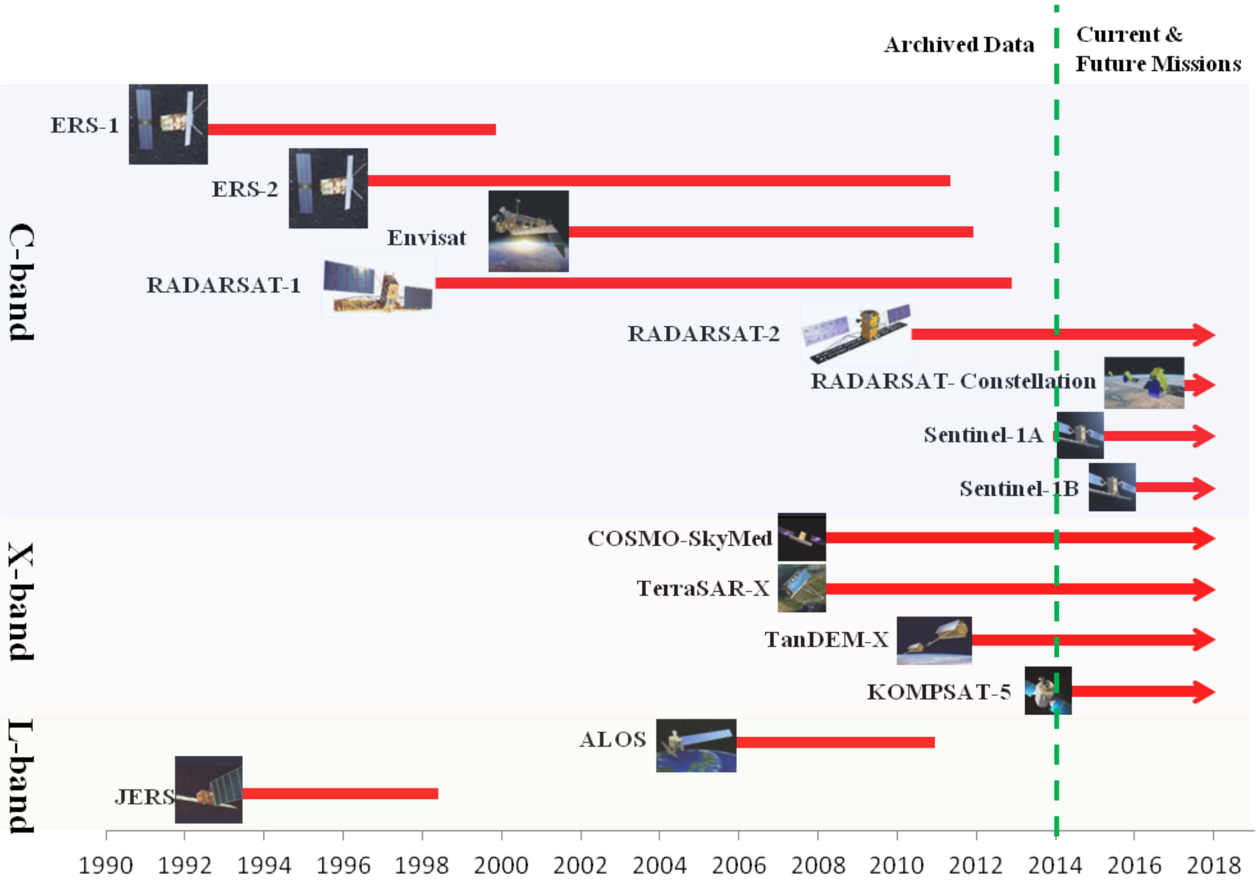

Figure 2.7: Past, current, and future satellite SAR missions.

The focused SAR data are the Single Look Complex (SLC) image, representing a two-dimensional array of complex numbers. The two fundamental components of the SAR image are amplitude and phase. Amplitude reflects the amount of the backscattered energy. Metals and hard objects have high reflective nature and as a consequence high amplitude values. The second element in the SAR image is the phase that is considered as the key information in the interferometric measurements.

The values of pixels phase of one single SLC are not of great important. In case of a second SLC acquired over the same area, in the same time of the first one or in another time by the same sensor, the second SLC can be interfered with the first one. The second scene has to be coregistered and resampled to the first scene; then the interferometric phase is calculated by multiplying the first scene with the complex conjugate of the second coregistered and resampled scene. The result of this process is the interferometric phase or the interferogram. In case of ignoring all decorrelation effects, for now, the interferometric phase due to change in the path length will be:

$$\Delta\phi = -\frac{4\pi}{\lambda}\Delta\rho \tag{2.17}$$

where $\Delta\phi$ is the interferometric phase, $\Delta\rho$ is the change in the path length and λ is the radar wavelength. The minus sign is because of the measured phase defined as phase delay. The phase difference $\Delta\phi$ caused by several effects, sometimes all are contributed or just a few are affected. The phase difference can be equal to the sum of all contributors

$$\Delta\phi = \phi_{base} + \phi_{topo} + \phi_{defo} + \phi_{atm} + \phi_{noise} \tag{2.18}$$

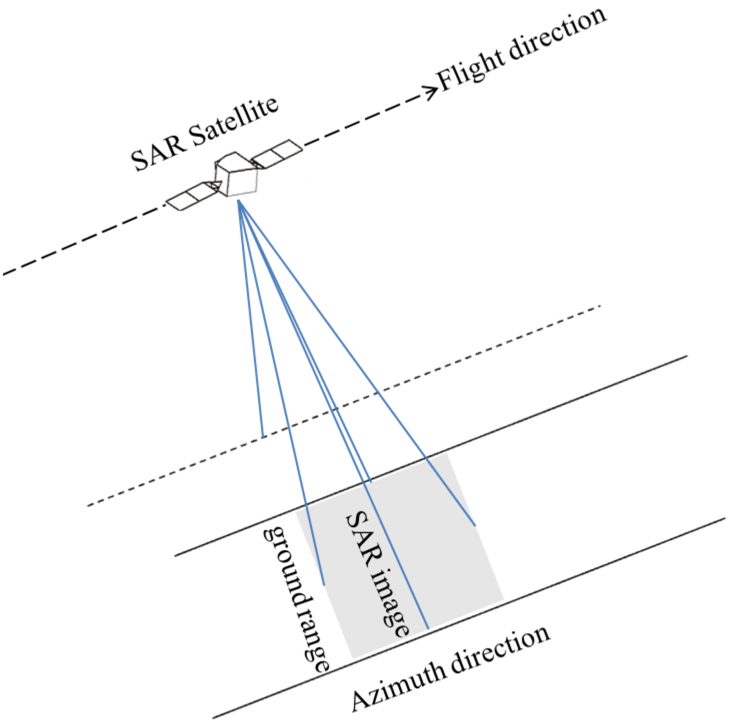

Figure 2.8: SAR imaging geometry.

where ϕ_{base} is the phase difference caused by the different positions of the satellite during the two images, ϕ_{topo} is the topography signal, ϕ_{defo} is the ground deformation contribution, ϕ_{atm} is the phase contribution due to the atmospheric delay and ϕ_{noise} is the contribution from other terms like system noise.

2.3.2.1 Differential InSAR

Figure 2.9 shows the interferometric configuration of two SAR antennas imaging the same area separated by a baseline B for either a repeat pass mode or two antennas mounted on one SAR satellite. In case of non-zero baseline between the two antennas, which is the most common case, the topography signal will be included in the interferogram. The signal due to topography can be estimated and removed from the interferogram using an external Digital Elevation Model (DEM) or from InSAR (Gabriel et al., 1989). The procedure of removing the signal due to topography from the interferogram is called Differential InSAR. (Massonnet et al., 1993) and (Zebker and Rosen, 1994) applied the DInSAR approach to image the co-seismic deformation associated with Landers earthquake (June 18, 1992, $M_w = 7.3$).

In the last two decades, DInSAR has been successfully used for different applications. This approach was applied to map the earth's topography (Zebker and Goldstein, 1986), Active volcanism ((Amelung et al., 2000); (Pritchard and Simon, 2002)), co- and post-seismic motions (Wright et al., 2001), ground subsidence from underground water withdrawal ((Amelung et al., 1999); (Hoffmann et al., 2001)), and active faults (Ryder and Bürgmann, 2008). The quality of results from the DInSAR approach is based on the degree of similarity between the SAR images or the Correlation. Changes in the imaging geometry and/or the nature of the surface being imaged may be lead to the decorrelation (Zebker and Villasenor, 1992).

Changes in the surface reflectivity with time (Temporal Decorrelation) due to vegetation, leaves grow and die and move as well, melting of snow, construction, erosion, and rapid movements due to large earthquakes, decorrelate the phase measurements significantly. These changes are sufficient to change the appearance of the surface characterization. Therefore, most of the DInSAR studies were focused on dry and sparsely vegetated areas. Variations in imaging geometry also lead to decorrelation. The difference in incidence angles, long perpendicular baselines, and change in squint angle which may alter the SAR Doppler frequency are different factors that produce spatial decorrelation (Zebker and Villasenor, 1992). In addition to the decorrelation effects, one more significant limitation of the DInSAR is the atmospheric effect on the SAR signal propagation that adds a contribution to the phase, equation (2.18) (Hanssen, 2001). The variation in phase due to an atmospheric effect comes from the variation in the water vapor in the atmosphere, which is often correlated with the topography (Onn and Zebker, 2006). As the time interval between SAR acquisitions is in the order of a month, for example, ERS and Envisat, the atmospheric effect is not correlated in time, therefore stacking multiple interferograms acquired over time is a way to reduce such effect.

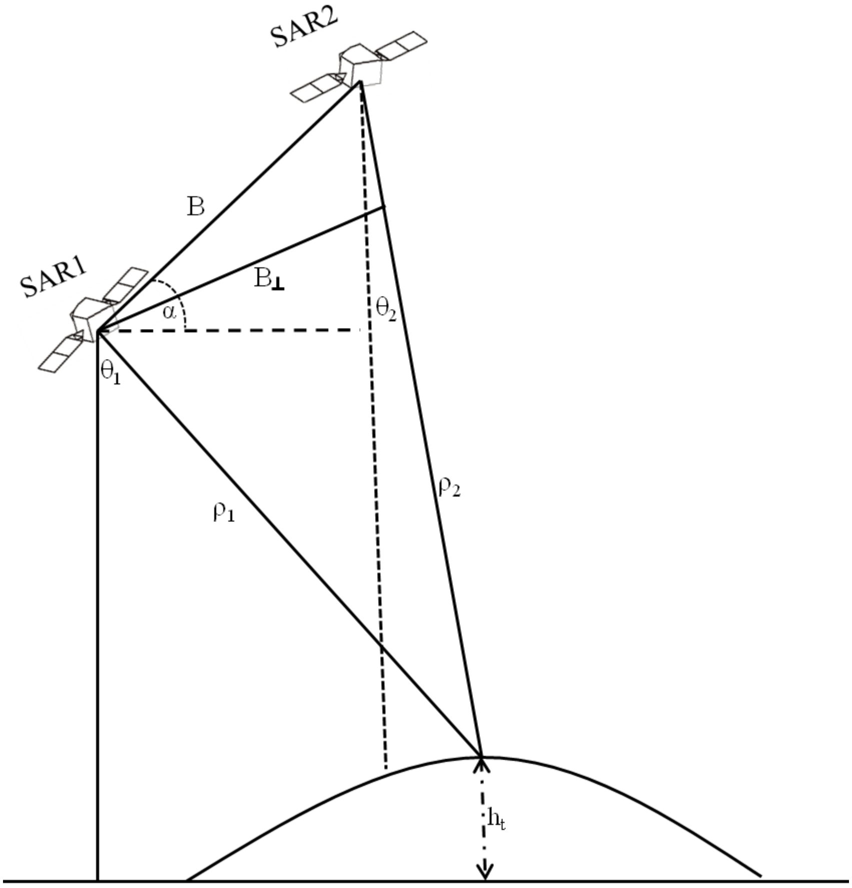

Figure 2.9: Interferometeric configuration of two SAR antennas separated by a baseline B, $B_{\perp}$ is the perpendicular baseline, θ_1 and θ_2 are the look angles of SAR1 and SAR2, ρ_1 and ρ_2 are the range (slant range) for SAR1 and SAR2, respectively, and h_t is the point's height.

2.3.2.2 Multi-temporal InSAR

Multi-temporal InSAR method is a step forward aimed to deal with the decorrelation problems and the delay due to the atmosphere. Simultaneous processing of multiple SAR scenes acquired over the same area give the chance to correct the uncorrelated phase noise and consequently reduce the error in the deformation estimates. The multi-temporal (time series) InSAR algorithms can be broadly categorized into two classes: Persistent Scatterer InSAR (PSI) and Small Baseline (SBAS) algorithm.

In any SAR scene, the reflected signal (phase and amplitude) for each pixel is the coherent sum of all scatterers within the pixel. When the pixel is composed of a single one scatterer, the variation in time of the received signal will be very small and as a result all interferograms can be used for estimating the ground deformation without error, which is not the case in reality. For pixels with no dominant scatterer, the phase due to decorrelation will be randomly distributed in the range $(-\pi,\pi)$ (Figure 2.10a). In such case, stacking interferograms between scenes separated by short time interval will result in low decorrelation noise (Sandwell and Price, 1998). Stacking is the base for SBAS approach. Currently, newer algorithms were developed to estimate the ground deformation from a stack of interferograms ((Berardino et al., 2002); (Schmidt and Bürgmann, 2003); (Hooper et al., 2012)).

If the signal of a stable scatterer in a resolution cell is significantly large, the phase decorrelation will be much reduced, the reflected signal is quite stable, and the ground deformation can be computed (Figure 2.10b). Such a case is the principle behind the "Persistent Scatterers" PS or "Permanent Scatterers" (Ferretti et al., 2001). Buildings and man-made structures represent the dominant scatterers in urban areas, whereas in non-urban areas the dominant scatterers could be an oriented rock. PS approach apply a statistical analysis to identify the PS pixels which are relatively less affected by decorrelation. The PS method is applied on a time series of interferograms that are formed with respect to one single master scene. A detailed description of PS method is discussed in Chapter 3 focusing on the Stanford Method for Persistent Scatterers (StaMPS) (Hooper et al., 2012); this method is used in this thesis for estimating the ground deformation from SAR data.

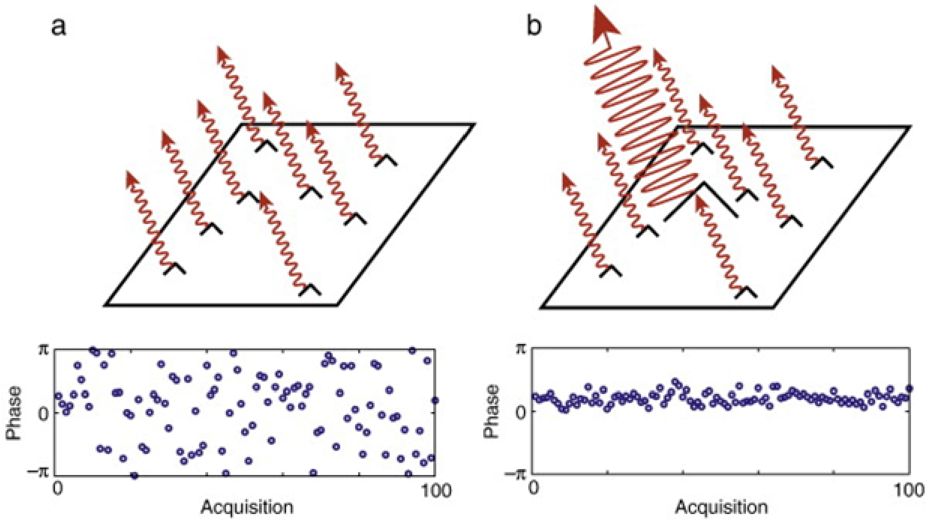

Figure 2.10: Simulated phase for (a) a distributed scatterer pixel and (b) a persistent scatterer pixel. The brighter scatterer in b is three times brighter than the sum of the smaller scatterers (Hooper, 2006).

2.3.2.3 Multi-dimensional InSAR

The current and even the planned SAR satellite missions are orbiting the Earth in near-polar orbit. They travel from the North toward the South (Descending) or from the South toward the North (Ascending), in both cases the heading is primarily in the North or South. What is determined by InSAR is the projection of the target's motion onto the Line-Of-Sight (LOS). Since the projection of the North component onto the LOS is quite equal to zero, the determined LOS is composed primarily of East-West and Up components. It is hard to estimate the true East-West and Up components from the LOS estimate unless a priori information is available on the true East-West and Up components. However, by adding the results from both ascending and descending, it is possible to obtain an accurate estimate of Up and East-West motion.

Many attempts have been done in combining the LOS velocity from InSAR with velocities from different techniques like GPS and leveling in order to map the ground deformation ((Aly and Cochran, 2011); (Wang and Wright, 2012); (Cakir et al., 2014)). The LOS velocity is a function of LOS angel (incidence angle θ). If the direction of the ground motion is close to the angle of the LOS, the measured and actual motions will be similar. However, in cases where the ground motion is horizontal, the LOS motion can often differ noticeably from the real value of motion. Viewing the same target from different directions (ascending and descending), may help to determine either the LOS velocity is horizontal or vertical. As shown in Figure 2.11, in case of vertical movement, the target moves away from the sensor in both directions, while the target moves away from one satellite and toward the other one in case of horizontal movement.

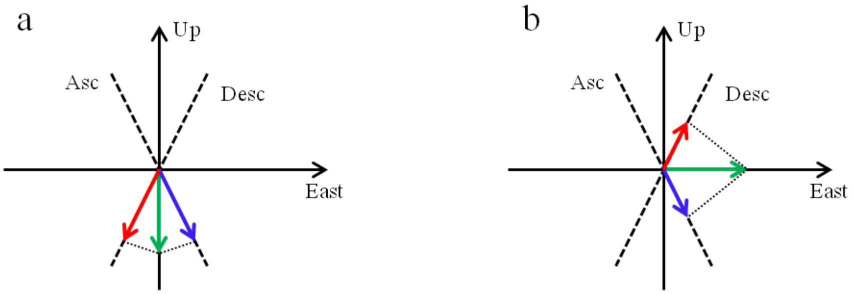

Figure 2.11: Combination of the results of both Ascending and Descending information. (a) in case of vertical motion, the target is moving away from the satellite in both directions and (b) in case of horizontal motion, the target is moving away from one satellite and toward the second.

With large areas, like the Nile Delta, it is common that the area is covered by more than one track and as a consequence the overlapped area between the adjacent tracks is observed by two different incidence angles. As shown in Figure 2.12, point P is observed by the two tracks (Tracks 1 and 2), but with different incident angles. It is close to the far-range of track 1 and at the same time close to the mid-range of track 2. For example, if this sensor is ERS2, point P is observed by track 1 and track 2 with approximately 26° and 23° incidence angles, respectively. Therefore, different estimates for the LOS velocity for the areas covered by overlapped tracks are expected due to the difference in the incidence angle for each track.

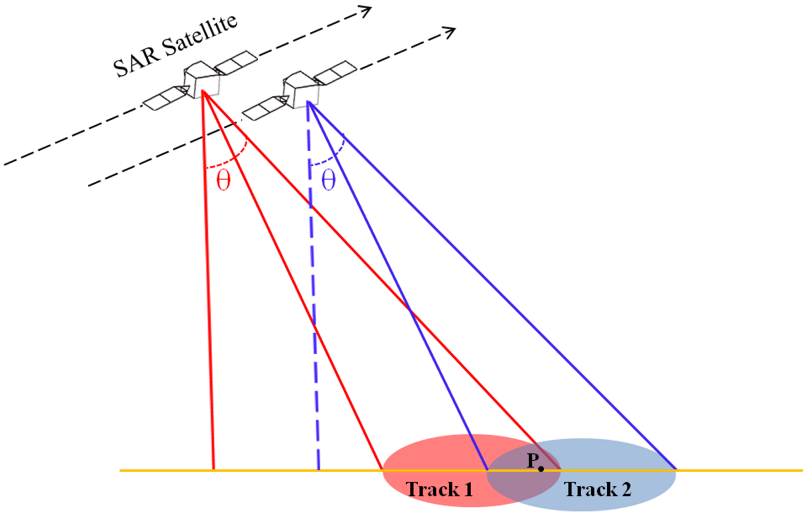

Figure 2.12: SAR geometry in case of imaging the same area by two adjacent tracks.

3 Data Processing

Although Egypt is not characterized by very high seismic activity, recent crustal movements may represent a significant seismic hazard due to its location. In fact, Egypt includes some areas that are active tectonically and seismically. Therefore, this study aims to throw light upon the geodynamical regime and the general tectonic framework of Egypt including the northeastern corner of Nubia using the Global Positioning System (GPS) and the Interferometric Synthetic Aperture Radar (InSAR). This chapter presents the processing steps of the available GPS and InSAR observations. The GPS section deals with the infrastructure of the Egyptian networks, development, equipment, the available GPS data from these networks, the selected permanent stations from different sources, IGS products, and processing strategy. On the other hand, the InSAR section will focus on the available SAR data used in this work in addition to Persistent Scatterers (PSI) processing steps following (Hooper et al., 2012) processing scheme.

3.1 GPS Data

In 1983, and after the Kalabsha earthquake in Aswan area (November 14, 1981, M_L5.6), south of Egypt, the National Research Institute of Astronomy and Geophysics (NRIAG) started a national project for studying the recent crustal movements and its relation to earthquake activity using terrestrial techniques around the active area northwest Lake Nasser and close to the Aswan High Dam. Later, after the Cairo earthquake (October 12, 1992, M_L5.9), the Global Positioning System (GPS) techniques were used instead of terrestrial techniques. NRIAG installed a number of local GPS geodetic networks around the active areas in Egypt, starting in 1997 around Greater Cairo region , consisting of 9 stations, followed by Aswan network in 2000, consisting of 11 stations. A network around the southern part of Sinai Peninsula and Gulf of Suez was established in 2003, which updated in 2007 to cover all the Gulf of Suez (11 stations). Another two networks around the Nile Valley (12 stations) and Abu-Dabbab area (11 stations), a small area on the western coast of the Red Sea, were established in 2007 and 2008, respectively. The epoch wise observation technique is the only technique that was applied to observe these networks.

In 2006, NRIAG started the establishment of the Egyptian Permanent GPS Network (EPGN). Basically, the site selection was aimed to cover geographically all the Egyptian territory but also considering the tectonic setting of Egypt. The chosen places for constructing these stations fulfilled the required criteria such as clear view without any obstructions, away from any electromagnetic sources, and accessibility. Three stations were located in the Eastern Desert on the Red Sea coast, two stations in Sinai Peninsula, three stations in the Western Desert, two stations in the Nile Valley, and six stations around Cairo and the Nile Delta. Figure 3.1 shows the geographic distribution of the Egyptian GPS sites, permanent and campaign, in addition to some of the SOPAC stations located northeast of Egypt. Due to the importance of the monumentation type and its quality which affects directly the stability of these stations, the geodetic stations were installed in homogeneous bedrock or consolidated sedimentary layers. In case of no bedrock at the site, the monumentation of the marker was prepared using reinforced concrete. The majority of EPGN stations were installed on concrete pillars; but in a few cases, some stations were installed on a roof of building such as the case in Helwan (PHLW) and Marsa-Alam (MRSA) for safety considerations. Starting from 4 stations in 2007 to 15 stations were achievable at the end of 2011 (4 in 2007, 2 in 2008, 3 in 2010, and 6 stations in 2011) (Saleh and Becker, 2014). In addition to these 15 stations, which were established and administrated by NRIAG, there is a station in Alexandria organized by a French institute called Centre d'Études Alexandrines (CEALX), and in this work, it will be considered as one of the EPGN stations. The GPS data from these 16 stations are collected by three different methods:

1. stations Helwan (PHLW), Asuit (ASUT), Nekhel (NKHL), Safaga (SAFG), Shalaten (SHLA), Saloum (SLUM), Dakhla (DKHL), and Farafra (FARF) sent the data to the Data Center in NRIAG by satellite.

2. stations Borg El-Arab (BORG), Abo-Simple (ABSM), Al-Arish (ARSH), Katameya (KATA), Mansoura (MNSO), Marsa-Alam (MRSA), and Mesalat (MSLT) the data is downloaded in field (from time to time someone goes to collect the data from these stations).
3. station Alexandria (ALEX) data can be downloaded from the official website for this station `www.station-gps.cea.com`.

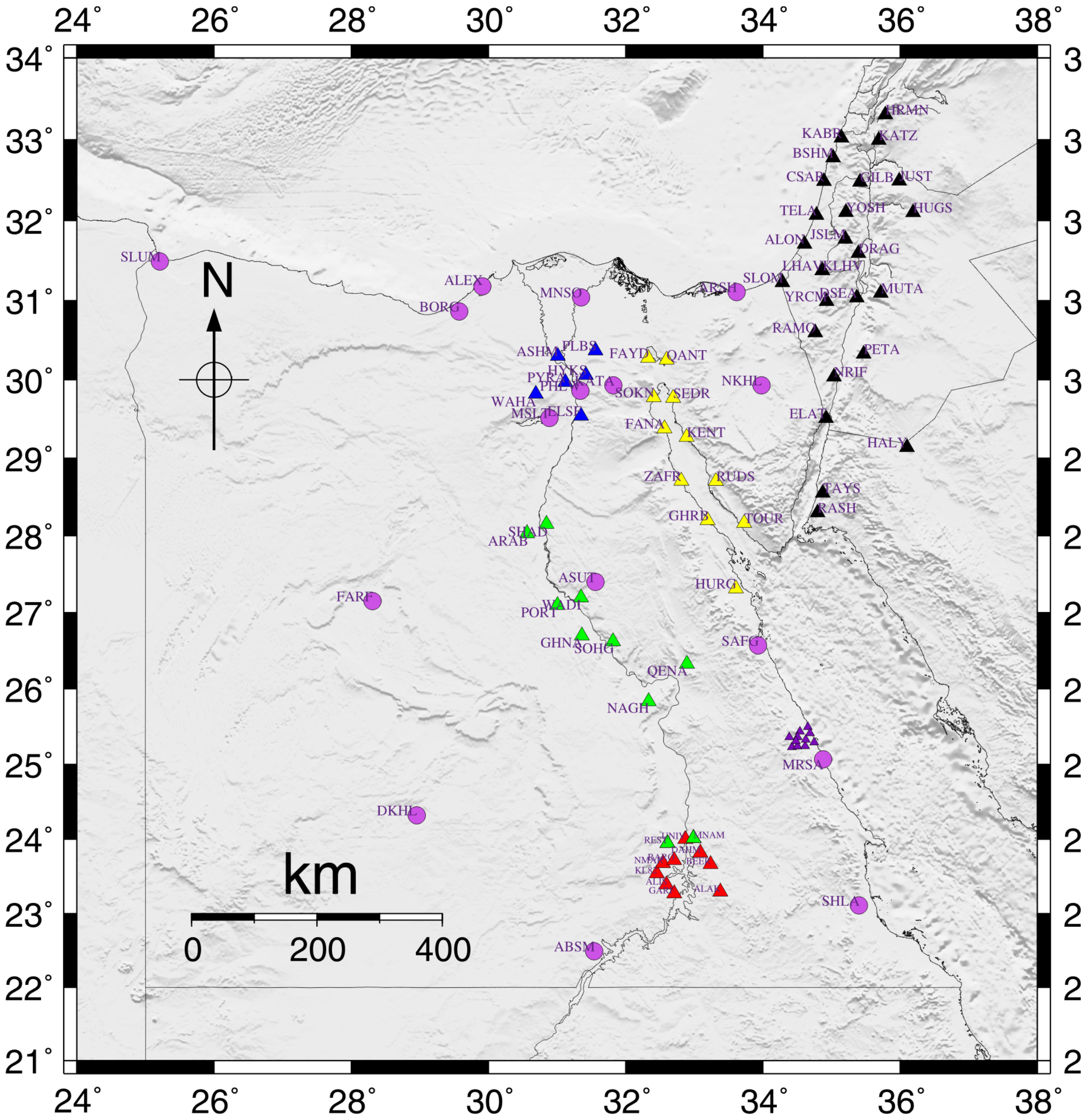

Figure 3.1: Geographic distribution of the Egyptian GPS stations, red triangle (Aswan), green triangle (Nile Valley), yellow triangle (Gulf of Suez), blue triangle (Greater Cairo), violet triangle (Abu-Dabbab) and violet circles (EPGN stations) in addition to SOPAC sites (black triangle).

Table 3.1 summarizes the station information in terms of the station name, 4-ID character, and equipment information (antenna type and receiver type). Figure 3.2 shows some photos for typical permanent and non-permanent stations. Figures 3.3 and 3.4 show the available GPS data between 2006-2012 which collected from the permanent network (EPGN) and the local networks (Aswan, Greater Cairo, Gulf of Suez, Nile Valley, and Abu-Dabbab), respectively. Due to the variety of communication equipment, in the permanent stations, and unfortunately due to frequent communication problems, considerable amount of data is lost as can be seen in the large number of gaps in almost all permanent stations, Figure 3.3.

Figure 3.2: Some photos for typical stations of the Egyptian Permanent GPS Network (EPGN) and non-permanent station (AD01 from Abu-Dabbab network).

Table 3.1: Equipment of permanent and non-permanent Egyptian stations.

Station / Network	4-ID chatacter	Antenna	Receiver	Organized by	Data Transfere
Helwan	PHLW	TRM41249.00	TRIMBLE 5700	NRIAG	By Satellite
Asuit	ASUT	TRM41249.00	TRIMBLE 5700	NRIAG	By Satellite
Nekhel	NKHL	TRM41249.00	TRIMBLE 5700	NRIAG	By Satellite
Safaga	SAFG	TRM41249.00	TRIMBLE 5700	NRIAG	By Satellite
Shalateen	SHLA	TRM41249.00	TRIMBLE 5700	NRIAG	By Satellite
Saloum	SLUM	TRM41249.00	TRIMBLE 5700	NRIAG	By Satellite
Dakhla	DKHL	TRM41249.00	TRIMBLE 5700	NRIAG	By Satellite
Farafra	FARF	TRM41249.00	TRIMBLE 5700	NRIAG	By Satellite
Abo-Simpel	ABSM	TRM55971.00	TRIMBLE NETR5	NRIAG	Downloading in field
Al-Arish	ARSH	TRM55971.00	TRIMBLE NETR5	NRIAG	Downloading in field
Borg el-Arab	BORG	TRM41249.00	TRIMBLE NETR5	NRIAG	Downloading in field
Katameya	KATA	TRM41249.00	TRIMBLE NETR5	NRIAG	Downloading in field
Mansoura	MNSO	TRM55971.00	TRIMBLE NETR5	NRIAG	Downloading in field
Marsa-Alam	MRSA	TRM55971.00	TRIMBLE NETR5	NRIAG	Downloading in field
Mesalat	MSLT	TRM41249.00	TRIMBLE NETR5	NRIAG	Downloading in field
Alexandria	ALEX	LEICA AT303	LEICA CRS1000	CEALX	Available online
Alexandria	ALEX	LEIAT504GG	LEICA GRX1200GGPRO	CEALX	Available online
Aswan Network	11 stations	TRM22020.00+GP	TRIMBLE 4000SSI/SSE	NRIAG	Downloading in field
Cairo Network	9 stations	TRM22020.00+GP	TRIMBLE 4000SSI/SSE	NRIAG	Downloading in field
Gulf of Seuz Network	11 stations	TRM22020.00+GP	TRIMBLE 4000SSI/SSE	NRIAG	Downloading in field
Nile Valley Network	12 stations	TRM22020.00+GP	TRIMBLE 4000SSI/SSE	NRIAG	Downloading in field
Abu-Dabbab Network	11 stations	TRM22020.00+GP	TRIMBLE 4000SSI/SSE	NRIAG	Downloading in field

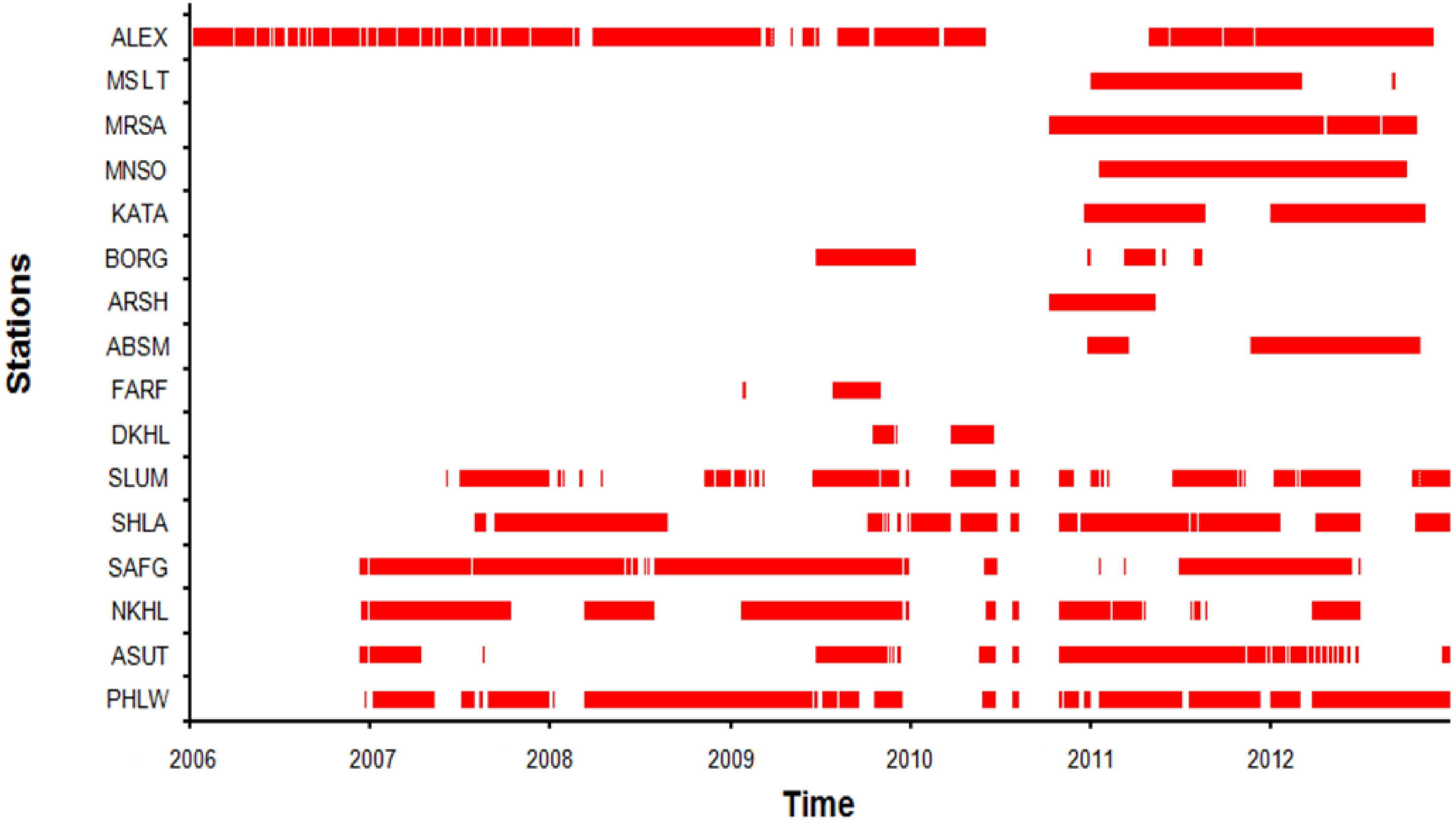

Figure 3.3: Availability of the EPGN stations.

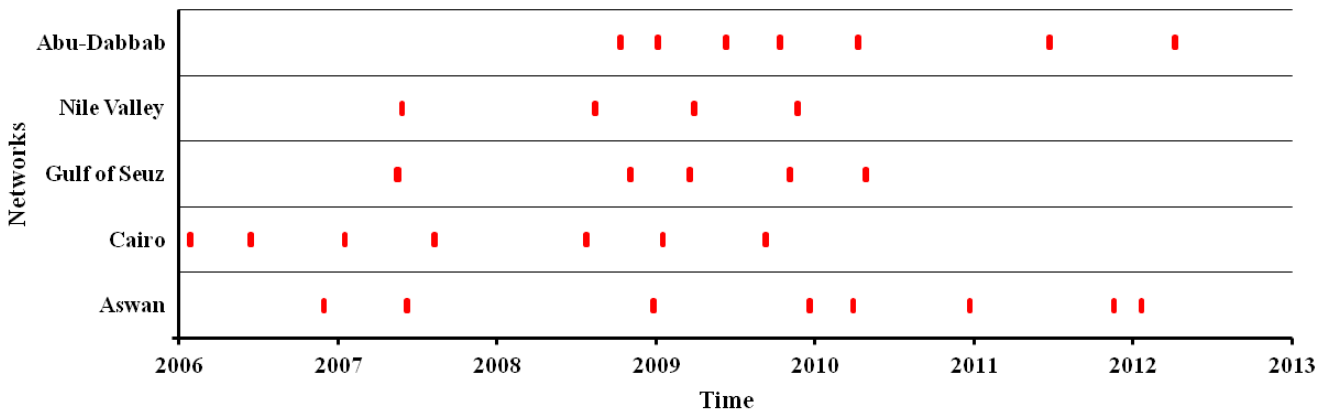

Figure 3.4: Availability of the campaign data for each local network, for the period 2006-2012.

3.1.1 Processing setup

In addition to the collected data from the five local geodetic networks and the 16 EPGN stations, seven years data of 86 permanent stations from different sources, IGS (International GNSS Service), EPN (EUREF Permanent Network), UNAVCO (University NAVSTAR Consortium), and SOPAC (Scripps Orbit and Permanent Array Center) were downloaded starting from the beginning of 2006 to 30.09.2012 (day 274 in 2012). The selection of these stations viewed at a good configuration around the Egyptian stations. As shown in Figure 3.5, the 86 selected permanent stations, with EPGN and local network stations, cover the north and the east of Egypt well. The west of Egypt is not well covered due to the absence of GPS stations in northern Africa, and to the south there are some IGS stations, but baselines are rather long. The selected 86 stations are belonging to three different tectonic plates, 47 stations from the African plate (Nubia, Somalia, Lwandle, and Sinai), 13 stations from the Arabian plate, and 26 stations from the Eurasian plate. 34 stations out of 86 are included in the International Terrestrial Reference Frame 2008 (ITRF2008, (Altamimi et al., 2011)), and they are used as fiducial points for datum definition.

Due to the absence of IGS reprocessed products that are consistent with ITRF2008, the reprocessed products from the Center for Orbit Determination in Europe (CODE) in Bern were used. CODE reprocessing series 2011 was generated based on the GNSS data from 1996 until the end of 2010, and it is available under `ftp://ftp.unibe.ch/aiub/REPRO_2011/CODE`. For the remaining period, 2011 to 2012, the final IGS orbits, satellite clocks, and Earth orientation parameters were used. These IGS products, starting from 2011, have been created using the same standards used for CODE reprocessing i.e. no inconsistencies between both products. The data were processed using Bernese GPS Software V.5.2 (Dach et al., 2007) using the following processing strategy:

1. ITRF2008 reference frame,
2. NNR-NUVEL-1A plate motion model for non-ITRF stations,
3. Usage the reprocessed CODE products till end 2010 and the final IGS products for the remaining period, 2011 to 2012,
4. Automatic baseline creation using MAX-OBS strategy,
5. Ionosphere free linear combination L_{IF},
6. Elevation cut-off angle 3°, and
7. Dry Niell as troposphere model with GMF (Global Mapping function) as mapping function.

To establish the ITRF2008 datum for the whole network (daily and combined), the 34 IGS stations being part of ITRF2008 were used as datum points. The processing procedure was carried out on a daily basis resulting in a set of 2463 daily solutions in the ITRF2008 datum, established by minimum constraints conditions. All estimated parameters (coordinates, troposphere Zenith Total Delay ZTD, ...) are stored in the normal equation files to be stacked later. Figure 3.6 shows the flow chart of the processing steps of the GPS data using Bernese 5.2.

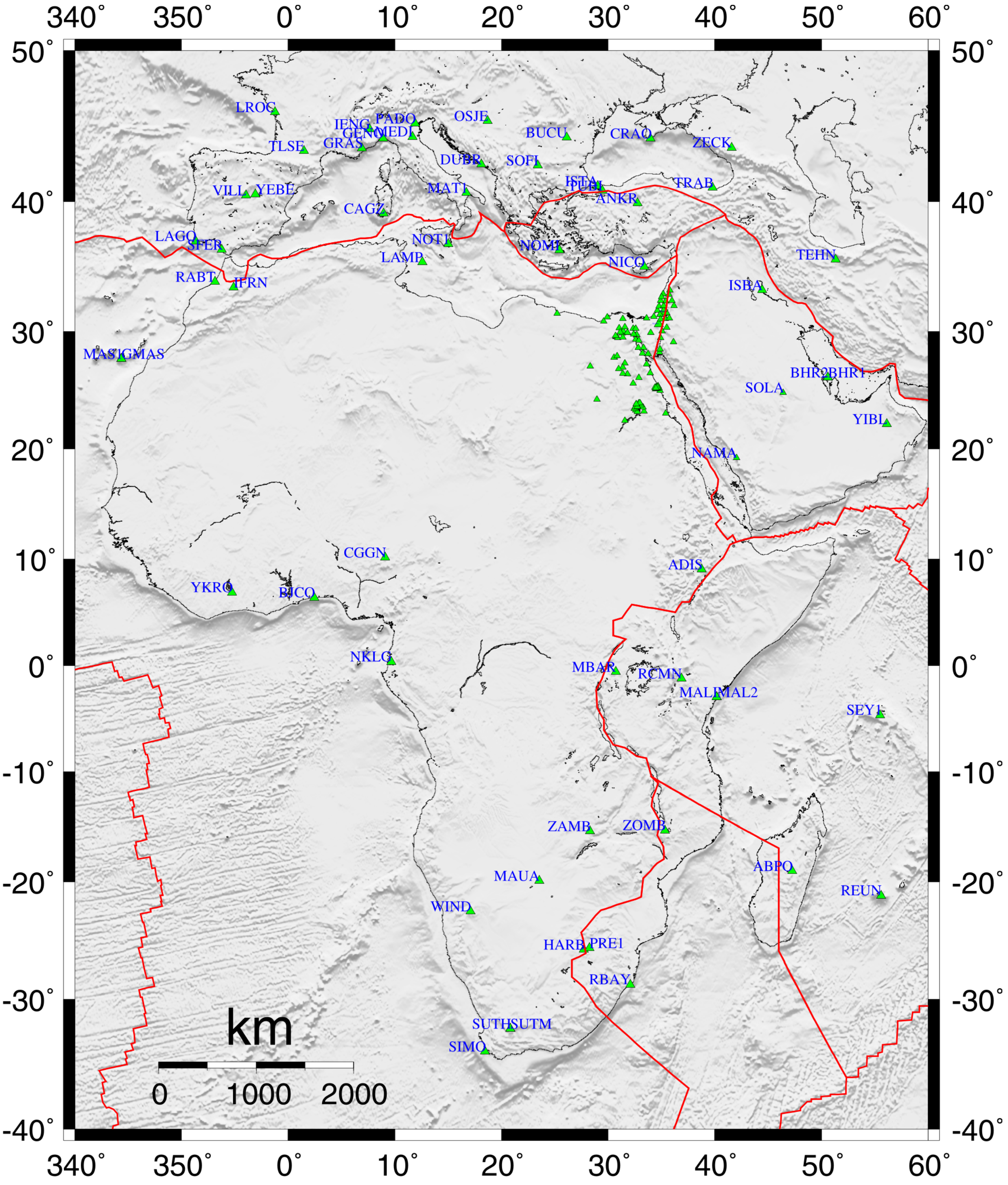

Figure 3.5: Selected permanent stations (IGS, EPN, UNAVCO, and SOPAC) and the Egyptian stations with plate boundaries (as in Figure 2.1).

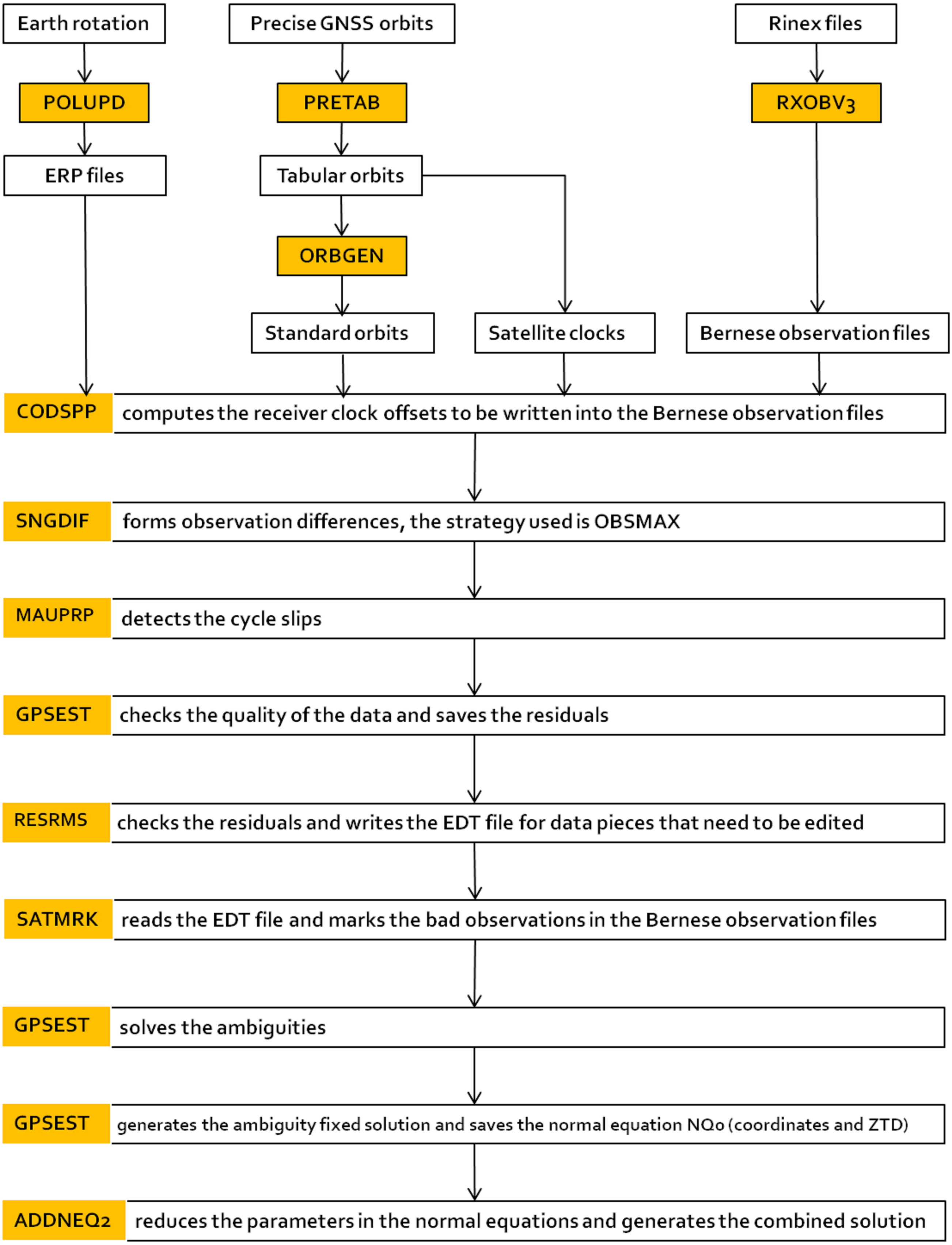

Figure 3.6: Flow diagram of the processing steps in Bernese GPS Software Version 5.2. The orange boxes represent programs.

3.1.2 GPS Combined Solution

The combination tool (ADDNEQ2) in Bernese software was used for the estimation of station position and velocity for all the processed stations. Again the combined solution is minimally constrained to the ITRF2008 datum represented by the 34 IGS stations. As a by-product of the combination process, in addition to station coordinate and station velocity, residuals for all stations and for each day, and full variance-covariance matrix were estimated. It is well known that the standard deviations of coordinates or velocities obtained from GNSS daily solutions are too optimistic and unrealistically small. This is because of the absence of adequate models for the time correlations of the GNSS data, in the estimation of the daily solution. These unrealistic standard deviations, sometimes named formal errors, represent the precision of the GNSS in the sense of no-correlation state, which is not the case in reality.

3.1.3 Error Assessment (Scaling)

In case of combining multiple daily solutions, another more realistic precision can be gained by using the residuals of the daily solutions with respect to the combined solution to calculate a tentative standard deviation (usually called repeatability). A ratio between the formal standard deviation and the repeatability can be used to scale the variance-covariance matrix to end up in a more realistic error assessment for the combined solution. However, this is a simple approximation of the observation precision and, of course, cannot perfectly model the absence of time correlation in the GNSS observations. Daily solutions with residuals larger than 3-sigma were rejected. Seventy-eight days out of 2463 were rejected during the process of outlier rejection representing 3.2 % of the daily solutions. Figure 3.7 (a and b) shows the repeatability of EPGN and the selected permanent stations, respectively. It is clear that the repeatability for the EPGN stations is about $1-3\ mm$ in the horizontal components, East and North, and $3-6\ mm$ in the Up component except FARF, DKHL, and ALEX stations. The stations FARF and DKHL have very short records (few months) which could be the reason for the high repeatability values. Whereas, the high repeatability value of ALEX may be regarded to benchmark instability. The repeatability for the selected non-Egyptian stations is similar to the EPGN stations and also there are some stations with high repeatability values especially in the Up component. An average value of the repeatability (σ_r), Figure 3.7, in each component was used in addition to the formal error (σ_f), Bernese standard deviation, to calculate the scale factor in order to compute the average scaled error (σ_s) for each component. Table 3.2 explains in details the values of all inputs and outputs. The ratios (scale factor) are different for North, East, and Up components, which ranging from 12 to 58 in the horizontal component and from 9 to 92 in the vertical component. These high values of the scale factor may be due to the fact that, especially in the horizontal component, the repeatability contains some other signals in addition to the linear signal.

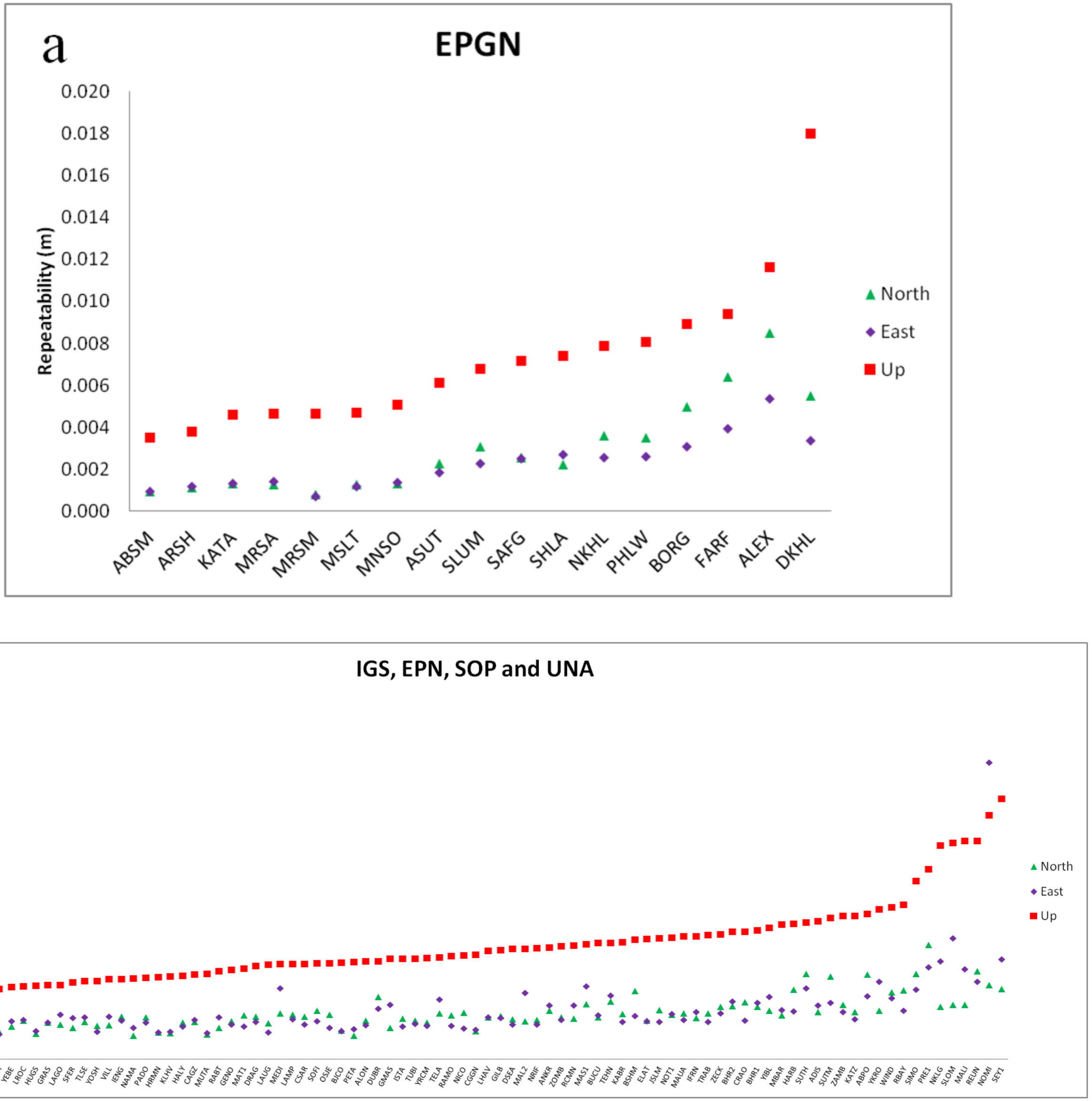

Figure 3.7: Repeatability of EPGN (a) and the selected stations from IGS, EPN, SOPAC, and UNAVCO (b).

Table 3.2: Estimation of the average scaled error for Aswan (AS), Greater Cairo (GC), Gulf of Suez (GS), Nile Valley (NV), Abu-Dabbab (AD), EPGN (Egyptian Permanent GPS Network) stations in North, East, and Up components.

Component	Network	Average formal coordinate error σ_f (mm)	Average repeatability σ_r (mm)	Scale factor = σ_r / σ_f	Average scaled velocity error σ_s (mm)
North	AS	0.19	4.04	22.49	1.99
	GC	0.19	4.79	25.35	2.74
	GS	0.22	4.76	22.85	5.95
	NV	0.18	3.62	20.52	2.95
	AD	0.25	4.78	18.90	2.31
	EPGN	0.10	3.03	53.59	1.18
East	AS	0.26	5.07	22.69	2.45
	GC	0.18	4.80	27.17	2.83
	GS	0.22	3.91	19.39	4.85
	NV	0.17	3.68	21.65	3.22
	AD	0.39	4.58	12.04	2.29
	EPGN	0.10	3.20	58.19	1.25
Up	AS	0.86	12.16	15.06	5.85
	GC	0.84	22.96	27.56	13.2
	GS	1.00	16.38	17.67	18.08
	NV	0.80	15.48	19.82	13.22
	AD	1.16	10.97	9.48	5.32
	EPGN	0.27	7.49	92.35	2.92

3.1.4 Time Series Analysis

As mentioned in the previous section, the problem of neglecting correlation in the GNSS time series required a scaling. The stochastic model in the sense of no time correlation between the daily solutions is called white noise. To describe time correlation, the power law noise stochastic model was introduced (Agnew, 1992). The one-dimensional frequency domain of such kind of stochastic model has the form

$$P_{\chi}(f) = P_0(f/f_0)^k \tag{3.1}$$

where f is the frequency, P_0 and f_0 are normalizing constants and k is the spectral index (Mandelbrot and Ness, 1968). In case of white noise, $k = 0$, the power spectral density is constant and the variance-covariance matrix have the form $C_{\chi} = aI$. On the other hand when $k \neq 0$ (colored noise) the variance-covariance matrix will be equal $a_k J_k$. Therefore, in case of the combination of both cases the variance-covariance matrix will have the form

$$C_{\chi} = aI + a_k J_k \tag{3.2}$$

where a and a_k are the scale factors of the amplitude of the white noise and colored noise, respectively, I is the identity matrix and J_k is the covariance matrix for the respective colored noise. The Maximum Likelihood Estimation (MLE) method, algorithm described by (Langbein and Johnson, 1997), was recommended for estimating the stochastic model parameters (k, a_k, a), in addition to the time series parameters like velocities and coordinates. The approach of estimating the linear parameters, coordinate, velocity, offsets (in case the antenna was changed), and annual periodic variation, in addition to the non-linear parameters, spectral index, scale factor of the amplitude of the colored noise, and scale factor of the amplitude of the white noise (k, a_k, a), is carried out in the CATS (Create and Analyze Time Series) software (Williams, 2008). CATS is a time series analysis software based on the MLE approach. Concept, theory, and more details beyond CATS are described in (Williams, 2003). It is worth to mention that CATS analyzes each coordinate component in the GNSS time series separately, which means that the correlation between East, North, and Up components is ignored. In this work the linear parameters in addition to non-linear parameters were estimated using four different stochastic models:

1. White noise, estimating the scale factor of the amplitude of the white noise (a).
2. White noise in addition to flicker noise($k = -1$), estimating the scale factors of the amplitude of the white noise and colored noise (a and a_k) at $k = -1$.
3. Power law noise with no additional white noise, estimating the spectral index and the amplitude of the colored noise (k and a_k).
4. White noise plus power law noise, estimating the spectral index, the scale factor of the amplitude of the colored noise, and the scale factor of the amplitude of the white noise (k, a_k, a).

Basically, the stochastic model of white noise plus power law noise offers the estimation of all parameters in equation (3.2), which may be considered as the most adequate model and may represent the time series noise properly. Figure 3.8 shows the processing steps of the CATS analysis, the analysis is based on the Bernese results for detecting the outliers, residuals, and offsets in the first iteration. Then, the clean solution is processed again using CATS to estimate the linear and non-linear parameters. Figure 3.9 shows the estimated stochastic model (white noise + power law noise) parameters. Spectral index (k), power law amplitude (a_k) and white noise amplitude (a) versus time were plotted for the selected stochastic model. During the CATS analysis and when it is difficult to calculate the white noise or the power law noise from the time series, the noise amplitude has the value zero. The spectral index (k)

is varying from zero to -1.5. From this figure no clear dependence of the stochastic model on the time length can be seen. However, it may be due to the used GNSS observation period still being not long enough to have a clear view about the correlation depending on time.

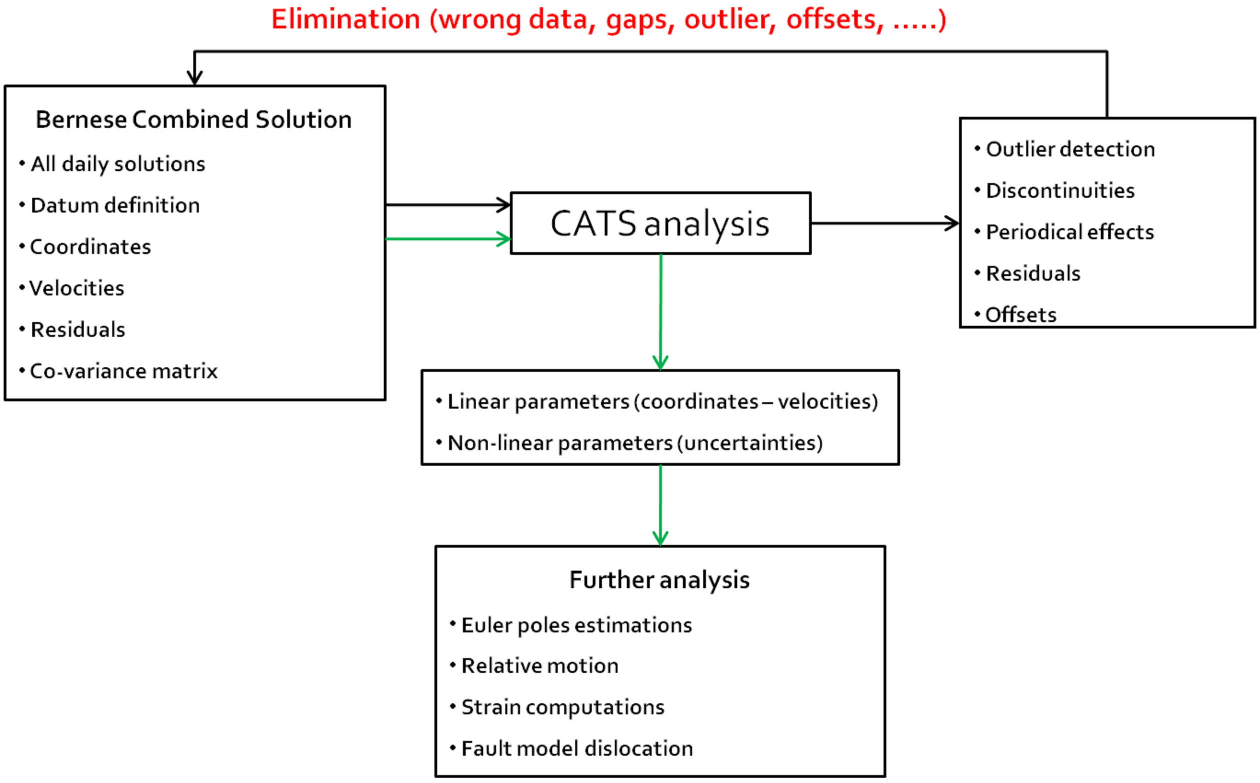

Figure 3.8: Flow diagram of the CATS processing scheme.

Figures 3.10 to 3.13 show examples for the CATS analysis, stations PHLW and SAFG from EPGN which are characterized by long record and stations WIND and SOFI from the selected IGS permanent stations. Again for the same four stations, PHLW, SAFG, WIND, and SOFI, a comparison between the estimated parameters, velocities and uncertainties, using different stochastic models and the estimated parameters from Bernese software is given in Table 3.3.

The table of comparison shows that the effect of the stochastic model on the velocity estimates is almost negligible especially in the North and East components, and slightly in the Up component. On the other hand, the uncertainties are very different between scaled standard deviation from Bernese results on one side and from CATS using different stochastic models on the other side. This comparison shows that the scaled uncertainty is too large with respect to the CATS ones. However, this may be due to the fact that the values of the repeatability, the main input for the scaling process, still contain other signals, like annual and periodic signals and few outliers. Even with the realistic-like values of the scaling uncertainties, it is not the best way to evaluate and estimate the GNSS time series parameters.

Unfortunately, it is difficult to apply the CATS approach for the epoch stations due to the discontinuity in these stations during the time series in addition to the short period of observations in each campaign, from three to five days. It is worth to mention that the results, velocities and uncertainties, of white noise plus power law noise stochastic model were selected because it offers the estimation of all parameters in equation (3.2). The first part of Chapter 4 will be dedicated to the results of CATS analysis.

Table 3.3: Velocities and their standard deviations from different stochastic models for stations PHLW, SAFG, WIND, and SOFI in mm/yr.

		Bernese scaled error	CATS white noise	CATS power law noise	CATS white noise + flicker noise (k=-1)	CATS white noise+ power law noise
PHLW	East	22.90 ± 3.45	21.69 ± 0.03	21.66 ± 0.17	21.61 ± 0.29	21.61 ± 0.30
	North	18.30 ± 2.81	17.94 ± 0.03	17.97 ± 0.15	17.98 ± 0.25	17.99 ± 0.25
	Up	−0.50 ± 5.06	−0.25 ± 0.08	−0.10 ± 0.46	−0.01 ± 0.84	−0.10 ± 0.46
SAFG	East	23.40 ± 3.45	23.55 ± 0.04	23.64 ± 0.20	23.72 ± 0.33	23.71 ± 0.31
	North	18.10 ± 2.81	17.95 ± 0.03	18.03 ± 0.14	18.10 ± 0.25	18.08 ± 0.21
	Up	−0.20 ± 5.70	−0.42 ± 0.08	−0.37 ± 0.30	−0.26 ± 0.68	−0.36 ± 0.32
WIND	East	18.60 ± 1.88	19.61 ± 0.07	19.64 ± 0.22	19.58 ± 0.48	19.60 ± 0.36
	North	24.30 ± 1.71	21.60 ± 0.07	21.47 ± 0.30	21.32 ± 0.55	21.35 ± 0.49
	Up	2.90 ± 4.20	2.87 ± 0.15	2.73 ± 0.58	2.37 ± 1.06	2.27 ± 1.61
SOFI	East	22.50 ± 1.36	23.63 ± 0.03	23.66 ± 0.09	23.73 ± 0.22	23.70 ± 0.14
	North	14.10 ± 1.06	12.40 ± 0.03	12.25 ± 0.17	12.06 ± 0.32	12.09 ± 0.29
	Up	1.40 ± 2.70	0.14 ± 0.07	0.33 ± 0.33	0.66 ± 0.71	0.36 ± 0.36

3.1.5 Euler Pole Parameters

Euler's fixed point theorem states that the motion of a rigid body on the surface of a sphere may be represented as a rotation about a rotation pole "Euler Pole". CATS derived velocities in North and East, for permanent stations, and Bernese velocities, for non-permanent stations, were used to estimate ITRF2008 and relative Euler pole parameters, latitude, longitude, and angular velocity for Nubian, Somalian, Eurasian, and Arabian plates in addition to Sinai sub-plate. The selected sites for Euler vector estimation should represent the stable plate interior. Selected sites should satisfy the following three criteria:

1. Observation time span longer than two years for each station.
2. Distance of 100 *km* or more away from deformation zones and plate boundaries.
3. Coordinate repeatability less than 3 *mm*.

Figure 3.14 shows four categories of site selection with different colors. Six sites are excluded after condition 1 (blue points in Figure 3.14). 26 sites (red points) are close to plate boundaries or located in deformation zones. 26 sites (black points) have a repeatability larger than 3 *mm*. 91 sites that satisfy the three conditions (green points) were selected for the Euler vector estimations. The absolute ITRF2008 Euler vectors for each plate were derived by a least-squares adjustment to the achieved velocities. Relative Euler vectors were calculated by differencing the ITRF2008 Euler vectors. Selected velocities satisfying the selection criteria mentioned above were used to estimate the ITRF2008 Euler pole parameters, Euler pole parameters in Eurasia-fixed frame, Nubia-fixed frame, Arabia-fixed frame, and Sinai-fixed frame. All velocity fields are presented in chapter 4.

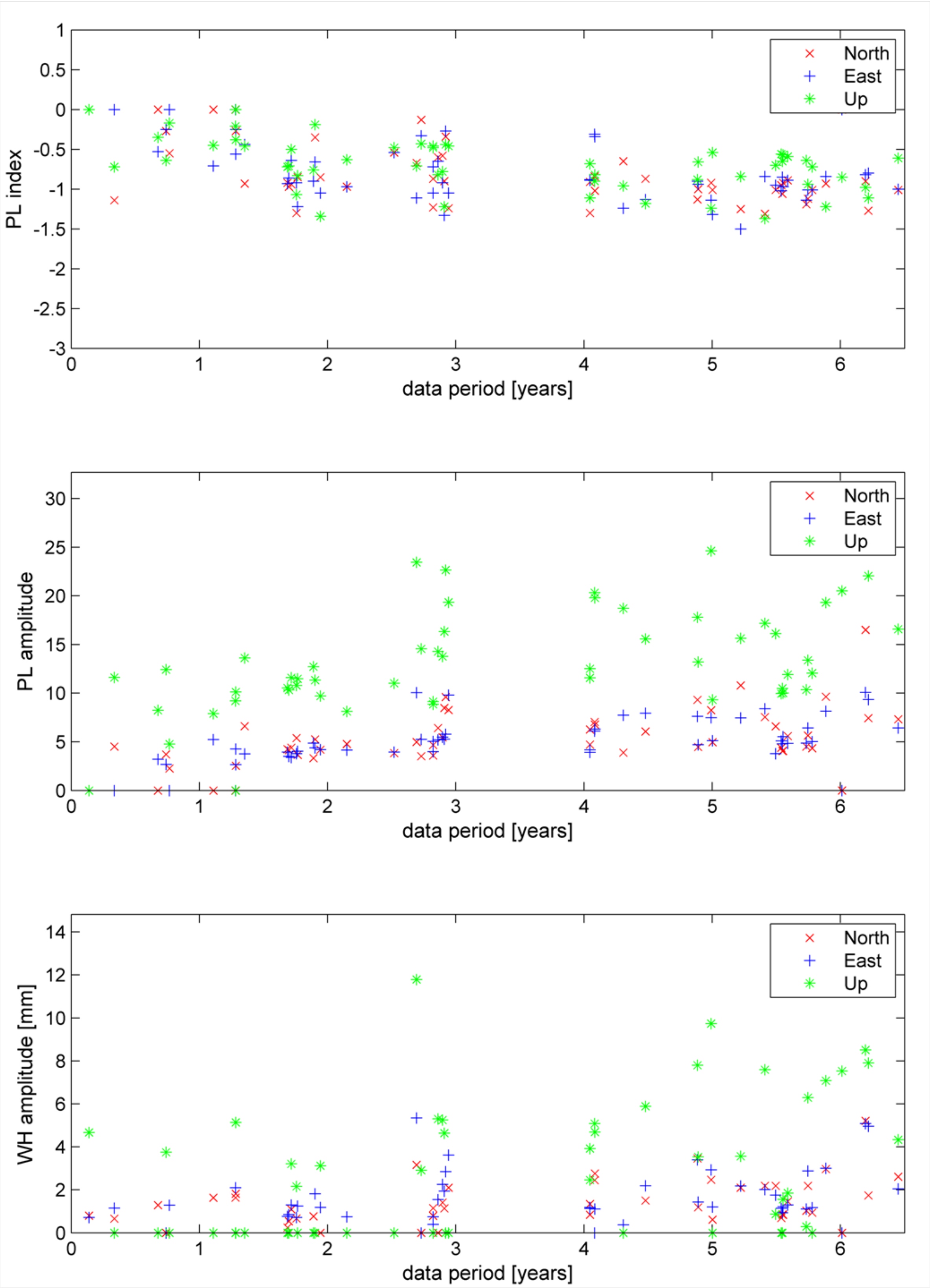

Figure 3.9: The estimated parameters $[k, a_k, a]$ of the white noise plus power law noise model over the data period. Each station represented by one dot in each component (East, North, and Up).

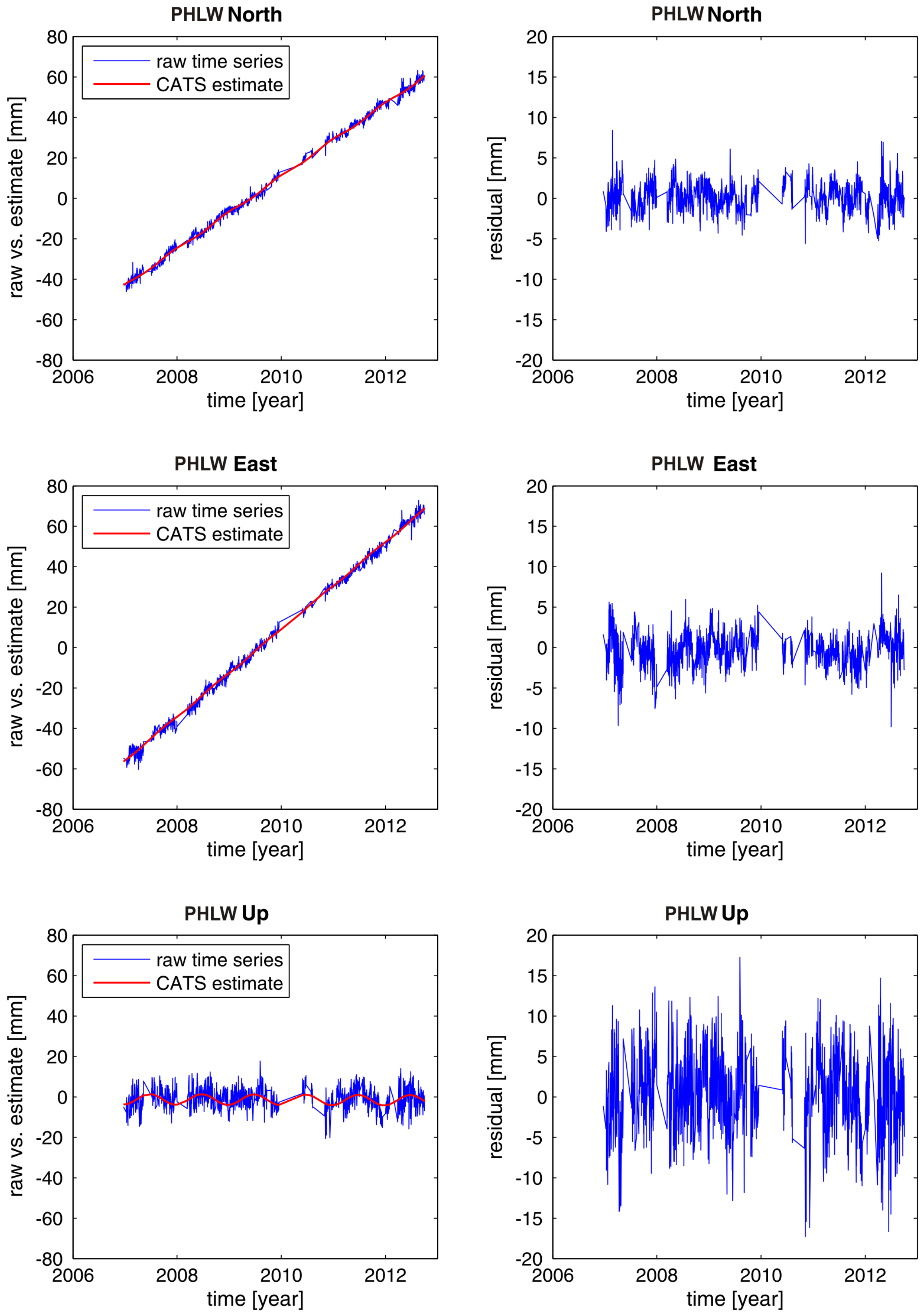

Figure 3.10: Bernese raw time series (blue line) and the estimated CATS time series (red line) for station PHLW in the left hand side and the residuals in the right hand side in each component. Stochastic model used is white noise plus power law noise.

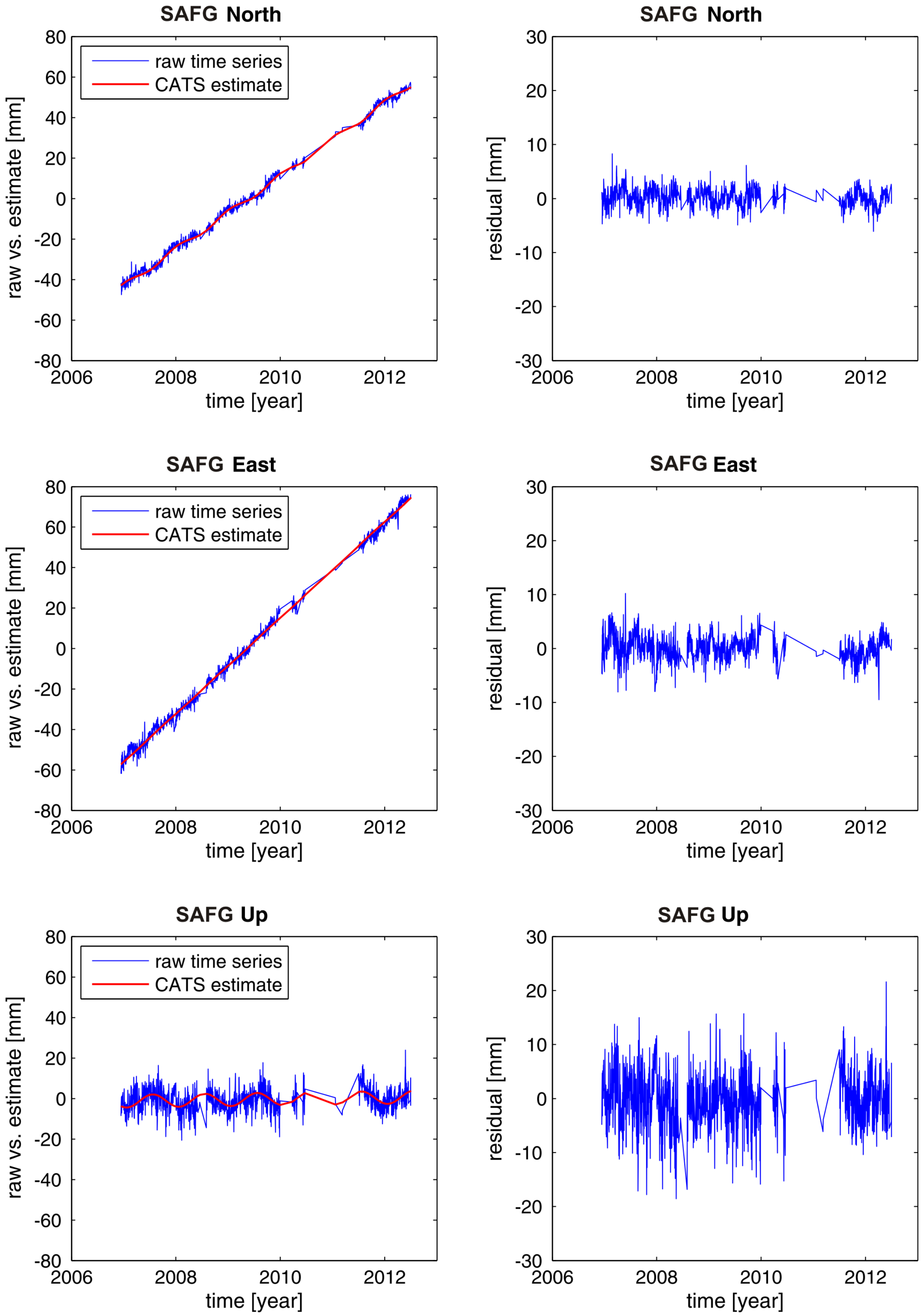

Figure 3.11: Bernese raw time series (blue line) and the estimated CATS time series (red line) for station SAFG in the left hand side and the residuals in the right hand side in each component. Stochastic model used is white noise plus power law noise.

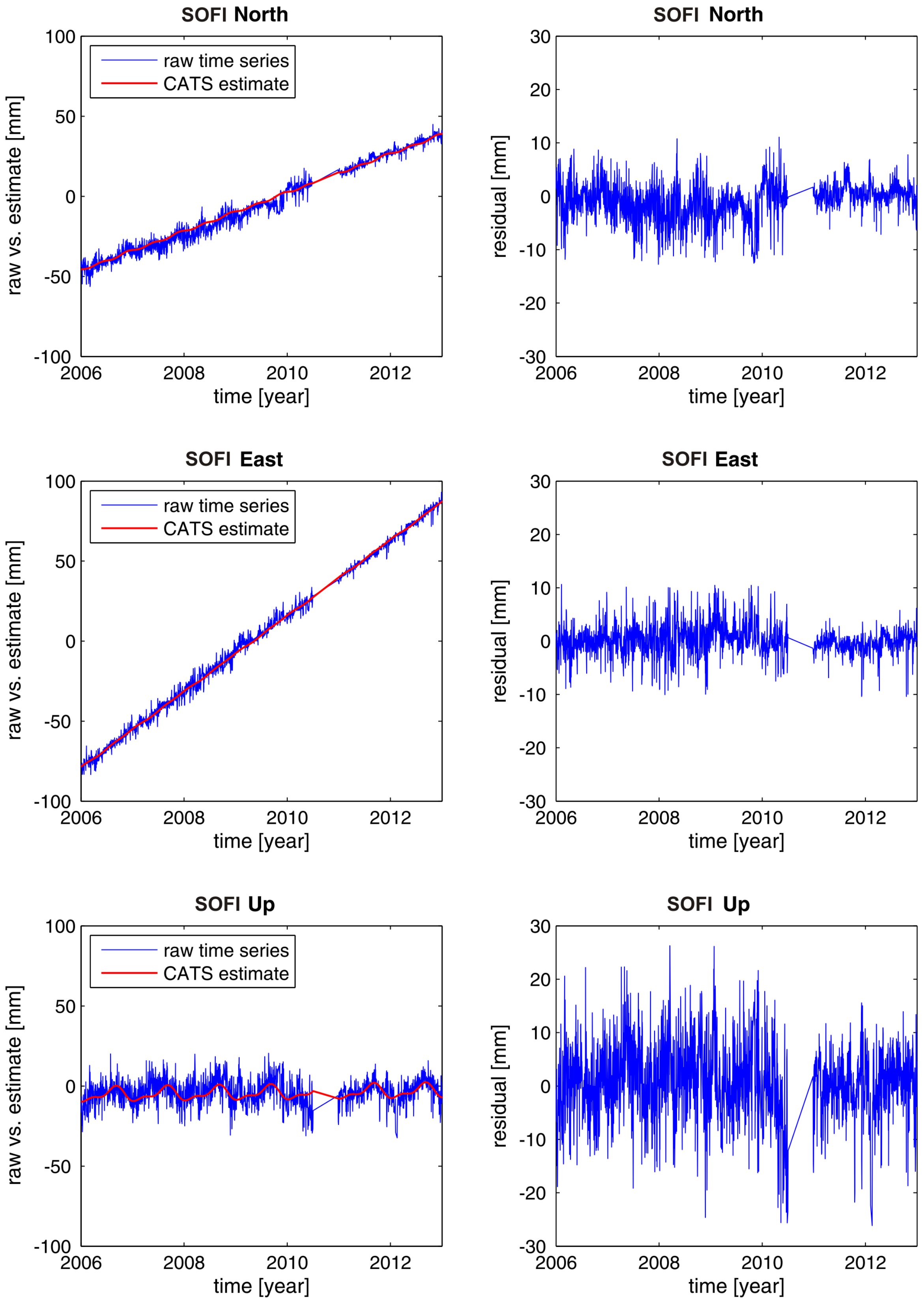

Figure 3.12: Bernese raw time series (blue line) and the estimated CATS time series (red line) for station SOFI in the left hand side and the residuals in the right hand side in each component. Stochastic model used is white noise plus power law noise.

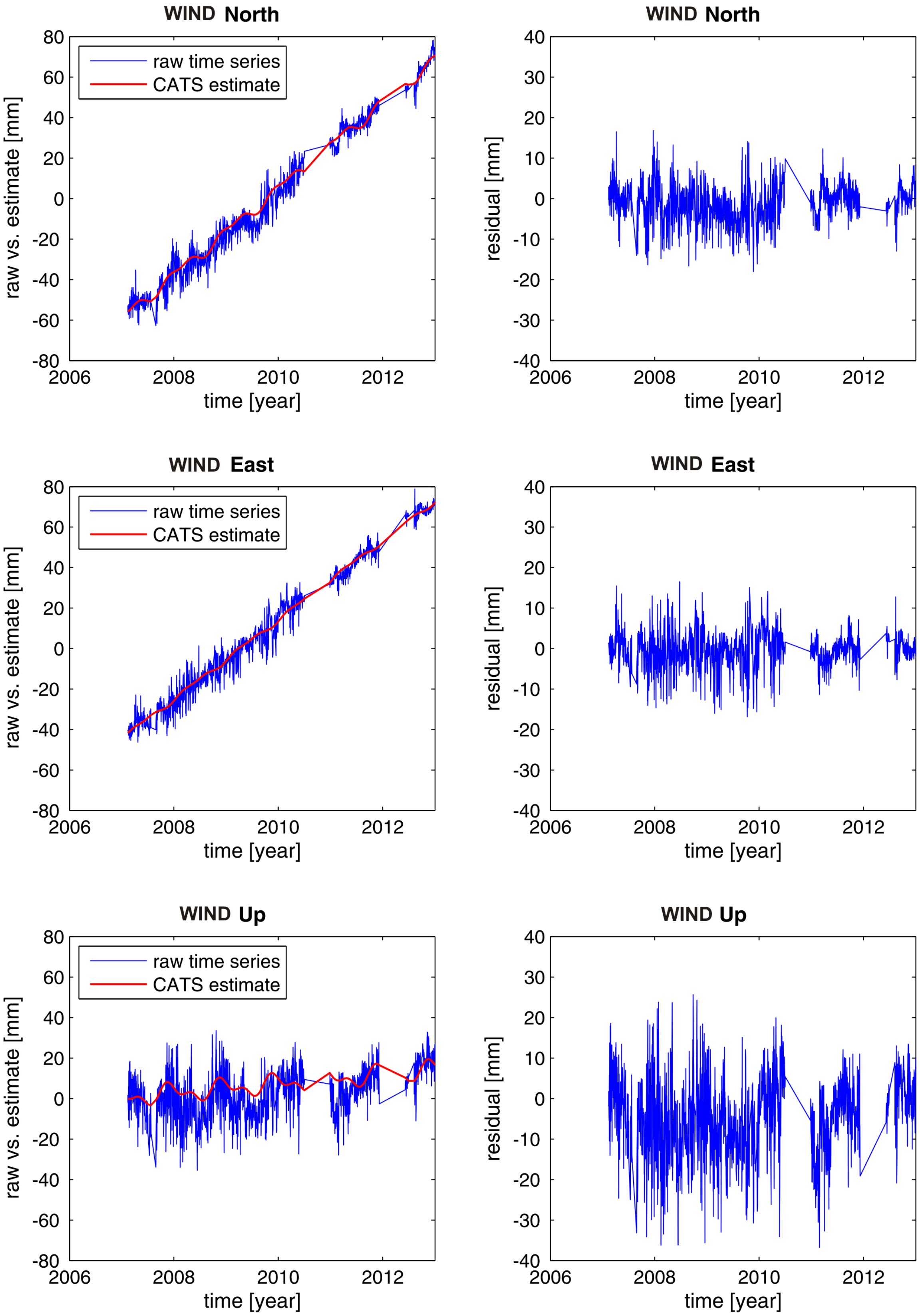

Figure 3.13: Bernese raw time series (blue line) and the estimated CATS time series (red line) for station WIND in the left hand side and the residuals in the right hand side in each component. Stochastic model used is white noise plus power law noise.

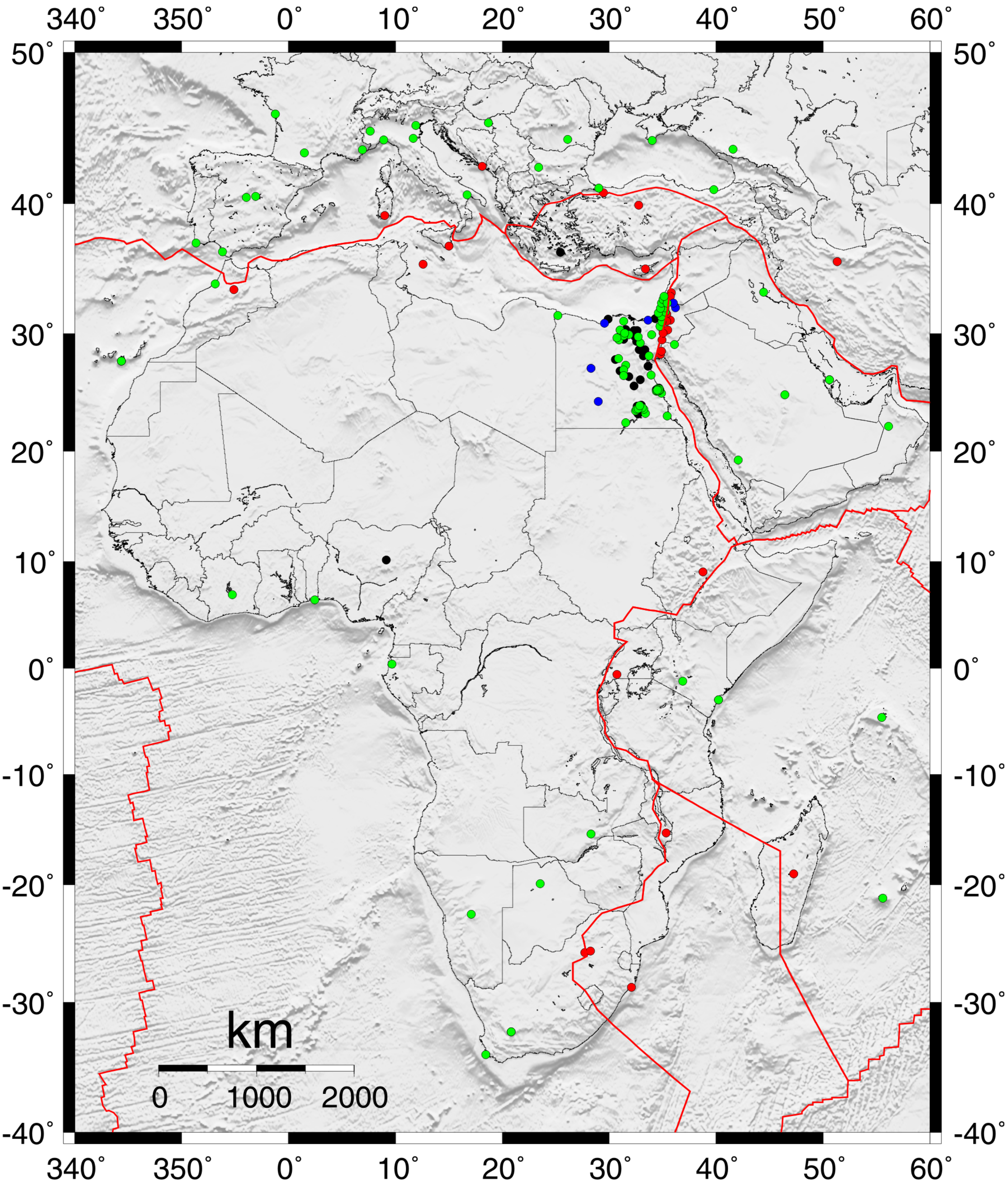

Figure 3.14: Selected sites for Euler poles estimation. Red: sites close to plate boundaries or in deformation zones. Blue: sites with observations less than two years. Black: sites with repeatability larger than 3 mm. Green: the final selection of 91 sites.

3.1.6 Strain Rate Tensor

The strain rate tensor is a physical quantity that describes the rate of change of the deformation of a material in the neighborhood of a certain point at a certain moment of time. Estimating the crustal strain rate could help in better understanding of the geodynamic processes along the active faults. A lot of information could be gained from such computations such as strain accumulation, forces affected, and the direction of these forces. Here, an interpolation for the estimated velocity field is used in order to estimate the strain rate tensor for Egypt including the borders between Nubian and Arabian plates.

With the assumption of small deformation, the strain rate tensor defined as:

$$\varepsilon_{en} = \frac{1}{2}\left(\frac{\partial \upsilon_e}{\partial \chi_n} + \frac{\partial \upsilon_n}{\partial \chi_e}\right) \tag{3.3}$$

where e and n are east and north, respectively. In this case, the eigenspace analysis would be a better way in order to get a full description of the deformation at every gridpoint. The eigenvectors of the strain rate represent the direction of maximum and minimum strain rates, while their associated eigenvalues λ_1 and λ_2 represent the magnitude (negative values for compression and positive values for extension). The maximum shear strain is a result of the linear combination of the maximum and minimum eigenvalues

$$\varepsilon_{max\_shear} = \frac{\lambda_1 - \lambda_2}{2} \tag{3.4}$$

while the the maximum shear is directed 45° form the eigenvector related to the largest eigenvalue

$$\theta_{1,2} = \frac{1}{2} arctan\left(\frac{2\varepsilon_{en}}{\varepsilon_{ee} - \varepsilon_{nn}}\right) \pm 45^\circ \tag{3.5}$$

The last equation gives two directions of the maximum shear strain (perpendicular to each other). More information is needed to constrain the direction.

The relative variation rate of the surface area, dilatation, can be obtained from the form

$$\delta = \varepsilon_{ee} + \varepsilon_{nn} \tag{3.6}$$

Applying the approach suggested by (Hackl et al., 2009) to estimate the strain rate field, the north and east velocity components were interpolated separately on a regular grid using the splines in tension algorithm described by (Wessel and Bercovici, 1998). The tension is controlled by factor T, which could be 0 for minimum curvature and 1 for maximum curvature. The value $T = 0.3$ was used as suggested by (Wessel and Bercovici, 1998). Setting very fine cell size will lead to highly irregular strain rate and on contrary, very coarse cell size will result in very low and highly delocalized strain rate. After some experiments the cell size = 0.04° was selected. The maximum shear strain, the dilatation, and the principle strain rate are presented in Chapter 4.

3.2 Interferometric Synthetic Aperture Radar (InSAR)

Due to the unique capability of InSAR in detecting the Earth's surface deformation over large areas within millimeter accuracy, here in this work an attempt is given to evaluate the sinking of the Nile Delta using the Persistent Scatterer InSAR (PSI). Figure 3.15 shows the location map of the Nile Delta. This section deals with the selection of the InSAR data used in this work and the processing steps using the Stanford Method for Persistent Scatterers (StaMPS) software, (Hooper et al., 2012).

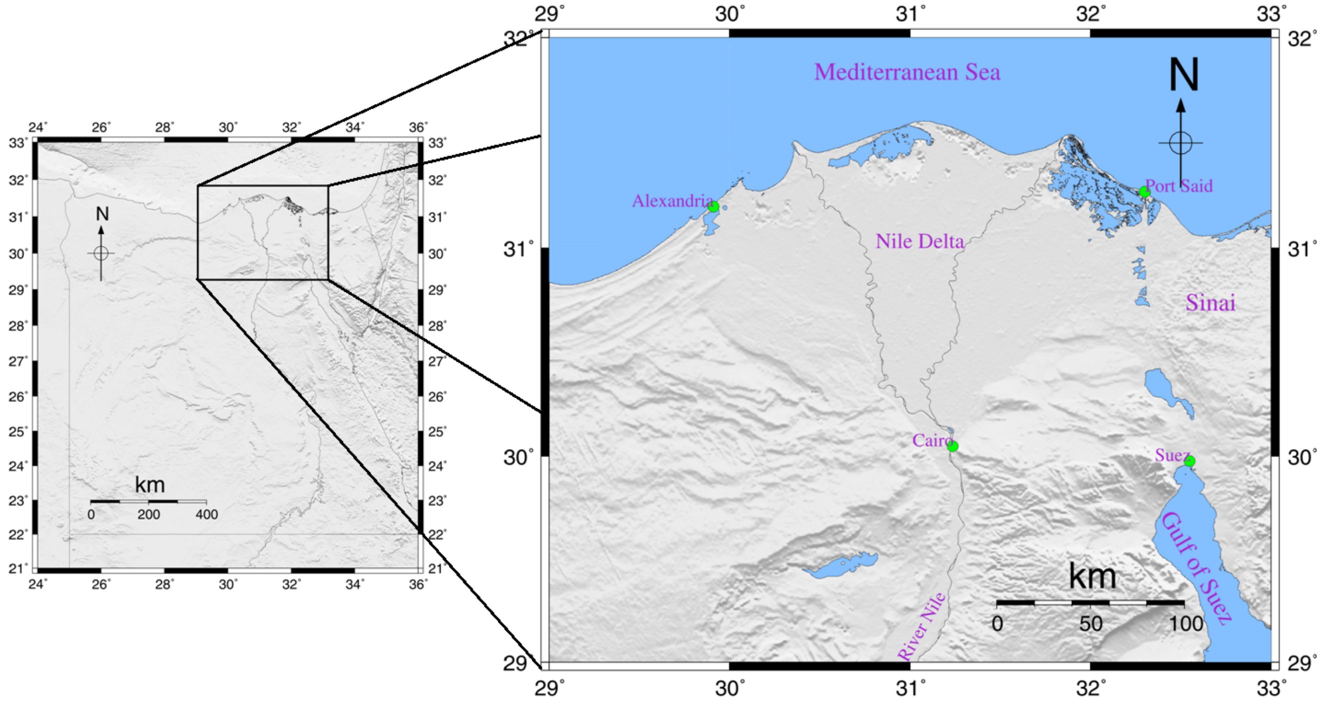

Figure 3.15: Key map of the Nile Delta

3.2.1 InSAR Data

In this work all the available archived SAR data from ERS1, ERS2, and Envisat satellite missions for the period from 1992 to 2010 were used. These satellite missions acquire the SAR images with 35-day time interval using C-band wavelength of 5.6 cm at $\simeq 800\ km$ height. The interferometric phase observation is in the millimeter level accuracy. In addition to the ground deformation, the main interest in this work, the interferometric phase contains contributions from different sources such as troposphere delay, topographic signal, orbital errors, and system noise (Equation (2.18)). The Nile Delta is highly vegetated area which subjected to rapid surface changes and as a consequence temporal decorrelation is expected. Therefore, a stacking of multiple SAR scenes is used to detect reliable ground targets based on their reflectivity behavior versus time. This approach was first realized by (Ferretti et al., 2001), enhanced by (Colesanti et al., 2003), and is called Permanent or Persistent Scatterers InSAR (PSI). The Nile Delta is covered by two ascending tracks, tracks number 200 and 429; and three descending tracks, tracks number 207, 436, and 479, as shown in Figure 3.16 (a and b). Table 3.4 shows the availability of the SAR scenes from ERS and Envisat satellite missions. Unfortunately, there is a remarkable decrease in the number of scenes over the Nile Delta in the ascending pass. There are only 7 scenes in each ascending track, in both satellite missions ERS and Envisat. A similar situation is exist in track number 479 in the descending pass, there are less than 20 scenes. These small amount of observations may be limit the PSI processing, which needs more than 20 scenes, and probably lead to unreliable results. Therefore, the two tracks in the descending pass, tracks number 207 and 436, which characterized by larger number of observations were used for the PSI processing.

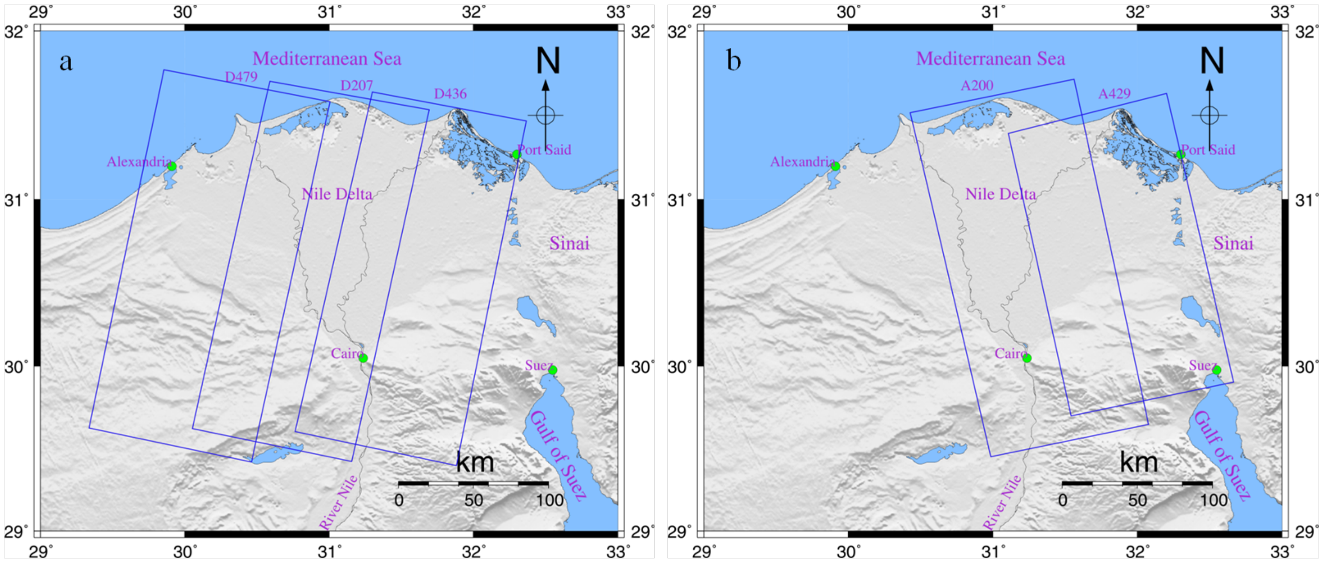

Figure 3.16: Satellite tracks covering the Nile Delta. (a) descending and (b) ascending tracks.

Table 3.4: Availability of the InSAR data from ERS and Envisat satellite missions with incidence angles. The values between parentheses represent the incidence angle of the middle of the swath.

Pass	Descending						Ascending			
Satellite	Envisat			ERS			Envisat		ERS	
Track No.	207	436	479	207	436	479	200	429	200	429
# of scenes	36	37	17	20	24	15	-	7	7	7
Incidence angel θ	19.2° - 26.7°			21° - (23°) - 26°			19.2° - 26.7°		21° - (23°) - 26°	

3.2.2 Persistent Scatterers InSAR Processing

Each single resolution cell in the SAR image consists of a grid of complex observations that come from the overlay of all the existing scatterer within the cell. The range resolution of the SAR scene depends on the system's bandwidth, while the azimuth resolution depends on the Doppler bandwidth (Hanssen, 2001).

3.2.2.1 Image Formation

The raw SAR data need to be focused to form an image. The focusing is done in the range direction through the knowledge of the time delay, and in the azimuth direction through combination of backscattered signals from multiple locations to synthesize a large antenna aperture. There are several algorithms for SAR focusing ((Curlander and McDonough, 1991); (Prati et al., 1990); (Massonnet et al., 1994); (Bamler and Hartl, 1998)). In this work the input to the interferometric processing scheme are the focused Single Look Complex (SLC) scenes. All SLCs in this work were focused using ROI_PAC version 3.0.1 ((Massonnet and Feigl, 1998); (Thompson et al., 1986); (Rosen et al., 2000); (Zebker and Goldstein, 1986)). ROI_PAC is the Repeat Orbit Interferometry Package developed at JPL and Caltech.

The interferogram is formed by the complex multiplication of the observations in each resolution cell of two coregistered SAR scenes (Master and Slave). All interferograms in this work were created using the Delft Object-oriented Radar Interferometric Software (DORIS), (Kampes et al., 2003). The interferogram, interferometric phase difference, is the observation used for the Earth's surface deformation estimation. Figure 3.17 shows the flowchart of the InSAR processing.

3.2.2.2 Master-scene Selection

With N+1 images collected at different times, N interferograms can be formed with respect to one master scene. The master scene should minimize the sum decorrelation, or maximize the sum correlation, of the formed interferograms (Hooper et al., 2007). The correlation depends on the time interval (T), perpendicular baseline $B_\perp$, Doppler Centroid Frequency (F_{DC}), and the thermal noise (Zebker and Villasenor, 1992).

$$\begin{aligned}\rho_{total} &= \rho_{temporal}\rho_{spatial}\rho_{doppler}\rho_{thermal} \\ &\simeq \left(1-f\frac{T}{T^c}\right)\left(1-f\frac{B_\perp}{B_\perp^c}\right)\left(1-f\frac{F_{DC}}{F_{DC}^c}\right)\rho_{thermal} \end{aligned} \tag{3.7}$$

$$where$$

$$f(x) = \begin{cases} x, \text{for } x \leqslant 1 \\ 1, \text{for } x > 1 \end{cases}$$

where ρ represents the correlation and the superscript c represents the critical value for each parameter. The critical values represent the limits of a possible correlation in the interferogram, which means, that beyond these values, the interferogram shows almost complete decorrelation. The critical values vary with different data set. Reasonable estimates for T^c, $B_\perp^c$ and F_{DC}^c are 5 $years$, 1100 m and 1380 Hz, respectively. Assuming the $\rho_{thermal}$ is constant, the master scene that maximizes the ρ_{total} has been selected. Figures 3.18, 3.19, 3.20, and 3.21 show the SAR images used to calculate the PS-InSAR velocity field and the selection of the master scene for each track.

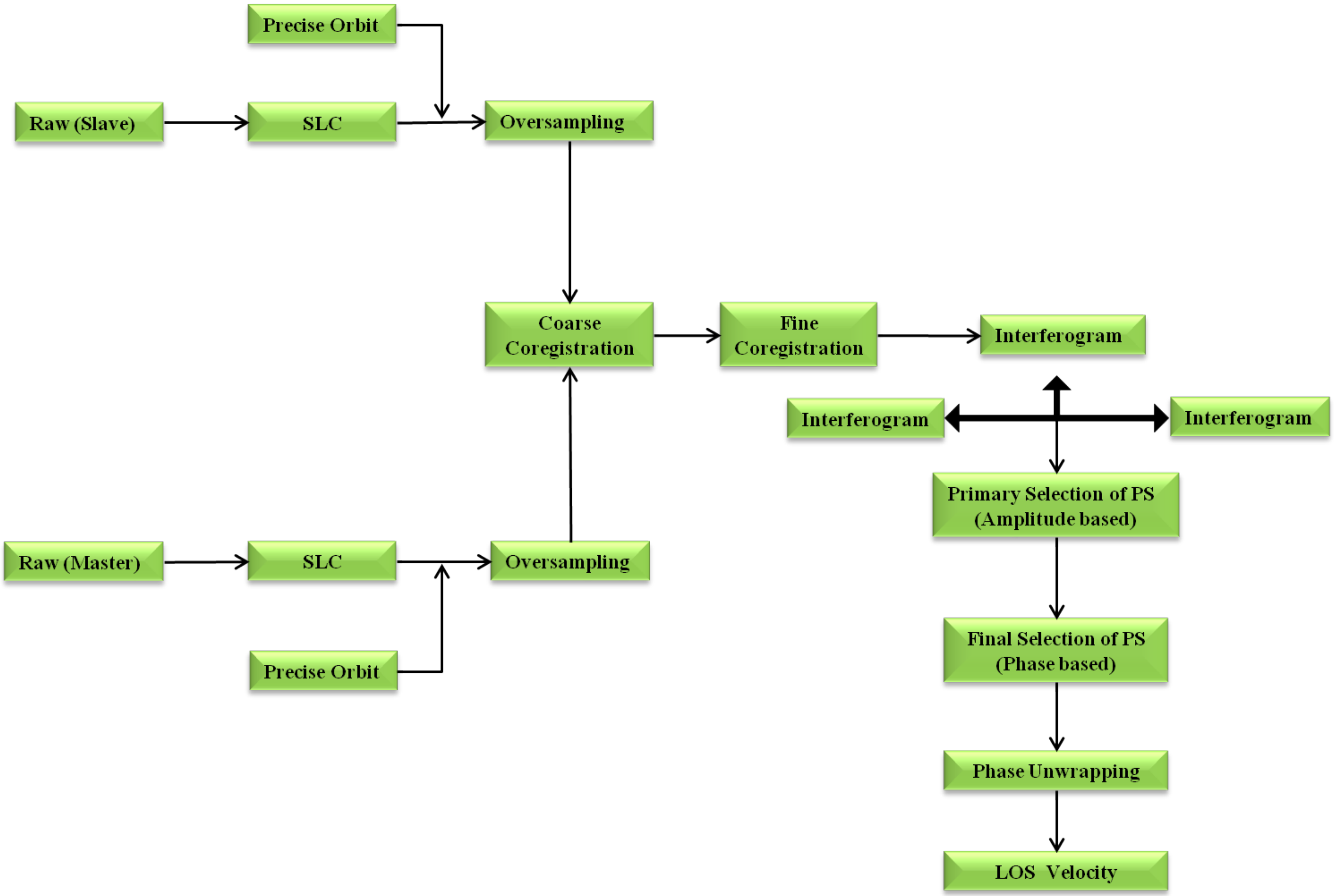

Figure 3.17: Simplified scheme of the PS processing steps.

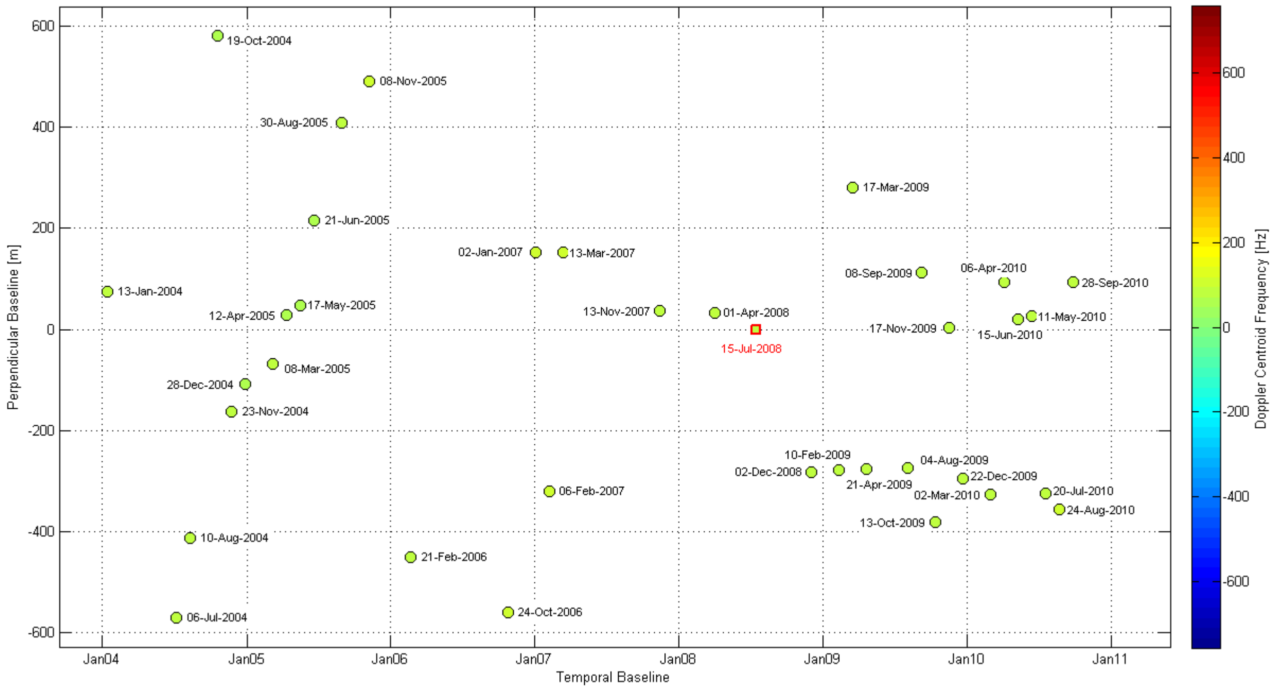

Figure 3.18: SAR images of track 207, Envisat satellite mission. Plotted circles are the SAR acquisitions. Circle's color represents the Doppler Centroid Frequency (F_{DC}). Square indicates master chosen for Persistent Scatterer InSAR analysis.

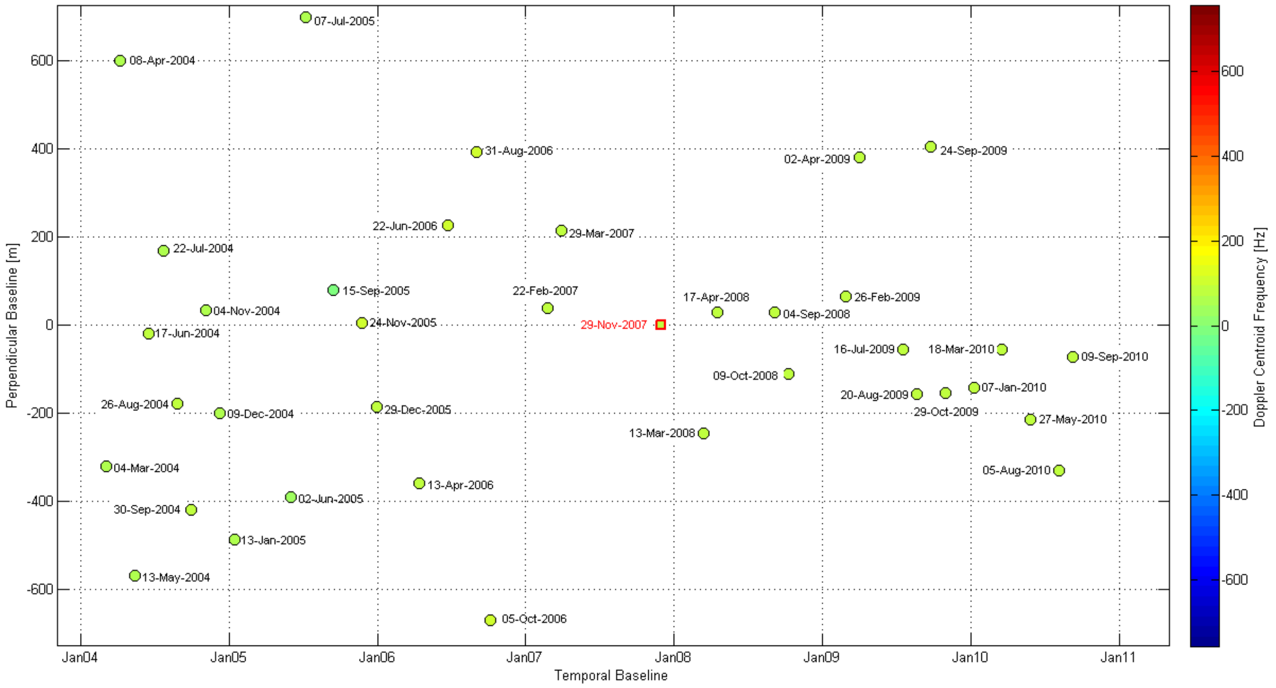

Figure 3.19: SAR images of track 436, Envisat satellite mission. Plotted circles are the SAR acquisitions. Circle's color represents the Doppler Centroid Frequency (F_{DC}). Square indicates master chosen for Persistent Scatterer InSAR analysis.

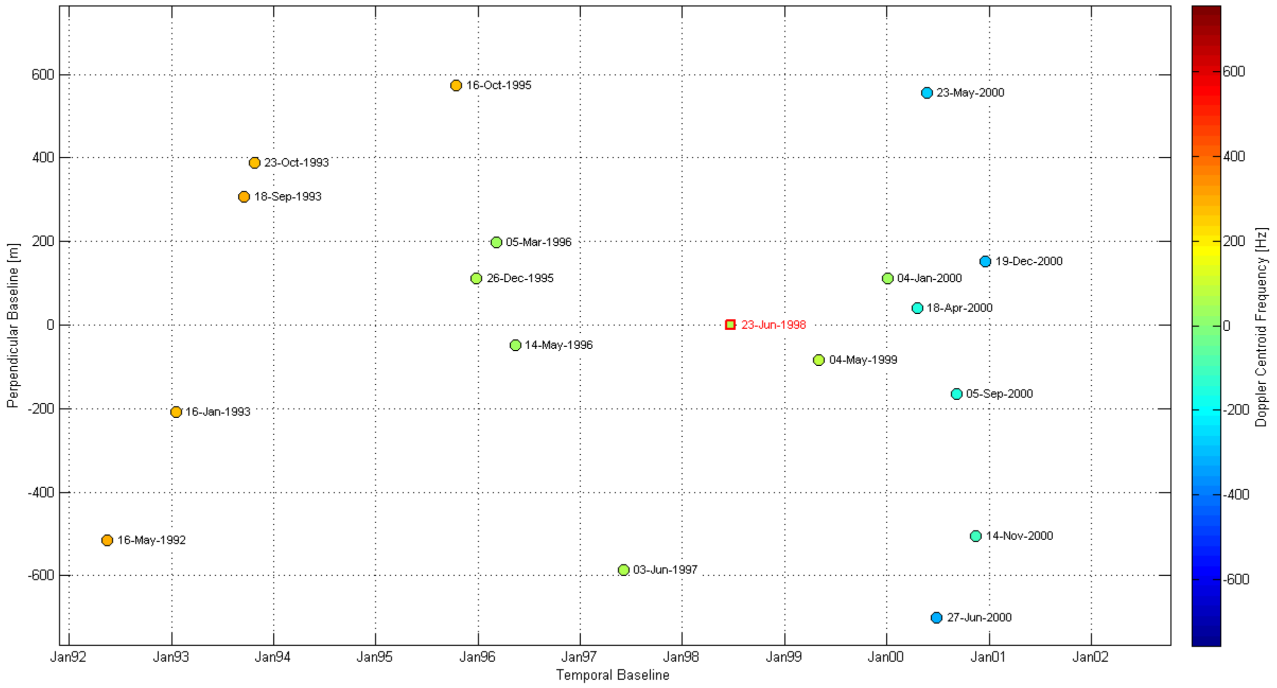

Figure 3.20: SAR images of track 207, ERS1&2 satellite mission. Plotted circles are the SAR acquisitions. Circle's color represents the Doppler Centroid Frequency (F_{DC}). Square indicates master chosen for Persistent Scatterer InSAR analysis.

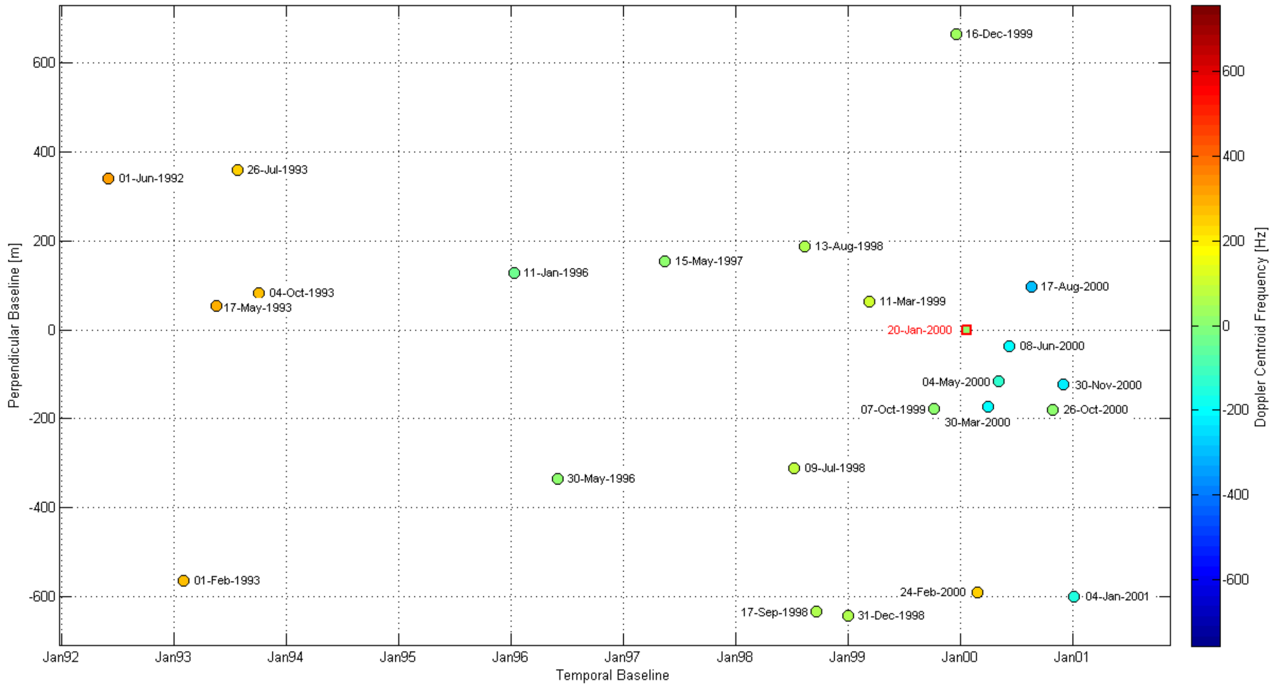

Figure 3.21: SAR images of track 436, ERS1&2 satellite mission. Plotted circles are the SAR acquisitions. Circle's color represents the Doppler Centroid Frequency (F_{DC}). Square indicates master chosen for Persistent Scatterer InSAR analysis.

3.2.2.3 Oversampling

After the generation of the SLC scenes and reading the precise orbits; precise orbit information was obtained from Delft Institute for Earth-Oriented Space Research ((Scharroo and Visser, 1998); (Doornbos et al., 2002); (Doornbos and Scharroo, 2004)), and before the coregistration and interferogram generation, the SAR scenes are oversampled in both range and azimuth directions by a factor of 2. After the oversampling, the pulse repetition frequency will be doubled and hence avoids the aliasing during the complex multiplication. In an oversampled SAR image, the target's location can be determined precisely while the SAR coordinates are at sub-pixel level with respect to the original sampling rate (Ketelaar, 2009).

3.2.2.4 Coregistration

The input for the coregistration process is the oversampled SLC and the precise orbits. The coregistration approach in the DInSAR processing, based on cross-correlation of amplitude, may fail in the PSI processing due to the fact that in some interferograms the values of temporal and perpendicular baselines are higher than commonly chosen for conventional InSAR. Therefore, a new algorithm introduced by (Hooper et al., 2007), which uses an amplitude based algorithm to estimate offsets between pairs of images where reasonable coherence is expected, is used. In this algorithm, The mapping function of the master image to each of the slave images is estimated by weighted least-squares inversion. In this work, all SCLs in each track are successfully coregistered to the master scenes using (Hooper et al., 2007) approach.

3.2.2.5 Interferogram Generation

Once the coregistration is finished and the slave images are resampled to the master scene, the interferometric phase difference (interferograms) between master and resampled slave scenes are generated. The interferogram is produced by pointwise multiplication of the corresponding pixels in the two SAR images (master and slave) as follows:

$$I = C_1 \cdot C_2^* = A_1 e^{i\phi_1} \cdot A_2 e^{-i\phi_2} = A_1 A_2 e^{i(\phi_1 - \phi_2)} = A \cdot e^{i\phi} \tag{3.8}$$

where C_1 is the amplitude and phase of the master scene, C_2 is the amplitude and phase of the resampled scene, the * denotes the complex conjugate, A is the amplitude of the interferogram, and ϕ is the phase of the interferogram. The interferometric phase contribution due to the difference in the real Earth's surface from the ellipsoid is subtracted using a Digital Elevation Model (DEM).

The interferogram contains in addition to the deformation signal, the signal of interest in this work, other signals due to atmospheric effects, topographic heights, and other noise sources like the residual orbital error. In order to estimate the ground deformation in the presence of these contributions, a SAR acquisition time series is used to select the good reflectors in each scene (Permanent Scatterers). The selection of these permanent scatterers is discussed in the next section.

3.2.2.6 Permanent Scatterers Selection

Decorrelation is expected in the densely vegetated areas, like the Nile Delta, and DInSAR may fail. Therefore, selecting candidate targets that show stable and consistent reflection behavior in time is needed to get coherent and interpretable measurement points. The stable reflection points are called Permanent or Persistent Scatterers PS (Ferretti et al., 2001), which could be a building or hard rock outcrop. These physical objects act as point scatterers and are less sensitive to the temporal decorrelation between the master and the slave scene. Many algorithms are developed to identify and isolate these PS pixels ((Ferretti et al., 2001); (Crosetto et al., 2003); (Lyons and Sandwell, 2003); (Werner et al., 2003); (Kampes, 2005)). To identify the PS pixels, all of these approaches use an approximate model for how the deformation changes with time. An initial set of PS pixels is identified based on a time series analysis of the amplitude for each pixel in a series of interferograms (Ferretti et al., 2001). For each pixel, the amplitude dispersion D_A is calculated by the ratio between the amplitude standard deviation σ_A and the amplitude mean μ_A.

$$D_A = \frac{\sigma_A}{\mu_A} \tag{3.9}$$

Points with low amplitude dispersion D_A, (Ferretti et al., 2001) used 0.25 as a threshold, are tested for phase stability by checking the phase differences for each pixel with the nearby ones. Finally, the pixels that are characterized by a phase history similar to the a priori deformation model are considered stable and as a consequence selected as PS pixels. This procedure may fail in the highly vegetated areas where the man-made features are rare, and the distribution of the PS pixels is sparse. Also, sometimes the deformation behavior of the area under study is unknown a priori, especially in case when the ground deformation is the aim of the study.

Therefore, (Hooper et al., 2007) introduced a new algorithm for identifying the PS pixels. In this approach, the PS pixels are identified based on their phase stability in the interferogram time series instead of amplitude analysis as in the previous approaches. Firstly, a primary subset of pixels were established using the analysis of their amplitudes. Again the amplitude dispersion D_A is used to select the initial subset of the pixels but with a higher threshold of 0.4 than selected by (Ferretti et al., 2001). This leads to select more PS pixels but with high probability of not being PS pixels. Secondly, the phase analysis is applied to the primarily selected pixels to estimate the phase stability. The wrapped phase ϕ_W is equal to

$$\phi_W = W\{\phi_{Def} + \phi_{Atm} + \Delta\phi_{Orb} + \Delta\phi_\theta + \phi_N\} \tag{3.10}$$

where ϕ_{Def} is the phase contribution due to the pixel motion in the LOS direction, ϕ_{Atm} is the phase contribution due to the atmospheric delay, $\Delta\phi_{Orb}$ is the residual phase contribution due to orbit errors, $\Delta\phi_\theta$ is the residual phase contribution due to look angle error, ϕ_N is the phase noise, and $W\{.\}$ is the wrapping operator. Considering the first three terms in equation (3.10), phase contribution due to deformation, atmospheric, and orbit error in addition to a part from the fourth term are spatially correlated, the noise for the pixel is estimated by spatial filtering of these four terms and then subtracted the spatially correlated phase that giving an estimate for the phase noise. Then reestimate the first four terms and subtract the reestimated values of equation (3.10) to have a new estimate of the phase noise. This process is iterated until the convergence (Hooper et al., 2007). The residual phase contribution due to look angle error, usually referred to DEM error, is modeled for the whole time series. Pixels with low phase noise are selected as PS pixels. In this work the StaMPS algorithm (Hooper et al., 2012) was used for the PS processing.

The coherence is a measure of the quality of the expected PSI results. It is ranging from 0 to 1, 0 for very poor coherence, which means nuisance PSI results, and 1 for very good coherence and very accurate PSI results would be expected. In StaMPS processing, the coherence is calculated from the phase residual noise instead of measuring the difference between the phase and an assumed model. the estimation of the coherence is based on the phase residual noise that left after removing the spatially correlated phase (deformation, atmospheric signal, and part of the DEM error) and the spatially uncorrelated DEM error.

3.2.2.7 Phase Unwrapping

After the PS pixels are identified, to extract the phase due to ground deformation, the phase unwrapping is needed. The interferometric phase measurement is given modulo 2π, i.e. it is wrapped. The wrapped phase, as it is limited to $-\pi$ and $+\pi$, does not infer range differences. Therefore, phase unwrapping is needed to reconstruct the absolute phase from measured phase known only modulo 2π on a finite grid of points, (Shanker, 2010). To resolve the interferometric phase ambiguity, the correct integer number of phase cycles ($n2\pi$) have to be added to every phase measurement. As the phase is of three dimensions, two in space and one in time, a three-dimensional unwrapping algorithm introduced by (Hooper and Zebker, 2007) is used for phase unwrapping. Finally, the topographically corrected unwrapped phase values are converted into displacement values, yielding the velocity in the LOS direction.

It is worth to mention that all velocity measurements in the LOS of the satellite's radar beam are relative to a point that is pre-selected as being stable and not moving. InSAR is a complementary tool that adds value to all pre-existing techniques for measuring surface deformation. Therefore, it should not be considered as a standalone solution. Although, the many strengths of PSI in the field of ground deformation monitoring such as millimeter accuracy, possible analysis of historic data back to 1992, Global coverage, and the cost effectiveness, the technique is limited by the presence of vegetation or snow cover, huge ground deformation, blind to the deformation parallel to the satellite flight direction, and the limitation of the data sampling by the repeat orbit cycles. The velocity field deduced from the processed InSAR scenes for the Nile Delta is presented in Chapter 4.

4 Results and Discussion

The first section of this chapter contains, based on the processed GPS stations (as explained in Chapter 3), the absolute and relative Euler vectors and as a consequence the absolute horizontal velocity field in the latest reference frame, ITRF2008 (Altamimi et al., 2011), in addition to the relative velocity fields in Eurasia fixed frame, in Nubia fixed frame, and in Sinai fixed frame. An estimates for the slip rate along the DST fault, resulted from the fault parallel analysis, the strain rates at the northeastern corner of Nubia, and the vertical velocity field are also presented in this section. In the second section, the LOS velocity of each satellite track and time series for selected regions are presented. The achieved results from both geodetic techniques, GPS and InSAR, are discussed in the third section.

4.1 GPS Results

The Bernese combined solution of about 150 GPS stations, for the period 2006-2012, was assessed using CATS. As mentioned in Chapter 3, the CATS analysis was used with four different stochastic models, white noise, power law noise, white noise plus flicker noise ($k = -1$), and white noise plus power law noise. The CATS analysis of white noise plus power law noise is selected as the most adequate one because this model offers the estimation of all stochastic parameters. Therefore, this model was selected for the assessment of the GPS results. Due to the discontinuities in the campaign data and the short period of observations in each campaign, it was difficult to apply CATS analysis for these data. The presented velocities and uncertainties for these stations are the Bernese velocities and scaled uncertainties(σ_s).

4.1.1 Absolute Horizontal Velocity Field

Table 4.1 and figure 4.1 show the absolute horizontal velocity field for the processed stations in ITRF2008. It is clear that the horizontal velocities are significant with 95% confidence region. For the sake of readability, Figure 4.2 shows the absolute horizontal velocity for Egypt-Sinai-DST fault region. Almost all the Egyptian stations are moving to the Northeast direction with magnitude $28 - 30\ mm/yr$. The absolute velocity field is not useful for geological interpretation, therefore, the absolute horizontal velocity field is converted into a relative velocity field that is geologically interpretable. The next section covers the estimated relative motion between the tectonic plates in the northeastern corner of Nubia.

Table 4.1: CATS velocities and uncertainties, stochastic model used is white noise plus power law noise, for permanent stations in addition to Bernese velocities and scaled error for the non-permanent stations. IGS stations (P-IGS), ITRF08 stations used for datum definition (P-IGS*), Egyptian permanent stations (P-EGY), Egyptian Epoch stations (E-EGY), SOPAC stations (P-SOP) and UNAVCO stations (P-UNA).

Stations	**Long.**	**Lat.**	V_e **(mm/yr)**	V_n **(mm/yr)**	σ_e **(mm)**	σ_n **(mm)**	**Tectonic Plate**	**Remarks**
ABPO	47.23	-19.02	17.56	13.81	0.46	0.78	SOMALIA	P-IGS
ABSM	31.55	22.49	20.49	19.29	1.04	0.64	NUBIA	P-EGY
AD01	34.66	25.50	28.68	21.89	3.47	2.36	NUBIA	E-EGY
AD02	34.54	25.44	24.98	19.48	2.10	1.90	NUBIA	E-EGY
AD03	34.50	25.36	22.67	18.44	2.76	1.75	NUBIA	E-EGY
AD04	34.38	25.36	21.49	18.53	2.61	2.57	NUBIA	E-EGY
AD05	34.42	25.23	25.14	19.34	2.16	1.99	NUBIA	E-EGY
AD06	34.50	25.24	22.27	20.40	2.67	2.68	NUBIA	E-EGY
AD07	34.62	25.24	23.77	19.24	1.90	2.32	NUBIA	E-EGY
AD08	34.75	25.29	25.54	18.13	2.52	2.55	NUBIA	E-EGY
AD09	34.69	25.41	24.36	18.54	1.64	2.91	NUBIA	E-EGY
AD10	34.63	25.33	23.03	17.50	1.95	2.09	NUBIA	E-EGY
AD11	34.48	25.31	23.69	18.53	1.40	2.31	NUBIA	E-EGY
ADIS	38.77	9.04	21.31	18.84	0.40	0.80	NUBIA	P-IGS
ALAK	33.38	23.29	20.50	17.70	1.88	1.63	NUBIA	E-EGY
ALEX	29.91	31.20	35.57	11.52	1.09	1.67	NUBIA	P-EGY
ALIS	32.59	23.39	21.90	16.20	1.88	3.70	NUBIA	E-EGY
ALON	34.61	31.71	22.70	18.55	0.20	0.28	SINIA	P-SOP

ANKR	32.76	39.89	4.84	12.15	0.49	0.46	ANATOLIA	P-IGS*
ARAB	30.56	27.87	20.20	14.65	5.07	2.98	NUBIA	E-EGY
ARSH	33.62	31.11	25.20	19.60	0.80	0.78	SINIA	P-EGY
ASHM	31.01	30.30	22.25	17.02	1.99	2.29	NUBIA	E-EGY
ASUT	31.56	27.40	22.97	18.06	0.12	0.33	NUBIA	P-EGY
BEER	33.24	23.66	21.40	18.70	2.45	0.98	NUBIA	E-EGY
BHR1	50.61	26.21	31.81	28.66	0.39	0.59	ARABIA	P-IGS*
BHR2	50.61	26.21	32.47	28.66	0.40	0.66	ARABIA	P-IGS*
BJCO	2.45	6.39	22.34	18.76	0.54	0.90	NUBIA	P-IGS
BORG	29.57	30.86	21.73	16.66	1.04	1.69	NUBIA	P-EGY
BSHM	35.02	32.78	23.22	19.95	0.30	0.95	SINIA	P-SOP
BUCU	26.13	44.46	24.18	11.83	0.47	0.22	EURASIA	P-IGS
CAGZ	8.97	39.14	21.51	15.77	0.15	0.16	EURASIA	P-IGS*
CGGN	9.12	10.12	30.83	8.74	0.71	1.63	NUBIA	P-IGS
CRAO	33.99	44.41	23.86	10.81	0.25	0.31	EURASIA	P-IGS
CSAR	34.89	32.49	22.37	19.08	0.21	0.37	SINIA	P-SOP
DAHM	33.09	23.82	20.90	18.60	2.62	1.32	NUBIA	E-EGY
DKHL	28.96	24.32	22.50	19.90	3.37	5.50	NUBIA	P-EGY
DRAG	35.39	31.59	23.03	19.56	0.26	0.60	SINIA	P-IGS*
DSEA	35.37	31.04	24.49	20.60	0.18	0.34	SINIA	P-SOP
DUBR	18.11	42.65	21.89	18.55	1.17	1.04	EURASIA	P-IGS*
ELAT	34.92	29.51	25.54	20.00	0.33	0.46	SINIA	P-SOP
ELSF	31.35	29.54	23.96	19.45	3.91	2.39	NUBIA	E-EGY
FANA	32.57	29.38	21.63	20.27	4.52	3.33	NUBIA	E-EGY
FARF	28.31	27.15	23.40	21.50	3.94	5.10	NUBIA	P-EGY
FAYD	32.33	30.28	28.32	19.78	5.87	4.68	NUBIA	E-EGY
GARF	32.71	23.27	22.40	16.90	3.20	2.39	NUBIA	E-EGY
GENO	8.92	44.42	21.06	15.61	0.16	0.10	EURASIA	P-IGS
GHNA	31.36	26.54	24.80	17.39	1.65	2.87	NUBIA	E-EGY
GHRB	33.19	28.20	22.21	18.79	2.89	2.59	NUBIA	E-EGY
GILB	35.42	32.48	22.27	19.94	0.26	0.34	SINIA	P-SOP
GMAS	-15.63	27.77	17.37	17.98	0.30	0.15	NUBIA	P-IGS*
GRAS	6.92	43.76	20.64	15.88	0.19	0.14	EURASIA	P-IGS*
HALY	36.10	29.14	26.93	23.24	0.25	0.29	ARABIA	P-SOP
HARB	27.71	-25.89	17.96	18.57	0.28	0.49	NUBIA	P-IGS*
HRMN	35.79	33.31	24.04	21.82	0.44	0.43	SINIA	P-SOP
HUGS	36.19	32.10	22.93	21.49	1.08	1.82	ARABIA	P-SOP
HURG	33.61	27.31	24.61	24.24	2.17	3.30	NUBIA	E-EGY
HYKS	31.42	30.06	21.67	17.46	2.85	2.62	NUBIA	E-EGY
IENG	7.64	45.02	20.77	15.31	0.22	0.14	EURASIA	P-IGS
IFRN	-5.11	33.54	18.27	16.60	0.33	0.19	NUBIA	P-UNA
ISBA	44.44	33.34	25.96	26.02	0.84	0.52	ARABIA	P-IGS
ISTA	29.02	41.10	24.30	10.68	0.26	0.22	EURASIA	P-IGS*
JSLM	35.20	31.77	23.29	19.26	0.28	0.41	SINIA	P-SOP
JUST	35.99	32.49	20.20	22.04	1.38	1.63	ARABIA	P-SOP
KABR	35.15	33.02	21.83	19.58	0.24	0.43	SINIA	P-SOP
KATA	31.83	29.93	24.57	18.53	0.31	0.50	NUBIA	P-EGY
KATZ	35.69	33.00	22.73	21.87	0.22	0.57	SINIA	P-SOP
KENT	32.89	29.27	26.31	16.79	3.93	4.36	SINIA	E-EGY
KL82	32.45	23.54	23.20	16.60	2.23	0.79	NUBIA	E-EGY
KLHV	34.87	31.38	22.88	18.81	0.29	0.33	SINIA	P-SOP
LAGO	-8.67	37.10	18.14	17.40	0.18	0.20	EURASIA	P-EPN
LAMP	12.61	35.50	21.42	16.20	0.29	0.42	NUBIA	P-EPN
LHAV	34.87	31.38	22.46	18.31	0.60	0.40	SINIA	P-SOP
LROC	-1.22	46.16	18.41	16.25	0.20	0.18	EURASIA	P-IGS
MAL2	40.19	-3.00	27.39	16.34	0.71	0.37	SOMALIA	P-IGS
MALI	40.19	-3.00	27.05	15.96	1.52	0.46	SOMALIA	P-IGS*
MNAM	32.99	24.02	22.60	18.10	3.27	2.78	NUBIA	E-EGY
MAS1	-15.63	27.76	17.29	18.25	0.48	0.52	NUBIA	P-IGS*
MAT1	16.71	40.65	24.12	18.03	0.25	0.28	EURASIA	P-IGS
MAUA	23.53	-19.90	19.03	19.30	1.01	0.90	NUBIA	P-UNA
MBAR	30.74	-0.60	24.37	17.64	0.22	0.24	SOMALIA	P-IGS*
MEDI	11.65	44.52	22.84	17.73	0.40	0.25	EURASIA	P-IGS*
MNSO	31.35	31.04	25.82	20.14	0.54	0.26	NUBIA	P-EGY
MRSA	34.88	25.07	25.80	18.38	0.34	0.37	NUBIA	P-EGY
MSLT	30.89	29.51	23.46	16.95	0.43	0.50	NUBIA	P-EGY
MUTA	35.72	31.10	20.76	19.39	0.61	0.59	ARABIA	P-SOP
NAGH	32.33	25.68	29.02	15.98	5.81	2.56	NUBIA	E-EGY
NAMA	42.05	19.21	33.67	27.00	0.91	0.28	ARABIA	P-SOP
NICO	33.40	35.14	19.31	15.84	0.20	0.54	ANATOLIA	P-IGS*
NKHL	33.98	29.93	23.76	18.46	0.17	0.49	SINIA	P-EGY
NKLG	9.67	0.35	23.41	19.56	0.36	0.64	NUBIA	P-IGS*
NMAR	32.54	23.68	22.60	16.70	1.81	2.49	NUBIA	E-EGY
NOMI	25.43	36.42	21.11	-16.94	5.66	0.80	ANATOLIA	P-UNA
NOT1	14.99	36.88	21.41	19.23	0.37	0.27	NUBIA	P-IGS*
NRIF	35.04	30.04	24.58	20.12	0.26	0.34	SINIA	P-SOP
OSJE	18.68	45.56	22.85	15.76	0.21	0.40	EURASIA	P-IGS
PADO	11.90	45.41	21.40	16.57	0.24	0.24	EURASIA	P-IGS
PETA	35.47	30.33	19.55	16.83	2.10	1.64	ARABIA	P-SOP
PHLW	31.34	29.86	21.61	17.99	0.30	0.25	NUBIA	P-EGY
PLBS	31.56	30.37	23.29	15.99	1.92	3.17	NUBIA	E-EGY
PORT	31.01	26.94	28.90	16.54	3.32	4.68	NUBIA	E-EGY
PRE1	28.22	-25.75	18.36	20.45	0.70	1.06	SOMALIA	P-IGS*
PYRA	31.12	29.97	22.18	16.39	3.32	2.52	NUBIA	E-EGY
QANT	32.60	30.25	18.81	19.78	7.61	13.86	SINIA	E-EGY
QENA	32.89	26.18	25.47	17.16	3.84	2.61	NUBIA	E-EGY

RABT	-6.85	34.00	16.99	18.02	0.23	0.13	NUBIA	P-IGS*
RAMO	34.76	30.60	23.57	18.86	0.19	0.46	SINIA	P-IGS*
RARO	32.71	23.72	21.90	19.70	2.61	1.11	NUBIA	E-EGY
RASH	34.80	28.30	25.46	21.37	0.49	0.64	ARABIA	P-SOP
RBAY	32.08	-28.80	16.30	18.11	1.36	1.94	SOMALIA	P-IGS*
RCMN	36.89	-1.22	26.79	16.66	0.38	0.40	SOMALIA	P-IGS
REST	32.61	23.95	22.20	16.20	3.35	2.95	NUBIA	E-EGY
REUN	55.57	-21.21	16.07	12.21	0.45	0.66	SOMALIA	P-IGS*
RUDS	33.32	28.70	16.08	0.10	6.98	9.03	SINIA	E-EGY
SAFG	33.93	26.57	23.45	18.37	0.32	0.26	NUBIA	P-EGY
SEDR	32.69	29.77	23.79	18.24	5.80	2.82	SINIA	E-EGY
SEY1	55.48	-4.67	24.19	11.17	0.46	0.33	SOMALIA	P-IGS
SFER	-6.21	36.46	16.34	16.95	0.15	0.10	EURASIA	P-IGS*
SHAD	30.84	27.99	24.67	15.22	2.54	2.40	NUBIA	E-EGY
SHLA	35.40	23.11	20.72	11.79	0.24	0.19	NUBIA	P-EGY
SIMO	18.44	-34.19	17.27	21.37	0.45	0.71	NUBIA	P-IGS*
SLOM	34.28	31.23	27.22	17.30	0.97	0.61	SINIA	P-SOP
SLUM	25.21	31.49	21.73	18.79	0.34	0.46	NUBIA	P-EGY
SOFI	23.40	42.56	23.70	12.09	0.14	0.29	EURASIA	P-IGS*
SOHG	31.82	26.47	25.33	18.42	1.72	3.28	NUBIA	E-EGY
SOKN	32.41	29.78	25.60	17.32	2.70	3.67	NUBIA	E-EGY
SOLA	46.40	24.91	31.79	28.84	0.36	0.37	ARABIA	P-SOP
SUTH	20.81	-32.38	17.13	19.33	0.46	0.61	NUBIA	P-IGS*
SUTM	20.81	-32.38	16.95	19.35	0.31	0.56	NUBIA	P-IGS*
TAYS	34.87	28.55	25.60	20.95	0.79	0.71	ARABIA	P-SOP
TEHN	51.33	35.70	27.13	18.79	0.78	0.46	EURASIA	P-IGS*
TELA	34.78	32.07	22.86	19.76	0.61	0.44	SINIA	P-SOP
TLSE	1.48	43.56	19.53	16.47	0.30	0.19	EURASIA	P-IGS*
TOUR	33.73	28.16	23.29	19.59	3.92	7.92	SINIA	E-EGY
TRAB	39.78	41.00	26.07	11.45	0.63	0.57	EURASIA	P-IGS
TUBI	29.45	40.79	20.25	11.09	0.27	0.22	EURASIA	P-IGS
UNIV	32.87	24.00	22.80	17.30	1.68	1.76	NUBIA	E-EGY
VILL	-3.95	40.44	18.86	16.17	0.23	0.15	EURASIA	P-IGS*
WADI	31.35	27.04	25.60	16.53	1.77	2.29	NUBIA	E-EGY
WAHA	30.69	29.66	24.38	16.27	2.35	2.88	NUBIA	E-EGY
WIND	17.09	-22.58	19.60	21.35	0.36	0.49	NUBIA	P-IGS*
YEBE	-3.09	40.53	19.04	16.07	0.15	0.13	EURASIA	P-IGS*
YIBL	56.11	22.19	33.34	30.98	0.57	0.59	ARABIA	P-IGS*
YKRO	-5.24	6.87	22.44	17.07	1.27	1.35	NUBIA	P-IGS
YOSH	35.21	32.10	22.71	19.71	0.27	0.82	SINIA	P-SOP
YRCM	34.93	30.99	23.32	18.70	0.22	0.21	SINIA	P-SOP
ZAFR	32.81	28.71	26.79	19.22	5.96	7.92	NUBIA	E-EGY
ZAMB	28.31	-15.43	20.12	19.14	0.20	0.34	NUBIA	P-IGS*
ZECK	41.57	43.79	25.94	11.15	0.33	0.38	EURASIA	P-IGS
ZOMB	35.33	-15.38	20.44	17.63	0.46	0.53	SOMALIA	P-UNA

4.1.2 Relative velocity Field

In order to constrain the relative motion between the tectonic plates, the CATS velocities and uncertainties, for permanent stations, and Bernese velocities and scaled uncertainties, for non-permanent stations, were used to calculate the Euler vectors as described in Chapter 3. Based on the criteria in chapter 3, 91 GPS sites were used to estimate the absolute ITRF2008 Euler vectors for Nubia, Eurasia, Somalia, Arabia and Sinai plates. Also, the Euler vectors in Eurasia fixed frame, the Euler vectors for Sinai and Arabian plates in Nubia fixed frame, and for Arabian in Sinai fixed frame were estimated, as shown in Table 4.2.

4.1.2.1 Eurasia Fixed Frame

72 GPS stations were used to estimate the Euler vectors for Nubian, Somalian, Arabian and Sinai plates referenced to the Eurasian plate as shown in Table 4.2. Figure 4.3 and Table A2 in the Appendix give the GPS sites velocity in the Eurasia fixed frame. Figure 4.3 shows a counterclockwise rotation that increases toward the Hellenic trench system as proposed by (McClusky et al., 2000) and (Reilinger et al., 2006) but with different magnitudes. The relative motion between northeastern corner of Nubia and Eurasia is $6.5 \pm 1\ mm/yr$, $14.2 \pm 1.4\ mm/yr$ in the North of the Arabian plate, $23.3 \pm 0.7\ mm/yr$ in the East of Arabia and $22.3 \pm 0.7\ mm/yr$ in eastern and central Turkey.

Focusing on the Egyptian region, as shown in Figure 4.4, it is clear that almost all sites are moving to the same direction with the same magnitude, in average $6.5 \pm 1\ mm/yr$ to the North to Northwest direction, except the sites in Sinai Peninsula of about $8.2 \pm 0.8\ mm/yr$ to the North to Northeast direction. This small difference in magnitude, about $1.7\ mm/yr$, and direction of the velocity between stable Nubia and Sinai Peninsula may support the idea of a separate Sinai sub-plate sandwiched between the Arabian and Nubian plates as previously suggested by (Mahmoud et al., 2005) and (Reilinger et al., 2006). In the next section, the relative motion of Sinai with respect to Nubian plate is estimated.

Figure 4.5 shows the differences, in location, between the GPS Nubia-Eurasia Euler pole, from different authors ((McClusky et al., 2000); (Sella et al., 2002); (Reilinger et al., 2006)), and NUVEL-1A (DeMets et al., 1994). It is clear that there are significant differences between the GPS derived and the NUVEL-1A Euler poles. Even within the GPS derived Euler poles, there are also significant differences which may be regarded to the different set of GPS sites used for each calculation.

Table 4.2: Estimated Euler vectors from this study, absolute and relative.

Plates	Reference	Lat. (°N)	σ_n	Long. (°E)	σ_e	Angular Velocity (°/myr)	σ_a	Number of sites
Nubia	ITRF2008	49.63	0.15	-81.10	0.41	0.267	0.0007	44
Eurasia	ITRF2008	50.80	0.37	-107.09	0.61	0.247	0.0009	19
Somalia	ITRF2008	47.61	0.86	-97.80	1.48	0.325	0.0060	5
Arabia	ITRF2008	52.33	0.29	-8.63	1.78	0.500	0.0090	7
Sinai	ITRF2008	54.89	0.95	-8.14	4.54	0.433	0.0268	16
Nubia	Eurasia	12.88	0.55	-16.27	0.57	0.080	0.0012	44
Somalia	Eurasia	-36.90	1.69	105.56	6.47	-0.088	0.0046	5
Arabia	Eurasia	29.78	0.19	16.33	0.88	0.421	0.0120	7
Sinai	Eurasia	27.91	0.42	21.00	1.26	0.357	0.0330	16
Sinai	Nubia	30.14	0.21	31.58	0.40	0.298	0.0340	16
Arabia	Nubia	32.36	0.27	24.33	0.78	0.358	0.0130	7
Arabia	Sinai	36.50	1.26	-10.91	9.84	0.071	0.0092	7

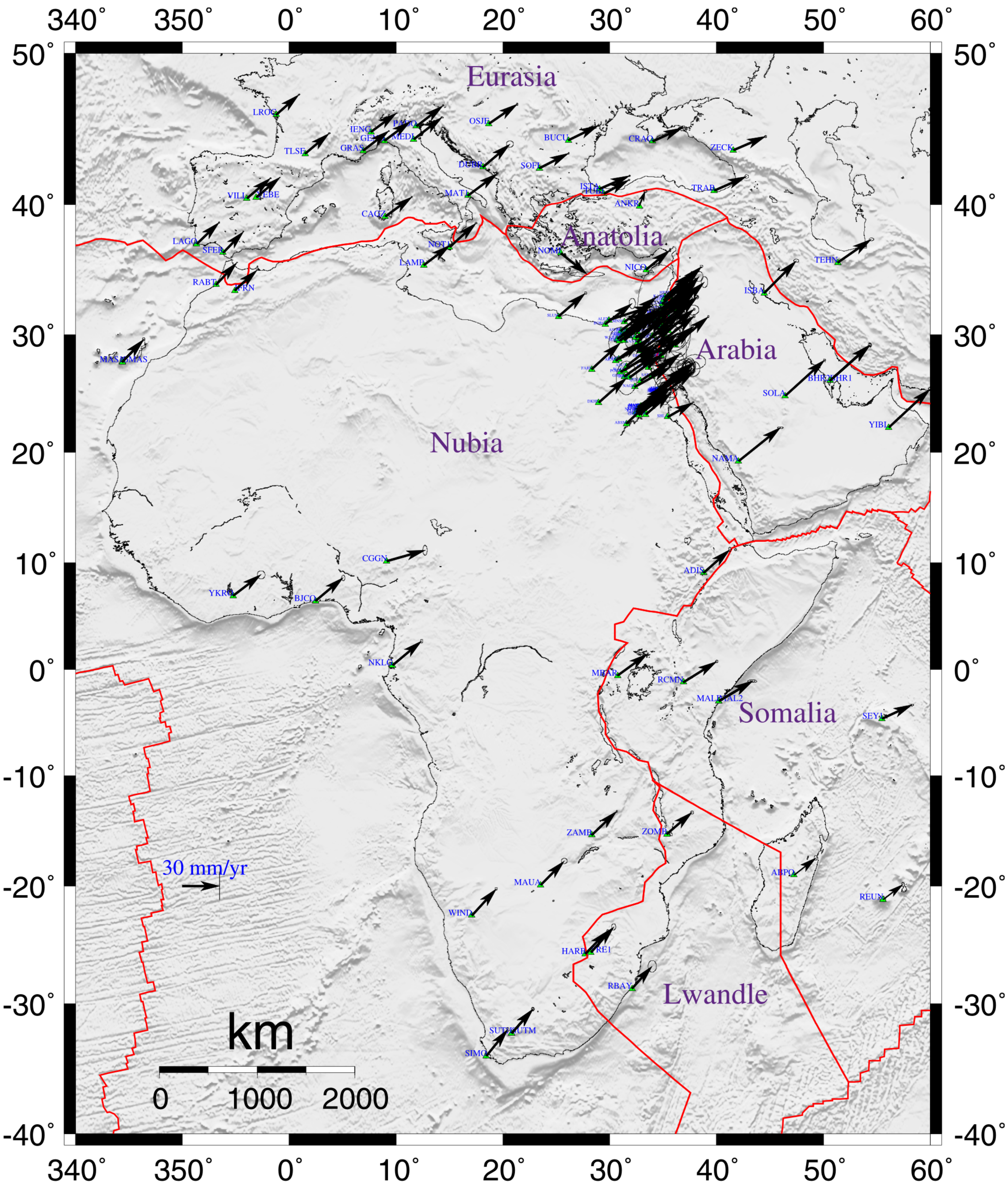

Figure 4.1: Estimated ITRF2008 horizontal velocities of the selected permanent stations in addition to Egyptian stations, permanent and epoch, with 95% confidence region. Red lines represent the plate boundaries (as in Figure 2.1).

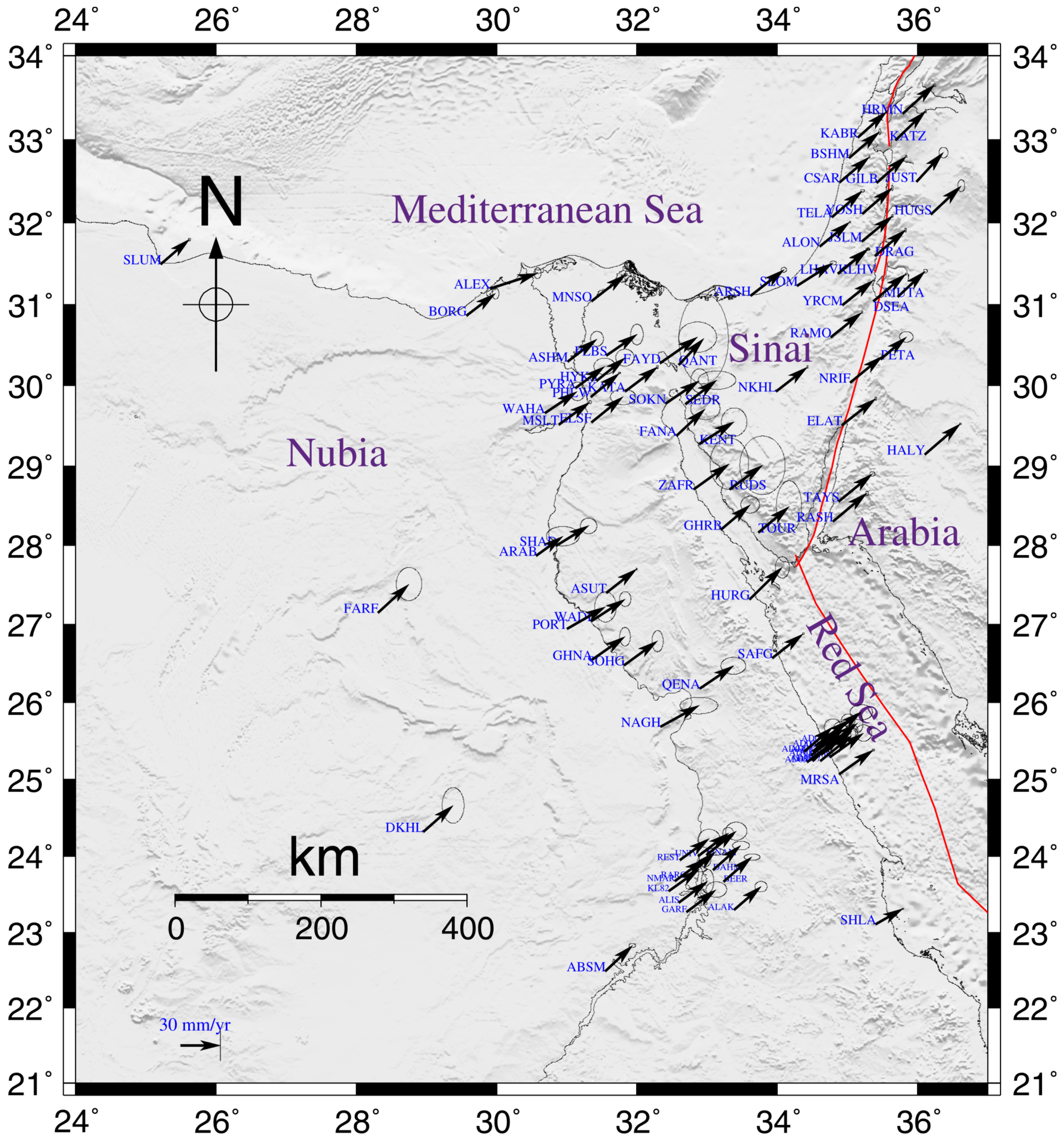

Figure 4.2: Estimated ITRF2008 horizontal velocities for Egypt-Sinai-DST fault region, with 95% confidence region. Red lines represent the plate boundaries (as in Figure 2.1).

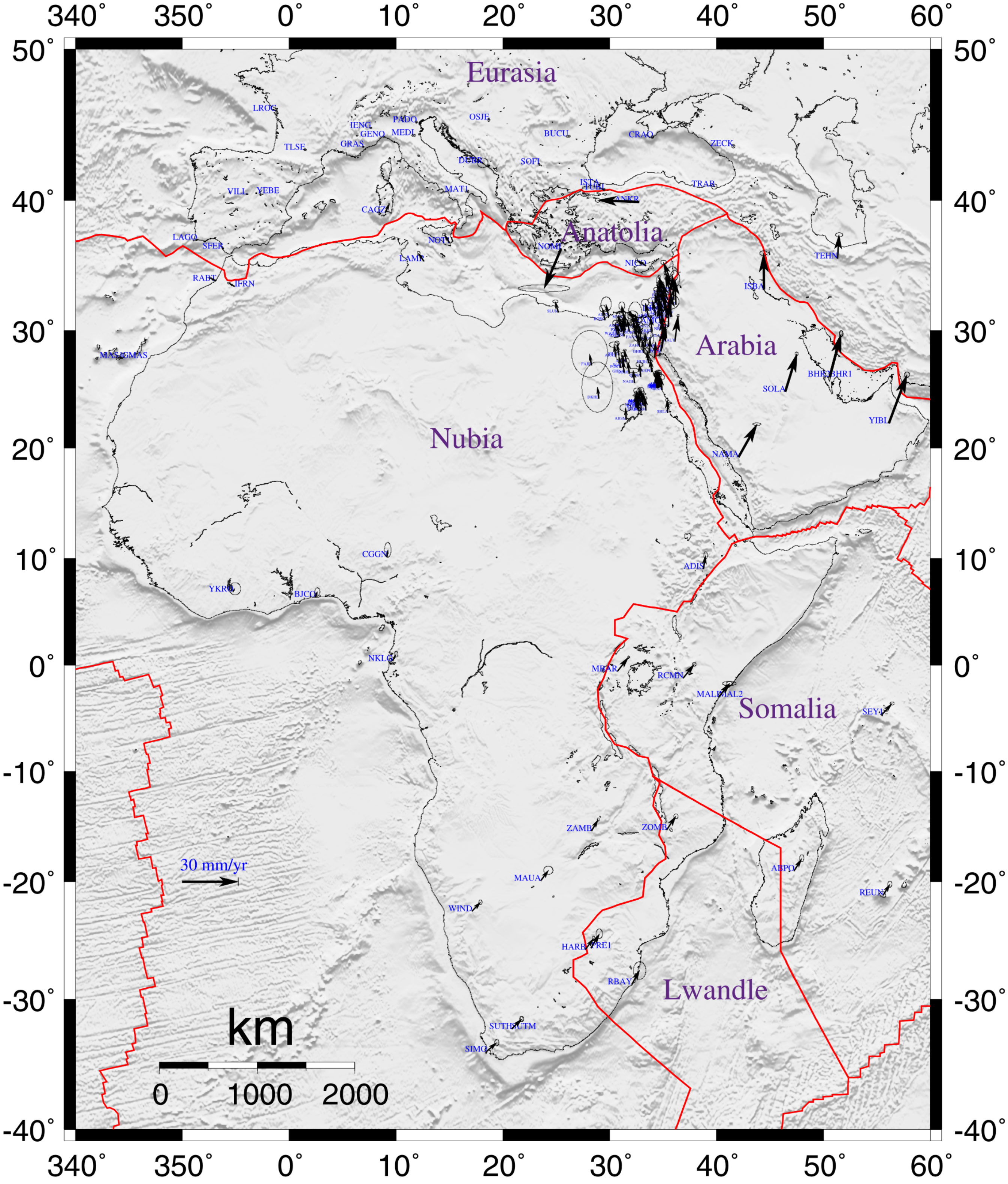

Figure 4.3: The estimated horizontal velocity in the Eurasia fixed reference frame with 95% confidence regions. Red lines represent the plate boundaries (as in Figure 2.1).

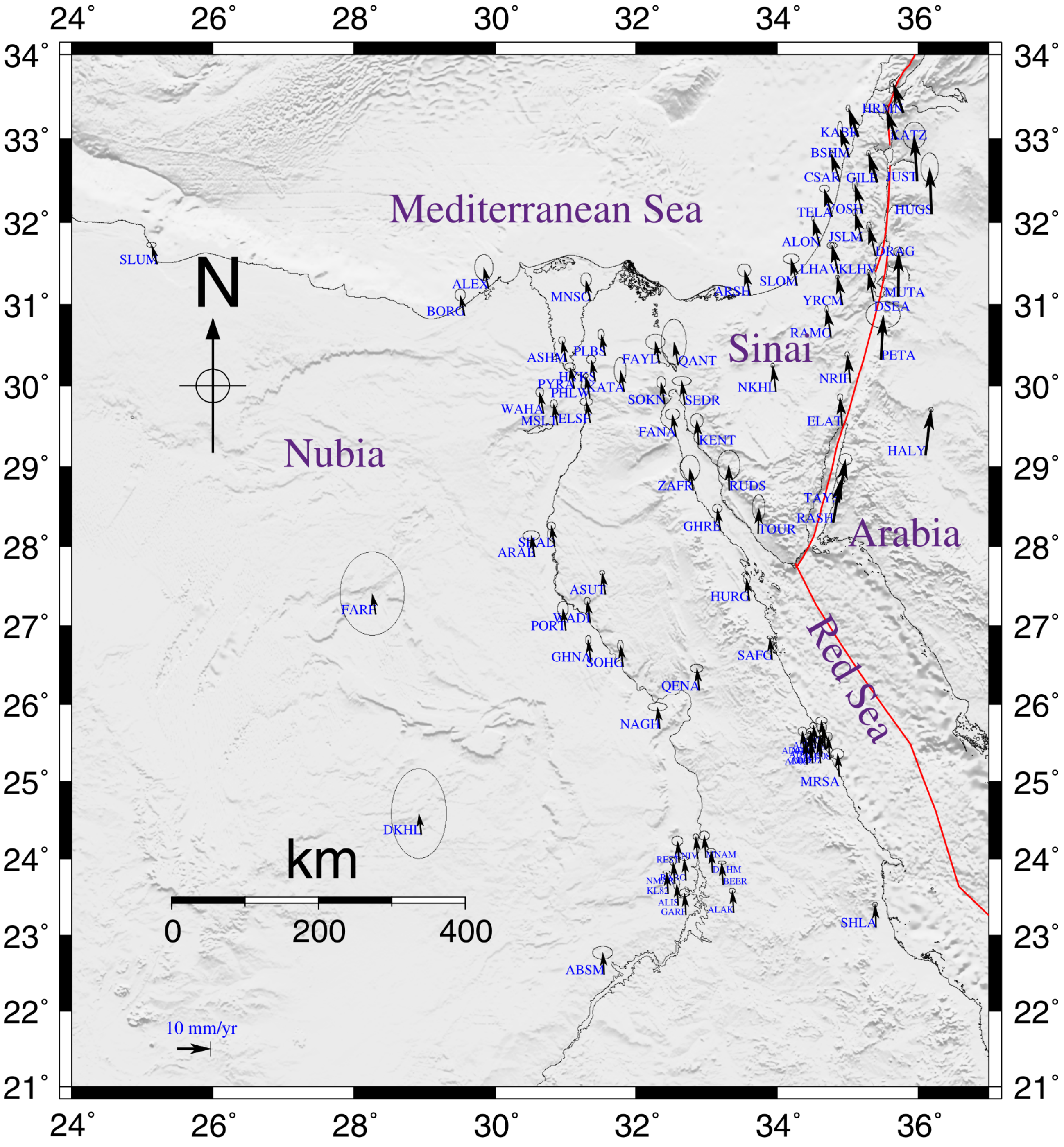

Figure 4.4: The estimated horizontal velocity in the Eurasia fixed reference frame with 95% confidence regions for Egypt-Sinai-DST fault region. Red lines represent the plate boundaries (as in Figure 2.1).

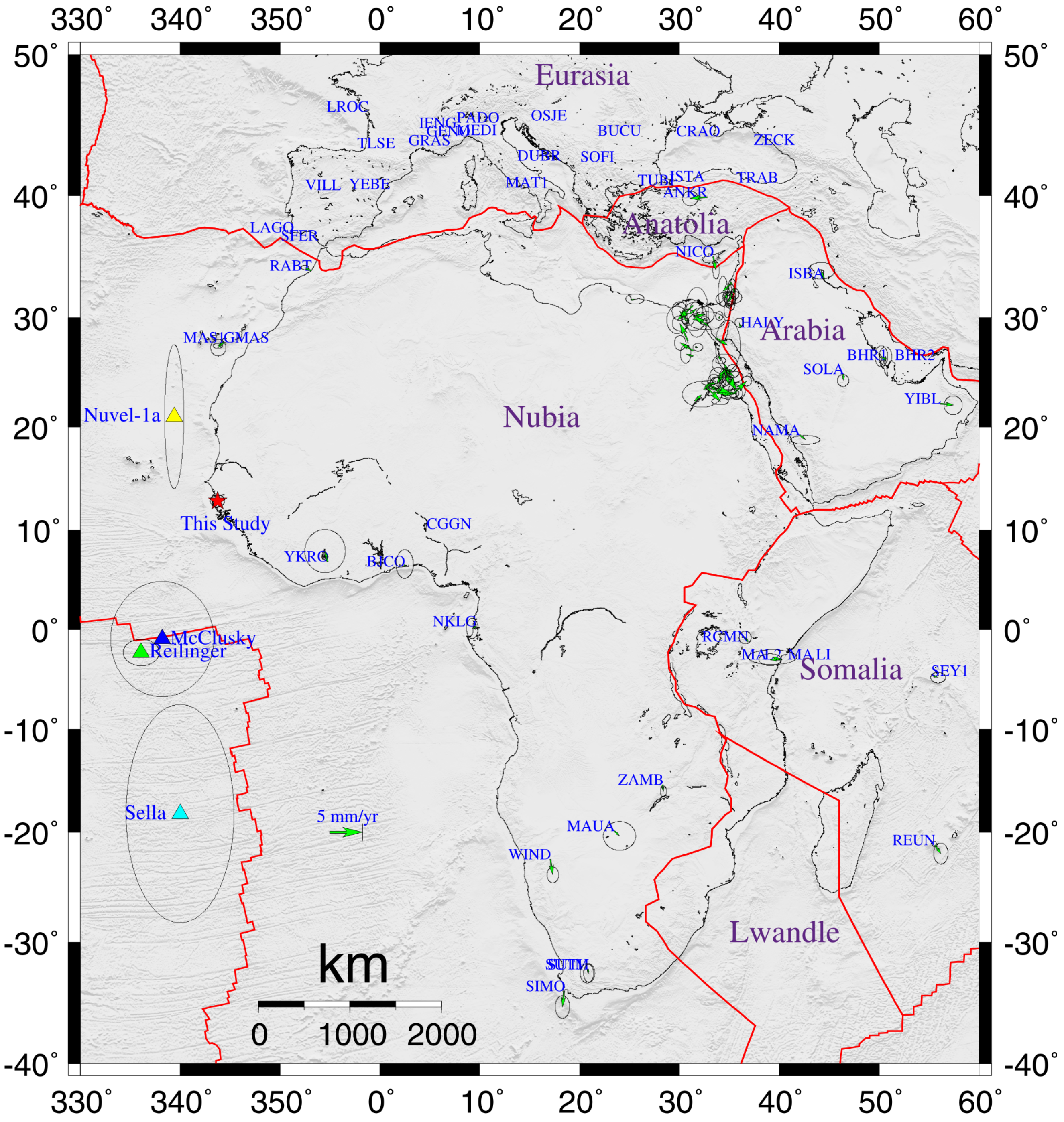

Figure 4.5: Estimated Nubia-Eurasia Euler poles with uncertainties in addition to Euler poles from different authors ((McClusky et al., 2003); (Reilinger et al., 2006); NUVEL1-A (DeMets et al., 1994); (Sella et al., 2002)) and GPS station residuals with 95% confidence level. Residuals in Arabia, Somalia and Sinai are from Arabia-Eurasia, Somalia-Eurasia, Sinai-Eurasia, respectively. Red lines represent the plate boundaries (as in Figure 2.1).

4.1.2.2 Nubia Fixed Frame

The available GPS sites were used to estimate the Euler vectors for Sinai and Arabian plates with respect to stable Nubia in order to examine the existence of a separate Sinai micro-plate sandwiched between the Arabian and Nubian plates and estimating the differential movement between Nubia and Arabia. Following the same criteria, for selecting the GPS sites for Euler vector estimation, 16 and 7 GPS sites were chosen for the estimation of the angular velocity of Sinai sub-plate and Arabian plate referenced to Nubia, respectively.

Some of the stations representing the Sinai sub-plate are belonging to the local geodetic network around the Gulf of Suez. Due to the small amount of GPS data collected from this network, ranging from three to five campaigns, and the presence of outliers which affect the repeatability, the main input to the scaling approach, the values of the scaled standard deviation (σ_s) are very high. Based on the CATS analysis for the permanent stations, the scaled error is a factor of 5 to 10 higher than the estimated CATS error. Therefore, to get a realistic error, the scaled error of the non-permanent stations of the Gulf of Suez network was divided by 5. However, it is a simple approximation of the non-permanent observation precision and, of course, cannot perfectly assess the precision of the achieved results which need more observations to improve the error estimation. From the different behavior during the campaigns, the standard deviation should be in the range of 2 mm for the horizontal component.

Figure 4.6 and Table A3 in the Appendix show the horizontal velocity with uncertainties of Sinai Peninsula and Arabian plate referenced to Nubian plate. It is clear from Figure 4.6 that the northwestern sites, close to DST fault, of the Arabian plate are moving to the North to Northeast direction of about $6.9 \pm 1.4\ mm/yr$, while the eastern and southern sites are moving to the Northeast direction of about $15.2 \pm 0.8\ mm/yr$. On the other hand, focusing on the Sinai-DST fault region (Figure 4.7), almost all the GPS sites in the western and southern part of Sinai and Gulf of Suez do not show any significant velocity with 95% of confidence level referenced to Nubia. Whereas, the eastern and northeastern sites show a systematic trend of horizontal velocity to the North to Northwest direction with respect to Nubia of about $1.7 \pm 0.9\ mm/yr$.

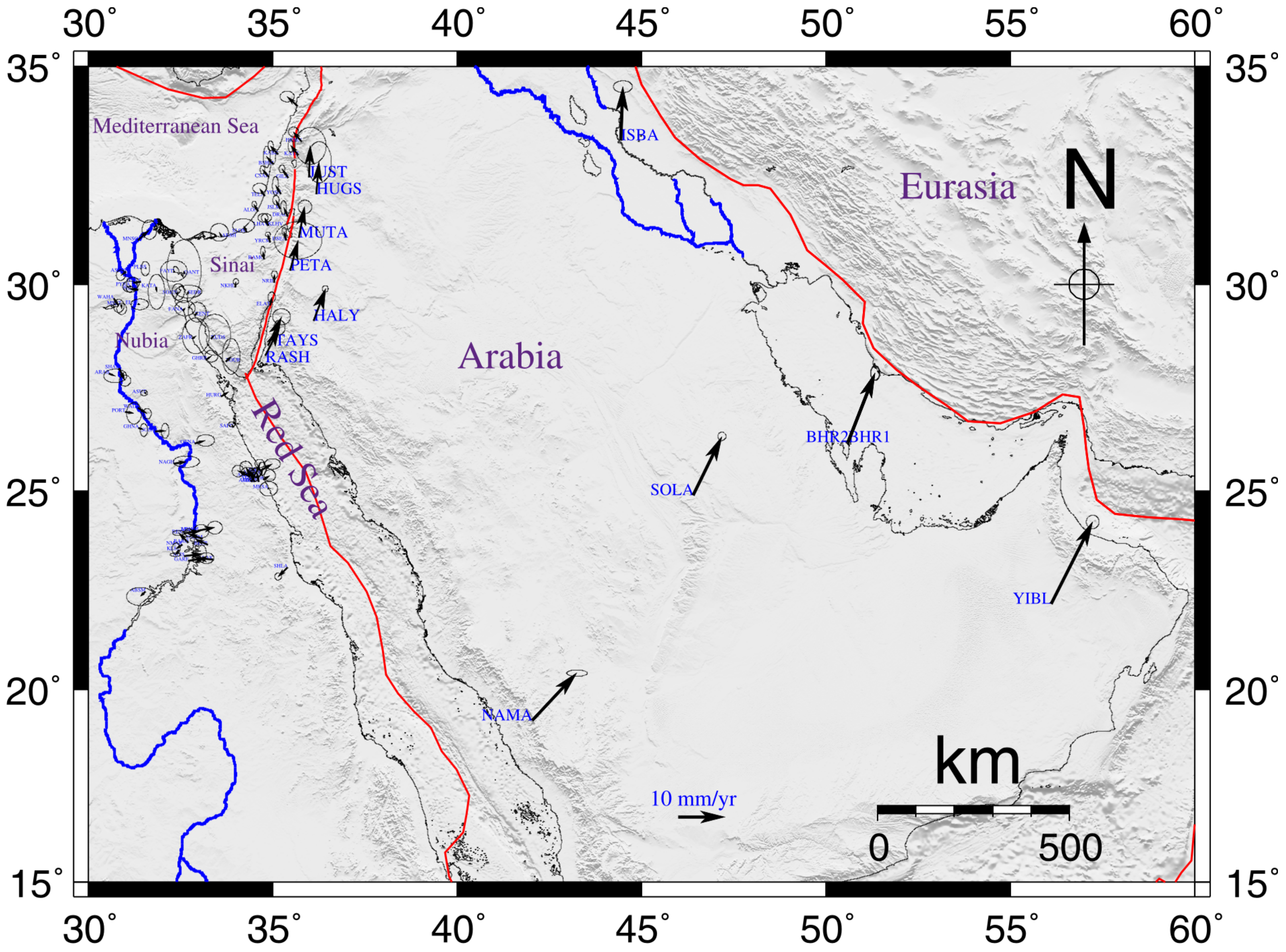

Figure 4.6: GPS horizontal velocities of Arabian and Sinai sites with 95% confidence level in the Nubia fixed frame. Red lines represent the plate boundaries (as in Figure 2.1).

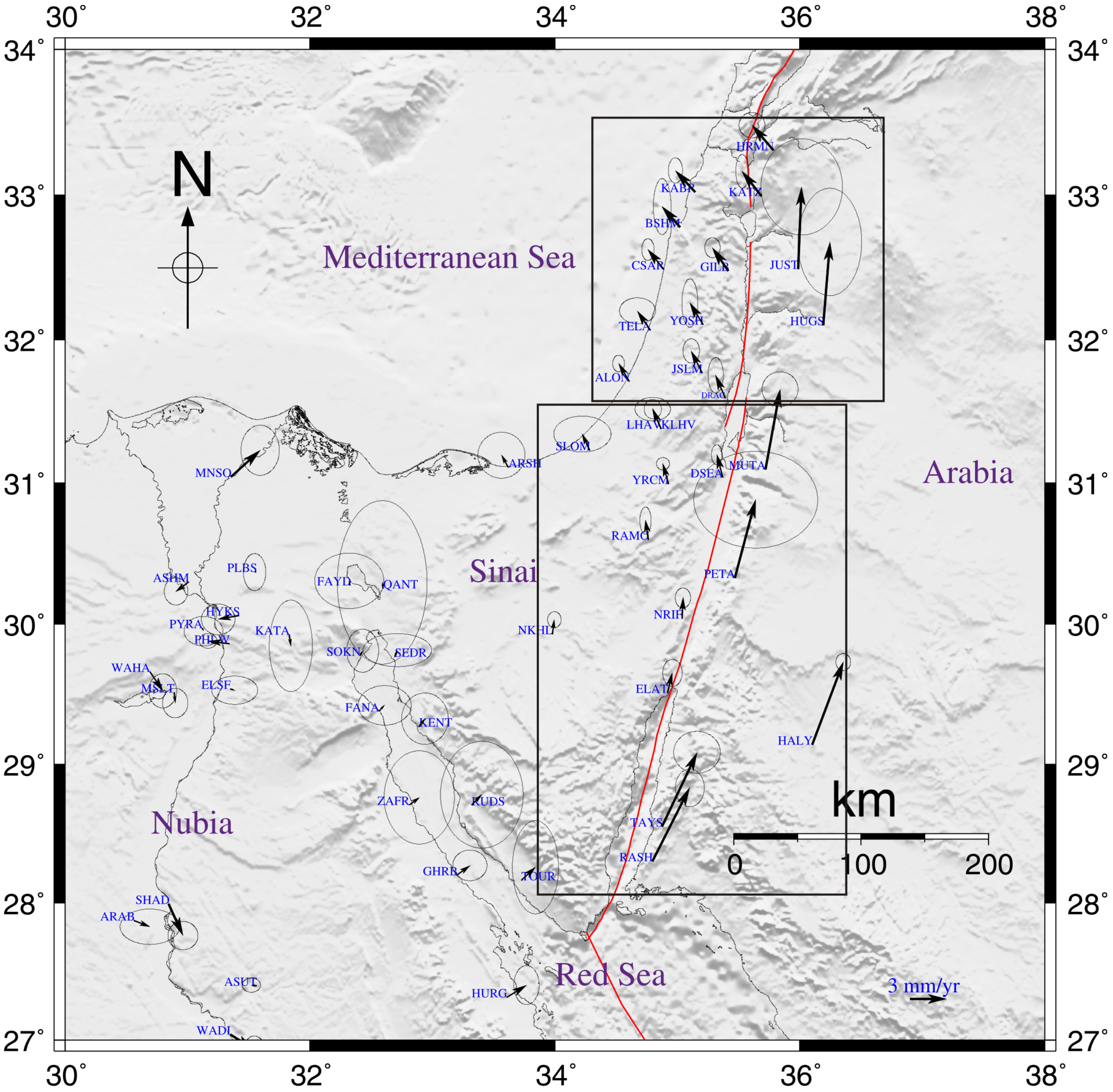

Figure 4.7: GPS horizontal velocities of Sinai with 95% confidence level in Nubia fixed frame. Red lines represent the plate boundaries (as in Figure 2.1). Black boxes contain the GPS sites used for the fault parallel inversion.

4.1.2.3 Sinai Fixed Frame

Many attempts are made to constrain the slip rate along the DST fault. (Wdowinski et al., 2004) estimated a slip rate of $3.7 \pm 0.4\ mm/yr$ from 10 GPS permanent stations. Combining both permanent and campaign data, (Le Beon et al., 2008) provided a $4.9 \pm 1.4\ mm/yr$ slip rate along the DST fault. Using larger data set than the previous studies, (Sadeh et al., 2012) introduced a slip rate for the southern part of the DST of $\sim 5\ mm/yr$ which decreases toward the north of the DST to $3.8\ mm/yr$. All these previous studies suffered from the lack of the GPS sites in the Egyptian region. Using for the first time the GPS sites in the Egyptian side, the Euler vectors for Arabia in the Sinai fixed frame was estimated. Figure 4.8 shows the horizontal velocity field in the Sinai fixed frame. Close to the DST fault the GPS sites are moving toward the Northeast direction with magnitude of about $5.0 \pm 1.4\ mm/yr$ in good agreement with the slip rate estimated by (Le Beon et al., 2008) and (Sadeh et al., 2012) (for the southern part of the DST fault). They are higher than the (Wdowinski et al., 2004) slip rate.

4.1.2.4 Slip Rate and Locking Depth Estimation

Estimating the slip rate is achieved by fitting the GPS velocities to a locked dislocation fault model that consists of an elastic seismogenic layer of thickness (D), it also called locking depth. In this work, the elastic fault model of (Savage and Burford, 1973) for an infinitely long fault was used. This model depends on three parameters. It assumes a seismogenic layer of thickness (D) (locking depth) that overlies two layers moving horizontally relative to each other at a constant velocity (V_0). Based on the assumption of infinitely long fault, the fault normal component is assumed to be zero, whereas the fault parallel component depends on the surface distance from the fault (x). Equation 4.1 describes the velocity field obtained at the surface from such a model.

$$V(X) = V_1 + V_0 \frac{1}{\pi} arctan\left(\frac{x}{D}\right), \tag{4.1}$$

where the V_1 is the velocity along the fault plane relative to a fixed reference frame, D is the locking depth (the thickness of the elastic seismogenic layer), x is the surface distance to the fault and V_0 is the far-field velocity (slip rate). To get an accurate estimate for the slip rate, the GPS sites should be away more than several times the locking depth from the fault (for example $> 40\ km$ for a locking depth of 15 km); while for an accurate estimate of the locking depth, the GPS sites should be close to the fault plane, roughly within half of the locking depth (for example $< 7\ km$). This model is applied to constrain the slip rate and the locking depth of the DST fault because it is the most active tectonic element in the study area, in addition to the fact that the movement along the DST fault is mainly strike-slip (horizontal). The velocities in Nubia fixed frame of 28 GPS sites were used in the slip rate V_0 and locking depth D inversion. Nine stations are located East of the DST fault and 19 stations are located West of the DST fault as shown in Figure 4.7. Figure 4.9(a, b, c) shows the fault parallel velocity for the DST fault. The slip rate along the DST fault is 6 mm/yr with a locking depth of 16 km. As shown in Figure 4.7, the DST fault consists of more than one segment, therefore the inversion is splitted into two parts, one for the southern segment of the DST fault and the other one for the northern segment of the DST fault. The boxes in Figure 4.7 contain the GPS sites used for each inversion. Figure 4.9b shows the fault parallel velocity along the northern segment of the DST fault. The estimated slip rate and locking depth for the northern segment are 5 mm/yr and 12 km, respectively. On the other hand the slip rate and the locking depth of the southern segment of the DST fault are 7 mm/yr and 18 km, respectively, which is much higher than the estimates of fault parallel velocity parameters of the northern segment of the DST fault and also the whole DST fault.

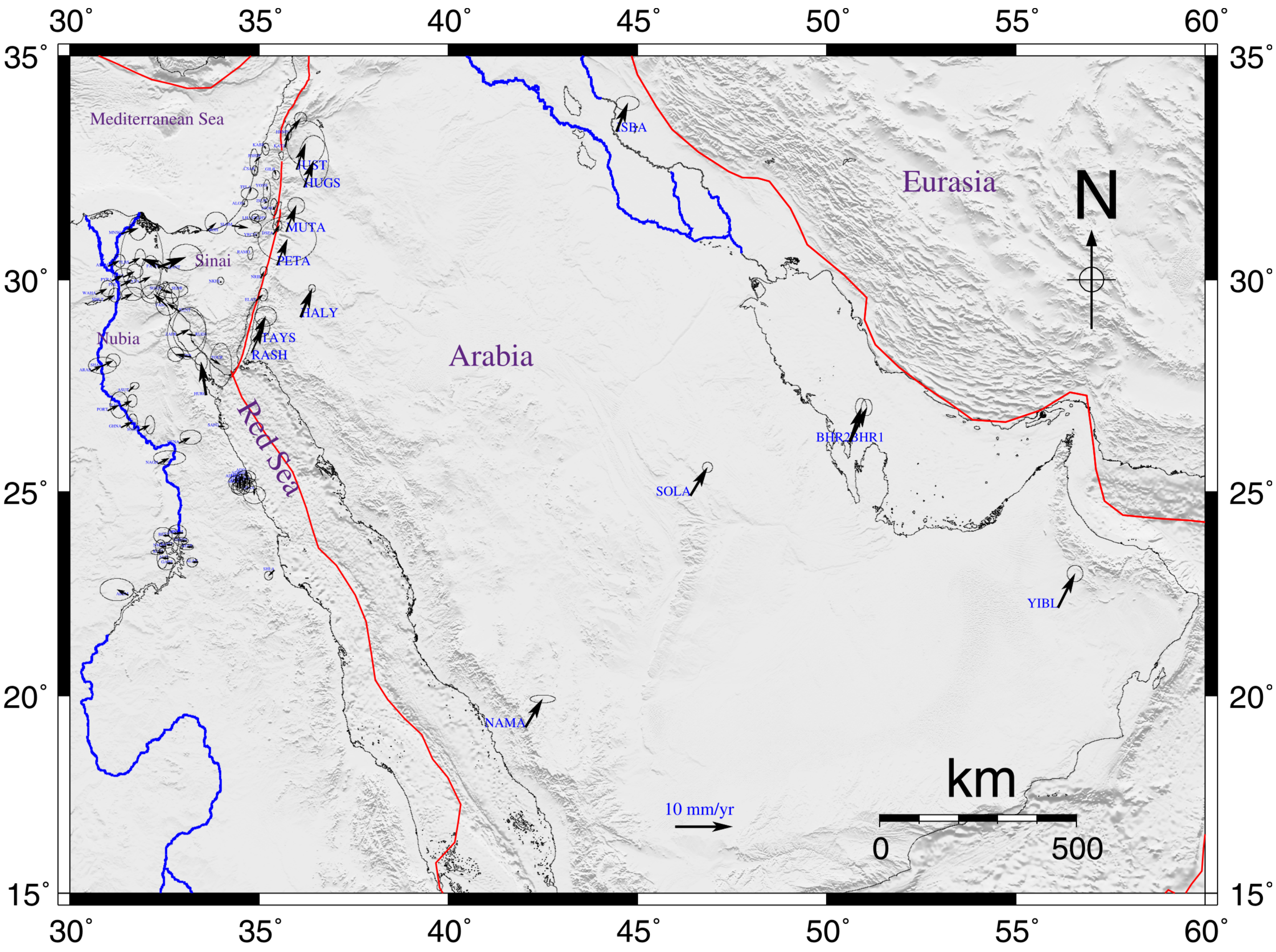

Figure 4.8: GPS horizontal velocities of the Arabian sites with 95% confidence level in Sinai fixed frame. Red lines represent the plate boundaries (as in Figure 2.1).

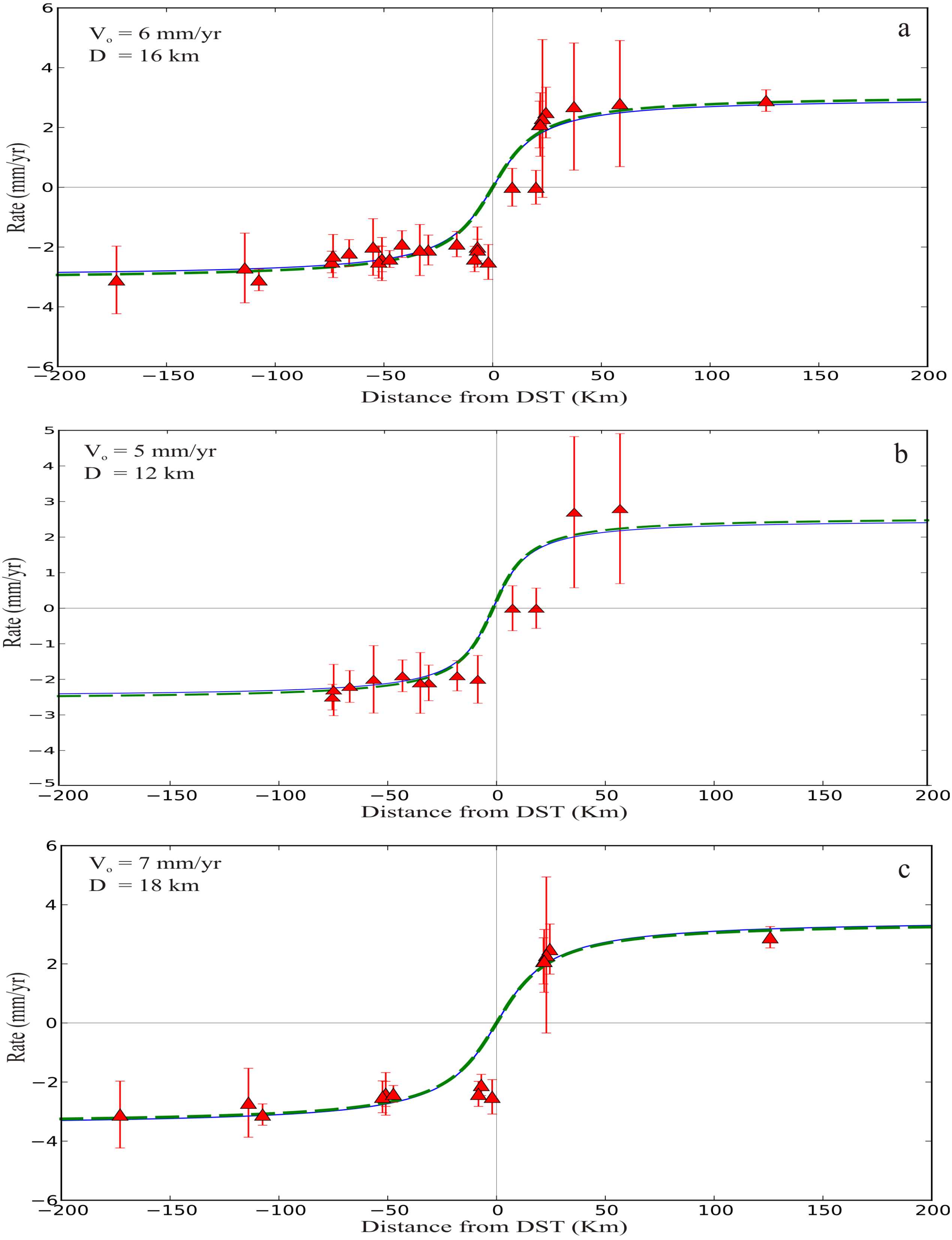

Figure 4.9: Fault parallel velocities for the DST fault: (a) for the whole DST fault , (b) the northern segment of DST fault, and (c) the southern segment of the DST fault. Green dashed curve represents the observed fault parallel velocities and the blue curve shows the best fit model. For each plot (a, b, and c), both observed and modeled estimates show very good agreement when choosing the best respective locking depth.

4.1.2.5 Strain Results

To calculate the strain rates in the northeastern corner of Africa, the GPS velocities in East and North components are interpolated separately, according to the approach of (Hackl et al., 2009) which described in Chapter 3. Figures 4.10, 4.11, and 4.12 show the maximum shear strain, the dilatation, and the principle strain rate, respectively. At the first glance on Figure 4.10, it is clear that the highest values of the shear strain are localized around the DST fault, that defines the plate boundary between Nubian and Arabian plates, and ranging from $40 - 90 \times 10^{-9}/yr$. The southern parts of Sinai and Gulf of Suez are characterized by low to moderate shear strain of $20 - 40 \times 10^{-9}/yr$. The rest of the northeastern corner of Africa (Egypt) seems to be stable, characterized by very low shear strain. The areas of high shear strain do not necessarily correspond to high seismic hazards, because the major parts of deformation are not accumulated as elastic energy ((Bürgmann et al., 2001); (Malservisi et al., 2005)).

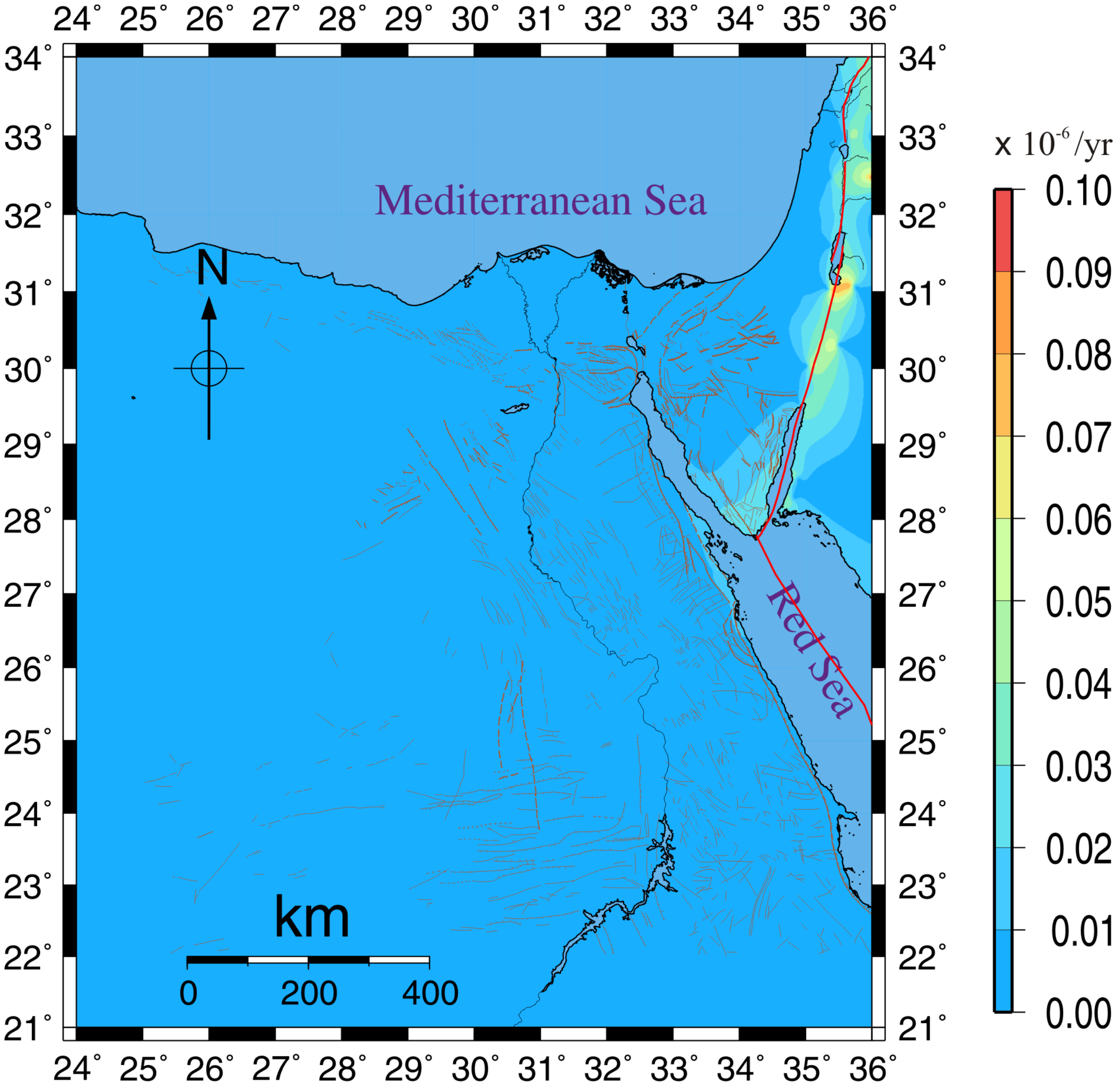

Figure 4.10: Maximum shear strain of northeastern corner of Africa. Brown lines represent surface faults (as in figure 2.4). Red lines represent the plate boundaries (as in Figure 2.1).

Figures 4.11 and 4.12 show the areas of extension and compression in the northeastern corner of Africa. As explained in the shear strain figure, the only area that experienced strain force is the southern part of the Gulf of Suez and Sinai, in addition the DST fault. The southern part of the Gulf of Suez and Sinai are affected by low extensional force while the compression force is predominant in Gulf of Aqaba. Northeast the Gulf of Aqaba, more complex pattern seems to prevail than in the surrounding areas.

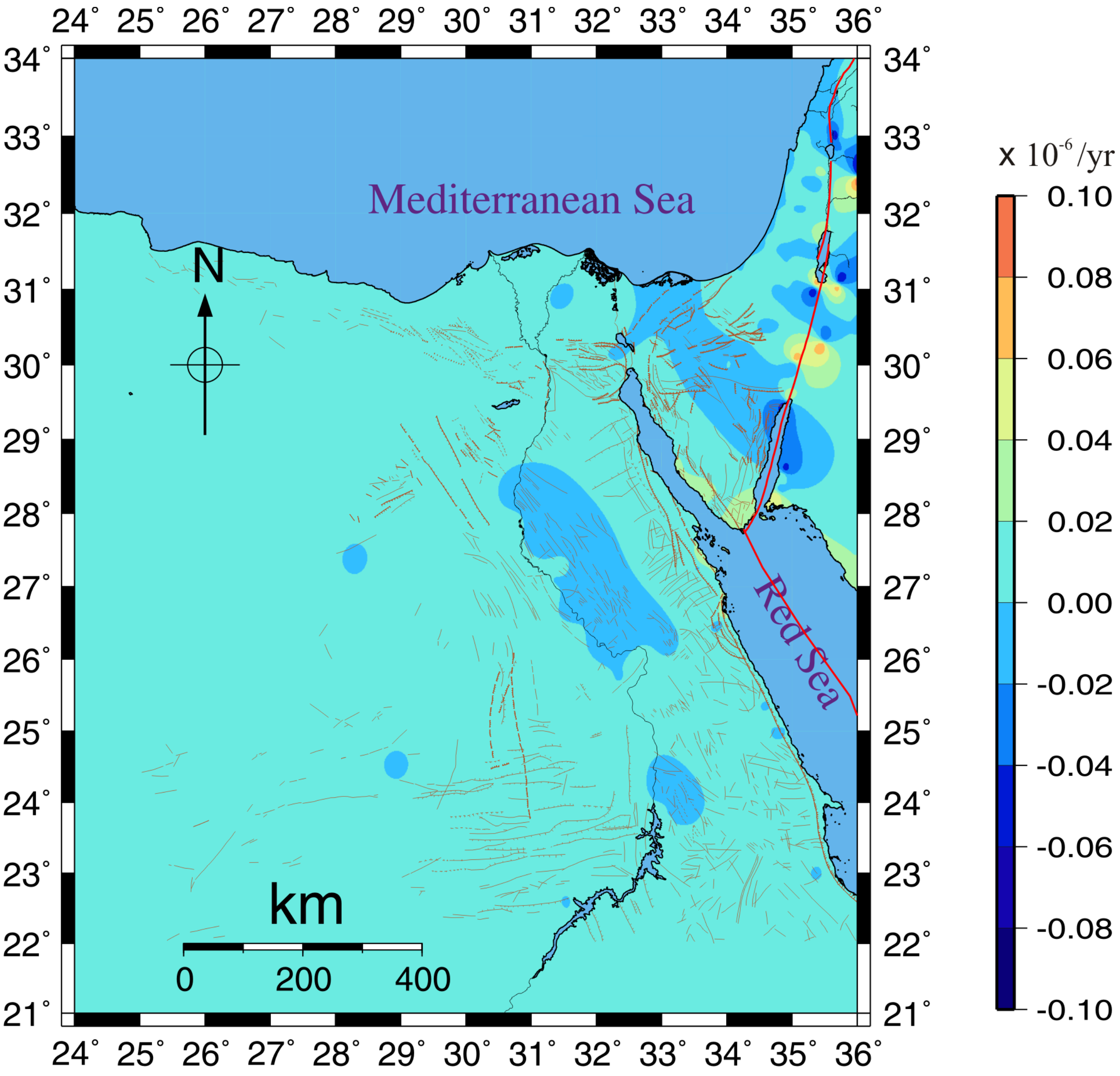

Figure 4.11: Dilatation strain of northeastern corner of Africa, where negative values represent compression and positive values represent extension. Brown lines represent surface faults (as in figure 2.4). Red lines represent the plate boundaries (as in Figure 2.1).

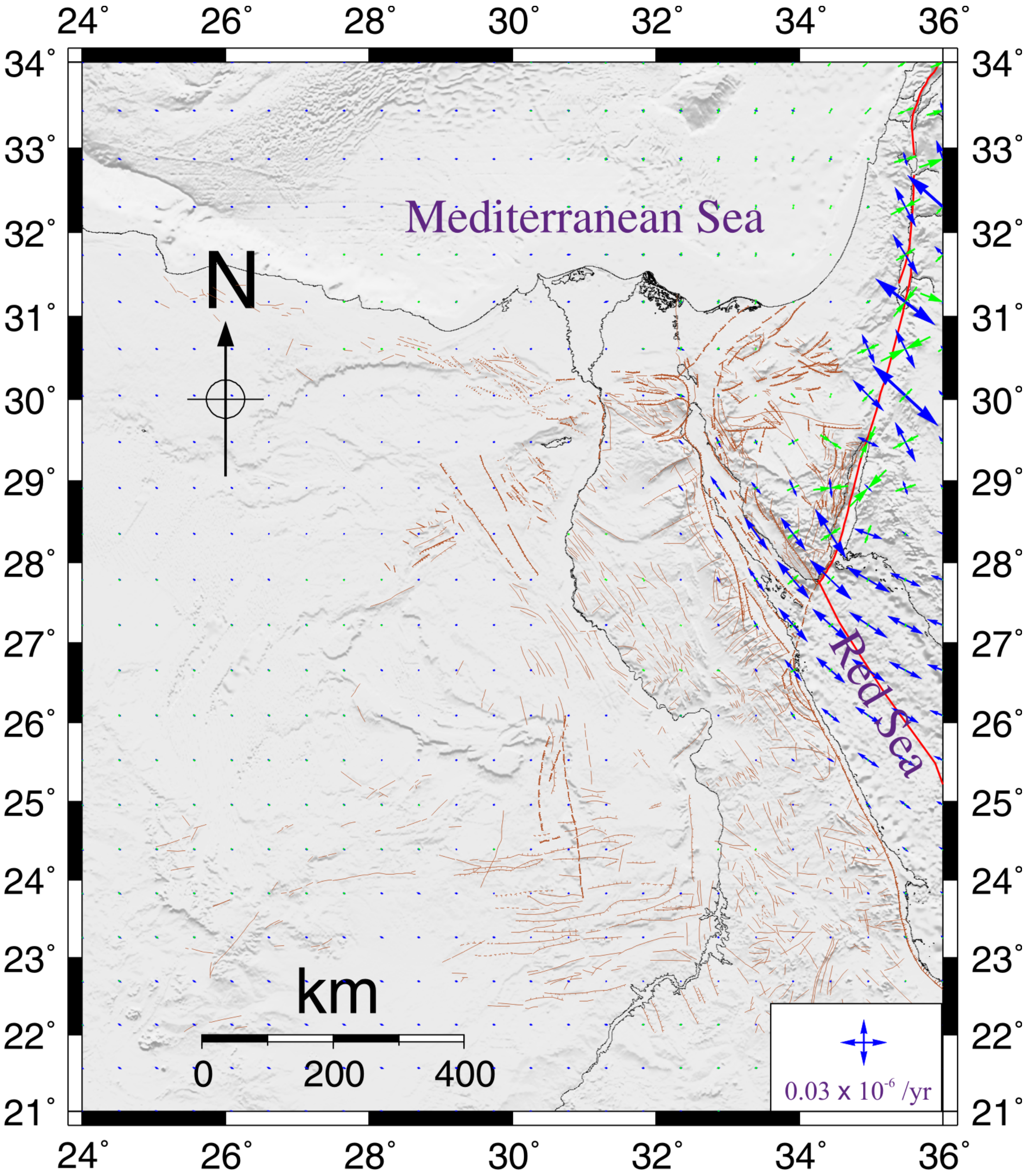

Figure 4.12: Principle strain rate of northeastern corner of Africa, where blue arrows represent extension and green arrows represent compression. Brown lines represent surface faults (as in Figure 2.4). Red lines represent the plate boundaries (as in Figure 2.1).

4.1.3 Absolute Vertical Velocity Field

Figure 4.13 shows the estimated vertical velocity field for Egypt. Due to the short records in the campaign data which affect the vertical velocity estimation, the vertical velocity field presented in Figure 4.13 is derived only from the EPGN stations. Almost all stations located at southern Egypt, below latitude 28°, do not show any significant vertical velocity. However, with the exception of ARSH which goes up of $4.9 \pm 2.5\ mm/yr$, all the stations in northern Egypt are showing a general trend of subsidence. Stations ALEX, MNSO, and KATA are going down with magnitudes $-2.9 \pm 0.9\ mm/yr$, $-14.2 \pm 1.7\ mm/yr$, and $-7.6 \pm 2.4\ mm/yr$, respectively. The other stations in northern Egypt do not show any significant vertical velocity.

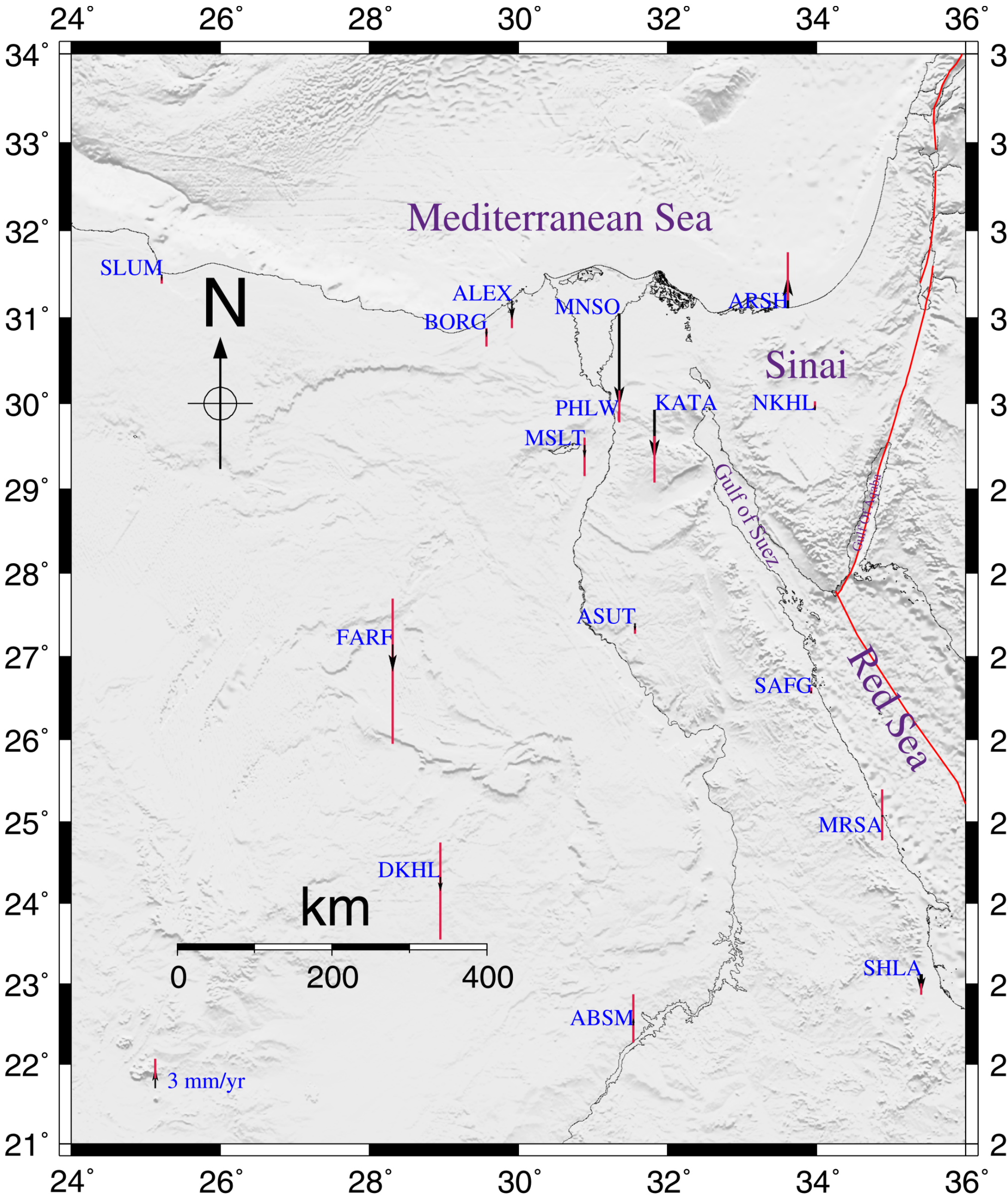

Figure 4.13: Estimated ITRF2008 vertical velocities for Egypt from EPGN. Red lines represent the plate boundaries (as in Figure 2.1).

4.2 InSAR Results

One of the aims of this work is to estimate the rate of subsidence of the Nile Delta using Persistent Scatterer InSAR PSI approach. All the available SAR scenes in the descending tracks 207 and 436 of the ERS1, ERS2, and Envisat satellite missions were processed using StaMPS software following the processing scheme mentioned in Chapter 3. 36 and 37 Envisat SAR scenes acquired on tacks 207 and 436, respectively, in addition to 20 and 24 ERS SAR scenes acquired on tracks 207 and 436, respectively, were processed to constrain the rate of subsidence of the Nile Delta. The raw SAR scenes were focused by the Repeat Orbit Interferometry Package ROI_PAC ((Massonnet and Feigl, 1998); (Thompson et al., 1986); (Rosen et al., 2000); (Zebker and Goldstein, 1986)), Delft Object-oriented Radar Interferometric Software DORIS (Kampes et al., 2003) for interferogram generation, and Shuttle Radar Topography Mission SRTM 90 m data for removing the topographic phase contribution. PS processing was carried out using Stanford Method for Persistent Scatterers software StaMPS (Hooper et al., 2012).

4.2.1 ERS Results

20 and 24 ERS descending scenes were processed from tracks 207 and 436, respectively. The master scenes used for tracks 207 and 436 are 19980623 and 20000120, respectively. During the time span of the ERS data (1992-2002), there was an earthquake that occurred close to Cairo on October 12, 1992 of magnitude 5.9, which may affect the estimated LOS velocity rates. Otherwise the Nile Delta is characterized by low seismic activity and the majority of these earthquakes are micro-earthquakes (magnitude less than 3). Figure 4.14 shows the LOS velocity field for the Nile Delta deduced from the processing of the ERS SAR scenes of tracks 207 and 436. The velocity field that covers a presumably undeforming part, represented as a green circle South of Cairo, is subtracted from the whole entire velocity field, producing a LOS velocity field in the Nubia fixed reference frame. The density of the PS pixels of the ERS results is very low in the northern part of the Nile Delta, which may be a result of the small number of SAR scenes available from ERS satellite missions. Therefore, the northern part of the Nile Delta seems to be decorrelated except the large cities such as Cairo, Tanta, Mahala, Mansoura, Damietta, and Port Said which show better correlation represented by the presence of PS pixels. On the other hand, the PS density for the southern part of the Nile Delta is high. The ERS results show that the Nile Delta seems to be stable, and the ground deformation is mainly concentrated in the previously mentioned large cities. The LOS velocity field for these cities is ranging from $-2.6\ mm/yr$ to $-10\ mm/yr$. The lowest deformation rate is estimated for Cairo and Tanta as $-2.3\ mm/yr$ and $-2.4\ mm/yr$, respectively. While, the highest deformation estimates are rated to Mansoura and Damietta as $-9.3\ mm/yr$ and $-10\ mm/yr$, respectively.

Figure 4.15 shows the standard deviation of the ERS LOS velocity field of the Nile Delta. The standard deviation is ranging from $0.2\ mm/yr$ to $1.8\ mm/yr$. The southern part of the Nile Delta is characterized by low standard deviation whereas the northern part is characterized by high standard deviation. It is clear that the high accuracy is connected to the areas of high PS density, such as the Western Desert and Eastern Desert as they mainly composed of hard rocks, and the low accuracy is linked to the areas of low PS density like the Nile Delta itself of high vegetation cover.

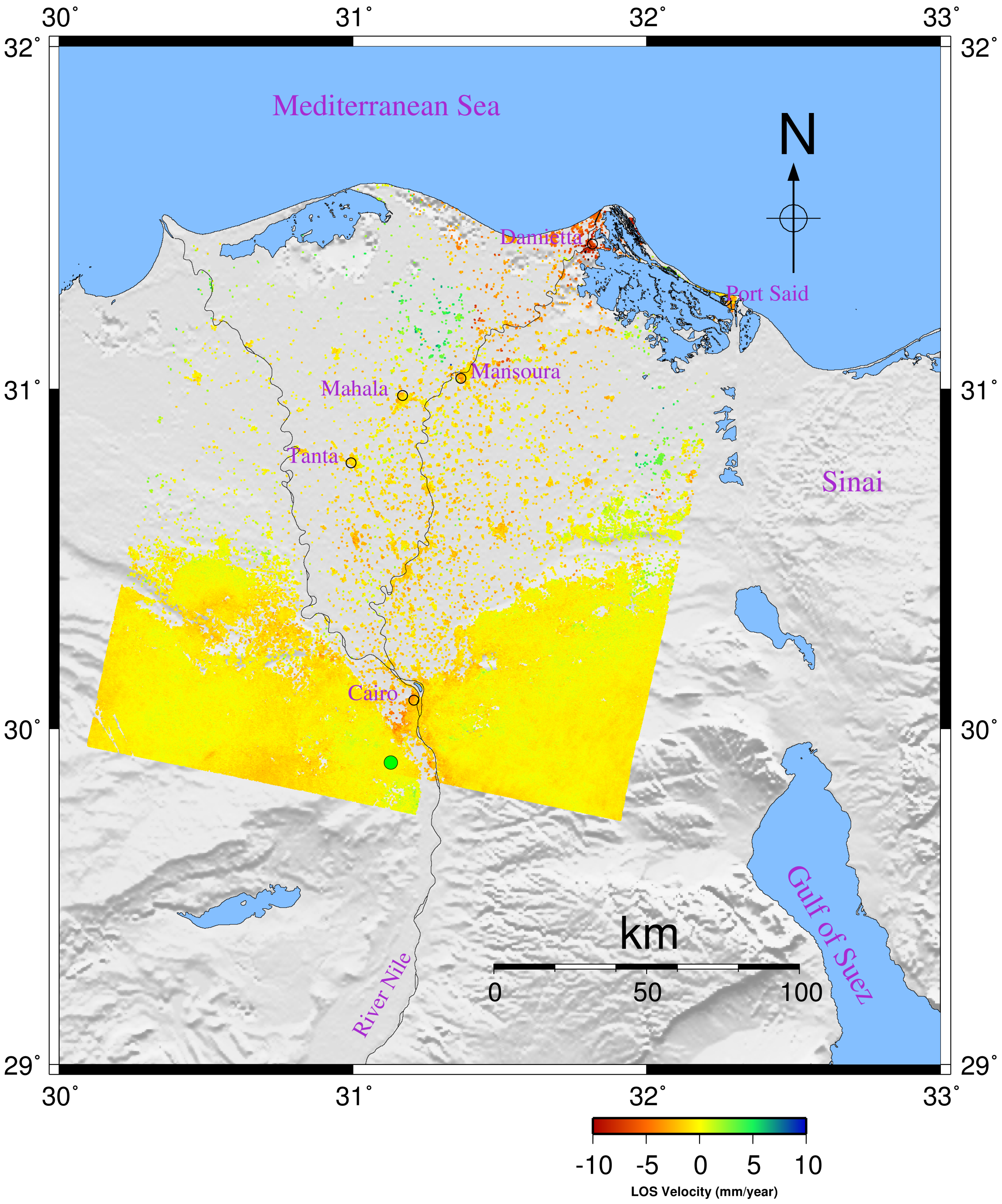

Figure 4.14: LOS velocities of ERS tracks 207 and 436 over the Nile Delta. Green circle represents the reference location. Hollow circle represents the selected PS from each city for the time series plot.

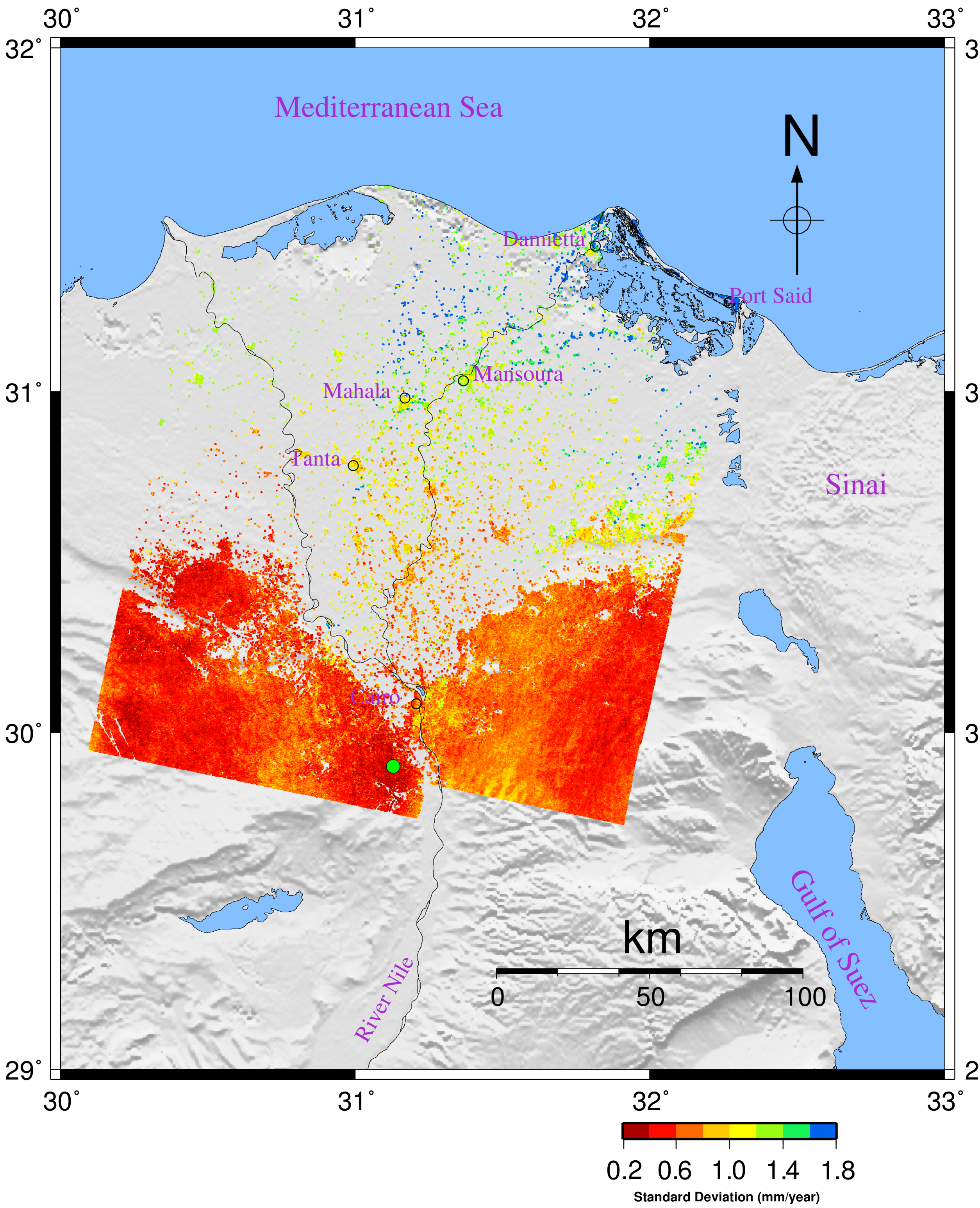

Figure 4.15: Standard deviation of the LOS velocities of ERS tracks 207 and 436 over the Nile Delta. Green circle represents the reference location.

4.2.1.1 Time Series

Due to the fact that the Nile Delta region is quite stable and the ground deformation is mainly concentrated in the large cities in the Nile Delta, hollow circles in Figure 4.14, a time series for selected PS pixels from these cities is constructed in order to estimate the rate of displacement for each city and the differences between the estimated rates from each track for the same PS. Figure 4.16 shows the time series of the selected PS from Cairo. The estimated rates are $-4 \pm 0.6\ mm/yr$ and $-2.3 \pm 0.6\ mm/yr$ from tracks 436 and 207, respectively. A smaller rate is estimated from the scenes of track 207 with respect to the rate estimated from the other track and the difference between the two estimates is about $1.7\ mm/yr$.

Figures 4.17, 4.18, and 4.19 present the time series of the selected PS pixels from Tanta, Mahala, and Mansoura, respectively. Tanta is covered only by one track, 207, and the estimated rate is $-3.5 \pm 1.0\ mm/yr$ as shown in Figure 4.17. The LOS velocity for Mahala that covered by both tracks 207 and 436 are $-2.4 \pm 1.2\ mm/yr$ and $-3.7 \pm 1.2\ mm/yr$, respectively. Whereas, the estimated LOS velocities from the ERS scenes of tracks 207 and 436 for Mansoura are $-4.4 \pm 1.6\ mm/yr$ and $-9.3 \pm 1.6\ mm/yr$, respectively. It is clear that the estimated rate from the ERS scenes of track 207 is low with respect to the one from the other track and the difference between two rates is quite high, about $5\ mm/yr$. The time series of the selected PS pixels from Damietta and Port Said cities, which are located along the Mediterranean coastline, are shown in Figures 4.20 and 4.21, respectively. These two cities are covered only by track 436. A rate of $-10 \pm 1.8\ mm/yr$ is estimated for Damietta and $-8.6 \pm 1.8\ mm/yr$ for Port Said. The displacement estimated from ERS scenes over time for these two cities is more scattered, with respect to the trend line than for the other cities.

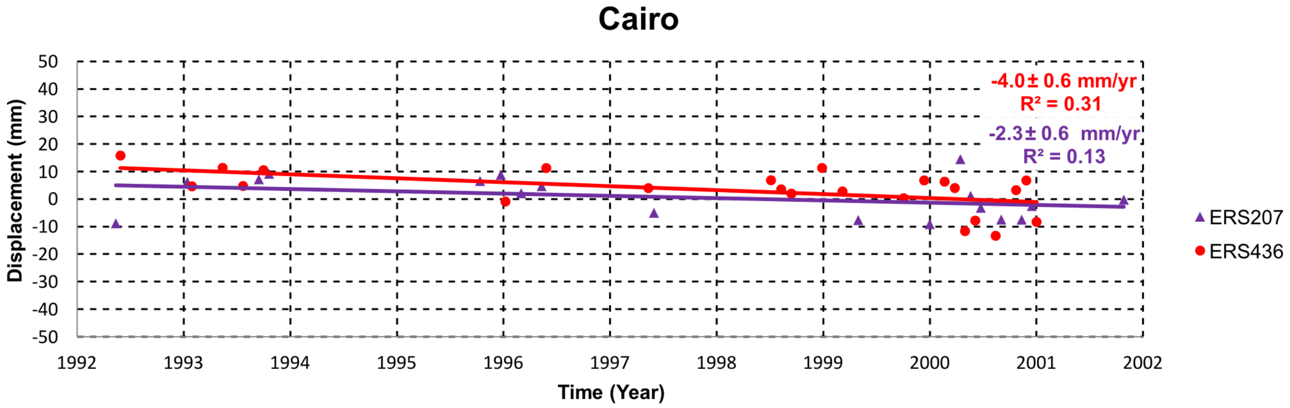

Figure 4.16: Displacement versus time for Cairo city from ERS descending scenes. Red dots represent the results from track 436 with the velocity trend (the red line). Whereas mauve triangles represent the track 207 results, the mauve line represents the velocity trend.

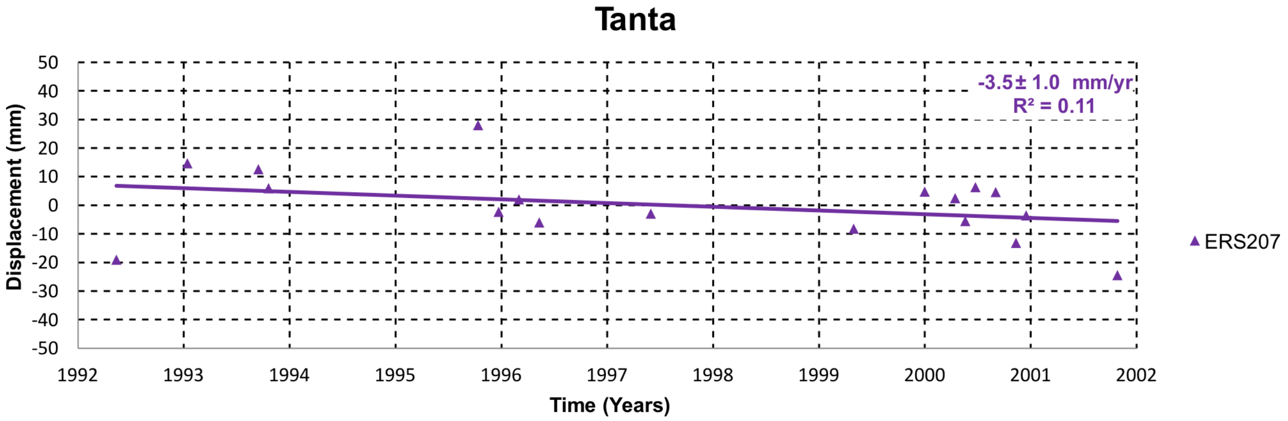

Figure 4.17: Displacement versus time for Tanta city from ERS descending scenes. Mauve triangles represent the results from track 207. The mauve line represents the trend.

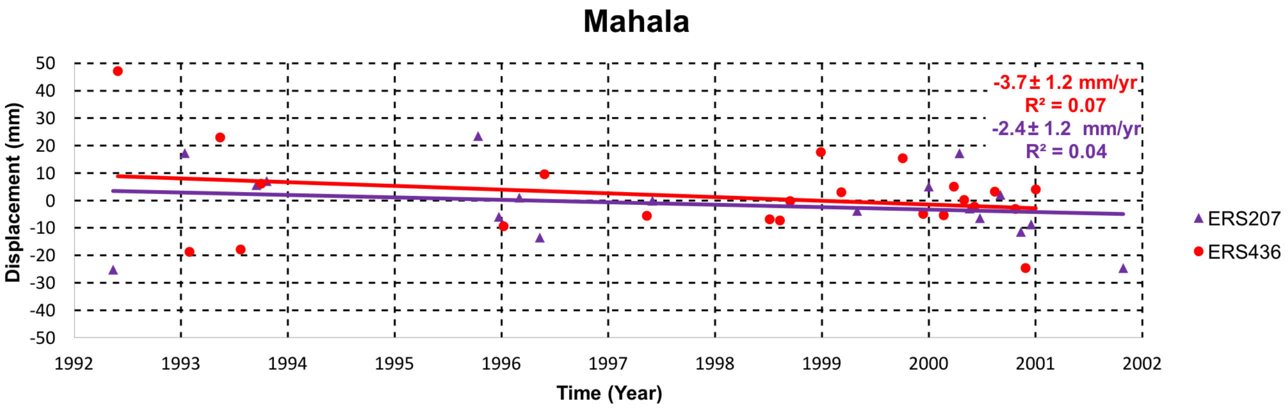

Figure 4.18: Displacement versus time for Mahala city from ERS descending scenes. Red dots represent the results from track 436 with the velocity trend (the red line). Whereas mauve triangles represent the track 207 results, the mauve line represents the velocity trend.

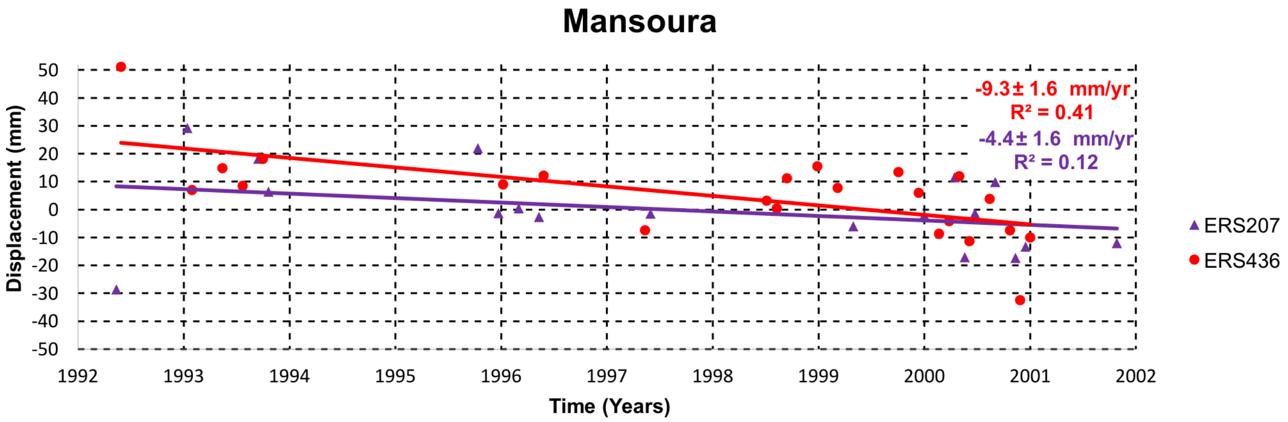

Figure 4.19: Displacement versus time for Mansoura city from ERS descending scenes. Red dots represent the results from track 436 with the velocity trend (the red line). Whereas mauve triangles represent the track 207 results, the mauve line represents the velocity trend.

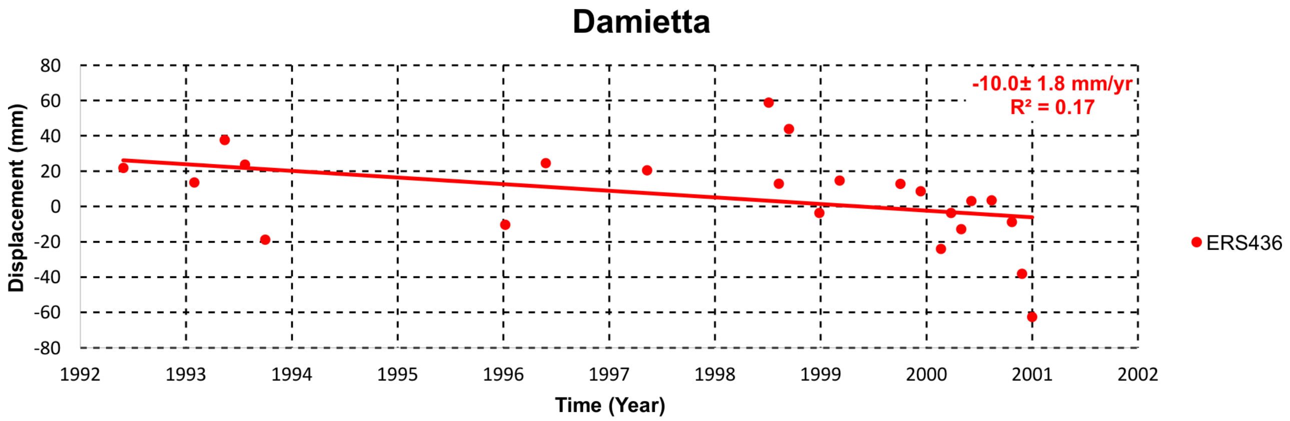

Figure 4.20: Displacement versus time for Damietta city from ERS descending scenes. Red dots represent the results from track 436. The red line represents the trend.

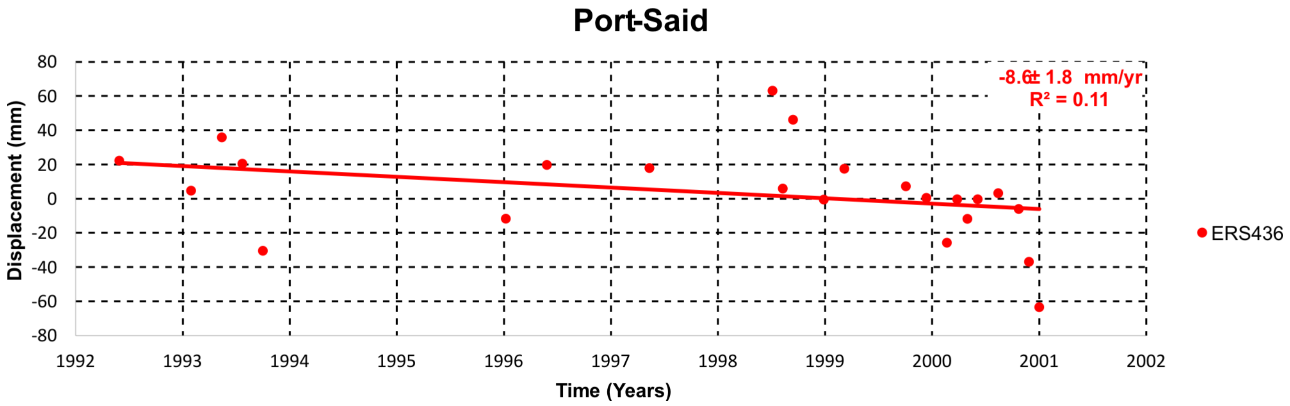

Figure 4.21: Displacement versus time for Port Said city from ERS descending scenes. Red dots represent the results from track 436. The red line represents the trend.

4.2.2 Envisat Results

Figure 4.22 shows the LOS velocity field deduced from the Envisat descending tracks 207 and 436 over the Nile Delta. The scene 20080715 is used as a master scene for track 207 whereas for track 436 the master scene is 20071129. Following the same procedure as for the ERS results, the velocity field of the same undeforming area located South of Cairo is subtracted from the entire velocity field, resulting a LOS velocity field in the Nubia fixed frame. During the time span of the Envisat SAR data (2003-2010), there were no earthquakes in the Nile Delta region of magnitude > 5.0 that could affect the estimated velocity field. As shown in Figure 4.22 the majority of the Nile Delta looks quite stable, represented by yellow dots, where the LOS velocity is around zero. However, there are some areas of negative LOS velocities that represented by orange-red dots, moving away from the satellite. From this figure, it is clear that the negative velocities are highly localized on the big cities in the Nile Delta (Cairo, Tanta, Mahala, Mansoura, Damietta, and Port Said). The LOS velocities for these cities are ranging from -3.6 to -9.3 mm/yr. The lowest velocity is estimated for Tanta and Port Said as -3.6 mm/yr and -4.4 mm/yr, respectively. While the highest estimated velocity is found in Damietta and Mansoura as -9.3 mm/yr. Therefore, in the next section, time series plots of selected PS pixels from these cities are presented.

With high matching with the ERS results, Figure 4.23 shows the standard deviation of the Envisat LOS velocity field of the Nile Delta. The standard deviation is ranging from 0.2 mm/yr to 1.6 mm/yr. The southern part of the Nile Delta is characterized by low standard deviation (high accuracy) whereas the northern part is characterized by high standard deviation (low accuracy). Although with the same manner of the standard deviation of the results from Envisat with the ones from the ERS, the Envisat standard deviations are less than the ERS ones of about $0.2-0.3$ mm/yr, especially for the urban areas. This could be regarded to the high number of SAR scenes available from Envisat compared to ERS.

4.2.2.1 Time Series

Again, similar to the ERS results, the time series for cities that characterized by negative LOS velocity field from the Envisat results is plotted. Figure 4.24 shows the time series for PS selected from Cairo from both tracks, 207 and 436. The estimated rates are -6.0 ± 0.4 mm/yr and -5.5 ± 0.4 mm/yr from tracks 436 and 207, respectively. The estimated rates from the two tracks are in good agreement where the difference in rates is 0.5 mm which is a small value. The good agreement between the two tracks is expected because the number of the processed scenes in each track are close to be the same. Whereas, 37 scenes and 36 scenes are processed from tracks 436 and 207, respectively.

Further North of Cairo, cities Tanta, Mahala, and Mansoura are suffering from negative LOS velocities. Figures 4.25, 4.26, and 4.27 show the time series of the selected PS pixels from Tanta, Mahala, and Mansoura, respectively. Tanta is covered only by track 207. Figure 4.25 shows that the estimated LOS velocity for Tanta is -3.6 ± 0.6 mm/yr. Mahala and Mansoura are covered by both tracks 436 and 207. The LOS velocities for Mahala are -5.3 ± 1.0 mm/yr and -3.4 ± 1.0 mm/yr resulted from tracks 436 and 207, respectively. The difference between the two estimates is about 2 mm/yr which is relatively high. On the other hand, The LOS rates for Mansoura are -9.3 ± 1.2 mm/yr and -8.7 ± 1.2 mm/yr from the processed scenes of tracks 436 and 207, respectively. 0.6 mm/yr is the difference between the two rates.

Along the Mediterranean coastline, Damietta and Port Said show negative LOS velocities. Both cities are covered only by track 436. Figure 4.28 shows the time series of the PS pixels selected from Damietta. The estimated velocity is -9.3 ± 1.6 mm/yr. It is clear that the results are more scattered along the trend line than the cities in the Nile Delta. The LOS velocity of Port Said is presented in Figure 4.29. The measured rate is -4.4 ± 1.6 mm/yr and a similar situation of scattering the results along the trend line like Damietta.

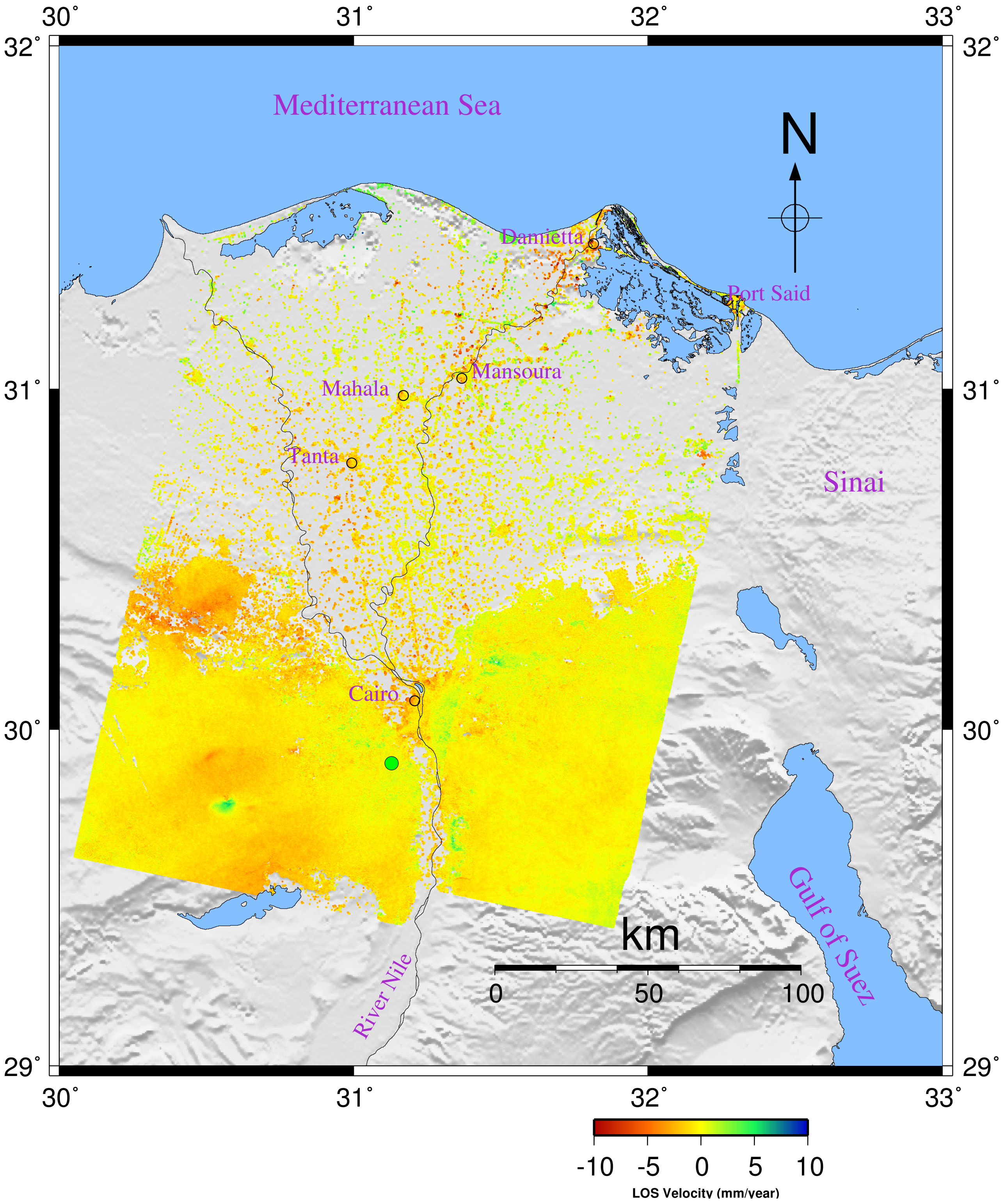

Figure 4.22: LOS velocities of Envisat tracks 207 and 436 over the Nile Delta. Green circle represents the reference location. Hollow circle represents the selected PS from each city for the time series plot.

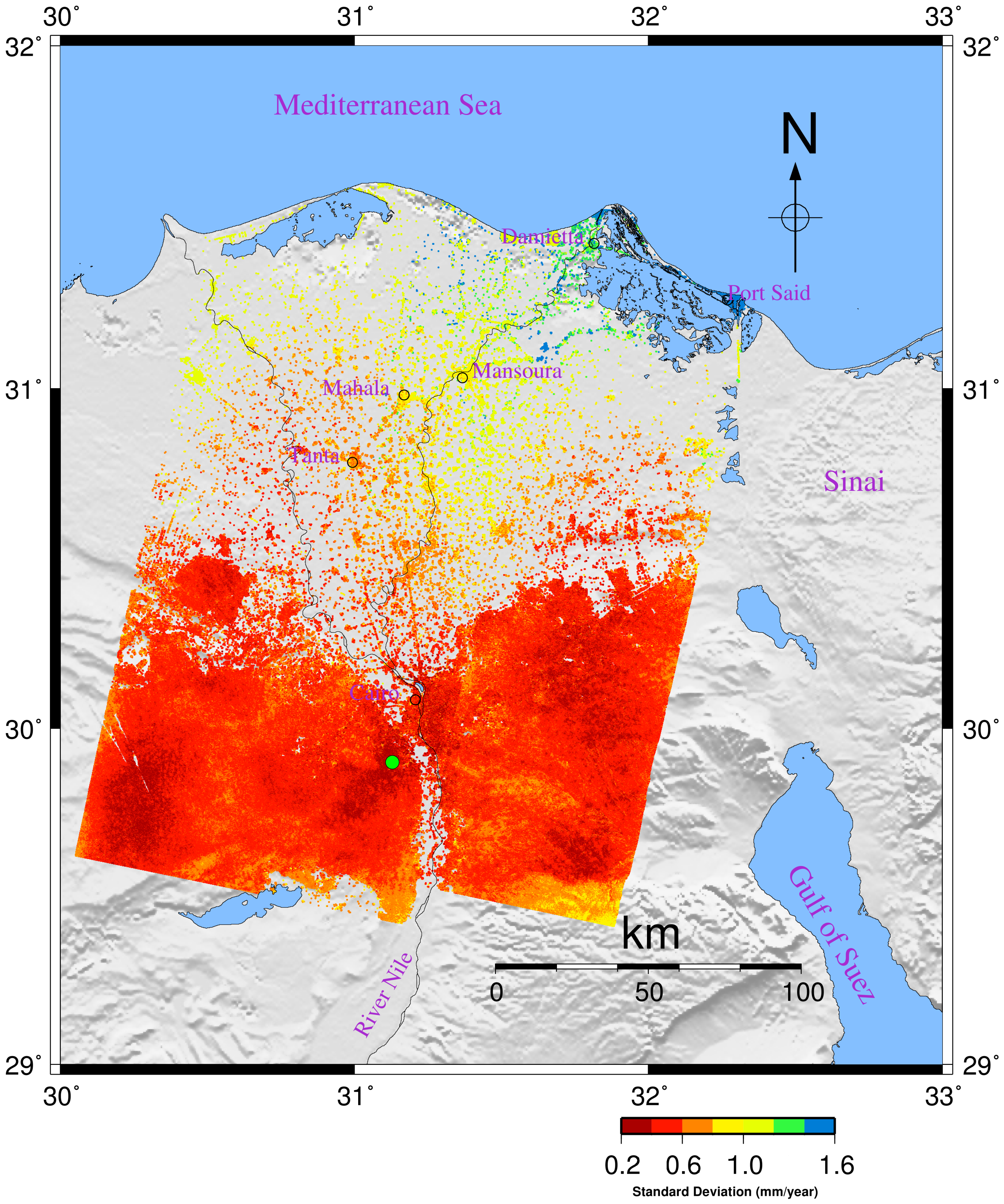

Figure 4.23: Standard deviation of the LOS velocities of Envisat tracks 207 and 436 over the Nile Delta. Green circle represents the reference location.

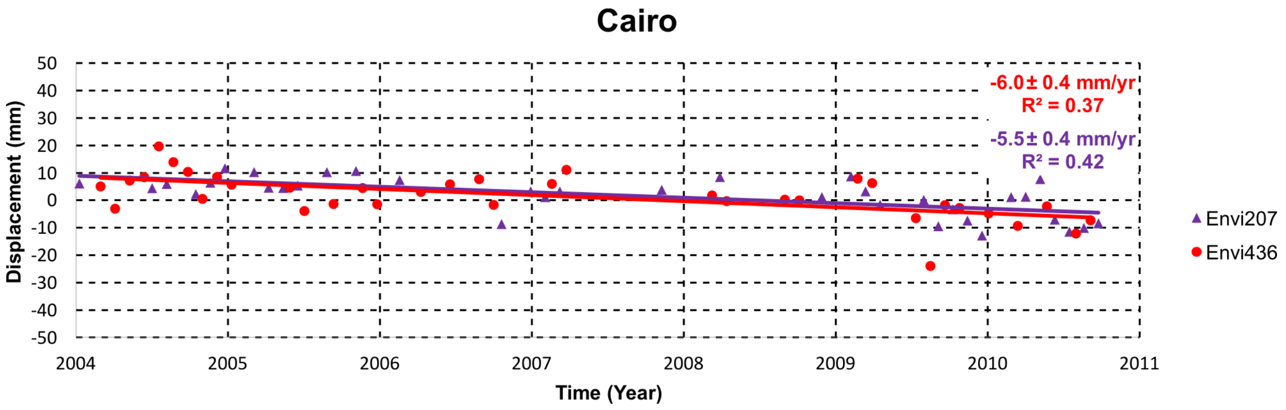

Figure 4.24: Displacement versus time for Cairo city from Envisat descending scenes. Red dots represent the results from track 436 with the velocity trend (the red line). Whereas mauve triangles represent the track 207 results, the mauve line represents the velocity trend.

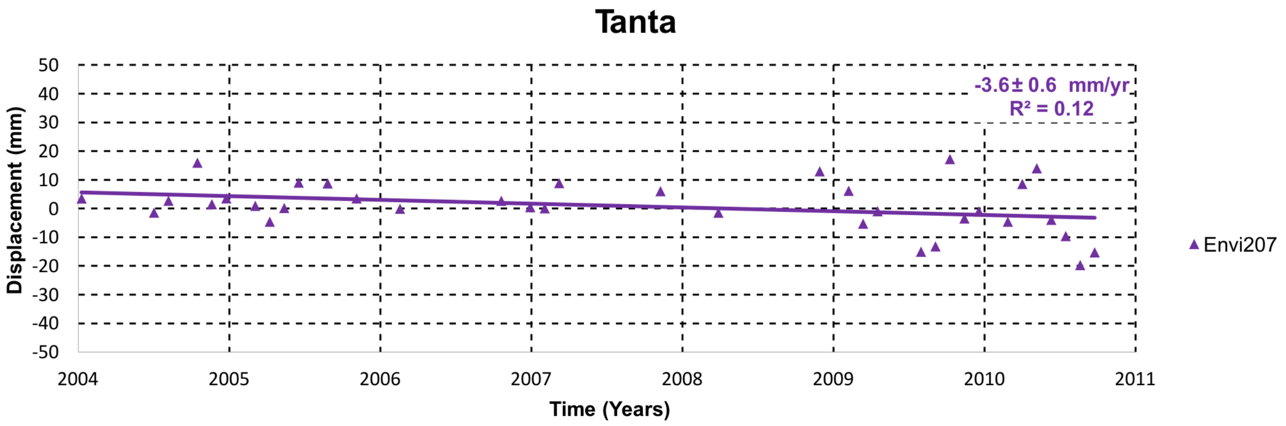

Figure 4.25: Displacement versus time for Tanta city from Envisat descending scenes. Mauve triangles represent the results from track 207. The mauve line represents the trend.

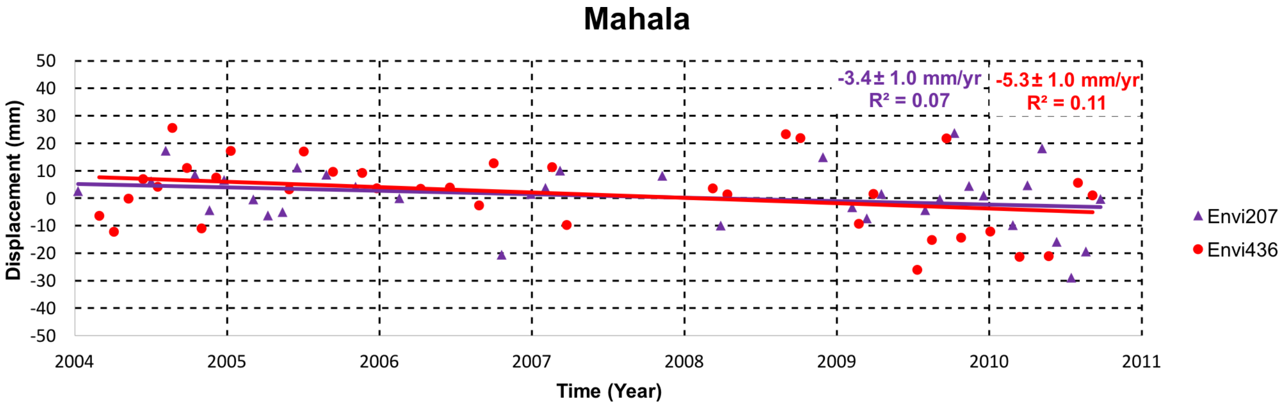

Figure 4.26: Displacement versus time for Mahala city from Envisat descending scenes.Red dots represent the results from track 436 with the velocity trend (the red line). Whereas mauve triangles represent the track 207 results, the mauve line represents the velocity trend.

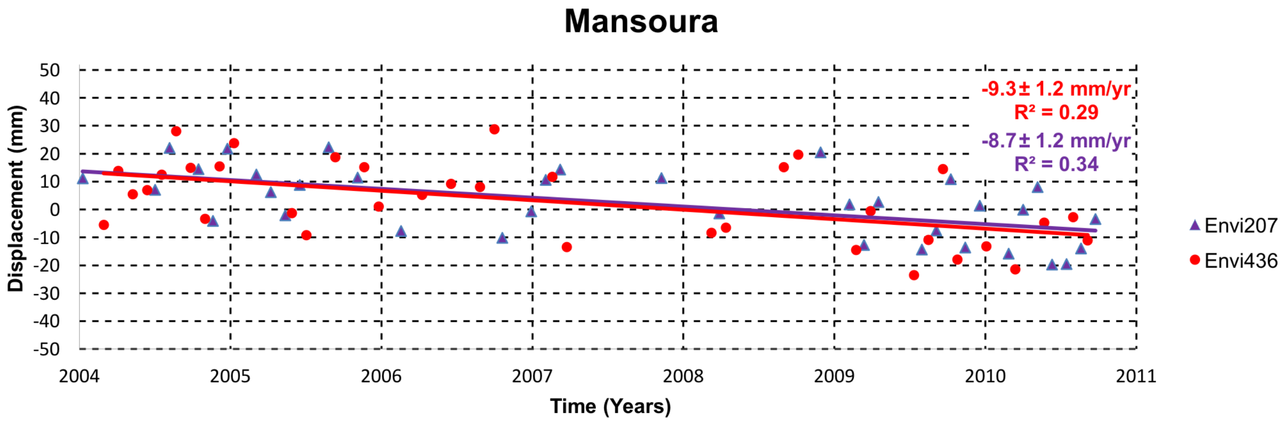

Figure 4.27: Displacement versus time for Mansoura city from Envisat descending scenes. Red dots represent the results from track 436 with the velocity trend (the red line). Whereas mauve triangles represent the track 207 results, the mauve line represents the velocity trend.

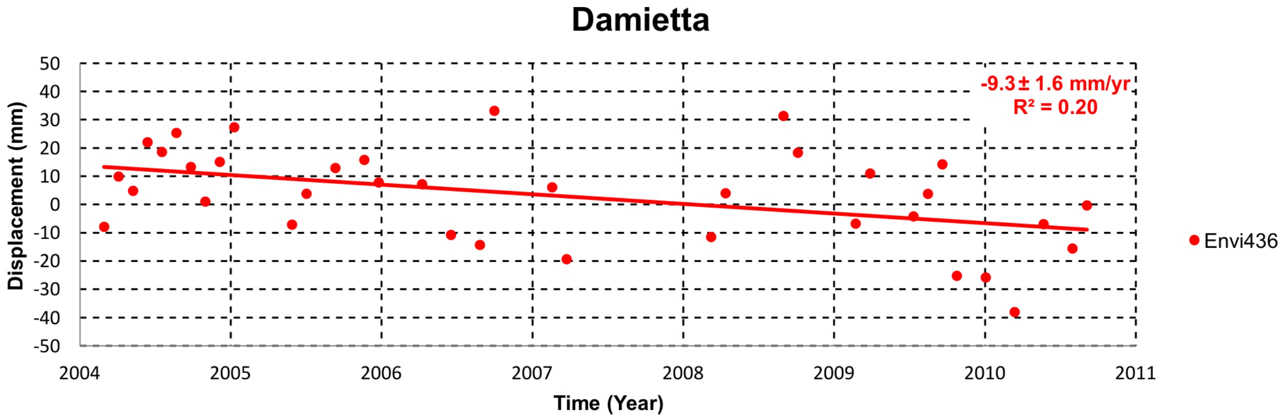

Figure 4.28: Displacement versus time for Damietta city from Envisat descending scenes. Red dots represent the results from track 436. The red line represents the trend.

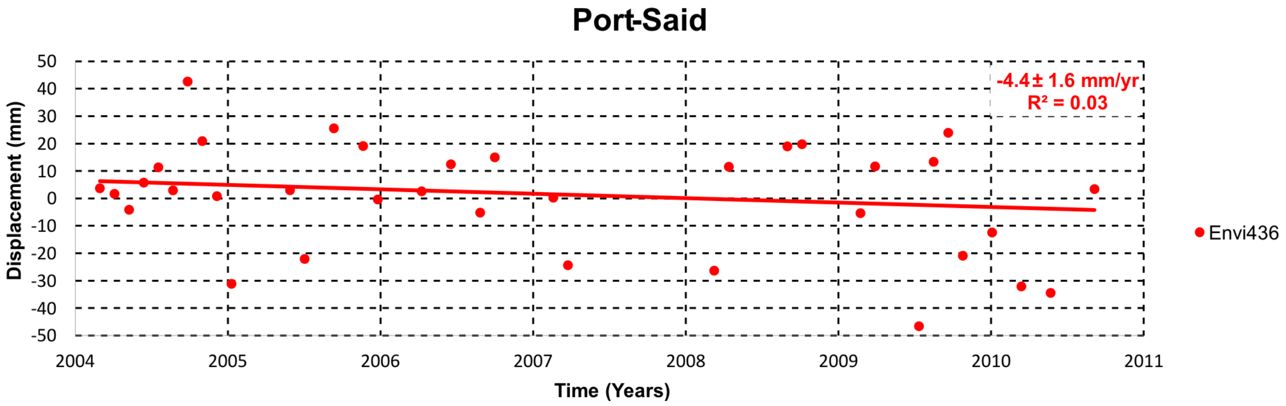

Figure 4.29: Displacement versus time for Port Said city from Envisat descending scenes. Red dots represent the results from track 436. The red line represents the trend.

The comparison between the achieved results from the ERS and Envisat SAR scenes, the possible causes for the variability of these results, and the interpretation of the achieved results in combination with the results from the available GPS stations in the Nile Delta will be presented in the discussion section.

4.3 Discussion

Egypt is not characterized by high seismic activity. Nevertheless, the tectonic setting and the crustal deformation of Egypt is affected by its location (northeastern corner of the Nubian plate). The available GPS stations covering the period 2006-2012 from Egypt in addition to 86 GPS permanent stations from the surrounding tectonic plates were used to constrain the crustal deformation of Egypt and the interaction between Nubian, Arabian, and Eurasian plates. Due to the fact that the accuracy of the achieved results for the Up component from campaign GPS stations is low, between $4-8\ mm/yr$, in addition to the coarse distribution of the permanent stations in the Nile Delta, InSAR technique was used to estimate the crustal deformation of the Nile Delta.

Very few attempts are made to derive the present day horizontal velocity field of the northeastern corner of Nubia, using GPS, and the interaction between Nubian, Sinai, Eurasian and Arabian plates due to the lack of GPS data in Egypt. Therefore, the presently available data from both permanent and non-permanent GPS stations in the northeastern corner of Nubia (Egypt), including Sinai and the DST fault, is used to better constrain the crustal deformation of Egypt and the interaction between the tectonic plates in the northeastern corner of Nubia. The GPS data processing was carried out using Bernese 5.2 (Dach et al., 2007). The velocity field was assessed using the CATS software with white noise plus power law noise stochastic model. Afterward, the velocities of stations well representing the plate interior were used to compute the absolute and relative Euler vectors for Nubian, Somalian, Eurasian, Arabian, and Sinai plates.

4.3.1 Nubia-Eurasia

Based on very few GPS data in northeastern Nubia, 7 stations in Egypt, (McClusky et al., 2000) and (Reilinger et al., 2006) provided a northward of northern Nubia of about 5 mm/yr with respect to Eurasia. Having new data in Nubia, a new Euler vector is estimated. A northward motion of northeastern Nubia of about $6.5 \pm 1\ mm/yr$ with respect to Eurasia is encountered, which is a much higher rate than the previously estimated rates by (McClusky et al., 2000) and (Reilinger et al., 2006) in addition to a similar anti-clockwise rotation which increased toward the Hellenic trench system. On the other hand, the GPS sites in Sinai Peninsula are moving to the north direction with a magnitude of about $8.2 \pm 0.8\ mm/yr$. This shows a differential motion between Sinai and the rest of Egypt of 1.7 mm/yr, which may support the suggestion of a Sinai micro-plate sandwiched between the Nubian and Arabian plates. A rate of $14.2 \pm 1.4\ mm/yr$ was determined for the sites in the north of the Arabian plate as shown in Figure 4.3. A comparison between the estimated Euler vectors from this study and the Euler vectors published by various other authors is presented in Figure 4.5. There are obviously significant differences between the GPS derived and the NUVEL-1A Euler vectors. Even among the GPS derived Euler poles, there are also significant differences which may be related to the different set of GPS sites used in each calculation.

4.3.2 Arabia-Sinai

All the previous attempts of estimating the slip rate of the DST faults suffered from the lack of GPS data on the Egyptian side. (Wdowinski et al., 2004); (Le Beon et al., 2008); (Sadeh et al., 2012) estimated a slip rate of the DST fault ranging from 3.7 mm/yr to 5 mm/yr. Using for the first time the unpublished GPS data on the Egyptian side, new Euler vectors for Arabia in the Sinai fixed frame are estimated. Figure 4.8 shows the horizontal velocity field in the Sinai fixed frame. The GPS sites in southern Arabia are moving to the northeast direction of about 15 mm/yr. Whereas, the GPS sites close to the DST fault are moving towards the northeast direction with magnitude of about 5.0 ± 1.4 mm/yr in good agreement with the slip rate estimated by (Le Beon et al., 2008) and (Sadeh et al., 2012) for the southern part of the DST. They are higher than the (Wdowinski et al., 2004) slip rate.

4.3.3 Sinai-Nubia

(Mahmoud et al., 2005), directly from GPS, suggested a separate Sinai micro-plate between Nubia and Arabia of 1.4 ± 0.8 mm/yr motion in the North direction and 0.4 ± 0.8 mm/yr in the East direction relative to Nubia. In order to better constrain the differential motion between Nubia and Sinai, the available Sinai GPS sites were used to estimate the Sinai-Nubia Euler pole vectors. Figure 4.7 shows that almost all the GPS sites in the western and southern part of Sinai Peninsula do not show any significant velocity with respect to Nubia at the 95% confidence level. On the other hand, the eastern and northeastern sites in Sinai show a systematic trend of horizontal velocity to north to northwest direction with respect to Nubia of about 1.7 ± 0.9 mm/yr. Due to the absence of surface faults and/or seismic activity and the lack of GPS observations north of the Gulf of Suez, it is difficult to define the western border of the proposed Sinai sub-plate accurately. More permanent GPS stations north the Gulf of Suez in addition to more GPS data from the local networks are required to improve the quality of the velocity results which may help to identify clearly the western border of this plate. With these results it might be reasonable to suggest that Sinai Peninsula is still connected to Nubia and the relative motion of the northeastern Sinai of 1.7 ± 0.9 mm/yr is probably due to the strike-slip movement along the DST fault which represents the boundary between the Nubian and the Arabian Plates (Saleh and Becker, 2015).

Figure 4.30 shows the estimated Euler pole from this study for Arabia-Sinai and Sinai-Nubia and the ones estimated by different authors ((Joffe and Garfunkel, 1987); (Wdowinski et al., 2004); (Reilinger et al., 2006); (Le Beon et al., 2008)).

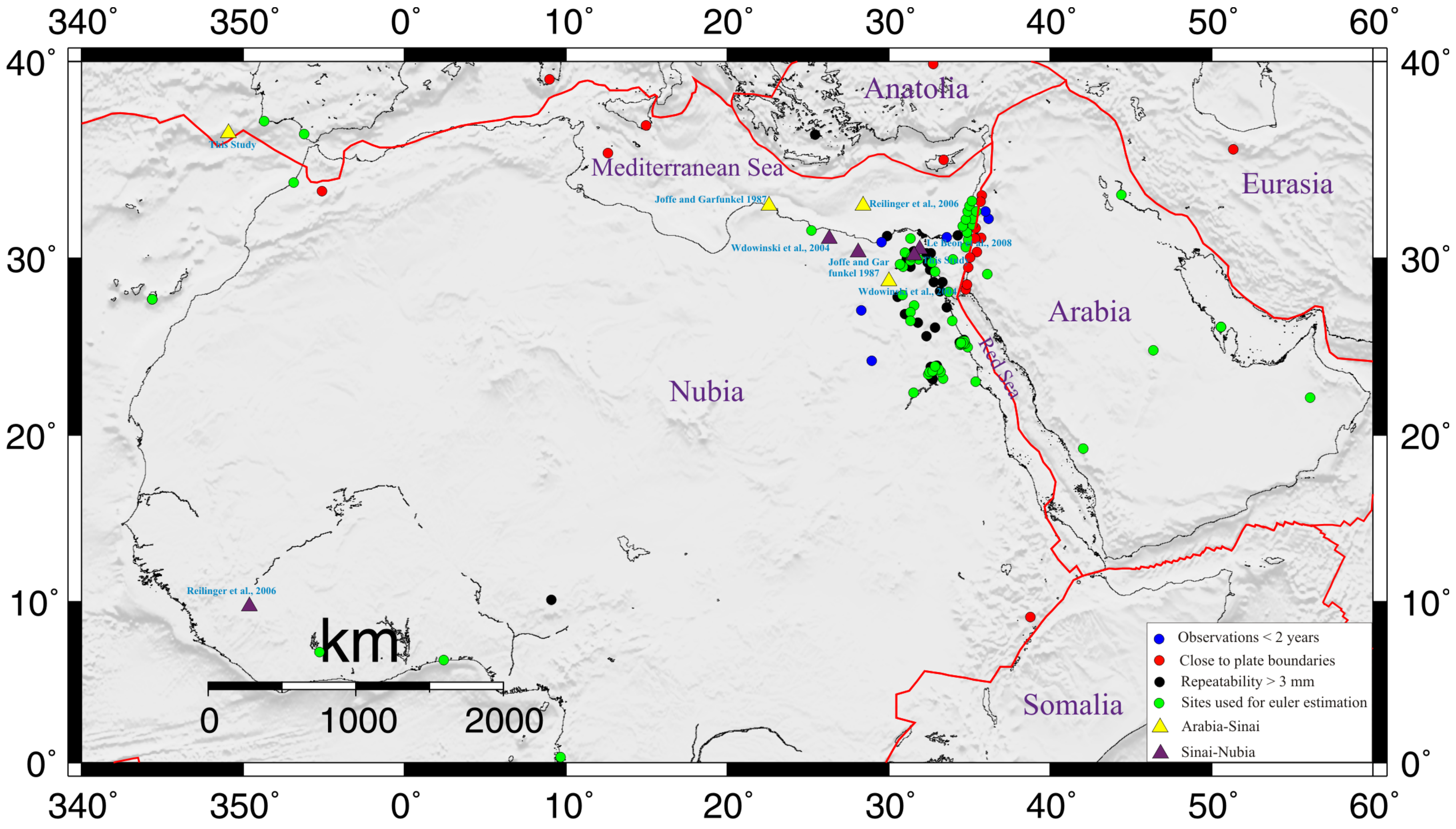

Figure 4.30: Comparison between the Euler poles estimated from this study for Arabia-Sinai and Sinai-Nubia with the ones estimated from different authors ((Joffe and Garfunkel, 1987); (Wdowinski et al., 2004); (Reilinger et al., 2006) and (Le Beon et al., 2008)) with plate boundaries(as in Figure 2.1).

4.3.4 DST Slip Rate and Locking Depth

Due to the importance of the DST fault, as it represents the tectonic plate boundary between the Nubian and Arabian plates, many attempts were made to constrain the slip rate of the DST fault directly from GPS ((Wdowinski et al., 2004); (Le Beon et al., 2008); (Sadeh et al., 2012)) and also from geological studies ((Klinger et al., 2000); (Meghraoui et al., 2003)). The estimates of the DST fault slip rate are $3-7\ mm/yr$. The slip rates based on GPS observations are always smaller than the others estimated from geological data. From the velocity field in Sinai fixed frame, a rough estimate for the slip rate could be about $5\ mm/yr$. Therefore, using the velocity field of 28 GPS sites in Sinai and northern Arabia, the fault parallel analysis is applied to estimate the slip rate and the locking depth of the DST fault. The estimated slip rate for the whole DST fault is $6\ mm/yr$ with a locking depth of $16\ km$ as seen in Figure 4.9a. This slip rate is higher than the previous estimates based on GPS observations by (Wdowinski et al., 2004) of $3.7\ mm/yr$; (Le Beon et al., 2008) $of 4.9\ mm/yr$; (Sadeh et al., 2012) of $5\ mm/yr$ and close to the estimated rate by (Klinger et al., 2000) of $5-6\ mm/yr$.

Due to the fact that the DST fault is consisting of more than one segment, it is more reasonable to apply the fault parallel velocity analysis for each segment separately. The estimated slip rate and locking depth for the northern segment of the DST fault are $5\ mm/yr$ and $12\ km$, respectively, while for the southern segment the slip rate and locking depth are $7\ mm/yr$ and $18\ km$, respectively, as shown in Figure 4.9 (b and c). There are some stations not fitting very well with the dislocation model, blue triangles in Figure 4.31. It may be regarded to that there is an additional segment that is not accounted for in this calculation. Due to the lack of GPS sites in this area, it is hard to apply the dislocation fault parallel analysis for this part of the DST fault.

These estimates are much higher than the previous estimates published by (Sadeh et al., 2012) of $5\ mm/yr$ for the southern segment which decreases to $3.8\ mm/yr$ in the northern segment. The estimated rates by (Sadeh et al., 2012) are affected by the absence of GPS sites in the Egyptian side and also east the Gulf of Aqaba. In spite of having two stations covering the Egyptian side and two other stations east the Gulf of Aqaba, more GPS data in the Egyptian side and northern Arabia are required to estimate the slip rate and the locking depth of the DST fault with better accuracy.

4.3.5 Strain Accumulation

To calculate the strain rates in the northeastern corner of Africa, the GPS velocities in the East and North components are interpolated separately, according to the approach of (Hackl et al., 2009). The strain rate map of the northeastern corner of Africa indicates high strain rates related to the DST fault, where the deformation is strongly localized close to the DST fault. The localization of the shear strain could be attributed to the strain accumulation along the DST fault. As explained in the previous section the strike-slip movement along the DST fault is estimated to $6\ mm/yr$, which resulted in the presence of high shear strain along the DST fault. On the other hand, the Gulf of Suez and southern Sinai are showing low to moderate strain rates while the rest of Egypt looks like a rigid plate, as presented in Figure 4.10. Although the strain rate can add valuable information for the seismic hazard assessment by the identification of regions of deformation, other studies, like modeling of the full lithospheric behavior, the seismic history and more geological studies are needed in order to fully constrain the amount of the accumulated elastic energy.

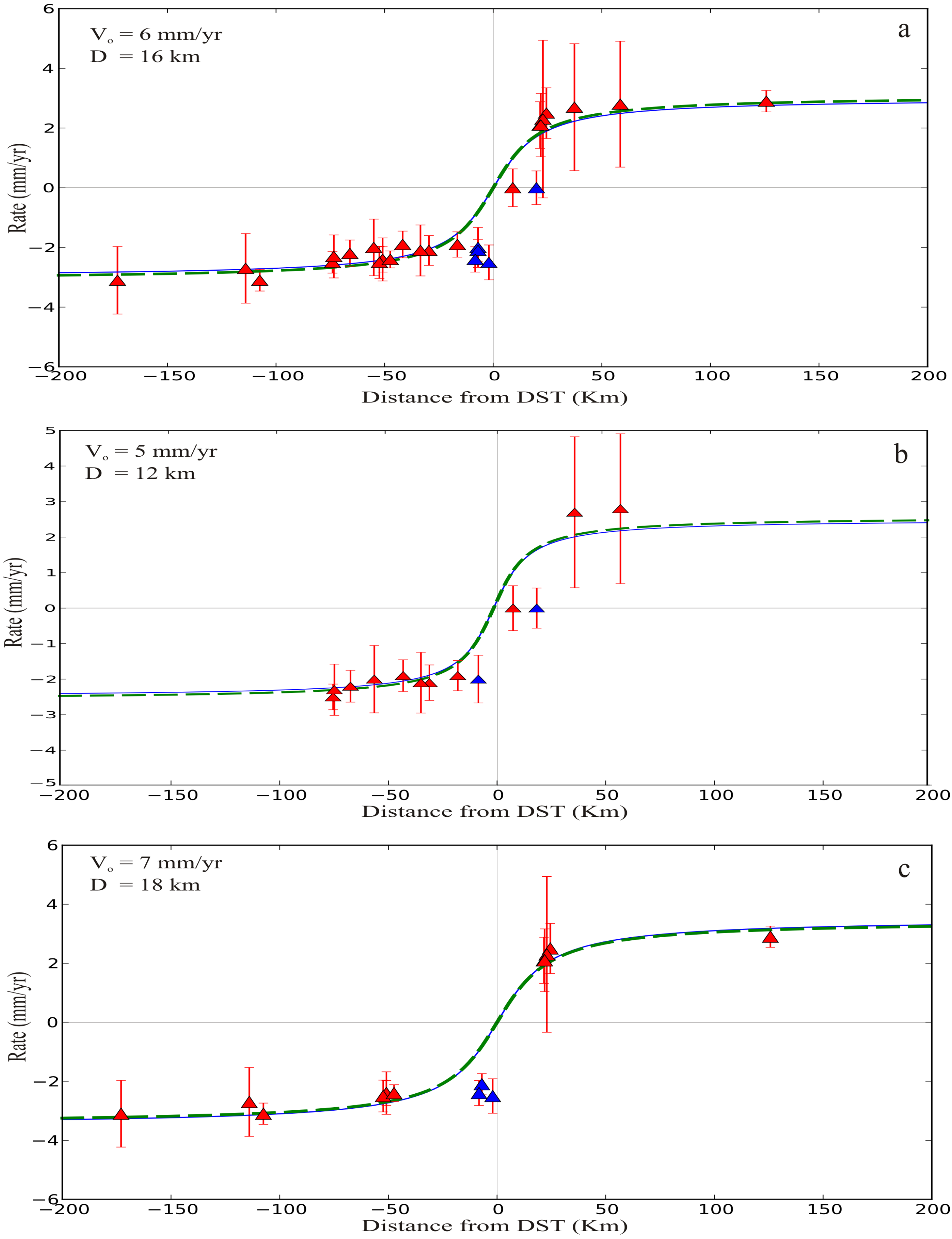

Figure 4.31: Fault parallel velocities for the DST fault: (a) for the whole DST fault , (b) the northern segment of DST fault, and (c) the southern segment of the DST fault. Green dashed curve represents the observed fault parallel velocities and the blue curve shows the best fit model. Blue triangles show the stations that did not fit the dislocation model.

Sinai is still connected to the Nubian plate, and there is no need to introduce a new micro-plate between the Nubian and Arabian plates. This finding based on the following results:

1. Almost all Sinai GPS sites did not show any significant horizontal velocities with respect to the Nubian plate, except the sites in the northeastern part of Sinai which show a systematic trend of 1.7 mm/yr, which is interpreted as an effect due to the left-lateral strike-slip movement along the DST fault,
2. the strain results did not show any significant strain accumulation north of the Gulf of Suez and its northern part. Only low shear strain is estimated for the southern part of the Gulf of Suez and Sinai peninsula,
3. the absence of surface faults north of the Gulf of Suez as seen in Figure 2.4, and
4. the absence of seismic activity north of the Gulf of Suez, as presented in Figure 4.32.

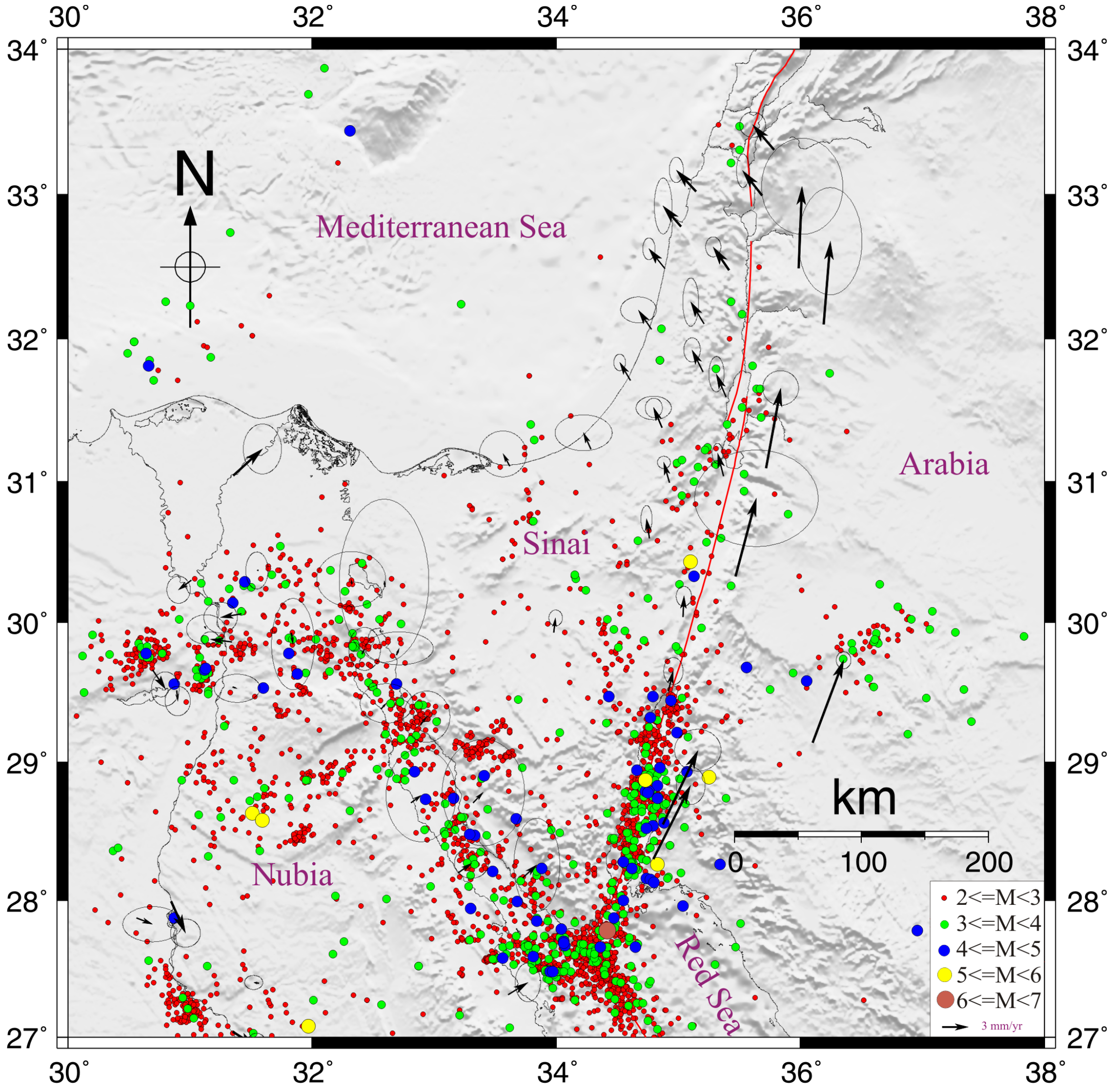

Figure 4.32: GPS horizontal velocity field of Sinai in Nubia-fixed frame with seismic activity recorded from ENSN during 1997-2012. Red lines represent the surface faults (as in Figure 2.4)

4.3.7 Nile Delta Subsidence

The Nile Delta is located in northern Egypt and it is formed in V shape by the sedimentation of silt and clay, that carried by the River during thousands of years. The Nile Delta is extended along the Mediterranean coastline from Alexandria in the West to Port Said in the East covering 240 km, and 160 km in the North to South direction (Figure 3.13). It is a very high populated area of more than 1000 persons/km^2 and produces about 60% of the Egyptian food. Due to the human activities such as damming and irrigation that resulted in the absence of the sediment supply, the Nile Delta is suffering from high rates of land subsidence and coastal erosion((Stanley and Warne, 1994) and (Stanley, 1996)). The Nile Delta suffered from subsidence with different rates; (Stanley, 1990), based on radiocarbon-age-dating for cores collected across the northern part of the Delta, observed a subsidence rate of $2.5-5$ mm/yr which increased from the western side of the Delta to the eastern side. On the other hand, the phenomenon of global warming is considered to be one of the most important challenges facing the Earth on the recent years, because of its negative impacts such as increasing the water levels in most of the world's oceans and seas including the Mediterranean, which may have a serious impact on the Nile delta. Globally, there is a general trend of sea level rise. Based on the satellite altimetry observations, the Mediterranean Sea is rising of about $0.8-2.0$ mm/yr((Fenoglio-Marc et al., 2012); (Fenoglio-Marc et al., 2013)). With longer period of satellite altimetry data (Fenoglio-Marc, 2015) estimated a higher rate of the sea level rise for the Egyptian coastline of the Mediterranean Sea of about 3.2 ± 0.6 mm/yr. Due to the strategic and economic importance of the Nile Delta, an attempt has been made here to estimate the rate of its subsidence. As mentioned in section 4.2, all the available ERS and Envisat SAR data from descending tracks 207 and 436 were used for this purpose. Figures 4.14 and 4.22 show the LOS velocity field of the Nile Delta from both ERS and Envisat satellite missions, respectively. The rate maps show that the number of PS density from the Envisat data are much higher than the PS density from the ERS scenes. The reason, besides other reasons, is the difference in the number of SAR scenes used for each PS processing. Compared to the available Envisat scenes, 36 from track 207 and 37 from track 436, the number of ERS scenes is little, 20 scenes from track 207 and 24 scenes from track 436.

The LOS $[d_{LOS}]$ velocity is the projection of the velocities in North, East, and Up components which can be expressed as

$$[d_{LOS}] = \begin{bmatrix} d_u \\ d_e \\ d_n \end{bmatrix} \begin{bmatrix} cos\theta & -sin\theta cos\phi & sin\theta sin\phi \end{bmatrix} \tag{4.2}$$

where d_u, d_e, and d_n are the displacements in Up, East, and North components, respectively. θ is the incidence angle and ϕ is the azimuth of the heading vector. InSAR is sensitive to surface displacement in the radar line of sight (LOS); due to the viewing geometry of all the current SAR satellites, this sensitivity is not the same for all directions. The displacement in the Up component can be detected with much better accuracy than the displacement of the horizontal component. On the other hand, the displacement of the the North component can not be detected accurately due to the satellite orbit geometry of near-polar orbit, such as ERS and Envisat missions. Many attempts were made to resolve the 3D displacements using interferograms with different viewing geometries (Wright et al., 2004).

The velocity of the Up component can be extracted from the LOS velocity in case of combining with results from different techniques such as GPS and/or precise leveling which are unfortunately not available in this work. Based on the fact that the Nile Delta is fairly stable and did not suffer from differential horizontal deformation, the LOS velocity will be considered as the velocity of the Up component. This assumption is not completely accurate, and the LOS velocity could be contaminated by a small amount of horizontal signal ($1-2$ mm/yr). The very few permanent GPS stations located in the Nile Delta shown in Figure 4.33 will be used to better estimate an appropriate rate of subsidence. It is clear that there is a general trend of subsidence, but it varies from one station to another. Along the Mediterranean Sea 2.9 ± 0.9 mm/yr rate of subsidence is estimated at station ALEX located in Alexandria. West of Alexandria, station BORG shows a small rate of subsidence of 1.1 ± 1.0 mm/yr. Further to the East at Mansoura city, the highest rate of subsidence is recorded at station MNSO of 14.2 ± 1.7 mm/yr. South of the Nile Delta, the rate of subsidence recorded from stations PHLW, KATA, and MSLT are 0.1 ± 0.5 mm/yr, 7.6 ± 2.4 mm/yr, and 1.7 ± 2.0 mm/yr. Due to the short period of GPS observations for some stations, such as MNSO and KATA which have data of about two years, the estimated subsidence rates from these stations could be not reliable.

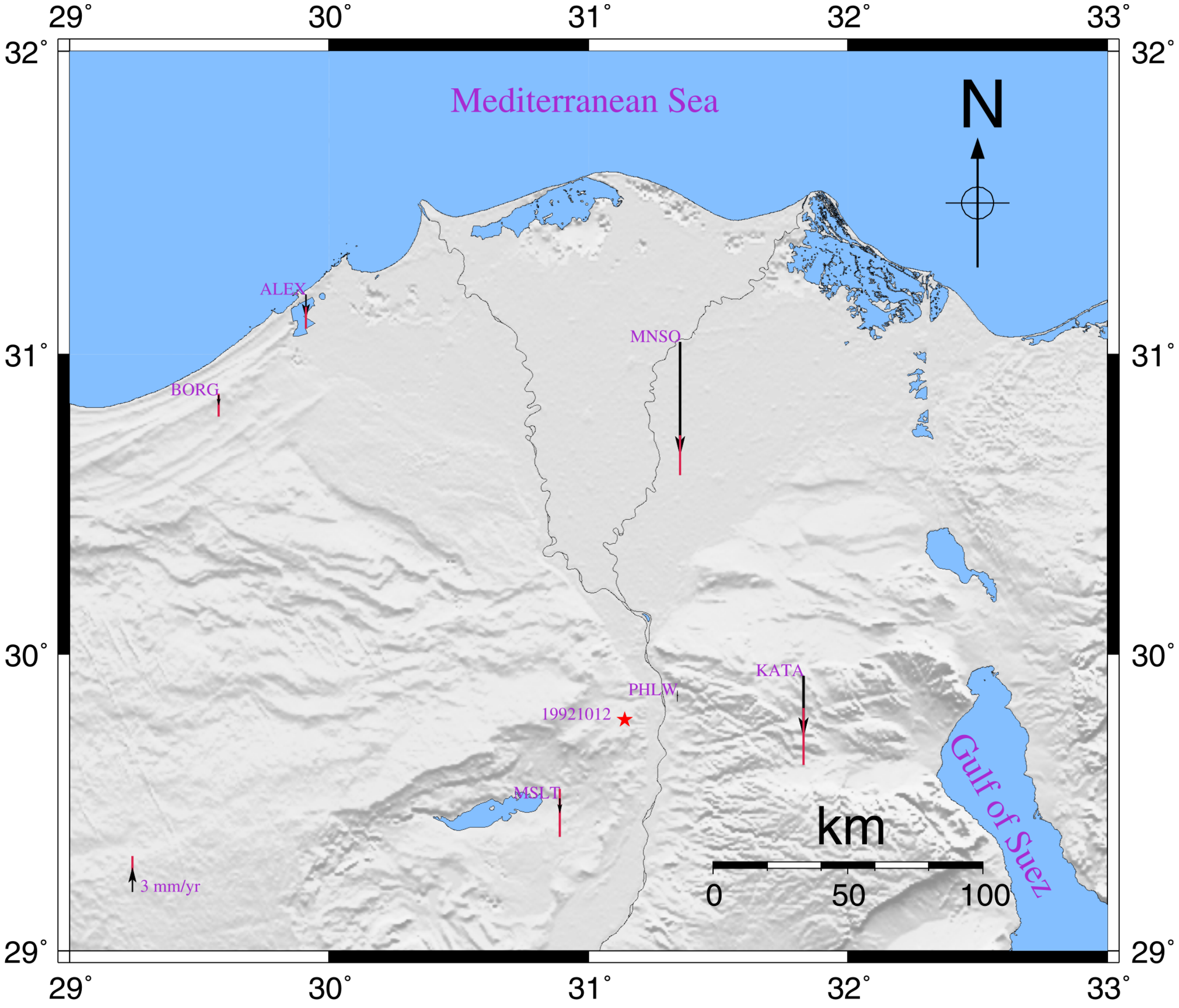

Figure 4.33: GPS vertical velocity field for the Nile Delta. Red star represents the Cairo earthquake on October 12, 1992 of magnitude 5.9.

The InSAR velocity maps show that almost all the Nile Delta did not show any ground deformation except for the big cities that are characterized by high subsidence rates, as shown in Figures 4.14 and 4.22. The cities of high recorded subsidence rates, from South to North, are Cairo, Tanta, Mahala, Mansoura, Damietta, and Port Said. Therefore, time series plots for selected PS pixels from these cities are made. The two tracks do not cover all the cities of high subsidence rates. Out of these six active cities, there are three cities covered by both tracks and they are used to estimate the consistency of the achieved results by checking the differences between the rates estimated for the same city from both tracks in each satellite mission. It is clear that the differences between the results from Envisat scenes of the two tracks are reasonable. The differences in rates are 0.5 mm/yr and 0.6 mm/yr for Cairo and Mansoura, respectively. Whereas the highest difference is 2.5 mm/yr recorded for Mahala. It is expected to have consistent results from both tracks of Envisat because the processed amount of data from both track is almost the same. On the other hand, the ERS results show much higher differences between the results of the two tracks. Difference of 1.7 mm/yr is found for Cairo, 1.3 mm/yr is presented for Mahala, and for Mansoura a difference of 4.9 mm/yr is recorded, which is a very high value.

It is expected to have differences between the estimated velocity for the same area from the two overlapped tracks due to the satellite geometry. The InSAR side-looking sensor configuration defines an incidence angle range (θ) which determines the angle of the InSAR beam with respect to the nadir. The incidence angle for ERS satellite mission is $\simeq 23°$ and changes from the near-range to the far-range across the swath. Therefore, for any point that is covered by two tracks, the LOS velocity for such a point will be slightly different due to the difference in the incidence angel of each track at the time of observation. The effect of viewing the same point with different incidence angles could contribute a part to the different rates estimated for the same city from the tracks 207 and 436 over the Nile Delta. Figure 3.34 shows the sensitivity of the SAR satellite for the ground deformation.

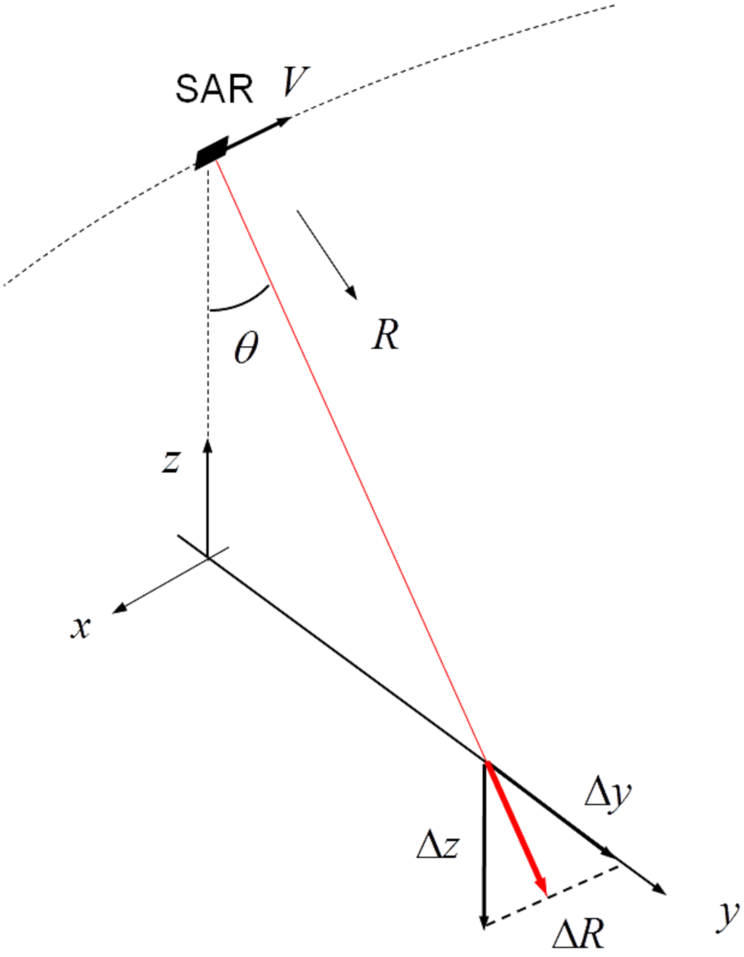

Figure 4.34: Sensitivity of SAR satellite for the ground motion (Bamler and Hartl, 1998).

$$\triangle R = \triangle y sin\theta - \triangle z cos\theta \qquad (4.3)$$

Focusing on Cairo city, figures 4.35 and 4.36 show the Cairo LOS velocity field from ERS and Envisat observations, respectively. The density of PS pixels is much higher in the Envisat than in the ERS results. It could be related to the amount of SAR data which is higher from Envisat than from ERS and/or large vegetated areas that altered to urban areas (a kind of desertification). Also, more features are visible in the Envisat than the ERS, such as bridges along the River Nile. The highest ground subsidence is localized along the Nile Valley close to the River Nile, where high population concentrated. The subsidence rate of Cairo is ranging from -5 to -8 mm/yr. The subsidence rate of Cairo downtown is -5 to -6 mm/yr while the areas at the border of Cairo are characterized by high subsidence rate of about -7 to -8 mm/yr that may be attributed to the excessive underground water withdraw to cover the needs of the people living in those areas. East of Cairo, which is mainly desert, looks relatively more stable than Cairo itself. On the other hand, the PS density in the West and Northwest of Cairo is very low because it is vegetated area.

The estimated subsidence rates, especially these deduced from Envisat scenes, from this study for Cairo and Mansoura cities of about $5.5-6.0$ mm/yr and $9.3-8.7$ mm/yr, respectively, are quite similar to the estimated rates by (Aly, 2006) of about 5 mm/yr and 9 mm/yr, respectively. On the other hand, the Mahala's subsidence rate of $3.4-5.9$ mm/yr is much lower than the estimated rate from (Aly, 2006) of 7 mm/yr. (Becker and Sultan, 2009) introduced a subsidence rate of $4-8$ mm/yr for the northern end of Damietta branch which is much smaller than the rate calculated from this work of $9.0-10.0$ mm/yr. The good agreement between my results and the ones from (Aly, 2006) could be attributed to that the amount of the processed in both studied is almost the same. (Aly, 2006) used 34 SAR scenes in his study which is close to the amount of SAR scenes used in this work, from Envisat, of 36-37 SAR scenes.

The first ERS1 scenes used in this work from tracks 207 and 436 were acquired on May 16, 1992 and June 1, 1992, respectively, which are about five months before the Cairo earthquake occurred on October 12, 1992. The location of this earthquake is presented in Figure 4.33. The 1992 earthquake had no recorded foreshock. The absence of seismic activity before the Cairo earthquake manifest a period of stress accumulation before this earthquake (El-Sayed et al., 1998). The result of the 1992 ERS1 scenes may be affected by the strain accumulation (Pre-seismic deformation) and as a consequence affects the estimated trend of subsidence. The effect of the pre-seismic might have not affected the whole Nile Delta, but it had a great effect on the area close to the earthquake epicenter. For that, the rate of subsidence estimated for Cairo deduced from the ERS data may do not reflect the real rate of subsidence and it may be corrupted by the pre-seismic deformation. To remove the effect of the pre-seismic deformation from the estimated trend, the time series plot is recreated without the result of the first scene in both ERS tracks. Figure 4.37 shows the time series plot for Cairo without the result of the first scene in both ERS tracks. The estimated rates for Cairo from tracks 207 and 436 are 3.8 mm/yr and 3.5 mm/yr, respectively. A small difference of about 0.3 mm/yr between the results of two tracks is found. Table 4.4 shows a comparison between the achieved InSAR results from both satellite missions.

The results of the ERS scenes collected from track 207 are small with respect to the results from the other ERS track or even from the Envisat scenes. Beside other effects like old technologies of ERS missions with respect to Envisat, the number of scenes affects the estimated rates. Even with 20 scenes in track 207, it is difficult to estimate a reliable subsidence rate for such a highly vegetated area like the Nile Delta. The situation is a bit better for track 436 with 24 scenes. The results from ERS scenes are smaller than the rates estimated from the Envisat scenes by about 2 mm/yr as shown in Table 4.3, especially for the big cities like Cairo and Mahala.

The localization of the ground deformation in the Nile Delta, which is represented here as a subsidence, at the big cities implies that the detected signals are not due to tectonic activity but are mainly due to human effect, such as underground water pumping. The difference in subsidence rates estimated from the ERS and Envisat, 2 mm/yr, could be related to the increase of the rate of underground water pumping to cover the needs of the rapidly growing population in the Nile Delta. Figure 4.38 shows the growing of Egypt's population in the last three decades. In the last thirty years, the population is increased by about 30 million inhabitants, a rate of 1.3 million inhabitants per year (World-Bank, 2015). Unfortunately, the records of the pumping of the underground water from the Nile Delta are not available for this work, which makes this interpretation hard to verify. In addition, the terrestrial measurements of the land deformation collected from the Nile Delta are very limited as shown in 4.33.

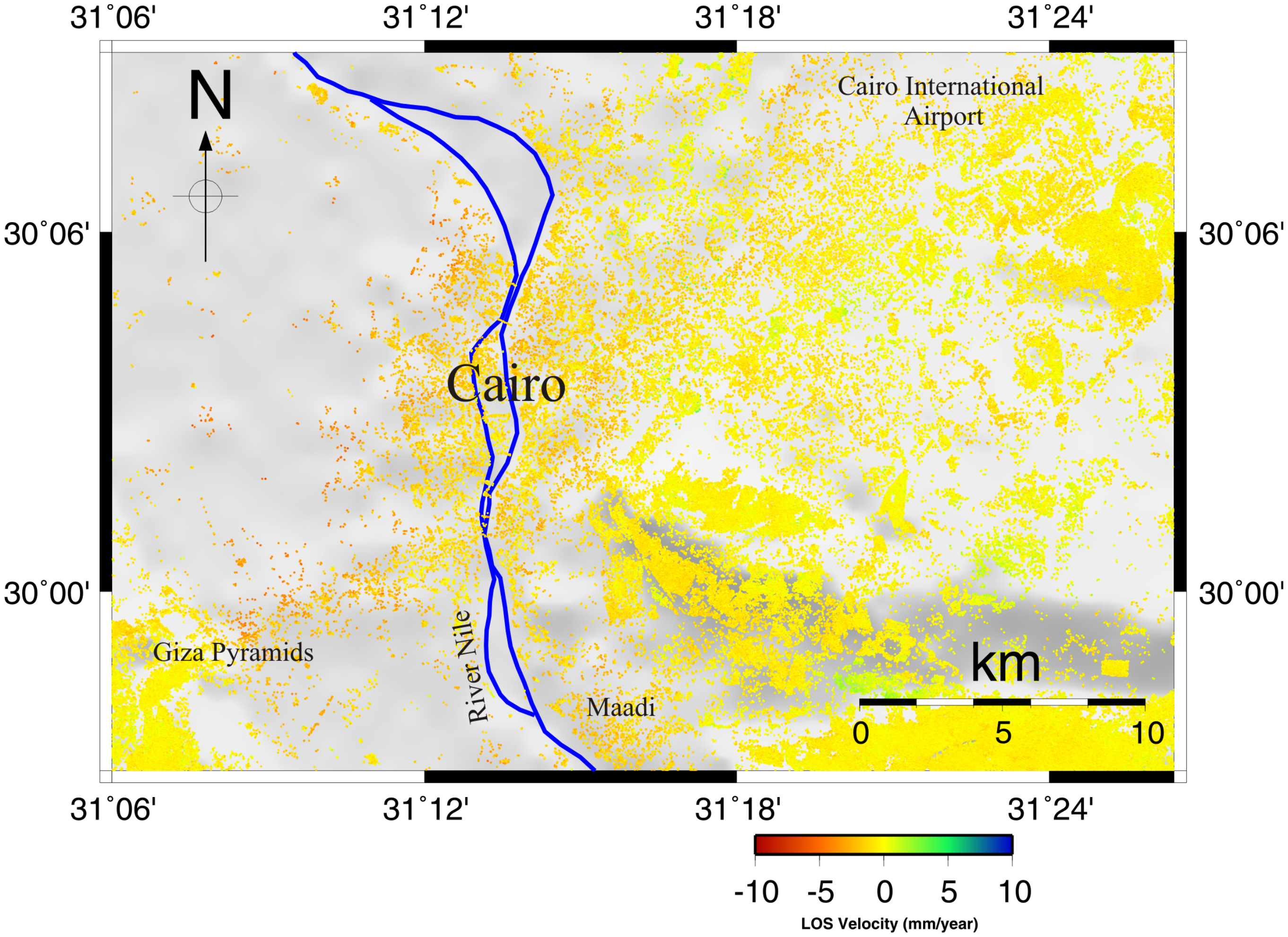

Figure 4.35: The LOS velocity field for Cairo from ERS1&2 tracks. Blue line represents the River Nile.

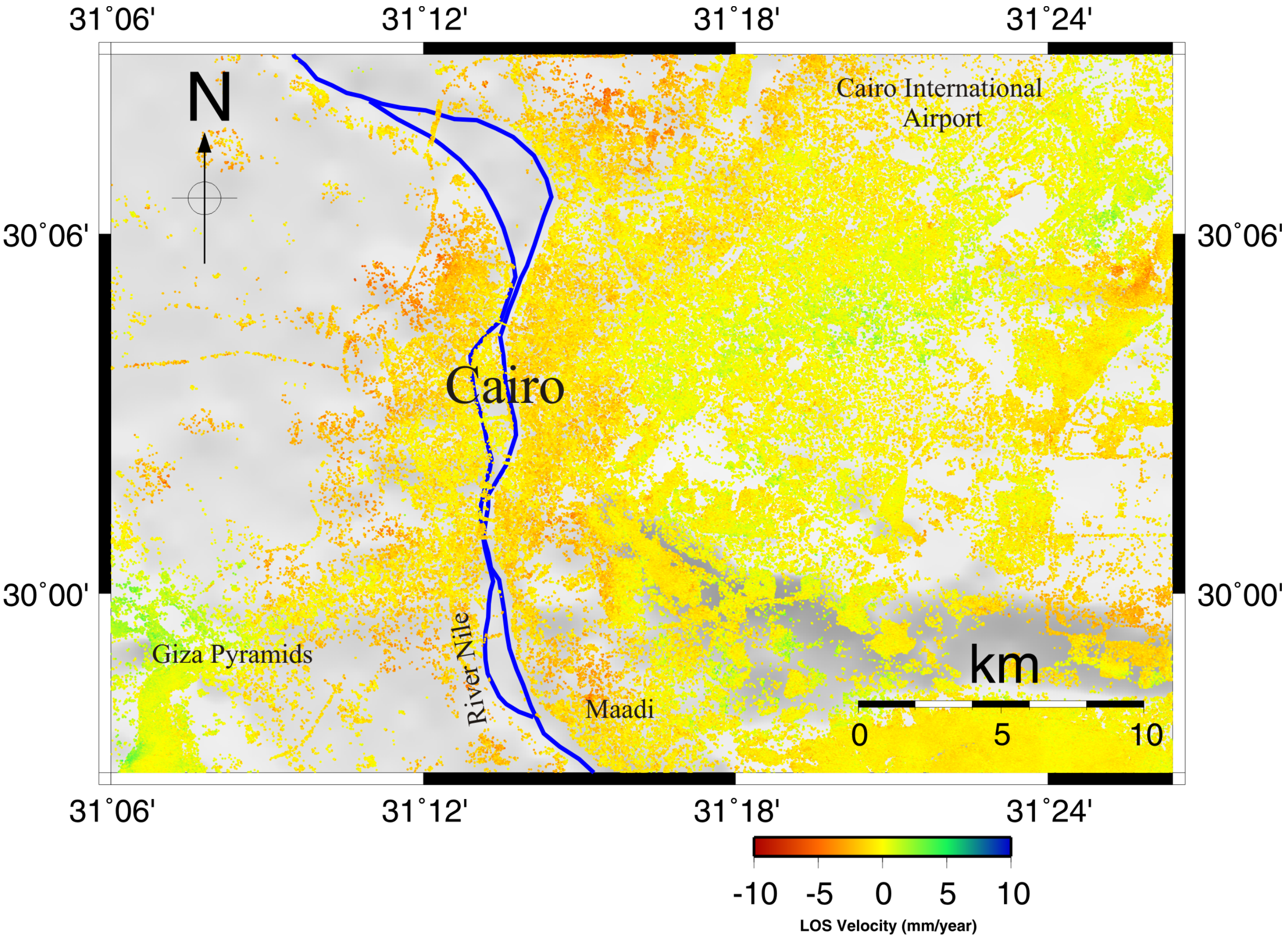

Figure 4.36: The LOS velocity field for Cairo from Envisat tracks. Blue line represents the River Nile.

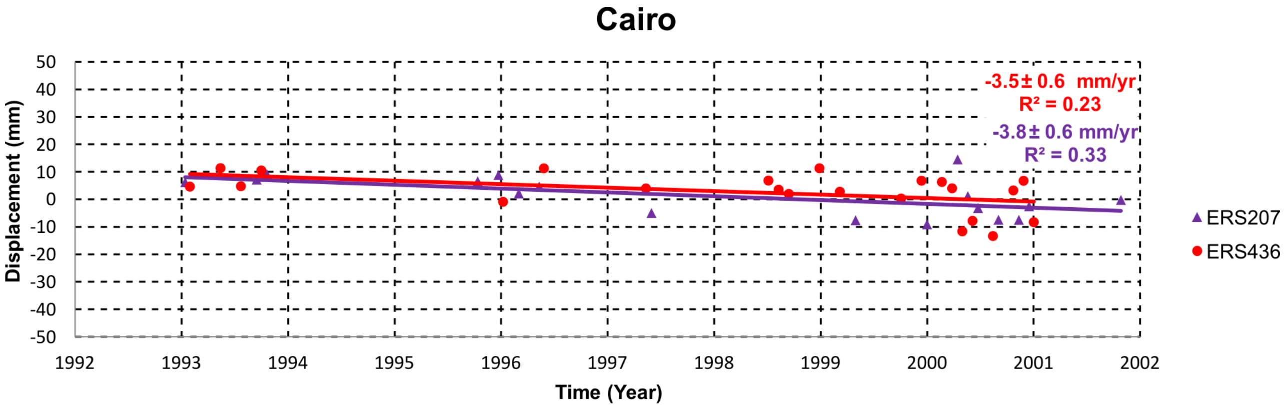

Figure 4.37: Displacement versus time for Cairo city from ERS descending scenes without the scenes acquired in 1992. Red dots represent the results from track 436 with the velocity trend, the red line. Whereas mauve dots represent the track 207 results, the mauve line represents the velocity trend.

Table 4.3: Comparison between the achieved results from both satellite missions (ERS and Envisat) in both tracks (207 and 436). (*) stands for the estimated trend excluding the scene in 1992.

	Envisat results (mm/yr)		ERS results (mm/yr)		ERS results (mm/yr)*	
	Track 207	Track 436	Track 207	Track 436	Track 207	Track 436
Cairo	5.5 ± 0.4	6.0 ± 0.4	2.3 ± 0.6	4.0 ± 0.6	3.8 ± 0.6	3.5 ± 0.6
Tanta	3.6 ± 0.6	-	3.5 ± 1.0	-	-	-
Mahala	3.4 ± 1.0	5.9 ± 1.0	2.4 ± 1.2	3.7 ± 1.2	-	-
Mansoura	9.3 ± 1.2	8.7 ± 1.2	4.4 ± 1.6	9.3 ± 1.6	-	-
Damietta	-	9.3 ± 1.6	-	10.0 ± 1.8	-	-
Port Said	-	4.4 ± 1.6	-	8.6 ± 1.8	-	-

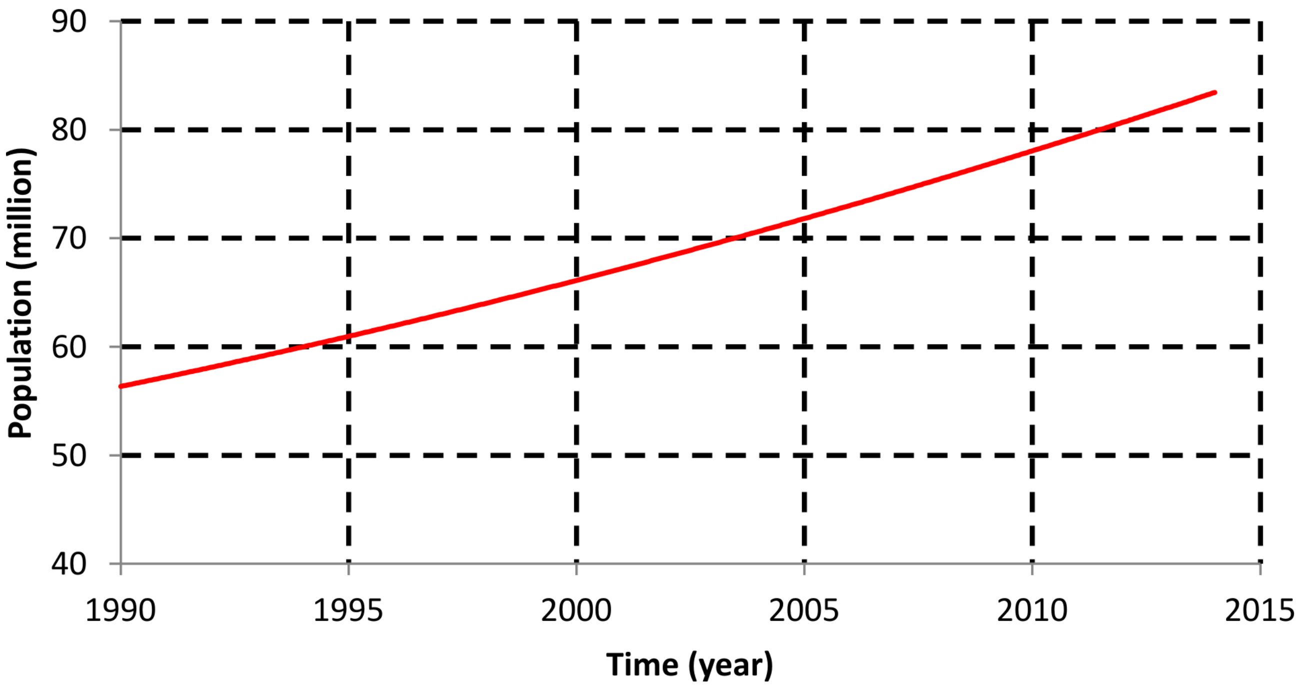

Figure 4.38: Egypt's population according to the World Bank (World-Bank, 2015).

5 Conclusions and Future Work

Under the action of forces, the Earth as a deformable body is subjected to changes in shape and size. These changes could be occurred either gradually or suddenly (Chen, 1983). The main world wide tools for monitoring the recent crustal movements are the repeated geodetic measurements (terrestrial and space techniques). The estimated crustal movement rates depend on the spatial and temporal density of these measurements and their accuracy. In addition to the tectonic activity, as a cause for the ground deformation, the crustal movements could also be resulted from human activities such as underground water pumping and oil extraction. Due to its location, in the northeastern corner of Africa, Egypt is subjected to several hazards. The subduction of northern Nubian plate under the Eurasian plate and the spreading along the Red Sea in addition to the activities at the Gulf of Suez and Gulf of Aqaba may control the surface deformation of Egypt. The seismic activities are mainly localized at the Red Sea spreading and the Gulfs of Suez and Aqaba. The seismic activities along the Gulf of Suez are extended to the West close to Cairo. There are a few seismic clusters occurred in Egypt. Some of these clusters are related to the activities along the Red Sea spreading, such as the clusters at Abu-Dabbab and Shalateen areas, while other clusters are related to induced seismicity such as the activities close to the Aswan Lake. Generally, the majority of seismic activities recorded in Egypt are micro-earthquakes ($M_L \leq 3.0$). In the last century, few earthquakes occurred in Egypt with magnitude $M_L > 5.0$. The largest earthquake with related destruction was on October 12, 1992 that occurred close to Cairo with magnitude $M_L = 5.9$. For this, 7 years of continuous and epoch GPS data were used to constrain better the geodynamical behavior of Egypt and determine the strain rates in addition to studying the interaction between the Nubian plate and surrounding tectonic plates.

On the other hand, after the establishment of the Aswan High Dam in 1970, which resulted in the absence of the sediment supply that carried by the River, the Nile Delta is suffering from land subsidence and coastal erosion. There were some attempts to estimate the subsidence rate of the Nile Delta but, unfortunately, their estimates are rough and covered only small parts of the Nile Delta. Therefore, there is a need to estimate the magnitude of the Delta subsidence with better accuracy. Using all the available ERS1, ERS2, and Envisat SAR data for the period 1992-2010, the subsidence rate of the whole Nile Delta was estimated applying the Persistent Scatterers (PS) approach.

5.1 Conclusions

NRIAG installed some geodetic networks to study the recent crustal movement and its relation to earthquake activity using terrestrial techniques, that were replaced later by GPS techniques. Five local geodetic networks around Aswan, Greater Cairo, Gulf of Suez, Nile Valley, and Abu-Dabbab areas were established and annually or semi-annually observed. In 2006, NRIAG started the establishment of the Egyptian Permanent GPS Network (EPGN). In this work, in addition to these five local networks, 16 permanent GPS stations belonging to EPGN were used.

The available data in the period from 2006 to 30.09.2012 of EPGN and local networks in addition to 86 permanent stations from different sources (IGS, EPN, SOPAC, and UNAVCO), belonging to three different tectonic plates, 47 stations from the African plate (Nubia, Somalia, Lawandle, and Sinai), 13 stations from the Arabian plate, and 26 stations from the Eurasian plate, aiming to set a good configuration around the Egyptian territory, were processed using the Bernese software V. 5.2. 34 stations out of 86 are included in the ITRF2008 and were used as fiducial stations. Due to the lack of an appropriate uncertainty assessment tool in Bernese at the time of processing, which resulted in a very small uncertainty, and in order to handle the absence of the time correlation in the GNSS results, new approaches were used to estimate a realistic uncertainty to assess the achieved results. The ratio between the formal standard deviation, from Bernese, and the repeatability, the residual of the daily solutions with respect to the combined solution, was used to scale the covariance matrix and ended up with the scaled error. However, this scaling process is not the best way to evaluate and estimate the GNSS time series parameters because it does not take into account the unique behavior of each station.

As an alternative approach, instead of the scaling process, a stochastic model accounting for the time correlation in the GNSS time series was used to get a proper estimation of the time series parameters as well as their uncertainties. In this wok, a combination of the power law noise with white noise was applied. The CATS software (Williams, 2008) was used as time series analysis tool for the uncertainty estimation accounting for the time correlation in the GNSS time series. The combination of white noise plus power law noise may be considered as an adequate model and may represent the time series noise properly due to the possibility of estimating of all stochastic parameters (spectral index, the scale factor of the amplitude of the colored noise, and the scale factor of the amplitude of the white noise (k, a_k, a)). For this reason, the results, velocities and uncertainties, of the white noise plus power law noise stochastic model are selected.

The comparison of time series and stochastic parameters between CATS and Bernese shows negligible effects of the stochastic models on the time series parameters (coordinate and velocity), especially in the horizontal component, but a large effect in the estimation of the stochastic parameters, i.e. uncertainties. CATS uncertainties is still too optimistic with respect to the scaled error. This could be attributed to the high repeatability values, the main input in the scaling process, the observations period, even with seven years of GNSS observations are still being not long enough to clearly estimate the correlation depending on time, and the periodic signals. Due to the discontinuities in the local network stations during the time series in addition to the short period of observations in each epoch, from three to five days, it was difficult to apply the CATS approach for these stations. Comparing both estimated scaled and CATS errors, the scaled error is a factor of 5 to 10 from the estimated CATS error. This approximation is used to get a more reliable error for the non-permanent stations, especially for the Gulf of Suez network.

CATS velocities for permanent stations and Bernese velocities for non-permanent ones were used to estimate the ITRF2008 and relative Euler pole parameters for Nubian, Somalian, Eurasian, Arabian, and Sinai plates. Firstly the Euler pole parameters were calculated for a given plate by a least-squares adjustment to the selected site velocities, well representing these plates. Then, about 72 stations were used to estimate the Euler pole parameters for Nubian, Somalian, Arabian, and Sinai plates in Eurasia fixed frame. The velocity field shows a relative motion between northern Nubia and Eurasia of about $6.5 \pm 1\ mm/yr$, $14.2 \pm 1.4\ mm/yr$ for the North of the Arabian plate. A zoom on the Egyptian region shows a homogeneous trend of all Egyptian sites of about $6.5 \pm 1\ mm/yr$ to North to Northwest direction, except the sites in Sinai Peninsula of about $8.2 \pm 0.8\ mm/yr$ to North to Northeast direction, resulting in a difference of about $1.7\ mm/yr$.

To test the existence of the Sinai micro-plate between Nubian and Arabian plates, the available Sinai GPS sites were used to estimate the Euler pole parameters with respect to stable Nubia. Almost all the GPS sites in the western and southern part of Sinai Peninsula do not show any significant velocity at 95% of confidence level with respect to Nubia. On the other hand, the eastern and northeastern sites in Sinai show a systematic trend of horizontal velocity to North to Northwest direction with respect to Nubia of about $1.7 \pm 0.9\ mm/yr$. Due to the absence of surface faults and the lack of GPS observations North of the Gulf of Suez, it is difficult to define the borders of the proposed Sinai sub-plate accurately, especially the western border. More permanent GPS stations North of the Gulf of Suez in addition to more GPS data from the local network along the Gulf of Suez are required to improve the quality of the velocity results which may help to better describe the velocity model for Sinai. Based on these results the Sinai Peninsula seems to be still connected to Nubia and the relative motion of its northeastern part is probably due to the left-lateral strike-slip movement along the DST fault that represents the boundary between the Nubian and Arabian Plates.

Velocities of 28 GPS sites located West and East the DST fault were used to estimate its locking depth (D) and slip rate (V_0) by applying the dislocation fault model of (Savage and Burford, 1973). The estimated slip rate of the DST fault is 6 mm/yr with locking depth 16 km. Due to the fact that the DST fault consists of more than one segment, the slip rate and locking depth inversion is made twice, one for the southern segment and one for the northern segment of the DST fault. A slip rate and locking depth for the southern segment of 7 mm/yr and 18 km were calculated, respectively. Whereas the slip rate and locking depth of the northern segment of the DST fault are 5 mm/yr and 12 km, respectively. The strain rates of the northeastern corner of Nubia are estimated by interpolating the GPS velocities in East and North components, according to (Hackl et al., 2009). The strain rate map of the northeastern corner of Nubia indicates high strain rates strongly localized close to the DST fault and ranging from $40 - 90 \times 10^{-9}/yr$. The Gulf of Suez and southern Sinai are showing low to moderate strain rates of about $20 - 40 \times 10^{-9}/yr$ while the rest of Egypt looks like a rigid plate. The main conclusion based on the results mentioned above is presented in Figure 5.1. The velocity field in the Eurasia fixed frame indicates counterclockwise rotation of a broad area including the Arabian, Anatolian, and Aegean regions which increases towards the Hellenic and Cyprus trench system. This model also includes the slip rates calculated from the dislocation fault parallel analysis for the DST fault.

Due to the great importance of the Nile Delta, as it produces more than 60% of the Egyptian food and it is a highly populated area, the Interferometric Synthetic Aperture Radar (InSAR) was used to estimate the rate of its subsidence. All available SAR scenes from C-band ERS1, ERS2, and Envisat satellite missions with a temporal resolution of 35 days were used to measure the ground deformation in the Nile Delta. The environment of the Nile Delta is not perfect for the SAR Interferometry due to the heavy vegetation cover and the expected very slow rate of deformation that requires long time to measure which may lead to phase decorrelation. To get over the decorrelation problems, the Permanent Scatterer (PS) technique has been applied instead of the conventional technique to estimate the land subsidence of the Nile Delta.

Due to the lack of SAR data in the ascending pass, as there is only about 7 scenes in each ascending track, the SAR scenes used in this work are collected only in the descending pass from both tracks 207 and 436 in ERS and Envisat satellite missions. The number of scenes collected from Envisat are much higher than the scenes collected from ERS. 36 and 37 Envisat scenes are collected from tracks 207 and 436, respectively, while 20 and 24 ERS scenes are collected from tracks 207 and 436, respectively, over the Nile Delta. The collected SAR data covers the period 1992-2010 ($\simeq 20\ years$). The SAR raw data were focused using the Repeat Orbit Interferometry Package ROI_PAC ((Massonnet and Feigl, 1998); (Thompson et al., 1986); (Rosen et al., 2000); (Zebker and Goldstein, 1986)). A master scene for each track is selected, which maximize the sum correlation. The selected master scenes are more or less in the middle spatially and temporally. The interferograms were created using the Delft Object-oriented Radar Interferometric Software DORIS (Kampes et al., 2003) for the oversampled and coregistered pairs of scenes (Master and Slave), and Shuttle Radar Topography Mission SRTM 90 m data were used for removing the topographic phase contribution. Then, the PS processing was carried out using Stanford Method for Persistent Scatterers software StaMPS (Hooper et al., 2012). The PS pixels were identified in two steps. The first is the initial selection that is based on the amplitude dispersion (D_A), the used threshold in this work is 0.4. The second step is the final selection of PS that depends on the phase stability. Finally, after the PS pixels were identified, the phase is unwrapped and converted into the Line-Of-Sight (LOS) velocity.

The density of the PS pixels mainly depends on the number of scenes used for each track, the more scenes used, the more PS pixels identified. The number of PS pixels selected from ERS are small with respect to the selected PS pixels from the Envisat scenes, which may be due to the less number of scenes available from ERS, as the number of available scenes is around 20 scenes. This resulted in the complete decorrelation of the northern part of the Nile Delta except the big cities such as Cairo, Tanta, Mahala, Mansoura, Damietta, and Port Said which show better correlation represented by the presence of PS pixels. On the other hand, the situation is much better in the Envisat results because the available SAR scenes are 36-37 scenes which resulted in higher density of PS pixels in the northern part of the Nile Delta. The density of PS pixels is very high for the southern part of the Nile Delta in both results from ERS and Envisat because it is an arid area and mainly composed of hard rocks that act as very good reflectors.

By applying the PSI analysis the LOS velocity field in the Nubia fixed frame for the Nile Delta was estimated. From the GPS results, the horizontal velocity of the Nile Delta in the Nubia fixed frame is very small ($1-2$ mm/yr. Therefore, in this work the LOS velocity field is considered as the velocity in the Up component with $1-2$ mm/yr as a contamination from the horizontal component. Due to the fact that the Nile Delta is almost stable and the estimated ground deformation is highly localized at the big cities, as shown in the InSAR velocity maps, the time series plots for selected PS pixels from these cities (Cairo, Tanta, Mahala, Mansoura, Damietta, and Port Said) are made. The estimated subsidence rates from Envisat scenes are $5.5-6.0 \pm 0.4$ mm/yr, 3.6 ± 0.6 mm/yr, $3.4-5.9 \pm 1.0$ mm/yr, $9.3-8.7 \pm 1.2$ mm/yr, 9.3 ± 1.6 mm/yr and 4.4 ± 1.6 mm/yr for Cairo, Tanta, Mahala, Mansoura, Damietta, and Port Said, respectively. The difference in rates between the Envisat tracks are 0.5 mm/yr, 0.6 mm/yr and 2.5 mm/yr for Cairo, Mansoura, and Mahala, respectively. Whereas, the estimated subsidence rates from ERS scenes are $2.3-4.0 \pm 0.6$ mm/yr, 3.5 ± 1.0 mm/yr, $2.4-3.7 \pm 1.2$ mm/yr, $4.4-9.3 \pm 1.6$ mm/yr, 10.0 ± 1.8 mm/yr and 8.6 ± 1.8 mm/yr for Cairo, Tanta, Mahala, Mansoura, Damietta, and Port Said, respectively. The differences in rates between the ERS tracks are 1.7 mm/yr, 1.3 mm/yr and 4.9 mm/yr for Cairo, Mansoura and Mahala, respectively.

The difference in rates, estimated for Cairo, between the ERS tracks of about 1.7 mm/yr may be related to the effect of the pre-seismic deformation of the October 12, 1992 Cairo earthquake. There is one scene in each ERS track that was acquired few months before this earthquake. For that, the estimated rate of subsidence for Cairo may be contaminated by the pre-seismic deformation and might not reflect the actual rate of subsidence. Removing the first scene in each ERS track lead to a better agreement in estimates of the subsidence rate of Cairo. The estimated rates for Cairo from tracks 207 and 436 are 3.8 mm/yr and 3.5 mm/yr, respectively, and the difference between the results of the two tracks is 0.3 mm/yr. However, with only 20 ERS scenes acquired from track 207, it is difficult to estimate a reliable subsidence rate for such a highly vegetated area like the Nile Delta. The subsidence rates of the highly populated cities like Cairo and Mahala estimated from ERS scenes are smaller than the rates estimated from the Envisat scenes of about 2 mm/yr. The localization of the subsidence rates at the big cities implies that the detected signals are mainly due to human activities, such as underground water pumping. The rapid increase of Egypt's population, and as a consequence the increase of the rate of underground water pumping rates, could be the reason for the difference in subsidence rates estimated from the ERS and Envisat of 2 mm/yr. Unfortunately, the lack of the rates of the underground water pumping and the limitation of the in-situ terrestrial data of the Nile Delta make it difficult to verify this interpretation.

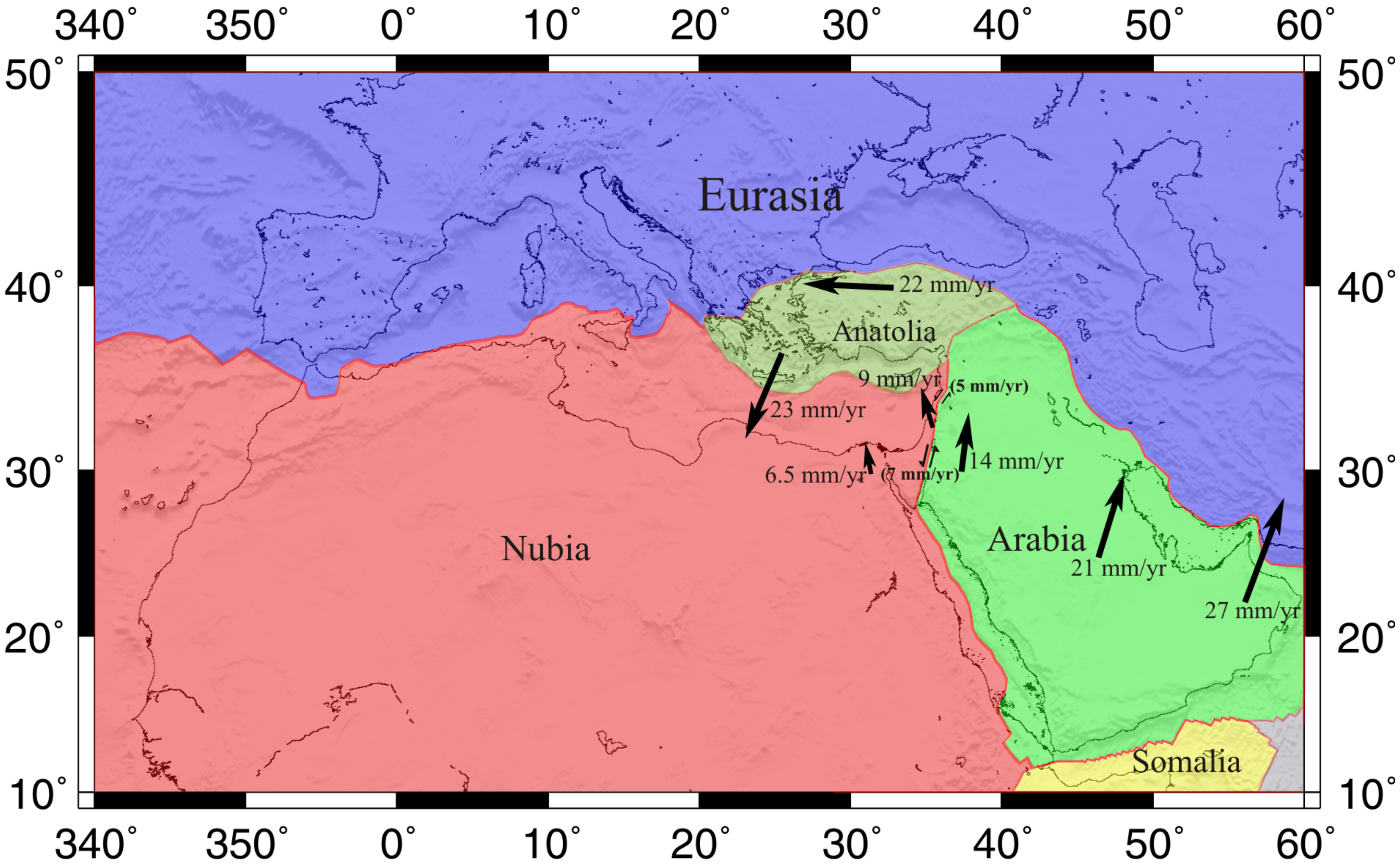

Figure 5.1: Schematic map of the Nubia-Arabia-Anatolia-Eurasia zone of plate interaction illustrating the principal results of this study. Paired arrows show the direction of the strike-slip motion. Rates in parentheses represent the slip rate along the DST fault. Dark arrows are the GPS-derived velocity rates (mm/yr) the in Eurasia fixed frame. Red lines represent the plate boundaries (as in Figure 2.1)

5.2 Future Work

The estimated crustal motion model of Egypt and the northeastern corner of Nubia, from this study, shows a high shear strain that is localized along the DST fault and low-moderate shear strain along the southern part of Sinai and Gulf of Suez. The rest of Egypt looks quite stable, and no significant strain rates are found. Seismically, Egypt is not characterized by high seismic activity. Nevertheless, there are some areas that are characterized by significant seismic activity. Even with 16 permanent stations and about 47 non-permanent stations, which succeeded to delineate the shear strain along the plate boundary, it is hard to investigate in detail the intraplate deformation. It was expected to have some shear strain at areas like west of Cairo, the location of the Cairo earthquake 1992, and northwest of Aswan Lake Nasser, along the active faults Kalabsha and Sayal. As the distribution of the GPS sites is coarse, it was difficult to monitor the areas of shear strain less than $20 \times 10^{-9}/yr$ and as a consequence more GPS data is required in order to observe such small strain values along these active areas.

Based on the estimated model from this study, Sinai Peninsula behaves as still connected to Nubia and there is no any significant differential motion between Sinai and Nubia and/or seismic activities or surface faults north of the Gulf of Suez, which implies that there is no separate Sinai sub-plate between Nubian and Arabian plates. Unfortunately, due to the limited GPS data available on both sides of the Gulf of Suez, this suggestion requires further confirmation. Currently, more permanent GPS stations are added to the EPGN network and an extension to 25 stations is expected by the end of year 2015. The difficulties of verifying our crustal motion model could be solved with the presence of more data. Figure 5.2 shows the expected distribution of the Egyptian stations by the end of 2015. The distribution of the new added permanent stations will be concentrated around the Nile Delta including Cairo region and also around the northern part of Aswan Lake, southern Egypt, densifying the existing network.

Similar subsidence rates as estimated for the big cities in the Nile Delta are also expected for all cities which are not covered by the processed SAR scenes in this work such as Alexandria. Due to the absence of the SAR data in the ascending pass in addition to the limited number of GPS sites in the Nile Delta, the separation of the velocity in the Up component from the LOS velocity was not possible. Using the new Sentinel-1A satellite mission data, launched on April 03, 2014 within the ESA-EU Copernicus Programme, will give the ability to monitor the crustal deformation for the first time with very high spatial and temporal resolution, 5 m and 12 days, respectively. The free access to this novel type of data is the basis for the development of the new integrated monitoring concept for the Nile Delta. Corner reflectors will be added close to the permanent GPS stations in the Nile Delta and a plan for some precise leveling profiles crossing cities that suffered from land subsidence is established. The final goal is to get a clear view about the ground deformation of the Nile Delta (causes and magnitudes) by combining all the achieved results from the Sentinel-1A, GPS, and precise leveling.

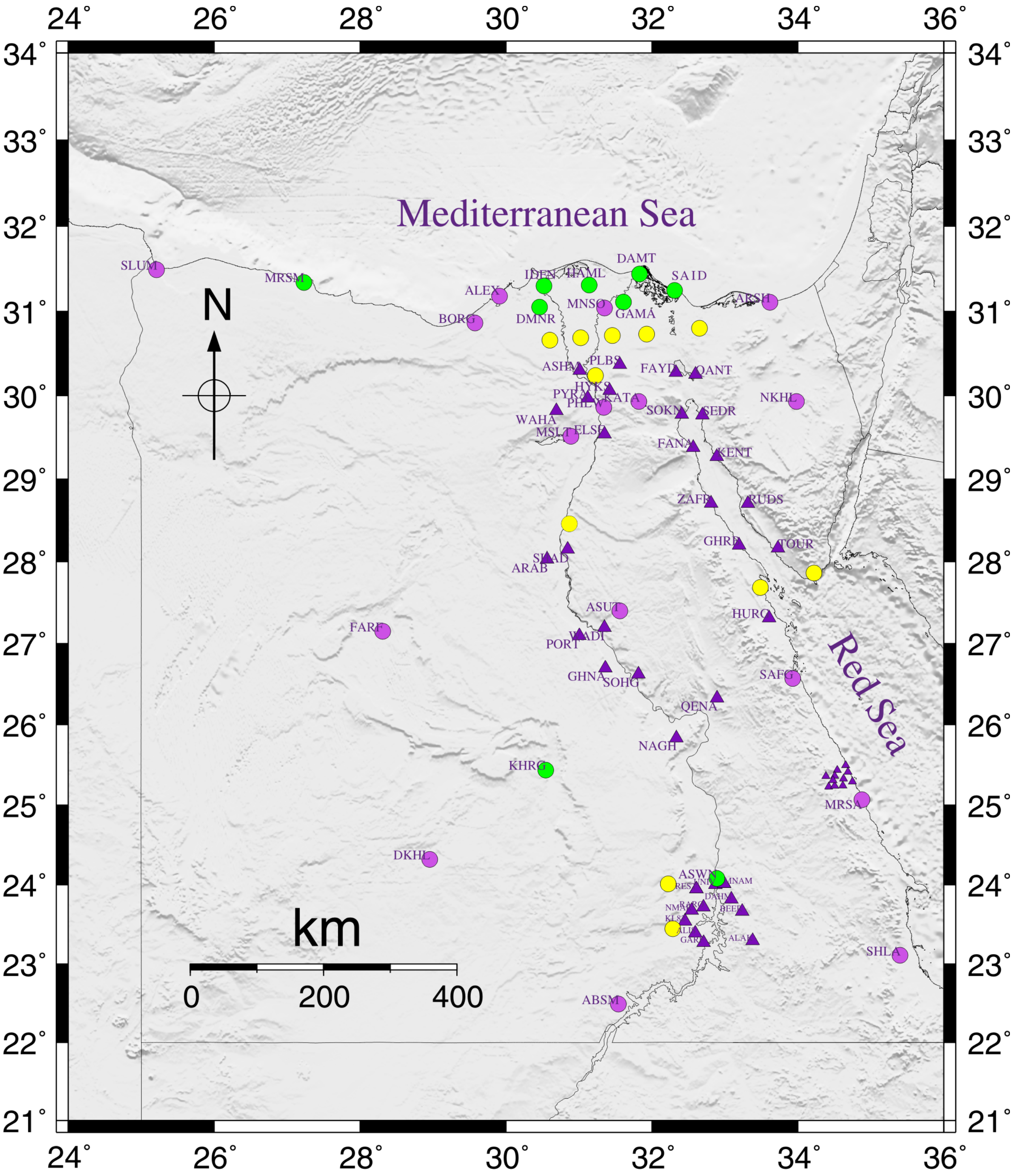

Figure 5.2: Updated figure of the Egyptian GPS station geographic distribution. Triangles for epoch stations and circles for the permanent stations. Violet for existing stations (permanent and epoch), Green for stations established during the time of this work that are currently operating, and yellow for the proposed stations.

References

Abou Elenean, K. (1997). *Seismotectonics of Egypt in Relation to the Mediterranean and Red Seas Tectonics*. PhD thesis, Ain Shams University, Cairo, Egypt.

Abou Elenean, K. M. (2007). Focal Mechanisms of Small and Moderate Size Earthqaukes Recorded by the Egyptian National Seismic Network (ENSN), Egypt. *NARIAG Journal of Geophysics*, 6(1):117–151.

Agnew, D. C. (1992). The time-domain Behavior of Power-law Noises. *Geophysical Research Letters*, 19(4):333–336.

Altamimi, Z., Collilieux, X., and Métivier, L. (2011). ITRF2008: an improved solution of the international terrestrial reference frame. *Journal of Geodesy*, 85(8):457–473.

Aly, M. H. (2006). *Radar Interferometry for Monitoring Land Subsidence and Coastal Change in the Nile Delta, Egypt*. PhD thesis, Texas A&M University.

Aly, M. H. and Cochran, E. S. (2011). Spatio-temporal Evolution of Yellowstone Deformation Between 1992 and 2009 from InSAR and GPS Observations. *Bulletin of Volcanology*, 73(9):1407–1419.

Amelung, F., Galloway, D. L., Bell, J. W., Zebker, H. A., and Laczniak, R. J. (1999). Sensing the ups and downs of las vegas: Insar reveals structural control of land subsidence and aquifer-system deformation. *Geology*, 27(6):483–486.

Amelung, F., Jonsson, S., Zebker, H., and Segall, P. (2000). Widespread uplift and ’trapdoor’ faulting on galapagos volcanoes observed with radar interferometry. *nature*, 407:993–996.

Argus, D. F., Gordon, R. G., Heflin, M. B., Ma, C., Eanes, R. J., Willis, P., Peltier, W. R., and Owen, S. E. (2010). The angular Velocities of the Plates and the Velocity of Earth’s Centre from Space Geodesy. *Geophysical Journal International*, 180(3):913–960.

Bamler, R. and Hartl, P. (1998). Synthetic Aperture Radar Interferometry. *Inverse Problems*, 14(4):R1.

Becker, R. H. and Sultan, M. (2009). Land subsidence in the Nile Delta: inferences from radar interferometry. *The Holocene*, 19(6):949–954.

Berardino, P., Fornaro, G., Lanari, R., and Sansosti, E. (2002). A new algorithm for surface deformation monitoring based on small baseline differential sar interferograms. *Geoscience and Remote Sensing, IEEE Transactions*, 40(11):2375–2383.

Bird, P. (2003). An updated digital model of plate boundaries. *Geochemistry, Geophysics, Geosystems*, 4(3).

Böhm, J., Heinkelmann, R., and Schuh, H. (2007). Short note: A global model of pressure and temperature for geodetic applications. *Journal of Geodesy*, 81(10):679–683.

Buderi, R. (1996). *The Invention that changed the world: How a small group of Radar pioneers won the second World War and launched a technological revolution*. Sloan technology series. Simon & Schuster.

Bürgmann, R., Kogan, M. G., Levin, V. E., Scholz, C. H., King, R. W., and Steblov, G. M. (2001). Rapid aseismic moment release following the 5 December, 1997 Kronotsky, Kamchatka, Earthquake. *Geophysical Research Letters*, 28(7):1331–1334.

Cakir, Z., Ergintav, S., Akoğlu, A. M., Çakmak, R., Tatar, O., and Meghraoui, M. (2014). InSAR velocity field across the North Anatolian Fault (eastern Turkey): Implications for the loading and release of interseismic strain accumulation. *Journal of Geophysical Research: Solid Earth*, 119(10):7934–7943.

Chen, Y.-Q. (1983). Analysis of deformation surveys- A generalized method. Technical report, University of New Brunswik.

Colesanti, C., Ferretti, A., Prati, C., and Rocca, F. (2003). Monitoring landslides and tectonic motions with the Permanent Scatterers Technique. *Engineering Geology*, 68(12):3–14. Remote sensing and monitoring of landslides.

Crosetto, M., Arnaud, A., Duro, J., Biescas, E., and Agudo, M. (2003). Deformation monitoring using remotely sensed radar interferometric data. In *Proc., 11th FIG Symposium on Deformation Measurements, Santorini, Greece*.

Curlander, J. and McDonough, R. (1991). *Synthetic Aperture Radar: systems and signal processing*. Balkema Rotterdam.

Dach, R., Hugentobler, U., Fridez, P., and Meindl, M. E. (2007). *Bernese GPS software version 5.0 user manual*. Astronomical Institute, Universtiy of Bern.

DeMets, C., Gordon, R. G., Argus, D. F., and Stein, S. (1990). Current plate motions. *Geophysical Journal International*, 101(2):425–478.

DeMets, C., Gordon, R. G., Argus, D. F., and Stein, S. (1994). Effect of recent revisions to the geomagnetic reversal time scale on estimates of current plate motions. *Geophysical Research Letters*, 21(20):2191–2194.

Doornbos, E. and Scharroo, R. (2004). Improved ERS and Envisat precise orbit determination. In *ENVISAT and ERS Symposium, Salzburg, Austria*.

Doornbos, E., Scharroo, R., Klinkrad, H., Zandbergen, R., and Fritsche, B. (2002). Improved modelling of surface forces in the orbit determination of ERS and ENVISAT. *Canadian Journal of Remote Sensing*, 28(4):535–543.

Dow, J., Neilan, R., and Gendt, G. (2005). The international {GPS} service: Celebrating the 10th anniversary and looking to the next decade. *Advances in Space Research*, 36(3):320 – 326. Satellite Dynamics in the Era of Interdisciplinary Space Geodesy.

Dziewonski, A., Chou, T., and Woodhouse, J. H. (1981). Determination of earthquake source parameters from waveform data for studies of global and regional seismicity. *Journal of Geophysical Research: Solid Earth*, 86(B4):2825–2852.

Egyptian Geological Survey and Mining Authority (EGSMA) (1981). Geologic Map of Egypt.

Ekström, G., Nettles, M., and Dziewoski, A. (2012). The global {CMT} project 2004-2010: Centroid-moment tensors for 13,017 earthquakes. *Physics of the Earth and Planetary Interiors*, 200-201:1 – 9.

El-Sayed, A., Arvidsson, R., and Kulhánek, O. (1998). The 1992 Cairo earthquake: A case study of a small destructive event. *Journal of Seismology*, 2(4):293–302.

El Shazly, E. (1977). The geology of the Egyptian region. In Nairn, A., Kanes, W., and Stehli, F., editors, *The Ocean Basins and Margins*, pages 379–444. Springer US.

Fenoglio-Marc, L. (2015). Sea level in the mediterranean sea. In *Sea level and associated climatic components as inferred from the ESA Climate Change Initiative*.

Fenoglio-Marc, L., Mariotti, A., Sannino, G., Meyssignac, B., Carillo, A., Struglia, M., and Rixen, M. (2013). Decadal variability of net water flux at the Mediterranean Sea Gibraltar Strait. *Global and Planetary Change*, 100(0):1 – 10.

Fenoglio-Marc, L., Rietbroek, R., Grayek, S., Becker, M., Kusche, J., and Stanev, E. (2012). Water mass variation in the Mediterranean and Black Seas. *Journal of Geodynamics*, 5-60(0):168 – 182. Mass Transport and Mass Distribution in the System Earth.

Ferretti, A., Prati, C., and Rocca, F. (2001). Permanent scatterers in SAR interferometry. *Geoscience and Remote Sensing, IEEE Transactions on*, 39(1):8–20.

Freund, R., Garfunkel, Z., Zak, I., Goldberg, M., Weissbrod, T., Derin, B., Bender, F., Wellings, F. E., and Girdler, R. W. (1970). The shear along the Dead Sea rift [and discussion]. *Philosophical Transactions of the Royal Society of London A: Mathematical, Physical and Engineering Sciences*, 267(1181):107–130.

Freund, R., Zak, I., and Garfunkel, Z. (1968). Age and rate of the sinistral movement along the Dead Sea rift. *nature*, 220:253–255.

Gabriel, A. K., Goldstein, R. M., and Zebker, H. A. (1989). Mapping small elevation changes over large areas: Differential radar interferometry. *Journal of Geophysical Research: Solid Earth*, 94(B7):9183–9191.

Garfunkel, Z. (1981). Internal structure of the dead sea leaky transform (rift) in relation to plate kinematics. *Tectonophysics*, 80(1-4):81–108. The Dead Sea Rift.

Gergawi, A. and El-Khashab, H. (1968). Seismicity of egypt. *Helwan Observatory Bull.*, 76.

Gomez, F., Karam, G., Khawlie, M., McClusky, S., Vernant, P., Reilinger, R., Jaafar, R., Tabet, C., Khair, K., and Barazangi, M. (2007). Global Positioning System measurements of strain accumulation and slip transfer through the restraining bend along the Dead Sea fault system in Lebanon. *Geophysical Journal International*, 168(3):1021–1028.

Hackl, M., Malservisi, R., and Wdowinski, S. (2009). Strain rate patterns from dense GPS networks. *Natural Hazards and Earth System Science*, 9(4):1177–1187.

Hammad, M. (1975). Geological Map of Egypt, Appendix 1, Soil Survey Papers no: 11.

Hanssen, R. (2001). *Radar interferometry: Data interpretation and error analysis*. Remote Sensing and Digital Image Processing. Springer.

Hoffmann, J., Zebker, H. A., Galloway, D. L., and Amelung, F. (2001). Seasonal subsidence and rebound in Las Vegas Valley, Nevada, observed by Synthetic Aperture Radar Interferometry. *Water Resources Research*, 37(6):1551–1566.

Hooper, A., Bekaert, D., Spaans, K., and Arikan, M. (2012). Recent advances in {SAR} interferometry time series analysis for measuring crustal deformation. *Tectonophysics*, 514-517:1–13.

Hooper, A., Segall, P., and Zebker, H. (2007). Persistent scatterer interferometric synthetic aperture radar for crustal deformation analysis, with application to volcán alcedo, galápagos. *Journal of Geophysical Research: Solid Earth*, 112(B7).

Hooper, A. and Zebker, H. A. (2007). Phase unwrapping in three dimensions with application to InSAR time series. *J. Opt. Soc. Amer. A*.

Hooper, A. J. (2006). *Persistent scatterer radar interferometry for crustal deformation studies and modeling of volcanic deformation*. PhD thesis, Stanford University.

Hopfield, H. S. (1963). The effect of tropospheric refraction on the doppler shift of a satellite signal. *Journal of Geophysical Research*, 68(18):5157–5168.

IGS (2015). IGS Products. https://igscb.jpl.nasa.gov/components/prods_cb.html.

Ismail, A. (1960). Near and local earthquakes at Helwan from 1903-1950. *Helwan Observatory Bull.*, 49.

Joffe, S. and Garfunkel, Z. (1987). Plate kinematics of the circum Red Sea-a re-evaluation. *Tectonophysics*, 141(13):5 – 22. Sedimentary basins within the Dead Sea and other rift zones.

Kampes, B., Hanssen, R., and Perski, Z. (2003). Radar interferometry with public domain tools. In *Proceedings of FRINGE 2003*.

Kampes, B. M. (2005). *Displacement parameter estimation using permanent scatterer interferometry*. PhD thesis, Delft University of Technology.

Kebeasy, R. (1990). Seismicity in Geology of Egypt (R. Said, Ed). *Balkema Rotterdam*, pages 51–59.

Ketelaar, V. B. H. (2009). *Satellite radar interferometry: Subsidence monitoring techniques*. Springer.

Klinger, Y., Avouac, J. P., Abou Karaki, N., Dorbath, L., Bourles, D., and Reyss, J. L. (2000). Slip rate on the Dead Sea transform fault in northern Araba valley (Jordan). *Geophysical Journal International*, 142(3):755–768.

Langbein, J. and Johnson, H. (1997). Correlated errors in geodetic time series: Implications for time-dependent deformation. *Journal of Geophysical Research: Solid Earth*, 102(B1):591–603.

Le Beon, M., Klinger, Y., Amrat, A. Q., Agnon, A., Dorbath, L., Baer, G., Ruegg, J.-C., Charade, O., and Mayyas, O. (2008). Slip rate and locking depth from GPS profiles across the southern Dead Sea Transform. *Journal of Geophysical Research: Solid Earth*, 113(B11).

Lyons, S. and Sandwell, D. (2003). Fault creep along the southern San Andreas from Iterferometric Synthetic Aperture Radar, permanent scatterers, and stacking. *J. Geophys. Res*, 108(1):2047.

Maamoun, M., Megahed, A., and Allam, A. (1984). Seismicity of Egypt. *Helwan Institute of Astronomy and Geophysics Bull.*, 4(Ser. B):102–109.

Mahmoud, S., Reilinger, R., McClusky, S., Vernant, P., and Tealeb, A. (2005). {GPS} evidence for northward motion of the Sinai Block: Implications for E. Mediterranean tectonics. *Earth and Planetary Science Letters*, 238(12):217 – 224.

Malservisi, R., Gans, C., and Furlong, K. (2005). Microseismicity and Creeping Faults: Hints from Modeling the Hayward Fault, California (USA). *Earth Plan. Sci. Lett.*, 234(3-4):421–435.

Mandelbrot, B. B. and Ness, J. W. V. (1968). Fractional brownian motions, fractional noises and applications. *SIAM Review*, 10(4):pp. 422–437.

Massonnet, D., Adragna, F., and Rossi, M. (1994). CNES general-purpose SAR correlator. *Geoscience and Remote Sensing, IEEE Transactions on*, 32(3):636–643.

Massonnet, D. and Feigl, K. L. (1998). Radar interferometry and its application to changes in the earth's surface. *Reviews of Geophysics*, 36(4):441–500.

Massonnet, D., Rossi, M., Carmona, C., Adragna, F., Peltzer, G., Feigl, K., and Rabaute, T. (1993). The displacement field of the Landers earthquake mapped by radar interferometry. *nature*, 364:138–142.

McClusky, S., Balassanian, S., Barka, A., Demir, C., Ergintav, S., Georgiev, I., Gurkan, O., Hamburger, M., Hurst, K., Kahle, H., Kastens, K., Kekelidze, G., King, R., Kotzev, V., Lenk, O., Mahmoud, S., Mishin, A., Nadariya, M., Ouzounis, A., Paradissis, D., Peter, Y., Prilepin, M., Reilinger, R., Sanli, I., Seeger, H., Tealeb, A., Toksöz, M. N., and Veis, G. (2000). Global Positioning System constraints on plate kinematics and dynamics in the eastern Mediterranean and Caucasus. *Journal of Geophysical Research: Solid Earth*, 105(B3):5695–5719.

McClusky, S., Reilinger, R., Mahmoud, S., Ben Sari, D., and Tealeb, A. (2003). GPS constraints on Africa (Nubia) and Arabia plate motions. *Geophysical Journal International*, 155(1):126–138.

Meghraoui, M., Gomez, F., Sbeinati, R., der Woerd, J. V., Mouty, M., Darkal, A. N., Radwan, Y., Layyous, I., Najjar, H. A., Darawcheh, R., Hijazi, F., Al-Ghazzi, R., and Barazangi, M. (2003). Evidence for 830 years of seismic quiescence from palaeoseismology, archaeoseismology and historical seismicity along the Dead Sea fault in Syria. *Earth and Planetary Science Letters*, 210:35 – 52.

Melbourne, W. G. (1985). The case for ranging in GPS based geodetic systems. In Goad, C., editor, *the 1st International Symposium on Precise Positioning with the Global Positioning System*, page 373Ű386.

Niell, A. E. (1996). Global mapping functions for the atmosphere delay at radio wavelengths. *Journal of Geophysical Research: Solid Earth*, 101(B2):3227–3246.

Onn, F. and Zebker, H. A. (2006). Correction for interferometric synthetic aperture radar atmospheric phase artifacts using time series of zenith wet delay observations from a GPS network. *Journal of Geophysical Research: Solid Earth*, 111(B9).

Prati, C., Rocca, F., Monti Guarnieri, A., and Damonti, E. (1990). Seismic migration for SAR focusing: Interferometrical applications. *Geoscience and Remote Sensing, IEEE Transactions on*, 28(4):627–640.

Pritchard, M. E. and Simon, M. (2002). A satellite geodetic survey of large-scale deformation of volcanic centres in the central Andes. *nature*, 418:167–171.

Quennell, A. M. (1958). The structural and geomorphic evolution of the Dead Sea rift. *Quarterly Journal of the Geological Society*, 114(1-4):1–24.

Reilinger, R., McClusky, S., Vernant, P., Lawrence, S., Ergintav, S., Cakmak, R., Ozener, H., Kadirov, F., Guliev, I., Stepanyan, R., Nadariya, M., Hahubia, G., Mahmoud, S., Sakr, K., ArRajehi, A., Paradissis, D., Al-Aydrus, A., Prilepin, M., Guseva, T., Evren, E., Dmitrotsa, A., Filikov, S. V., Gomez, F., Al-Ghazzi, R., and Karam, G. (2006). Gps constraints on continental deformation in the Africa-Arabia-Eurasia continental collision zone and implications for the dynamics of plate interactions. *Journal of Geophysical Research: Solid Earth*, 111(B5).

Rosen, P., Hensley, S., Joughin, I., K.Li, F., Madsen, S., Rodriguez, E., and Goldstein, R. M. (2000). Synthetic Aperture Radar interferometry. *Proceedings of the IEEE*, 88(3):333–382.

Ryder, I. and Bürgmann, R. (2008). Spatial variations in slip deficit on the central San Andreas Fault from InSAR. *Geophysical Journal International*, 175(3):837–852.

Saastamoinen, J. (1972). Contributions to the theory of atmospheric refraction. *Bulletin gĕodĕsique*, 105(1):279–298.

Sadeh, M., Hamiel, Y., Ziv, A., Bock, Y., Fang, P., and Wdowinski, S. (2012). Crustal deformation along the Dead Sea Transform and the Carmel Fault inferred from 12 years of GPS measurements. *Journal of Geophysical Research: Solid Earth*, 117(B8).

Said, R. (1962). *The Geology of Egypt / edited by Rushdi Said*. Elsevier.

Said, R. (1990). *The Geology of Egypt / edited by Rushdi Said*. Balkema Rotterdam.

Saleh, M. and Becker, M. (2014). A new velocity field from the analysis of the Egyptian Permanent GPS Network {EPGN}. *Arabian Journal of Geosciences*, 7(11):4665–4682.

Saleh, M. and Becker, M. (2015). New constraints on the Nubia-Sinai-Dead Sea fault crustal motion. *Tectonophysics*, 651-652(0):79 – 98.

Sandwell, D. T. and Price, E. J. (1998). Phase gradient approach to stacking interferograms. *Journal of Geophysical Research: Solid Earth*, 103(B12):183–204.

Savage, J. C. and Burford, R. O. (1973). Geodetic determination of relative plate motion in central California. *Journal of Geophysical Research*, 78(5):832–845.

Scharroo, R. and Visser, P. (1998). Precise orbit determination and gravity field improvement for the ERS satellites. *Journal of Geophysical Research: Oceans*, 103(C4):8113–8127.

Schmidt, D. A. and Bürgmann, R. (2003). Time-dependent land uplift and subsidence in the Santa Clara valley, California, from a large interferometric synthetic aperture radar data set. *Journal of Geophysical Research: Solid Earth*, 108(B9).

Sella, G. F., Dixon, T. H., and Mao, A. (2002). REVEL: A model for Recent plate velocities from space geodesy. *Journal of Geophysical Research: Solid Earth*, 107(B4):ETG 11–1–ETG 11–30.

Shanker, P. A. (2010). *Persistent scatterer interferometry in natural terrain*. PhD thesis, Stanford University.

Stanley, D. J. (1990). Recent subsidence and northeast tilting of the Nile delta, Egypt. *Marine Geology*, 94:147–154.

Stanley, D. J. (1996). Nile delta: extreme case of sediment entrapment on a delta plain and consequent coastal land loss. *Marine Geology*, 129:189–195.

Stanley, D. J. and Warne, A. G. (1994). Worldwide initiation of holocene marine deltas by deceleration of Sea-level rise. *Science*, 265(5169):228–231.

Thompson, A. R., Moran, J. M., and Swenson, G. W. (1986). *Interferometry and synthesis in radio Astronomy*. Wiley-Interscience.

Wang, H. and Wright, T. (2012). Satellite geodetic imaging reveals internal deformation of western Tibet. *Geophysical Research Letters*, 39(7).

Wdowinski, S., Bock, Y., Baer, G., Prawirodirdjo, L., Bechor, N., Naaman, S., Knafo, R., Forrai, Y., and Melzer, Y. (2004). GPS measurements of current crustal movements along the Dead Sea Fault. *Journal of Geophysical Research: Solid Earth*, 109(B5).

Werner, C., Wegmuller, U., Strozzi, T., and Wiesmann, A. (2003). Interferometric point target analysis for deformation mapping. In *Geoscience and Remote Sensing Symposium, 2003. IGARSS '03. Proceedings. 2003 IEEE International*, volume 7, pages 4362–4364 vol.7.

Wessel, P. and Bercovici, D. (1998). Interpolation with splines in tension: A Green's function approach. *Mathematical Geology*, 30(1):77–93.

Williams, S. (2008). CATS: GPS coordinate time series analysis software. *GPS Solutions*, 12(2):147–153.

Williams, S. D. P. (2003). The effect of coloured noise on the uncertainties of rates estimated from geodetic time series. *Journal of Geodesy*, 76(9-10):483–494.

World-Bank (2015). World DataBank. http://www.worldbank.org/.

Wright, T., Fielding, E., and Parsons, B. (2001). Triggered slip: Observations of the 17 august 1999 Izmit (Turkey) earthquake using radar interferometry. *Geophysical Research Letters*, 28(6):1079–1082.

Wright, T. J., Parsons, B. E., and Lu, Z. (2004). Toward mapping surface deformation in three dimensions using InSAR. *Geophysical Research Letters*, 31(1).

Wübbena, G. (1985). Software developments for geodetic positioning with GPS using TI 4100 code and carrier measurements. In Goad, C., editor, *the 1st International Symposium on Precise Positioning with the Global Positioning System*, pages 403–412.

Zebker, H. and Rosen, P. (1994). On the derivation of coseismic displacement fields using differential radar interferometry: The Landers earthquake. In *Geoscience and Remote Sensing Symposium, 1994. IGARSS 94. Surface and Atmospheric Remote Sensing: Technologies, Data Analysis and Interpretation., International*, volume 1, pages 286–288.

Zebker, H. and Villasenor, J. (1992). Decorrelation in interferometric radar echoes. *Geoscience and Remote Sensing, IEEE Transactions on*, 30(5):950–959.

Zebker, H. A. and Goldstein, R. M. (1986). Topographic mapping from interferometric synthetic aperture radar observations. *Journal of Geophysical Research: Solid Earth*, 91(B5):4993–4999.

Tables

Table A1. Parameters of focal mechanisms plotted in Figure 2.5 for earthquakes occurred in Egypt from 1976-2012. The earthquake focal mechanism solutions are from the global CMT and Abou Elenean (2007).

Location		Mechanism			Magnitude	Date	
Long.	Lat.	Strike	Dip	Rake	M_L	D M Y	Remarks
35.59	30.54	197	40	-4	5.89	23041979	CMT
32.38	23.88	146	72	-15	6.17	14111981	CMT
33.85	25.86	281	45	-110	5.04	02071984	CMT
30.63	29.74	136	42	-75	5.55	12101992	CMT
34.40	28.62	139	36	-122	1.76	03081993	CMT
34.08	28.36	142	13	-123	4.65	03081993	CMT
34.73	29.07	196	59	-15	7.21	22111995	CMT
34.48	29.31	199	77	7	3.85	23111995	CMT
34.37	29.03	132	30	-104	1.14	21021996	CMT
27.36	31.39	154	44	89	1.98	28051998	CMT
35.31	31.62	340	50	-15	1.15	11022004	CMT
26.06	33.92	306	33	116	1.62	30052005	CMT
25.74	33.94	138	80	178	5.82	02092005	CMT
35.32	33.27	71	69	-167	6.56	15022008	CMT
26.68	33.97	117	46	-18	1.26	04082008	CMT
25.50	34.00	295	32	108	5.85	01072009	CMT
34.01	27.57	343	33	-75	2.39	30012012	CMT
31.02	32.44	206	44	131	3.96	19102012	CMT
27.64	31.45	322	42	67	6.00	28051998	Abou Elenean (2007)
31.22	26.44	291	45	-80	5.40	14121998	Abou Elenean (2007)
31.54	28.65	129	62	-49	5.10	11101999	Abou Elenean (2007)
31.50	30.24	107	70	-85	4.30	28121999	Abou Elenean (2007)
33.12	28.55	311	80	-23	3.20	09052000	Abou Elenean (2007)
32.58	29.99	6	56	-10	2.50	01062000	Abou Elenean (2007)
33.48	28.21	131	52	-51	4.60	25062000	Abou Elenean (2007)
31.59	29.55	135	48	-48	4.00	29062000	Abou Elenean (2007)
32.71	23.68	336	85	-7	4.20	16102000	Abou Elenean (2007)
32.71	23.67	337	84	-24	4.40	18102000	Abou Elenean (2007)
32.84	28.93	119	46	-76	4.40	03112000	Abou Elenean (2007)
31.09	30.28	307	59	-60	3.40	29122000	Abou Elenean (2007)
33.27	28.47	167	57	-66	3.70	05012001	Abou Elenean (2007)
31.55	28.75	173	25	-35	3.30	08042001	Abou Elenean (2007)
31.49	29.02	336	70	-2	2.60	09062001	Abou Elenean (2007)
31.15	29.66	320	40	-82	4.10	12062001	Abou Elenean (2007)
30.62	29.95	25	18	-33	2.30	07082001	Abou Elenean (2007)
34.01	27.47	232	55	-30	3.90	18082001	Abou Elenean (2007)
33.96	27.45	261	60	-19	3.50	20082001	Abou Elenean (2007)
33.95	27.45	197	66	-33	3.10	20082001	Abou Elenean (2007)
34.01	27.43	247	62	-22	4.60	20082001	Abou Elenean (2007)
33.98	27.44	249	68	-13	3.90	20082001	Abou Elenean (2007)
32.51	30.04	203	52	-12	3.10	16102001	Abou Elenean (2007)
30.88	29.57	320	45	-83	4.20	17122001	Abou Elenean (2007)
31.82	28.73	178	66	-39	2.90	28012002	Abou Elenean (2007)
33.67	27.99	124	30	-80	3.70	13022002	Abou Elenean (2007)
32.71	23.63	330	84	-8	3.70	21052002	Abou Elenean (2007)
31.08	29.66	303	41	-74	3.20	22062002	Abou Elenean (2007)
31.12	29.88	308	71	-47	3.60	07082002	Abou Elenean (2007)

31.35	30.15	280	50	-90	4.30	24082002	Abou Elenean (2007)
29.88	27.49	343	57	-13	4.80	18092002	Abou Elenean (2007)
33.62	27.53	270	40	-105	3.80	25102002	Abou Elenean (2007)
34.62	28.23	175	76	-64	4.10	10112002	Abou Elenean (2007)
32.24	29.96	164	36	-73	3.60	05122002	Abou Elenean (2007)
34.74	27.29	330	62	-49	3.60	07122002	Abou Elenean (2007)
32.14	29.65	16	46	-10	3.30	06012003	Abou Elenean (2007)
32.63	28.92	318	55	-84	3.40	15012003	Abou Elenean (2007)
32.88	28.51	155	27	-67	3.30	01042003	Abou Elenean (2007)
32.77	29.13	182	44	-22	3.10	03042003	Abou Elenean (2007)
32.75	28.99	174	66	-51	3.50	22042003	Abou Elenean (2007)
30.65	29.75	165	86	-25	3.50	18052003	Abou Elenean (2007)
32.01	27.10	292	44	-85	5.10	04062003	Abou Elenean (2007)
31.14	29.65	128	44	-60	3.10	27062003	Abou Elenean (2007)
32.34	29.82	356	64	-16	3.00	03072003	Abou Elenean (2007)
31.77	29.35	330	75	-80	2.70	31072003	Abou Elenean (2007)
32.74	28.92	116	56	-53	3.80	09092003	Abou Elenean (2007)
32.34	29.84	323	46	-54	3.10	10092003	Abou Elenean (2007)
32.35	29.82	339	48	-31	3.60	11092003	Abou Elenean (2007)
33.80	28.03	269	42	-105	3.00	11102003	Abou Elenean (2007)
31.10	29.81	136	52	-71	2.80	12102003	Abou Elenean (2007)

Table A2. GPS horizontal Velocities in Eurasia-fixed reference frame.

Stations	**Long.**	**Lat.**	V_e **(mm/yr)**	V_n **(mm/yr)**	σ_e **(mm)**	σ_n **(mm)**	**Tectonic Plate**	**Remarks**
ABPO	47.23	-19.02	4.23	6.69	0.46	0.78	SOMALIA	P-IGS
ABSM	31.55	22.49	-0.40	6.44	1.04	0.64	NUBIA	P-EGY
AD01	34.66	25.50	-0.57	6.75	3.47	2.36	NUBIA	E-EGY
AD02	34.54	25.44	-0.56	6.74	2.10	1.90	NUBIA	E-EGY
AD03	34.51	25.36	-0.56	6.74	2.76	1.75	NUBIA	E-EGY
AD04	34.38	25.36	-0.56	6.73	2.61	2.57	NUBIA	E-EGY
AD05	34.42	25.23	-0.55	6.73	2.16	1.99	NUBIA	E-EGY
AD06	34.50	25.24	-0.55	6.74	2.67	2.68	NUBIA	E-EGY
AD07	34.62	25.24	-0.54	6.75	1.90	2.32	NUBIA	E-EGY
AD08	34.75	25.29	-0.54	6.76	2.52	2.55	NUBIA	E-EGY
AD09	34.69	25.41	-0.55	6.75	1.64	2.91	NUBIA	E-EGY
AD10	34.63	25.33	-0.55	6.75	1.95	2.09	NUBIA	E-EGY
AD11	34.48	25.31	-0.55	6.73	1.40	2.31	NUBIA	E-EGY
ADIS	38.77	9.04	1.18	7.13	0.40	0.80	NUBIA	P-IGS
ALAK	33.38	23.29	-0.40	6.63	1.88	1.63	NUBIA	E-EGY
ALEX	29.91	31.20	-1.42	6.28	1.09	1.67	NUBIA	P-EGY
ALIS	32.59	23.39	-0.45	6.55	1.88	3.70	NUBIA	E-EGY
ALON	34.61	31.71	-2.12	8.26	0.20	0.28	SINIA	P-SOP
ANKR	32.76	39.89	-22.32	0.99	0.49	0.46	ANATOLIA	P-IGS
ARAB	30.56	27.87	-1.02	6.34	5.07	2.98	NUBIA	E-EGY
ARSH	33.62	31.11	-1.78	7.67	0.80	0.78	SINIA	P-EGY
ASHM	31.01	30.30	-1.26	6.39	1.99	2.29	NUBIA	E-EGY
ASUT	31.56	27.40	-0.92	6.45	0.12	0.33	NUBIA	P-EGY
BEER	33.24	23.66	-0.45	6.61	2.45	0.98	NUBIA	E-EGY
BHR1	50.61	26.21	6.04	22.90	0.39	0.59	ARABIA	P-IGS
BHR2	50.61	26.21	6.04	22.90	0.40	0.66	ARABIA	P-IGS
BJCO	2.45	6.39	1.06	2.79	0.54	0.90	NUBIA	P-IGS
BORG	29.57	30.86	-1.40	6.24	1.04	1.69	NUBIA	P-EGY
BSHM	35.02	32.78	-2.81	8.51	0.30	0.95	SINIA	P-SOP
BUCU	26.13	44.46	0.00	0.00	0.47	0.22	EURASIA	P-IGS
CAGZ	8.97	39.14	2.09	4.44	0.15	0.16	EURASIA	P-IGS
CGGN	9.12	10.12	0.58	3.73	0.71	1.63	NUBIA	P-IGS
CRAO	33.99	44.41	0.00	0.00	0.25	0.31	EURASIA	P-IGS
CSAR	34.89	32.49	-2.62	8.43	0.21	0.37	SINIA	P-SOP
DAHM	33.09	23.82	-0.47	6.60	2.62	1.32	NUBIA	E-EGY
DKHL	28.96	24.32	-0.71	6.17	3.37	5.50	NUBIA	P-EGY
DRAG	35.39	31.59	-1.98	8.73	0.26	0.60	SINIA	P-IGS
DSEA	35.37	31.04	-1.60	8.72	0.18	0.34	SINIA	P-SOP
DUBR	18.11	42.65	0.00	0.00	1.17	1.04	EURASIA	P-IGS
ELAT	34.92	29.51	-0.60	8.45	0.33	0.46	SINIA	P-SOP
ELSF	31.35	29.54	-1.16	6.42	3.91	2.39	NUBIA	E-EGY
FANA	32.57	29.38	-1.08	6.55	4.52	3.33	NUBIA	E-EGY
FARF	28.31	27.15	-1.06	6.10	3.94	5.10	NUBIA	P-EGY
FAYD	32.33	30.28	-1.18	6.52	5.87	4.68	NUBIA	E-EGY
GARF	32.71	23.27	-0.43	6.56	3.20	2.39	NUBIA	E-EGY
GENO	8.92	44.42	0.00	0.00	0.16	0.10	EURASIA	P-IGS
GHNA	31.36	26.54	-0.84	6.43	1.65	2.87	NUBIA	E-EGY
GHRB	33.19	28.20	-0.92	6.61	2.89	2.59	NUBIA	E-EGY
GILB	35.42	32.48	-2.57	8.75	0.26	0.34	SINIA	P-SOP

GMAS	-15.63	27.77	-2.29	0.10	0.30	0.15	NUBIA	P-IGS
GRAS	6.92	43.76	0.00	0.00	0.19	0.14	EURASIA	P-IGS
HALY	36.10	29.14	1.69	13.75	0.25	0.29	ARABIA	P-SOP
HARB	27.71	-25.89	4.52	6.04	0.28	0.49	NUBIA	P-IGS
HRMN	35.79	33.31	-3.10	8.96	0.44	0.43	SINIA	P-SOP
HUGS	36.19	32.10	-0.61	13.81	1.08	1.82	ARABIA	P-SOP
HURG	33.61	27.31	-0.81	6.65	2.17	3.30	NUBIA	E-EGY
HYKS	31.42	30.06	-1.21	6.43	2.85	2.62	NUBIA	E-EGY
IENG	7.64	45.02	0.00	0.00	0.22	0.14	EURASIA	P-IGS
IFRN	-5.11	33.54	-3.06	1.68	0.33	0.19	NUBIA	P-UNA
ISBA	44.44	33.34	-0.27	19.16	0.84	0.52	ARABIA	P-IGS
ISTA	29.02	41.10	0.00	0.00	0.26	0.22	EURASIA	P-IGS
JSLM	35.20	31.77	-2.11	8.62	0.28	0.41	SINIA	P-SOP
JUST	35.99	32.49	-0.94	13.68	1.38	1.63	ARABIA	P-SOP
KABR	35.15	33.02	-2.96	8.58	0.24	0.43	SINIA	P-SOP
KATA	31.83	29.93	-1.17	6.47	0.31	0.50	NUBIA	P-EGY
KATZ	35.69	33.00	-2.90	8.91	0.22	0.57	SINIA	P-SOP
KENT	32.89	29.27	-0.58	7.24	3.93	4.36	SINIA	E-EGY
KL82	32.45	23.54	-0.47	6.54	2.23	0.79	NUBIA	E-EGY
KLHV	34.87	31.38	-1.87	8.42	0.29	0.33	SINIA	P-SOP
LAGO	-8.67	37.10	0.00	0.00	0.18	0.20	EURASIA	P-EPN
LAMP	12.61	35.50	-2.80	4.20	0.29	0.42	NUBIA	P-EPN
LHAV	34.87	31.38	-1.87	8.42	0.60	0.40	SINIA	P-SOP
LROC	-1.22	46.16	0.00	0.00	0.20	0.18	EURASIA	P-IGS
MAL2	40.19	-3.00	5.72	7.14	0.71	0.37	SOMALIA	P-IGS
MALI	40.19	-3.00	5.72	7.14	1.52	0.46	SOMALIA	P-IGS
MNAM	-15.63	27.76	-2.29	0.10	3.27	2.78	NUBIA	E-EGY
MAS1	16.71	40.65	0.00	0.00	0.48	0.52	NUBIA	P-IGS
MAT1	23.53	-19.90	4.14	5.57	0.25	0.28	EURASIA	P-IGS
MAUA	30.74	-0.60	5.88	7.58	1.01	0.90	NUBIA	P-UNA
MBAR	11.65	44.52	0.00	0.00	0.22	0.24	SOMALIA	P-IGS
MEDI	32.99	24.02	-0.49	6.59	0.40	0.25	EURASIA	P-IGS
MNSO	31.35	31.04	-1.32	6.42	0.54	0.26	NUBIA	P-EGY
MRSA	34.88	25.07	-0.51	6.77	0.34	0.37	NUBIA	P-EGY
MSLT	30.89	29.51	-1.18	6.38	0.43	0.50	NUBIA	P-EGY
MUTA	35.72	31.10	0.12	13.50	0.61	0.59	ARABIA	P-SOP
NAGH	32.34	25.68	-0.70	6.52	5.81	2.56	NUBIA	E-EGY
NAMA	42.05	19.21	9.92	17.64	0.91	0.28	ARABIA	P-SOP
NICO	33.40	35.14	-5.12	2.92	0.20	0.54	ANATOLIA	P-IGS
NKHL	33.98	29.93	-0.96	7.89	0.17	0.49	SINIA	P-EGY
NKLG	9.67	0.35	1.94	3.80	0.36	0.64	NUBIA	P-IGS
NMAR	32.55	23.68	-0.48	6.55	1.81	2.49	NUBIA	E-EGY
NOMI	25.43	36.42	-9.01	-21.09	5.66	0.80	ANATOLIA	P-UNA
NOT1	14.99	36.88	-2.87	4.51	0.37	0.27	NUBIA	P-IGS
NRIF	35.04	30.04	-0.95	8.52	0.26	0.34	SINIA	P-SOP
OSJE	18.68	45.56	0.00	0.00	0.21	0.40	EURASIA	P-IGS
PADO	11.90	45.41	0.00	0.00	0.24	0.24	EURASIA	P-IGS
PETA	35.47	30.33	0.69	13.33	2.10	1.64	ARABIA	P-SOP
PHLW	31.34	29.86	-1.19	6.42	0.30	0.25	NUBIA	P-EGY
PLBS	31.56	30.37	-1.24	6.45	1.92	3.17	NUBIA	E-EGY
PORT	31.01	26.94	-0.90	6.39	3.32	4.68	NUBIA	E-EGY
PRE1	28.22	-25.75	4.56	7.66	0.70	1.06	SOMALIA	P-IGS
PYRA	31.12	29.97	-1.22	6.40	3.32	2.52	NUBIA	E-EGY
QANT	32.60	30.25	-1.27	7.06	7.61	13.86	SINIA	E-EGY
QENA	32.89	26.18	-0.72	6.58	3.84	2.61	NUBIA	E-EGY

RABT	-6.85	34.00	-3.15	1.42	0.23	0.13	NUBIA	P-IGS
RAMO	34.76	30.60	-1.35	8.36	0.19	0.46	SINIA	P-IGS
RARO	32.71	23.72	-0.48	6.56	2.61	1.11	NUBIA	E-EGY
RASH	34.80	28.30	2.21	12.88	0.49	0.64	ARABIA	P-SOP
RBAY	32.08	-28.80	4.09	7.53	1.36	1.94	SOMALIA	P-IGS
RCMN	36.89	-1.22	5.83	7.32	0.38	0.40	SOMALIA	P-IGS
REST	32.61	23.95	-0.50	6.55	3.35	2.95	NUBIA	E-EGY
REUN	55.57	-21.21	3.67	6.02	0.45	0.66	SOMALIA	P-IGS
RUDS	33.32	28.71	-0.17	7.50	6.98	9.03	SINIA	E-EGY
SAFG	33.93	26.57	-0.71	6.68	0.32	0.26	NUBIA	P-EGY
SEDR	32.69	29.77	-0.93	7.12	5.80	2.82	SINIA	E-EGY
SEY1	55.48	-4.67	5.47	6.02	0.46	0.33	SOMALIA	P-IGS
SFER	-6.21	36.46	0.00	0.00	0.15	0.10	EURASIA	P-IGS
SHAD	30.85	27.99	-1.02	6.37	2.54	2.40	NUBIA	E-EGY
SHLA	35.40	23.11	-0.29	6.82	0.24	0.19	NUBIA	P-EGY
SIMO	18.44	-34.19	5.66	4.95	0.45	0.71	NUBIA	P-IGS
SLOM	34.28	31.23	-1.82	8.07	0.97	0.61	SINIA	P-SOP
SLUM	25.21	31.49	-1.71	5.76	0.34	0.46	NUBIA	P-EGY
SOFI	23.40	42.56	0.00	0.00	0.14	0.29	EURASIA	P-IGS
SOHG	31.82	26.47	-0.81	6.47	1.72	3.28	NUBIA	E-EGY
SOKN	32.41	29.78	-1.13	6.53	2.70	3.67	NUBIA	E-EGY
SOLA	46.40	24.91	6.28	20.37	0.36	0.37	ARABIA	P-SOP
SUTH	20.81	-32.38	5.39	5.24	0.46	0.61	NUBIA	P-IGS
SUTM	20.81	-32.38	5.39	5.24	0.31	0.56	NUBIA	P-IGS
TAYS	34.87	28.55	2.02	12.93	0.79	0.71	ARABIA	P-SOP
TEHN	51.33	35.70	0.74	12.68	0.78	0.46	EURASIA	P-IGS
TELA	34.78	32.07	-2.35	8.37	0.61	0.44	SINIA	P-SOP
TLSE	1.48	43.56	0.00	0.00	0.30	0.19	EURASIA	P-IGS
TOUR	33.73	28.16	0.23	7.74	3.92	7.92	SINIA	E-EGY
TRAB	39.78	41.00	0.00	0.00	0.63	0.57	EURASIA	P-IGS
TUBI	29.45	40.79	0.00	0.00	0.27	0.22	EURASIA	P-IGS
UNIV	32.87	24.00	-0.50	6.58	1.68	1.76	NUBIA	E-EGY
VILL	-3.95	40.44	0.00	0.00	0.23	0.15	EURASIA	P-IGS
WADI	31.35	27.04	-0.89	6.42	1.77	2.29	NUBIA	E-EGY
WAHA	30.69	29.66	-1.21	6.36	2.35	2.88	NUBIA	E-EGY
WIND	17.09	-22.58	4.62	4.78	0.36	0.49	NUBIA	P-IGS
YEBE	-3.09	40.53	0.00	0.00	0.15	0.13	EURASIA	P-IGS
YIBL	56.11	22.19	9.75	26.01	0.57	0.59	ARABIA	P-IGS
YKRO	-5.24	6.87	0.95	1.66	1.27	1.35	NUBIA	P-IGS
YOSH	35.21	32.10	-2.34	8.62	0.27	0.82	SINIA	P-SOP
YRCM	34.93	30.99	-1.61	8.46	0.22	0.21	SINIA	P-SOP
ZAFR	32.81	28.71	-0.99	6.57	5.96	7.92	NUBIA	E-EGY
ZAMB	28.31	-15.43	3.56	6.10	0.20	0.34	NUBIA	P-IGS
ZECK	41.57	43.79	0.00	0.00	0.33	0.38	EURASIA	P-IGS
ZOMB	35.33	-15.38	4.98	7.39	0.46	0.53	SOMALIA	P-UNA

Table A3. Horizontal velocity field of Sinai and Arabian GPS sites in Nubia-fixed frame with uncertainties.

Stations	Long.	Lat.	V_e (mm/yr)	V_n (mm/yr)	σ_e (mm)	σ_n (mm)	Remarks
ALON	34.61	31.71	-0.89	1.51	0.20	0.28	Sinai
ARSH	33.62	31.11	-0.55	1.02	0.80	0.78	Sinai
BSHM	35.02	32.78	-1.50	1.72	0.30	0.95	Sinai
CSAR	34.89	32.49	-1.33	1.65	0.21	0.37	Sinai
DRAG	35.39	31.59	-0.81	1.90	0.26	0.60	Sinai
DSEA	35.37	31.04	-0.49	1.89	0.18	0.34	Sinai
ELAT	34.92	29.51	0.39	1.67	0.33	0.46	Sinai
GILB	35.42	32.48	-1.32	1.92	0.26	0.34	Sinai
HRMN	35.79	33.31	-1.79	2.10	0.44	0.43	Sinai
JSLM	35.20	31.77	-0.91	1.81	0.28	0.41	Sinai
KABR	35.15	33.02	-1.64	1.78	0.24	0.43	Sinai
KATZ	35.69	33.00	-1.61	2.05	0.22	0.57	Sinai
KENT	32.89	29.27	0.51	0.65	0.79	0.87	Sinai
KLHV	34.87	31.38	-0.69	1.64	0.29	0.33	Sinai
LHAV	34.87	31.38	-0.69	1.64	0.60	0.40	Sinai
NKHL	33.98	29.93	0.14	1.20	0.23	0.27	Sinai
NRIF	35.04	30.04	0.09	1.73	0.26	0.34	Sinai
QANT	32.60	30.25	-0.06	0.51	1.52	2.77	Sinai
RAMO	34.76	30.60	-0.24	1.59	0.19	0.46	Sinai
RUDS	33.32	28.71	0.84	0.87	1.40	1.81	Sinai
SEDR	32.69	29.77	0.22	0.55	1.16	0.56	Sinai
SLOM	34.28	31.23	-0.61	1.35	0.97	0.61	Sinai
TELA	34.78	32.07	-1.09	1.60	0.61	0.44	Sinai
TOUR	33.73	28.16	1.15	1.07	0.78	1.58	Sinai
YOSH	35.21	32.10	-1.10	1.81	0.27	0.82	Sinai
YRCM	34.93	30.99	-0.47	1.67	0.22	0.21	Sinai
YIBL	56.11	22.19	8.94	17.71	0.57	0.59	Arabia
BHR1	50.61	26.21	5.80	14.89	0.39	0.59	Arabia
BHR2	50.61	26.21	5.80	14.89	0.40	0.66	Arabia
SOLA	46.40	24.91	6.20	12.63	0.36	0.37	Arabia
ISBA	44.44	33.34	0.45	11.56	0.84	0.52	Arabia
NAMA	42.05	19.21	9.58	10.23	0.91	0.28	Arabia
HALY	36.10	29.14	2.58	6.86	0.25	0.29	Arabia
HUGS	36.19	32.10	0.56	6.91	1.08	1.82	Arabia
JUST	35.99	32.49	0.28	6.79	1.38	1.63	Arabia
MUTA	35.72	31.10	1.22	6.64	0.61	0.59	Arabia
PETA	35.47	30.33	1.73	6.50	2.10	1.64	Arabia
RASH	34.80	28.30	3.09	6.11	0.49	0.64	Arabia
TAYS	34.87	28.55	2.92	6.15	0.79	0.71	Arabia

Figures

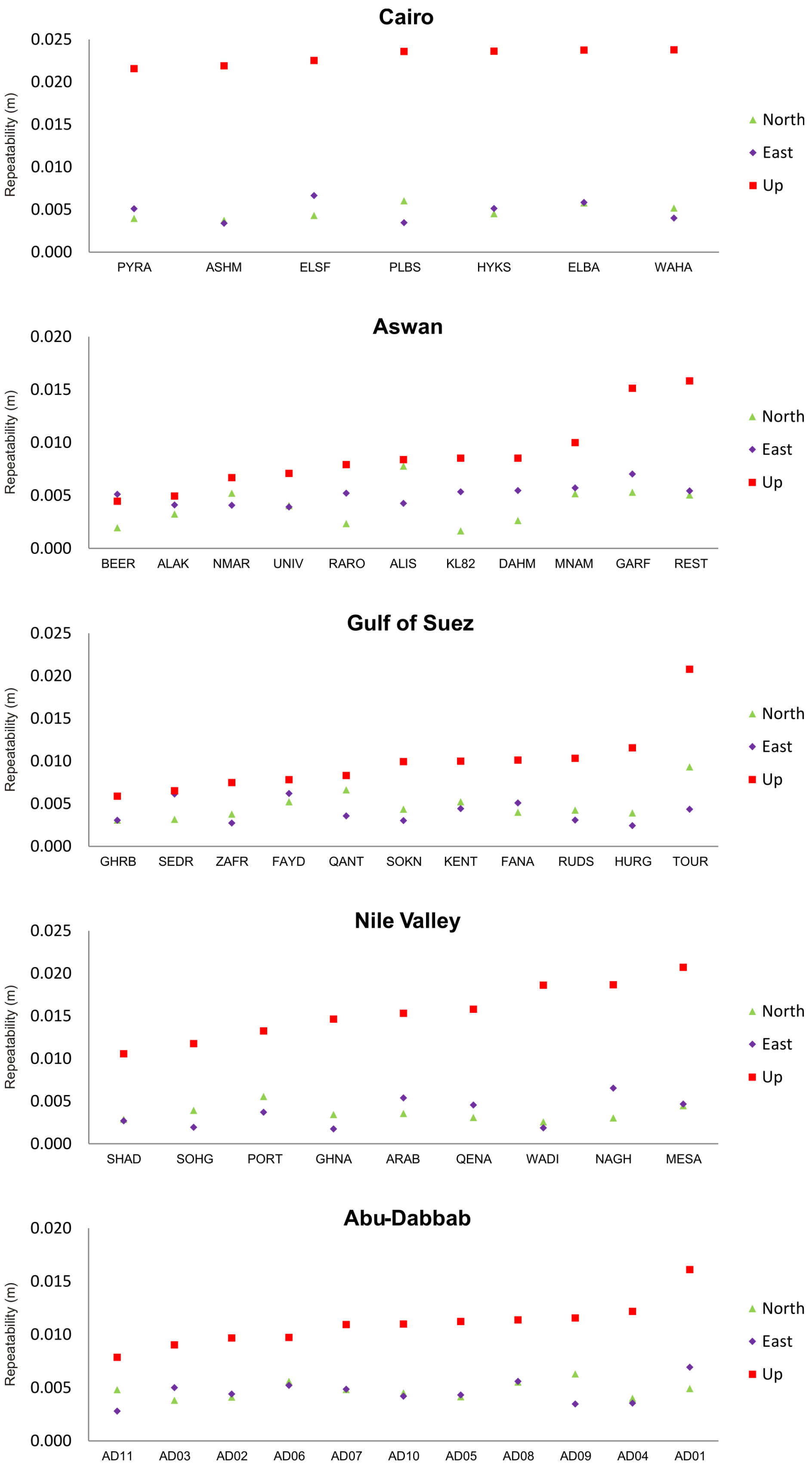

Figure A1. Repeatabilities of the local geodetic networks, Cairo, Aswan, Gulf of Suez, Nile Valley and Abu-Dabbab.

Curriculum Vitae

Name	Mohamed Saleh Ahmed Mohamed
Date of birth	26.10.1983
Place of birth	Cairo
Nationality	Egyptian

Education

2012 -	**Technische Universität Darmstadt, Fachgebiet für Physikalische Geodäsie und Satellitengeodäsie, TU- Darmstadt, Germany** Ph.D. Student
2008 - 2011	**Al-Azhar University, Cairo, Egypt** M.Sc. Geophysics
2007 - 2008	**Al-Azhar University, Cairo, Egypt** Pre-Master in Geophysics
2001 - 2005	**Al-Azhar University, Cairo, Egypt** B.Sc. In Geology

Experience

2011 -	**National Research Institute of Astronomy and Geo-physics (NRIAG), Helwan, Egypt** Assistant Research
2007 - 2011	**National Research Institute of Astronomy and Geo-physics (NRIAG), Helwan, Egypt** Research Assistant

Membership

2012 -	**ICTP North African Group for Earthquake and Tsunami studies**
2011 -	**Egyptian Geophysical Society**